



FR9704887

ORSAY  
Numéro d'ordre:

LAL 96-43  
Juin 1996

UNIVERSITE de PARIS-SUD  
Centre d'Orsay

THESE

*présentée  
pour obtenir*

*Le grade de DOCTEUR EN SCIENCES  
de l'Université de Paris XI Orsay*

par

Yong BAN

**Études de la partie électrofaible des interactions  
Electron(Positron)-Proton à HERA**

Thèse soutenue le 11 Juin 1996, devant la Commission d'examen:

M.	J.	LEFRANÇOIS	Président
	A.	CORDIER	
Mme.	A.	JACHOLKOWSKA	
M.	D.	HAIDT	
	F.	RENARD	
	P.	ROUDEAU	

## Abstract

The Standard Model of the Electroweak Theory can be tested at HERA, the electron-proton collider, through the study of the deep-inelastic  $ep$  scattering at the center of mass energy of about 300 GeV, complementary to the previous experiments by extending the kinematic domain to a region where the weak propagators of  $W$  and  $Z$  play a predominant role.

This work presents an analysis on the charged current and the neutral current processes from the 1993 and 1994 electro(positron)-proton interaction data at HERA acquired by the H1 detector. We have measured the ratio between the integrated cross sections of the neutral current and the charged current processes, and the integrated charged current cross sections, with a cut at 25 GeV on the hadronic transverse momentum. The charged current and the neutral current events were selected in parallel, i.e. following the same vertex, trigger and technical requirements, and the background rejection cuts were applied to the NC and CC samples in the same way. The kinematic variables were calculated only using the informations from the hadronic energy flow. We have also measured the differential cross sections as a function of the momentum transfer variable in four bins for both processes.

The results agree well with the Standard Model predictions. The mass of the weak intermediate  $W$  boson implied by these results is also in good agreement with the previous measurements in other laboratories. The effect of the  $W$ -propagator in the Deep Inelastic charged current process is observed, for the first time, in these measurements.

### Key words:

HERA

H1

Electroweak interaction

Charged Current

Neutral Current

# Remerciements

Tout d'abord, je veux exprimer ma reconnaissance à Michel Davier et Jacques Lefrançois, directeurs du Laboratoire de l'Accélérateur Linéaire, qui m'ont accueilli dans leur laboratoire afin de pouvoir préparer cette thèse; à Agnieszka Jacholkowska, mon directeur de thèse, pour ses conseils, ses explications et sa patience incessante au cours de ces années de recherche.

Je remercie chaleureusement Jacques Lefrançois qui a bien voulu accepter la présidence du jury, et les membres du jury: Alain Cordier, Dieter Haidt, particulièrement Fernand Renard et Patrik Roudeau, qui ont accepté d'être rapporteurs de ce travail et m'ont donné de nombreux commentaires.

Je remercie avec une attention toute particulière Violette Brisson et Christian Pascaud, pour leurs conseils et encouragements dans l'analyse, leur lecture attentive du manuscrit et leurs nombreuses remarques.

Merci à tout le groupe de H1-LAL dirigé par Christian Pascaud: Jean-Claude Bizot, André Courau, Benoit Delcourt, Laurent Favart, Michel Jaffré, Smain Kermiche, Georges Lobo, Peter Loch, Fabrice Squinabol et Fabien Zomer pour leur aide au cours de cette thèse, auprès desquels le travail fut agréable grâce à la bonne ambiance qu'ils ont su faire régner. Je remercie particulièrement Zhiqing Zhang pour l'aide qu'il m'a apportée, surtout au début de ce travail.

Je tiens également à remercier tous les membres de Electrofaible Groupe de H1 collaboration guidée par Dieter Haidt, Claude Vallée et Rolf Beyer. Notamment, j'ai eu beaucoup de profit à discuter avec Achim Braemer, Lars Büengener, Axel Pieuchot et André Schöening, et eu beaucoup de plaisir à travailler en leur compagnie.

Merci enfin à toute l'équipe du secrétariat scientifique du LAL dirigée par Nicole Mathieu, pour la réalisation matérielle de cette thèse.

# Contents

<b>1</b>	<b>Introduction</b>	<b>1</b>
<b>2</b>	<b>Electroweak Interactions In Deep Inelastic <math>e - p</math> Scattering</b>	<b>5</b>
2.1	Theoretical Aspects of the Electroweak Physics . . . . .	5
2.1.1	Standard Model of the Electroweak Interactions . . . . .	6
2.1.2	Electroweak Parameters in the Standard Model . . . . .	12
2.2	Deep Inelastic $ep$ Scattering at HERA . . . . .	13
2.2.1	Kinematics Variables In Deep Inelastic Scattering . . . . .	13
2.2.2	Cross Sections In NC and CC Processes . . . . .	16
2.3	Measurement of the Electroweak Parameters . . . . .	22
2.3.1	Choice of the Set of Electroweak Parameters at HERA . . . . .	24
2.3.2	Measurement of the $\sigma^{NC}/\sigma^{CC}$ Ratio . . . . .	25
<b>3</b>	<b>HERA And H1 Experiment</b>	<b>33</b>
3.1	The HERA $ep$ Collider . . . . .	33
3.2	The H1 Detector . . . . .	36
3.2.1	Calorimeter . . . . .	39
3.2.2	Tracking System . . . . .	49

3.2.3	H1 Trigger And Data Acquisition System . . . . .	57
<b>4</b>	<b>Selection of The Charged and Neutral Current Events</b>	<b>63</b>
4.1	Technical requirements on luminosity runs . . . . .	65
4.1.1	Event Classification . . . . .	66
4.1.2	Technical requirements . . . . .	68
4.2	Selection of Charged current events . . . . .	69
4.2.1	$P_{t.miss}$ cut . . . . .	69
4.2.2	Vertex requirement . . . . .	78
4.2.3	Trigger requirement . . . . .	93
4.2.4	Background rejection . . . . .	94
4.3	Selection of Neutral current events . . . . .	101
4.3.1	Electron identification . . . . .	102
4.3.2	$P_{t.had.}$ cut . . . . .	106
4.3.3	Vertex requirement . . . . .	107
4.3.4	Trigger requirement . . . . .	109
4.3.5	Background rejection . . . . .	109
4.4	Final CC and NC sample . . . . .	109
<b>5</b>	<b>Measurements of NC/CC Ratio And CC Integrated Cross Sections</b>	<b>117</b>
5.1	Measurement of NC/CC Ratio . . . . .	118
5.1.1	The NC/CC Ratio Calculation . . . . .	118
5.1.2	Systematic Effect In Ratio Measurement . . . . .	135
5.1.3	Conclusions and Physics Implications of NC/CC Ratio Measurement . . . . .	143
5.2	The Integrated Charged Current Cross Sections . . . . .	145

<i>CONTENTS</i>	III
<b>6 The Cross Sections of CC and NC as a Function of <math>Q^2</math></b>	<b>151</b>
6.1 Experimental Measurement of the Kinematic Variables . . . . .	152
6.1.1 Jacquet-Blondel Method . . . . .	152
6.1.2 The Kinematic Distributions of CC and NC events . . . . .	153
6.2 Differential Cross Sections . . . . .	157
6.3 $W$ Mass from the Fit to the $Q^2$ -Distributions of the Charged Current .	166
<b>7 Conclusions</b>	<b>169</b>

# Chapter 1

## Introduction

The theoretical framework to describe the fundamental electromagnetic, weak and strong interactions is the Standard Model. The electromagnetic and weak interactions are unified under the gauge group  $SU(2)_L \otimes U(1)_Y$ , where the interactions are mediated via the exchange of the corresponding spin-1 gauge fields: 1 massless photon for the electromagnetic interactions, and 3 massive bosons  $W^\pm$  and  $Z^0$  for the weak interactions. The Standard Model is one of the most outstanding achievements in modern physics, which can successfully explain most of the experimental facts in particle physics.

The electroweak Standard Model is a renormalizable gauge field theory with several free parameters. Besides the fermion masses and the mass of the Higgs scalar, there are three free parameters in the gauge sector. To test the theory, three independent experimental input data are required to fix the  $SU(2)$  and  $U(1)$  gauge coupling constants  $g, g'$ , and the vacuum expectation value  $v$  of the Higgs field. For deep inelastic scattering, a practical choice of the electroweak parameters are the electromagnetic fine structure constant  $\alpha$  and the masses of the  $Z$  and  $W$  bosons characterizing the photon, neutral current  $Z$  and charged current  $W$  exchanges. The masses  $M_H, m_t$  of the Higgs boson and of the top quark enter the higher order calculations as additional free parameters.

The electroweak Standard Model is continuously tested by the precise measurements in the neutrino sector together with weak boson  $W, Z$  sector in  $e^+e^-$  and  $p\bar{p}$  colliders. The kinematic domain relevant for the electroweak physics is given by  $Q^2$  of the order of  $M_W^2$ . Previously, all direct knowledge on the properties of the  $W$  came from  $p\bar{p}$

colliders at CERN and Fermilab. Information on the mass is deduced from the observed transverse mass distributions and jet analysis.

The HERA collider, which is composed of a 30 GeV electron (positron) beam and a 820 GeV proton beam cumulated in a storage ring, provides an opportunity to study the deep-inelastic electron-proton scattering at the center of mass energy of about 300 GeV, complementary to the  $e^+e^-$  range by extending the low  $Q^2$  lepton-nucleon interactions to values of order  $M_{W,Z}^2$ . At HERA, the weak interactions can be investigated by exploring the charged current process  $e^\pm p \rightarrow \nu_e X$  and the neutral current process  $e^\pm p \rightarrow e^\pm X'$  ( $X, X'$  are the final hadronic states) in an energy regime where the weak propagators of  $W$  and  $Z$  play a prominent role. Thus, the study at HERA provides an additional, important check of the Standard Model and Electroweak Theory.

New informations on the electroweak parameters can be extracted from the experimental observables based on the differential charged current and neutral current cross sections. The  $Q^2$  distribution of the weak charged current cross section can be used to study the effect of the  $W$  propagator, which will provide information about the  $W$  mass. The weak neutral current process provides a check of the overall coupling strength at high  $Q^2$  (the  $\rho$  parameter).

This work presents an analysis on the charged current and neutral current processes based on the 1993  $e^-p$  and 1994  $e^\pm p$  interaction data at HERA acquired by the H1 detector. We have chosen a simple quantity: the ratio between the integrated cross sections of neutral current and charged current processes  $R$  (defined as  $\sigma^{NC}/\sigma^{CC}$  with a cut on the hadronic transverse momentum), as the experimental observable to study the electroweak parameters. The advantages of using the  $R$  ratio are that, while the sensitivity to the electroweak parameters is kept, the systematic uncertainties from the luminosity measurement and from the energy calibration of the calorimeters are canceled or diminished by forming the ratio. Moreover, the theoretical prediction of the ratio is little sensitive to the choice of the structure function parameterization and to the initial state radiation.

In order to get a compromise between the sensitivity to the electroweak parameters and a reasonable statistics, we apply a cut on the transverse momentum of the final hadronic system  $P_t^{had}$ ,  $P_t^{had} > 25$  GeV (corresponding to  $Q^2 > 625$  GeV<sup>2</sup>), in the selection of charged and neutral current events. The quantity  $P_t^{had}$  is measured directly from the experiment, thus by applying this cut the event selection procedure is also simplified. Our choice of  $P_t^{had}$  cut also excludes automatically the low Bjorken- $x$  and high Bjorken- $y$  region which are subject to experimental problems.

The charged and neutral current events are selected in the same way, to ensure that the information on the dependence of the ratio  $R$  on the weak interaction can be extracted properly. The same pre-requirement on beam conditions and run selections (thus the same luminosity) and on the trigger conditions and interaction vertex position are applied to both charged and neutral current events.

In Chapter 2 we will review some theoretical aspects of the electroweak physics, where we will firstly outline the construction of the Standard Model of the electroweak interactions and the derivation of the differential cross sections for charged and neutral current processes in the deep-inelastic-scattering, then we will discuss the measurement of the electroweak parameters at HERA. Chapter 3 gives a brief description of the HERA collider and the H1 detector, where the emphasis is put on the energy measurement in the calorimeter and on the direction measurement in the tracker. The selections of the charged and the neutral current events are discussed in Chapter 4, where we summarize the selection procedures in various steps: the  $P_t^{had}$  cut, the calculation of the event interaction vertex based on the hadronic tracks, the charged current trigger conditions, the background rejection, and after the visual scan, finally we give the numbers of the selected events for 1993 and 1994 data. The ratio  $R$  is given in Chapter 5, where firstly the efficiencies and migration factors from various selection criteria are calculated, and the numbers of events are corrected accordingly. Then the statistical and systematic uncertainties of the  $R$  measurement are investigated in details. The integrated cross sections of the charged current process for 1993 and 1994 data are also given in this chapter. The physics implications of the results are discussed at the end. In Chapter 6, we will give the  $Q^2$  distributions of the charged and neutral current processes for 1993 and 1994 data. The efficiencies, the uncertainties on the  $Q^2$  measurement and the comparison with the theory are discussed. Finally we give some conclusions of this analysis in Chapter 7.

**NEXT PAGE(S)  
left BLANK**

## Chapter 2

# Electroweak Interactions In Deep Inelastic $e - p$ Scattering

The deep inelastic lepton-proton scattering at HERA collider provides important means to study the fundamental electromagnetic, weak and strong interactions at the quark-lepton level. In this chapter, we will first briefly review the general aspects of the electroweak physics in the framework of the Standard Model [1]; then we will outline the calculations of the neutral current and the charged current cross sections in the deep inelastic  $ep$ -scattering process, and discuss the possible measurement of the electroweak parameters at HERA.

### 2.1 Theoretical Aspects of the Electroweak Physics

The theoretical framework which describes the electromagnetic and weak interactions is contained in the quantum field theory of the Standard Model. In the following we will trace back the construction of the Standard Model of the electroweak physics - a gauge theory with four spin-1 gauge fields: 1 massless photon for the electromagnetic interaction and 3 massive bosons  $W^\pm$  and  $Z^0$  for the weak interaction, based on the non-Abelian symmetry gauge group  $SU(2) \otimes U(1)$ . We will end by a discussion of the electroweak Standard Model parameters.

### 2.1.1 Standard Model of the Electroweak Interactions

#### Electromagnetic and weak interactions

The prototypical weak interaction process is  $\beta$ -decay  $n \rightarrow pe^- \bar{\nu}_e$ . In 1930's Fermi developed a theory for the weak processes. In postulating a four-point fermion interaction for the weak processes, he guessed that, by analogy with QED, in weak interaction one would have similar vector currents  $J_\mu$ , which leads to “current · current” Lagrangian:

$$\mathcal{L} = \frac{G_F}{\sqrt{2}} J_{(e)}^\mu J_{(n)\mu} + h.c. \quad (2.1)$$

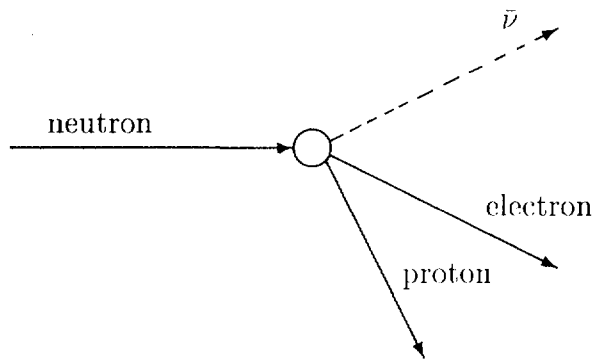


Fig.2.1  $\beta$ -decay:  $n \rightarrow pe^- \bar{\nu}_e$ .

where  $G_F$  is the Fermi coupling constant,  $J_{(n)}^\mu$  is the current from neutron to proton,  $J_{(e)}^\mu$  is the current from electron to neutrino:

$$J_{(e)}^\mu = \bar{\nu}_e \gamma^\mu \left( \frac{1 - \gamma^5}{2} \right) e \quad (2.2)$$

The value of  $G_F$ , which can be derived from the measurement of the muon lifetime [2] taking into account the leading radiative QED corrections, is known very precisely:

$$G_F = (1.16639 \pm 0.00002) \times 10^{-5} \text{GeV}^{-2} \approx \frac{1}{(293 \text{GeV})^2}. \quad (2.3)$$

The main differences of this  $V - A$  type interaction with QED are,

- the range of interaction;
- the current is charged (charge rising  $e^- \rightarrow \nu_e$ , or charge lowering  $\nu_e \rightarrow e^-$ );
- it violates maximally the parity conservation ( the term  $\gamma^\mu(1-\gamma^5)$  was postulated and discovered by Mrs. Wu et.al. of the parity violation in the  $^{60}\text{Co}$  decay experiment.)

Several difficulties appeared in the extended Fermi theory:

- unitary violation for processes such as neutrino scattering on electrons;
- the theory is not renormalizable: the higher order diagrams for  $\nu_e e^- \rightarrow \nu_e e^-$  lead to divergent integrals.

In QED, these divergences are solved by the renormalization procedure owing to the presence of the photon propagator. This brings the idea to introduce the intermediary bosons  $W^\pm$  for the weak interactions which will play a similar role as the photon in QED, as shown by the following diagram:

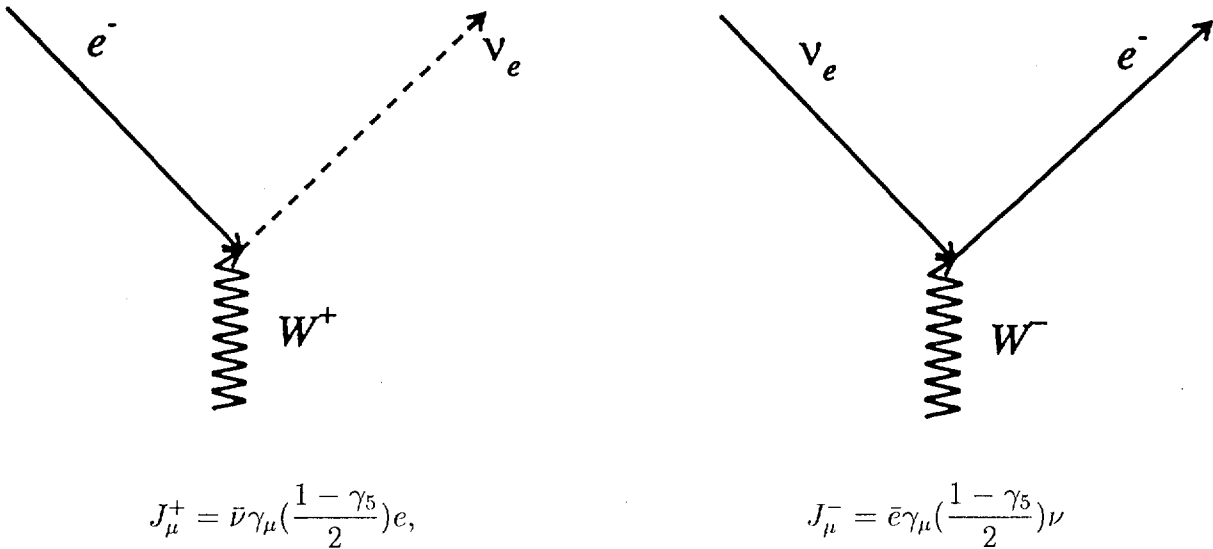


Fig.2.2 Charged current in weak interaction.

For example, to describe the low energy 3-body muon decay  $\mu^- \rightarrow e\bar{\nu}_e\nu_\mu$ , the amplitude will contain a propagator term [3]:

$$\mathcal{A} = \left[ \frac{g}{\sqrt{2}} \bar{\nu}_\mu \gamma^\mu \left( \frac{1 - \gamma^5}{2} \right) \mu \right] \frac{1}{M_W^2 - q^2} \left[ \frac{g}{\sqrt{2}} \bar{e} \gamma^\mu \left( \frac{1 - \gamma^5}{2} \right) \nu_e \right] \quad (2.4)$$

where  $g$  is the dimensionless charged current Standard Model constant, and  $q^2$  is the four momentum transfer in the interaction. For values of  $|q^2| \ll M_W^2$ , the condition

$$\frac{g^2}{8M_W^2} = \frac{G_F}{\sqrt{2}} \quad (2.5)$$

leads to the Fermi theory.

The new intermediary bosons  $W^\pm$  allow to keep the cross sections limited at high energy, but the theory is still not renormalizable. Only the appearance of the gauge theories, together with the Higgs mechanism, permitted the construction of the renormalizable models.

## Electroweak Standard Model

An attempt to unify electromagnetic and weak interactions (charged and neutral currents) was proposed by Glashow [4] in 1961. The Glashow model was based on the non-Abelian symmetry group  $SU(2)_L \otimes U(1)$ . It is a chiral theory, as the left and right chiral components of the fermion fields are treated differently.

To construct a combined weak and electromagnetic theory an additional extra current  $J_\mu^Y$  has been introduced to account for interaction with right-handed electron.  $J_\mu^Y$  was called weak hypercharge current and is related to the weak hypercharge  $Y$  by:

$$Q = T^3 + \frac{Y}{2} \quad (2.6)$$

where  $Q$  is the electric charge in units of  $e$ ,  $T^3$  is the third component of the weak isospin.

The known leptons and quarks are grouped in a 3-fold generation structure, which has identical properties (gauge interactions) but different mass and flavour quantum numbers. Each generation of leptons and quarks have similar weak isospin doublet with

the same quantum numbers ( $l$  stands for  $(e, \mu, \tau)$ ,  $u$  stands for  $(u, c, t)$  and  $d$  stands for  $(d, s, b)$ ):

$$\begin{pmatrix} \nu_l \\ l^- \end{pmatrix}_L, \quad \begin{pmatrix} q_u \\ q_d \end{pmatrix}_L \quad (2.7)$$

completed by their right-handed singlets:

$$l_R^-, \quad (q_u)_R, \quad (q_d)_R, \quad (2.8)$$

The weak current has three components in  $SU(2)$  and is completed by the  $J_\mu^Y$ . The basic electroweak interaction Lagrangian is therefore:

$$\mathcal{L}_{EW} = gW_i^\mu J_\mu^i + \frac{g'}{2}B^\mu J_\mu^Y \quad (i = 1 - 3) \quad (2.9)$$

where  $g$  and  $g'$  are two different coupling constants corresponding to two different symmetry groups:  $W_\mu^i$  equals to the isotriplet weak field and  $B_\mu$  equals to the single electromagnetic vector field.

To identify physical fields - the photon and the vector bosons  $W^\pm, Z^0$  (the neutral boson  $Z^0$  is introduced as a mediator of the neutral weak interaction), an orthogonal mixture is used:

$$W_\mu^\pm = \frac{1}{\sqrt{2}}(W_\mu^1 \mp iW_\mu^2) \quad (2.10)$$

$$Z_\mu^0 = \cos\theta_W W_\mu^3 - \sin\theta_W B_\mu \quad (2.11)$$

$$A_\mu = \sin\theta_W W_\mu^3 + \cos\theta_W B_\mu \quad (2.12)$$

The angle  $\theta_W$  is the weak mixing angle. Identifying  $A$  to the photon implies:

$$g\sin\theta_W = g'\cos\theta_W = e, \quad \text{or,} \quad \frac{1}{g^2} + \frac{1}{g'^2} = \frac{1}{e^2} \quad (2.13)$$

Thus the neutral current piece comprises the standard QED electromagnetic interaction mediated by  $\gamma$  with strength  $e$  and a weak interaction mediated by  $Z^0$  with strength  $g/\cos\theta_W$ .

Finally, the EW Lagrangian in  $SU(2)_L \otimes U(1)_Y$  frame is:

$$\mathcal{L}_{EW} = -\frac{g}{\sqrt{2}}[J_\mu^+ W^{+\mu} + J_\mu^- W^{-\mu}] \quad (CC) \quad (2.14)$$

$$-eJ_\mu^{em} A^\mu - \frac{g}{\cos\theta_W}[J_\mu^3 - \sin^2\theta_W J_\mu^Y] Z^\mu \quad (NC) \quad (2.15)$$

where

$$J_\mu^{em} = J_\mu^3 + \frac{1}{2}J_\mu^Y \quad (2.16)$$

The relative strength of the neutral current part to the charged current part can be expressed by the parameter  $\rho$  defined as  $\rho = M_W^2/(M_Z^2 \cos^2\theta_W)$ . In the Standard Model the value of  $\rho$  equals to 1.

So far, the  $\mathcal{L}_{EW}$  describes massless gauge bosons and massless fermions. Adding mass terms to the Lagrangian (which breaks symmetry) will generate (unrenormalizable) divergences for loop diagrams. To generate the particle masses in a gauge invariant way, the Higgs mechanism was used. In the Weinberg-Salam model [5], [6] the masses of the gauge bosons  $W^\pm, Z^0$  are generated by the Spontaneous Symmetry Breaking mechanism, ensuring the conservation of  $U(1)_{em}$  ( $m_\gamma = 0$ ).

For a  $SU(2)_L$  doublet of complex scalar field [5]  $\phi(x) \equiv \begin{pmatrix} \phi^{(+)}(x) \\ \phi^{(0)}(x) \end{pmatrix}$ , a gauge scalar Lagrangian  $\mathcal{L}_S$ , which is composed of a covariant derivative and a potential of the scalar field [7], is added to the massless Glashow model:

$$\mathcal{L}_S = (D_\mu \phi)^\dagger D^\mu \phi - V(\phi) \quad (2.17)$$

$$V(\phi) = -\mu^2 \phi^\dagger \phi + \lambda(\phi^\dagger \phi)^2 \quad (2.18)$$

When a particular ground state is chosen, the  $SU(2)_L \otimes U(1)_Y$  symmetry is spontaneously broken, and the neutral field part acquires a vacuum expectation value  $v^2$

( $v^2 = \mu^2/\lambda$ ). The Higgs potential is then introduced to account for the field interactions. As the result of this procedure, the Higgs boson acquires a mass

$$M_H^2 = -2\mu^2 > 0, \quad (2.19)$$

as well as  $W^\pm$  and  $Z^0$  bosons

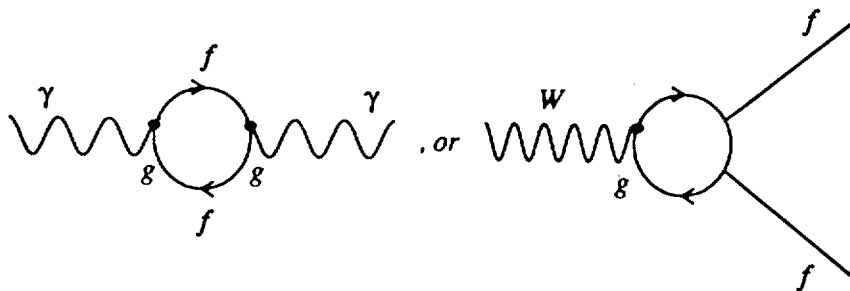
$$M_W = \frac{1}{2}gv, \quad M_Z = \frac{1}{2}\sqrt{(g^2 + g'^2)} v, \quad (2.20)$$

while the photon still remains massless. These expressions give rise to the relationship between the heavy boson masses:

$$M_Z \cos\theta_W = M_W = vg/2. \quad (2.21)$$

This relation (which implies  $\rho = 1$ ) holds if the Higgs sector of the theory contains only one Higgs doublet. The  $\rho$  value different from 1 would reflect the presence of other heavy bosons, such as  $W'$  or  $Z'$ , coupling to fermions with different strength and mixing with  $W$  and  $Z^0$  with another angle.

On the other hand, the higher order weak corrections arising from graphs like:



which occur in the computation of the running coupling of  $\alpha(M_W^2)$ , lead to the expression:

$$M_W^2 = \frac{\pi\alpha}{\sqrt{2}G_F \sin^2\theta_W} \rho = \frac{\pi\alpha}{\sqrt{2}G_F \sin^2\theta_W} \frac{1}{1 - \Delta r} \quad (2.22)$$

where the correction factor  $\Delta r$  to  $\rho$  is of the order of a few %.

In conclusion, by introducing the massive boson fields  $W^\pm$  and  $Z^0$ , together with the massless photon, the weak and electromagnetic interactions are successfully unified and described in the Standard Model.

### 2.1.2 Electroweak Parameters in the Standard Model

The Standard Model of electroweak interactions is a renormalizable gauge field theory with several free parameters. Ignoring the quark sector and the QCD parameters, there are overall fifteen parameters which may be divided up as:

- couplings:  $e(\alpha), g, g', G_e, G_\mu, G_\tau$ ;
- masses:  $M_W, M_Z, M_H, m_e, m_\mu, m_\tau$ ;
- Higgs sector:  $\mu^2, \lambda(v^2 = \mu^2/\lambda)$
- mixing angle:  $\sin^2\theta_W$ .

Seven out of those fifteen parameters are independent which need inputs from the experiment; the others can be derived from the relationship between them, such as  $M_W/M_Z = \cos\theta_W$ ,  $M_W = \frac{1}{2}gv$ ,  $e = g \cdot \sin\theta_W$  etc. The set of the seven independent parameters  $\{\vec{p}\}$  can be chosen in various ways, for example,

$$\{\vec{p}\} = \{g, g', G_e, G_\mu, G_\tau, \mu^2, \lambda\}; \text{ or}$$

$$\{\vec{p}\} = \{\alpha, M_W, M_Z, M_H, m_e, m_\mu, m_\tau\}; \text{ or}$$

$$\{\vec{p}\} = \{\alpha, \sin^2\theta_W, M_H, v, G_e, G_\mu, G_\tau\}.$$

Thus, apart from the fermion masses, there are four free parameters in the gauge and scalar sector of the electroweak SM.

Including the electroweak quark sector will give rise to ten extra parameters from the CKM matrix  $V$  (three angles and one complex phase, plus quark mass matrices).

Including QCD we have two more parameters:  $\Lambda_{QCD}$  and QCD  $\gamma$ -parameter involved in the strong CP problem. Thus, the complete  $SU(3)_C \otimes SU(2)_L \otimes U(1)_Y$  Standard Model Lagrangian is determined by at least 19 free parameters, since the possible parameters from neutrino mass and mixing are not counted here.

A model with at least 19 undetermined parameters, in which the particular representations containing fermions and scalars are a mysterious replication of three generations, does not seem to be a likely ultimate fundamental theory. There are still pieces of the SM Lagrangian that have not been precisely analyzed by the experiment and there are still many unanswered questions. On the other hand, the achieved partial unification of weak and electromagnetic forces leads to a product of simple groups each with its own coupling constant  $g$  and  $g'$  related by the weak mixing angle, not determined by the theory.

The new physics beyond the present electroweak SM frontiers should exist, it is possible that the new gauge interactions become visible already at TeV energies. Various extensions of the gauge SM theory are suggested on different theoretical grounds in the frame of Grand Unified theory, in which all of the particles would lie inside bigger irreducible representations. The models with an additional  $U(1)$  symmetry ( $SU(2)_L \otimes U(1)_Y \otimes U(1)_{Y'}$  group) contained in the unified group  $E_6$  [8], and the models with right-handed currents based on the symmetry group  $SU(2)_L \otimes SU(2)_R \otimes U(1)_{B-L}$  [9] have attracted particular attention in the study of the electroweak physics at HERA [10].

## 2.2 Deep Inelastic $ep$ Scattering at HERA

The electroweak interaction can be studied in the deep inelastic scattering processes: the neutral and charged current interactions. The HERA collider, which has a 820 GeV proton beam and a 30 GeV electron beam, opens a new kinematic domain for such study.

### 2.2.1 Kinematics Variables In Deep Inelastic Scattering

The neutral and charged current deep inelastic lepton-proton scattering process

$$l + p \rightarrow l' + X \tag{2.23}$$

is a four-fermion scattering process between the lepton and the quarks inside the nucleon. Here  $l$  and  $p$  represent the incoming lepton and proton,  $l'$  represents the scattered lepton and  $X$  represents the final state hadronic system. In the Standard Model, this process is of pure electroweak origin mediated by the exchange of a photon,  $Z^0$  and  $W^\pm$  bosons in the lowest order.

Fig.2.3 illustrates the lepton-proton deep inelastic scattering, where the four-vector for the incoming and outgoing leptons and the incoming protons are denoted as  $k, k'$  and  $P$  respectively, and the four-vector carried by the exchanged boson ( $\gamma/Z^0$  for neutral current interaction and  $W^\pm$  for charged current interaction) is denoted as  $q$ .

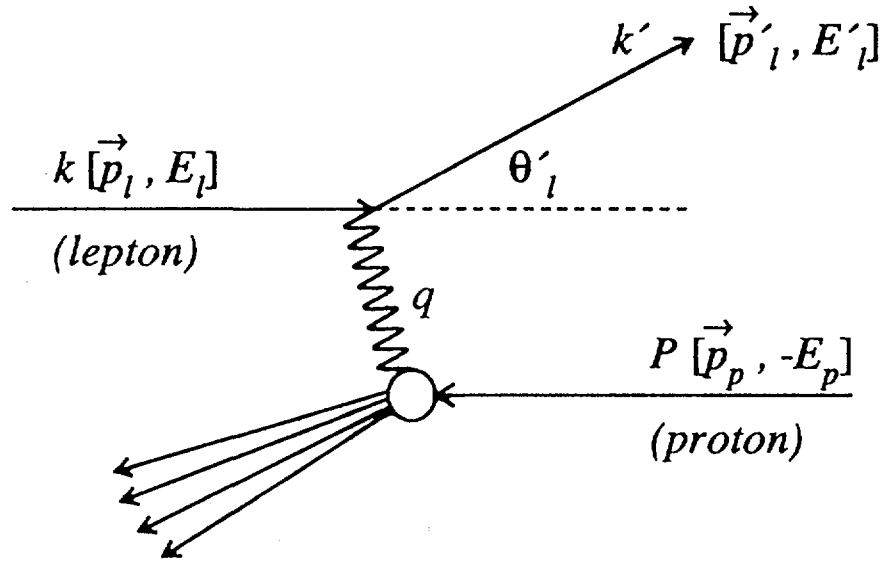


Fig.2.3 Basic diagram for deep inelastic scattering.

We have:

$$q = k - k' \quad (2.24)$$

The total invariant mass squared is

$$s = (k + P)^2 \simeq 4E_l E_p \quad (2.25)$$

here  $E_l$  and  $E_p$  are the energies of the incoming lepton and proton. This is a good approximation at HERA energy where the masses of the incoming proton and lepton and of the outgoing lepton can be neglected.

The positive momentum transfer variable  $Q^2$  is defined from the four-momentum transfer:

$$Q^2 \equiv -q^2 = -(k - k')^2 \quad (2.26)$$

The value of  $Q^2$  is between 0 and the total invariant mass squared  $s$ . The dimensionless scaling variables Bjorken- $x$  and  $y$  are defined as:

$$x \equiv \frac{Q^2}{2P \cdot q} \quad (2.27)$$

$$y \equiv \frac{P \cdot q}{P \cdot k} = \frac{2P \cdot q}{s} = \frac{Q^2}{xs} \quad (2.28)$$

The values of  $x$  and  $y$  are always between 0 and 1.

The momentum transfer variable  $Q^2$  and the dimensionless scaling variables  $x$  and  $y$  are used as the kinematic variables in the deep inelastic physics study. There are only two independent variables in the overall event kinematics, all other kinematic variables can be derived from these two. For example,  $Q^2, x, y$  can be derived from the energy  $E_l'$  and polar angle  $\theta_l'$  of the scattered lepton:

$$Q^2 = 4E_l E_l' \sin^2 \frac{\theta_l'}{2}; \quad x = \frac{E_l E_l' \sin^2 \frac{\theta_l'}{2}}{E_p (E_l - E_l' \cos^2 \frac{\theta_l'}{2})}; \quad y = \frac{E_l - E_l' \cos^2 \frac{\theta_l'}{2}}{E_l} \quad (2.29)$$

The momentum conservation gives that the transverse momentum of the lepton  $P_t^l$  equals to that of the hadrons  $P_t^{had}$ . From the above formulae we can easily get the relation between  $Q^2, x, y$  and the transverse momentum:

$$(P_t^{had})^2 = (P_t^l)^2 = (E_l' \sin \theta_l')^2 = Q^2(1 - y) = sxy(1 - y) \quad (2.30)$$

For cross section formulae, the two independent variables are frequently chosen as  $(x, y)$  or  $(x, Q^2)$ .

### 2.2.2 Cross Sections In NC and CC Processes

The electroweak part of the  $ep$  interaction can be extracted from the measured differential cross sections for the charged and neutral current processes:  $d\sigma^{CC}$  and  $d\sigma^{NC}$ . Other quantities formed with  $d\sigma^{NC}$  and  $d\sigma^{CC}$ , such as the integrated and differential ratios between NC and CC processes, the ratio between cross sections from different incoming leptons ( $e^-$  or  $e^+$ ) and asymmetries due to the polarization of the incoming lepton, can also be used for the comparison with the Standard Model.

To calculate the NC and CC cross sections one may use the Fermi's "Golden Rule":

$$d\sigma = \frac{2\pi}{\hbar} |A|^2 \times (\text{phase space}) \quad (2.31)$$

where  $A$  is invariant amplitude for a given process, it contains all dynamics of the reaction and can be determined from Feynman diagrams [11].

#### Low energy case - structure functions

Considering the inelastic scattering process  $ep \rightarrow eX$  via photon exchange:

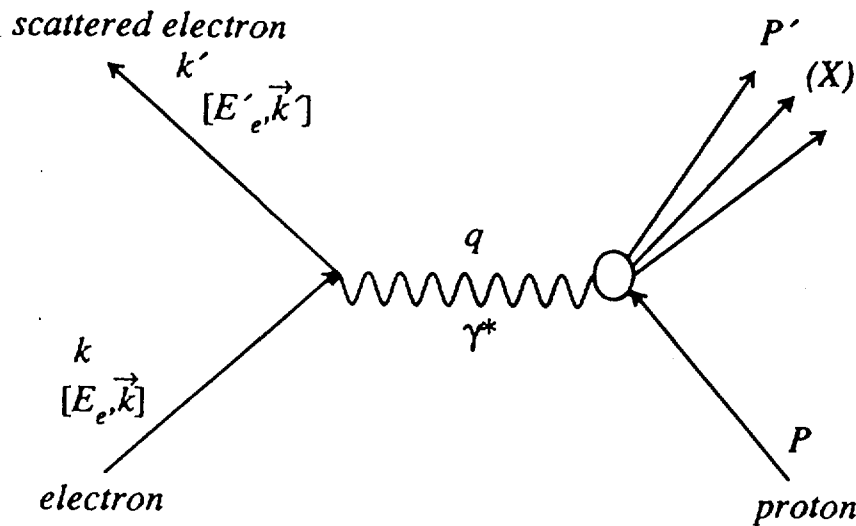


Fig.2.4  $ep \rightarrow eX$  scattering via photon exchange.

the invariant amplitude  $A_X$  is a product of the leptonic and hadronic currents with coupling factors and propagators. It's square can be expressed as a product of the leptonic and hadronic tensors and the photon propagator:

$$|A_X|^2 = \frac{\alpha^2}{Q^4} L^{\mu\nu} W_{\mu\nu} \quad (2.32)$$

The leptonic tensor  $L^{\mu\nu}$  is completely calculable, as discussed in previous section:

$$L^{\mu\nu} = 2(k^\mu k'^\nu + k^\nu k'^\mu) - g^{\mu\nu}(k \cdot k' - m_e^2) \quad (2.33)$$

where  $m_e$  is the electron mass. The hadronic tensor  $W_{\mu\nu}(X)$  is an “unknown” quantity describing the subprocess  $\gamma^* + P \rightarrow X$ . The most general form of  $W_{\mu\nu}$  can be constructed from linear combinations of  $P$  and  $q$  variables:

$$W_{\mu\nu} = C_1 g_{\mu\nu} + C_2 q_\mu q_\nu + C_3 P_\mu P_\nu + C_4 (P_\mu q_\nu + q_\mu P_\nu) + C_5 (P_\mu q_\nu - q_\mu P_\nu) + C_6 \epsilon_{\mu\nu\alpha\beta} P^\alpha q^\beta \quad (2.34)$$

The 6 complex coefficients can only depend on independent scalars constructed with  $P$  and  $q$ :  $q^2$  and  $P \cdot q$ . The symmetry properties of  $W_{\mu\nu}$  and the current conservation leads to only two independent coefficients. As Bjorken  $x$  and  $Q^2$  are both Lorentz invariant, one may use them as variables in the  $W_{\mu\nu}$  expression:

$$W_{\mu\nu} = \frac{1}{M_P} \left( -g_{\mu\nu} + \frac{q_\mu q_\nu}{q^2} \right) F_1(x, Q^2) + \frac{1}{\nu M_P} \left( P_\mu - \frac{P \cdot q}{q^2} q_\mu \right) \left( P_\nu - \frac{P \cdot q}{q^2} q_\nu \right) F_2(x, Q^2) \quad (2.35)$$

The proton is not a simple point charge particle, and the function  $F_i(x, Q^2)$  are interpreted as electromagnetic structure functions of the proton. Finally the differential cross section can be written as [12] [13]:

$$\frac{d^2\sigma}{dx dQ^2} = \frac{4\pi\alpha^2}{xQ^4} [y^2 x F_1(x, Q^2) + (1-y) F_2(x, Q^2)] \quad (2.36)$$

### The Parton Model

The parton model is introduced by Feynman in 1969 [14] to explain the particle spectroscopy, first postulated by Gell Mann and Zweig in 1964. The model is based on the assumption that the proton is a bound system of fundamental point-like spin 1/2 particles, and that in the deep-inelastic-scattering region the interactions between the constituents of the proton (the partons) and the mass effect can be neglected. The partons can be understood as the sub-constituents of the proton, i.e. the valence quark or the sea quark. The deep-inelastic-scattering process is viewed as the scattering between an electron and a parton, confined inside the proton which is considered to be free during the interaction. Fig.2.5 illustrates the electron-proton deep-inelastic-scattering in the parton model:

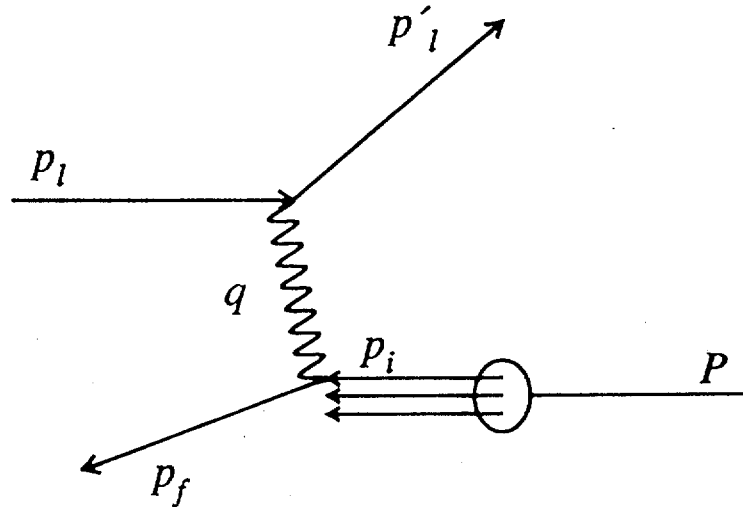


Fig.2.5 Diagram for deep inelastic scattering in quark-parton model.

To see the physical meaning of the Bjorken  $x$  variable in the parton model, assume that the current couples to a quark with four-vector  $p_i = \xi(E_p, 0, 0, -E_p)$ , and assume the initial and final quark to be massless ( $p_i^2 = p_f^2 = 0$ ), by definition,

$$x = \frac{Q^2}{2P \cdot q} = \xi \frac{-q^2}{2p_i \cdot q} = \xi \frac{-q^2}{(p_i + q)^2 - q^2} = \xi \frac{-q^2}{p_f^2 - q^2} = \xi \quad (2.37)$$

thus Bjorken  $x$  can be interpreted as the momentum fraction of the proton carried by the struck quark under these assumptions. The variable  $y$  is actually the fraction of the energy transferred to the proton in the proton rest system.

The scale invariance, i.e. the independence of the structure functions on  $Q^2$ , was observed in the deep-inelastic scattering experiments in the 1960's [15]. The parton model leads to exact scaling of the structure functions which depend only on the variable  $x$ . In the later electron-nucleon DIS experiments and also in the neutrino experiments, the violation of the scale invariance, i.e. the  $Q^2$  dependence of the structure function, was discovered. The  $Q^2$ -dependence of the structure functions can be derived from the quantum chromodynamics (QCD), which is based on the concept that hadrons consist of quarks and that interactions between quarks are mediated by massless vector particles, the gluons. Taking into account the interactions between quarks and gluons, the corrections to the parton model predictions can be calculated. The observed deviation from scaling is relatively small and can be considered as a correction to the main effect.

### Cross sections of deep-inelastic scattering at high energy

For the neutral current process  $ep \rightarrow eX$  ( $X$  are the hadronic final states) in the deep inelastic scattering, the interactions are mediated by the exchange of the neutral vector bosons  $Z$  and photon. In the lowest order of the perturbation theory, the amplitude for NC process is given by a sum of these two contributions: one from photon exchange ( $A^\gamma$ ) and the other from the  $Z^0$  exchange ( $A^{Z^0}$ ). The square of the invariant amplitude in this case is an extension of the equation (2.32):

$$|A_X|^2 = \sum_{i=\gamma, \gamma Z^0, Z^0} L_{\mu\nu}^i W_i^{\mu\nu} \eta^i \quad (2.38)$$

The factors  $\eta^i$  collect some kinematic quantities such as coupling constants and the relative weights of different propagators. As the weak interactions appearing with increasing energy are parity violating, the tensor  $W_i^{\mu\nu}$  needs to be expressed by three form factors. The third structure function  $F_3(x, Q^2)$  is introduced to describe the parity violating part due to the  $\gamma Z^0$  interference and  $Z^0$  contributions. Consequently, the Born cross section is given by [16]:

$$\frac{d^2\sigma_{NC}(e^\pm p)}{dx dQ^2} = \frac{4\pi\alpha^2}{xQ^4} [y^2 x \mathcal{F}_1(x, Q^2) + (1-y) \mathcal{F}_2(x, Q^2) \pm (y - \frac{y^2}{2}) x \mathcal{F}_3(x, Q^2)] \quad (2.39)$$

Assuming the Callan-Gross relation  $2xF_1 = F_2$ , which holds for spin 1/2 partons neglecting quark masses, the intrinsic transverse momenta and the QCD effects, the NC differential cross section can be written as:

$$\frac{d^2\sigma_{NC}(e^\pm p)}{dx dQ^2} = \frac{2\pi\alpha^2}{xQ^4} [(1 + (1-y)^2)\mathcal{F}_2(x, Q^2) \mp (1 - (1-y)^2)x\mathcal{F}_3(x, Q^2)] \quad (2.40)$$

The structure functions  $\mathcal{F}_i(x, Q^2)$  are the so-called generalized structure functions containing the proton structure functions and also the electroweak coupling constant and propagator terms:

$$\mathcal{F}_2(x, Q^2) = F_2 - K_Z(Q^2)v_e G_2 + K_Z^2(Q^2)(v_e^2 + a_e^2)H_2 \quad (2.41)$$

$$\mathcal{F}_3(x, Q^2) = \pm K_Z(Q^2)a_e x G_3 \mp 2K_Z^2(Q^2)v_e a_e x H_3 \quad (2.42)$$

As presented in the previous section, the electroweak coupling constants for the electron are

$$v_e = -\frac{1}{2} + 2\sin^2\theta_W, \quad a_e = -\frac{1}{2} \quad (2.43)$$

In the quark-parton model these structure functions are related to the parton distributions:

$$[F_2, G_2, H_2] = x \sum_q [e_q^2, 2e_q v_q, v_q^2 + a_q^2] [q(x, Q^2) + \bar{q}(x, Q^2)] \quad (2.44)$$

$$[xG_3, xH_3] = 2x \sum_q [e_q a_q, v_q a_q] [q(x, Q^2) - \bar{q}(x, Q^2)] \quad (2.45)$$

$v_f$  and  $a_f$  are the vector and axial couplings of the quarks, which take the general form:

$$v_f = T_f^3 - 2Q_f \sin^2\theta_W, \quad a_f = T_f^3 \quad (2.46)$$

The function

$$K_Z(Q^2) = \left( \frac{Q^2}{Q^2 + M_Z^2} \right) \frac{1}{4\sin^2\theta_W \cos^2\theta_W} \quad (2.47)$$

determines the relative strength of the contributions due to the  $Z^0$  exchange. Fig.2.6 [17] presents the relative contributions of  $\gamma$  (pure electromagnetic term),  $\gamma Z^0$  (interference term) and  $Z^0$  (pure weak term) to the cross sections as a function of  $Q^2$ . A sizable effect maybe observed at HERA for  $Q^2 > 10^3 \text{ GeV}^2$ .

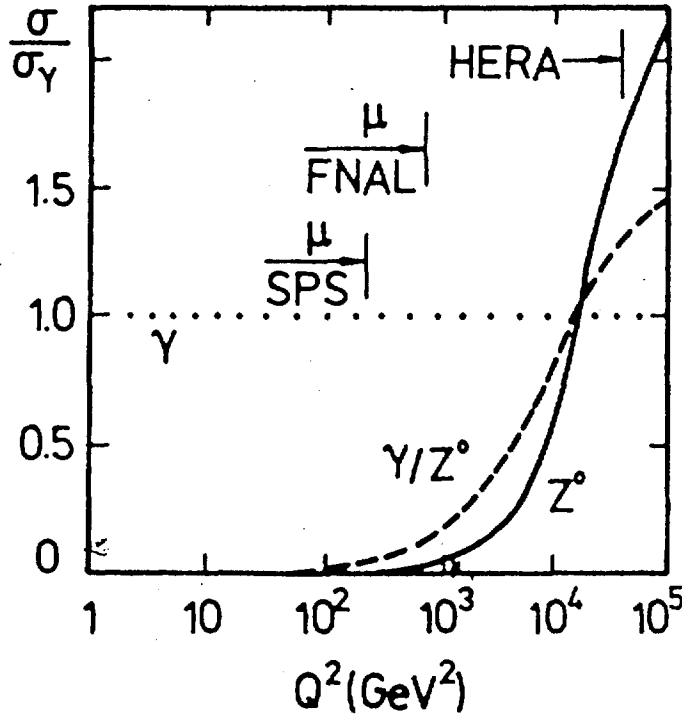


Fig.2.6 The contributions from  $\gamma$ ,  $\gamma Z^0$  and  $Z^0$  to the NC cross sections as a function of  $Q^2$  [17].

For the charged current process  $ep \rightarrow \nu X'$  ( $X'$  are the hadronic final states), the interaction is a pure weak process mediated by charged vector bosons  $W^\pm$  exchange. The CC differential cross section can be derived in the similar way. In the QPM frame it can be written as:

$$\frac{d^2\sigma_{CC}(e^-p)}{dx dQ^2} = \frac{G_F^2}{2\pi} \frac{1}{(1 + Q^2/M_W^2)^2} [(u + c) + (1 - y)^2(\bar{d} + \bar{s} + \bar{b})] \quad (2.48)$$

$$\frac{d^2\sigma_{CC}(e^+p)}{dx dQ^2} = \frac{G_F^2}{\pi} \frac{1}{(1 + Q^2/M_W^2)^2} [\bar{u} + \bar{c} + (1 - y)^2(d + s + b)] \quad (2.49)$$

where  $G_F = \pi\alpha/(\sqrt{2}\sin^2\theta_W \cdot M_W^2)$  is the Fermi coupling constant, and  $q, \bar{q}$  ( $q \equiv u, c, d, s, b$ ) are quark (anti-quark) densities, which are actually obtained by the parameterization of experimental data. Previously, such parameterization of the quark distribution are obtained from lower  $Q^2$  experimental data on  $F_2$  and  $F_3$ [18] which are independent of the electroweak parameters, and has been extrapolated to higher  $Q^2$  ranges. Recently  $F_2$  at high  $Q^2$  has been measured from the neutral current process in the H1 experiment. Several parameterizations have been done based on the fixed target lepton scattering data with a  $Q^2$  dependence described by the Altarilli-Parisi equations in the leading logarithm approximation of perturbative QCD [19]. The effect of the precision of the parameterizations on the measurements of the electroweak parameters will be discussed in the following section.

At HERA energy, when  $Q^2 \geq 10^3 \text{ GeV}^2$ , the pure electromagnetic contribution to NC is sufficiently suppressed, and NC and CC cross sections become comparable. Since the transverse momentum of the final hadronic states  $P_t^{had}$  is related to the kinematics  $Q^2, x, y$  as indicated in formula (2.30) ( $P_t^2 = Q^2(1 - y) = sxy(1 - y)$ ), a similar tendency can be seen with respect to  $P_t^{had}$ . Fig.2.7 gives the differential cross section of NC and CC as a function of  $P_t^{had}$  for  $e^-p$  and  $e^+p$  interactions respectively. The distributions were calculated using the generator HERACLES [20] where the QED and weak corrections are taken into account.

## 2.3 Measurement of the Electroweak Parameters

The electroweak SM can be tested at the  $e - p$  collider HERA by a simultaneous measurement of the deep-inelastic neutral current process and the charged current process, with the options to choose  $e^-$  or  $e^+$  beams, and in the future the foreseen options to choose longitudinally polarized  $e^\pm$  beams. The simultaneous measurement of the  $e^+p$  and  $e^-p$  neutral and the charged current cross sections provides additional constraint on the  $W$  mass determinations, as it will be discussed the Chapter 5.

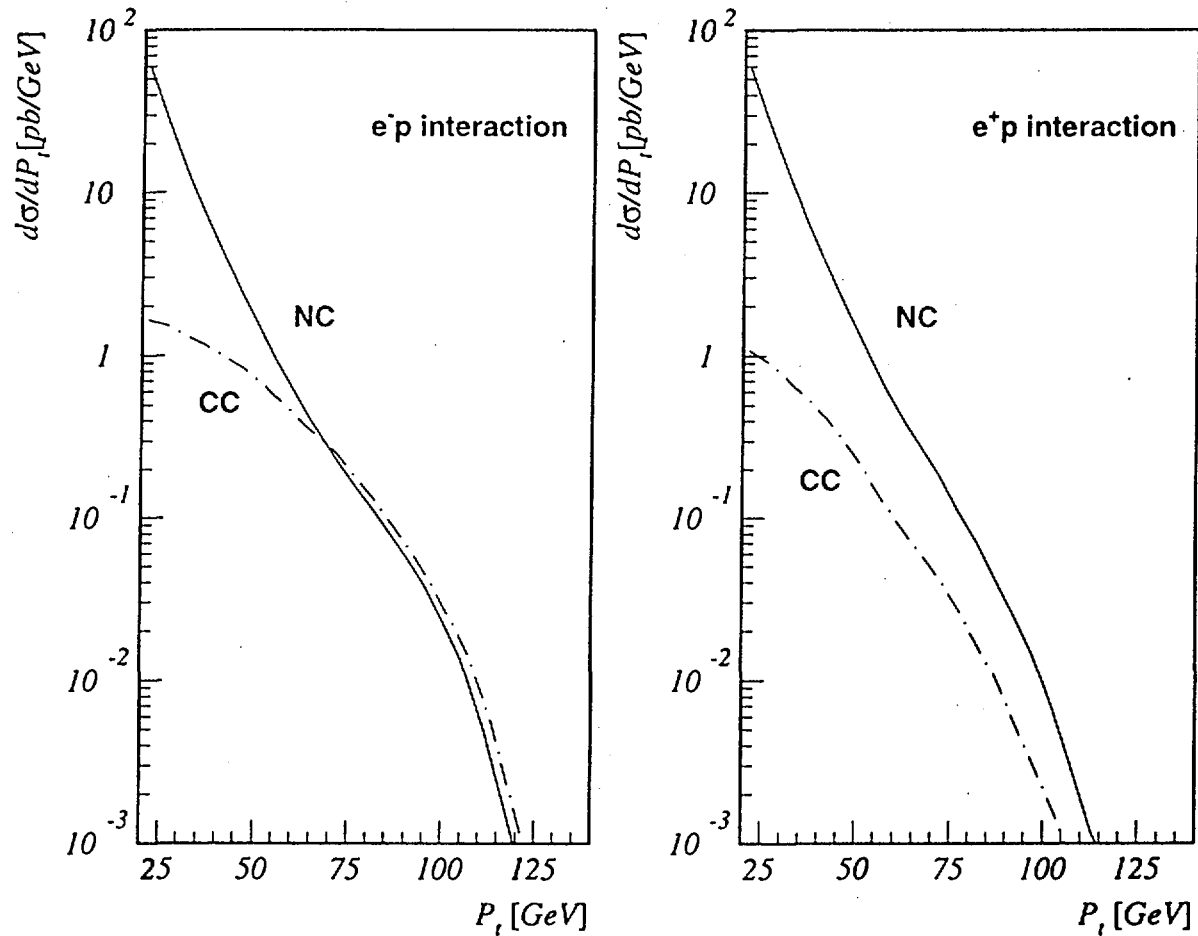


Fig.2.7 The differential cross section of NC and CC as a function of  $P_t^{had}$ , for  $e^-p$  and  $e^+p$  interactions respectively.

The kinematic region covered at HERA energies reaches a  $Q^2$  range of order of  $M_W^2$  and beyond where electromagnetic and weak effects are of comparable magnitude. The informations on the electroweak interaction can thus be extracted from the experimentally measured quantities at HERA. By fixing some of the electroweak parameters to values measured previously with higher precision in other more specialized experiments, one can obtain more accurate results on the remaining parameters values.

To relate the electroweak parameters with the experimental measurable quantities in the lepton-proton scattering experiment, a particular normalization scheme should be chosen and a parameterization of the proton structure functions should be adopted. The experimental measurable quantities can then be predicted in terms of these parameters.

### 2.3.1 Choice of the Set of Electroweak Parameters at HERA

Besides the mass of the Higgs scalar in the four free parameters in the gauge and scalar sector of the electroweak SM, three parameters in the gauge sector will determine two gauge coupling constants and one vacuum expectation value. As discussed above, not all electroweak parameters are independent. We have the relation:

$$\frac{G_F}{\sqrt{2}} = \frac{e^2}{8M_W^2 \sin^2 \theta_W} \quad (2.50)$$

THCHP2.TEX To get a numerical prediction of the electroweak experimental observables, such as the differential cross section of the NC and CC process, one needs to specify a set of independent parameters to which these cross sections are sensitive.

In the on-shell renormalization scheme [21], a practical choice of the three electroweak parameters in deep-inelastic  $ep$  scattering experiments is the electromagnetic fine structure constant  $\alpha$ , together with the weak boson masses  $M_W$  and  $M_Z$ . In the higher order, the parameters get contributions from self energy and vertex correction diagrams, which leads to additional parameters entering the calculation: the Higgs mass  $M_H$  and the fermion masses  $m_f$ , including the mass  $m_t$  of the top quark. Thus, with the set of the parameters

$$\{\vec{p}\} = \{\alpha, M_Z, M_W, M_H, m_t\} \quad (2.51)$$

this scheme gives the amplitudes for 4-fermion processes in terms of  $M_Z$  and  $M_W$  besides  $\alpha$ , together with  $m_t, M_H$  in the loop contributions.

Various efforts were made in different experiments recently to measure the electroweak parameters:

- the results from LEP give the  $Z^0$  mass  $M_Z = 91.1884 \pm 0.0022$  GeV;
- the direct measurement of the  $W$  mass by CDF at Tevatron (1995) gives  $M_W = 80.41 \pm 0.18$  GeV, and the indirect measurement by LEP1 gives  $1\sigma$  limit  $M_W = 80.32 \pm 0.06$  GeV [22]. Taking into account all previous direct measurements (CDF(1990), UA2(1992), D0(1994 prelim.), CDF(1995)), the world average is  $M_W = 80.26 \pm 0.16$  GeV;
- the first result on the top quark mass measurement from CDF gives  $m_t = 174 \pm 10_{-12}^{+13}$  GeV [26], while the LEP+SLD+( $p\bar{p}$  and  $\nu N$ ) data gives  $m_t = 178 \pm 8_{-20}^{+17}$  GeV [23];

- the present bound on the Higgs mass  $M_H$  is  $M_H > 65$  GeV [22].

The Fermi constant  $G_F$  is well measured from the muon lifetime, and it is related to the electroweak parameters as given in equation (2.50). When higher order contributions are considered,  $M_W$  can be expressed as a function of other electroweak parameters (see Section 2.1.1):

$$M_W^2 = \frac{\pi\alpha}{\sqrt{2}G_F \sin^2\theta_W} \frac{1}{1 - \Delta r} \quad (2.52)$$

where  $\Delta r$  measures the deviation of  $\rho$  parameter from 1. The contribution from a  $Z'$  to the neutral current differential cross section in  $e^\pm p$ -scattering would give a sensitivity for  $M_{Z'}$  up to  $\sim 400$  GeV at HERA [24]. The possibility to derive bounds on  $m_t, M_H$ , or to predict  $M_W$  for given  $m_t, M_H$  values were studied at HERA [25]. It has been found that, corresponding to the top mass range of 100 to 200 GeV, the sensitivity of the NC/CC ratio has the order of a few % for the high luminosity samples (100 - 200  $pb^{-1}$ ). The sensitivity to the Higgs mass seems to be less clear.

Based on a set of electroweak parameters chosen as in equation (2.51) and the relations (2.52), the predictions on  $M_W, m_t$  and  $M_H$  can be made, which will reflect their intrinsic uncertainties. Confronted with the values measured in previous experiments, the new experimental results from HERA will lead to a constraint among these parameters, and a non-trivial test of the electroweak theory of the Standard Model.

### 2.3.2 Measurement of the $\sigma^{NC}/\sigma^{CC}$ Ratio

Any prediction of the electroweak quantity has to be obtained from the experimental measurable double differential cross section, which is the function of a set of the electroweak parameters  $\vec{p}$ :

$$\frac{d^2\sigma}{dx dy} \equiv \varphi(x, y|\vec{p}) \quad (2.53)$$

or in terms of  $x, Q^2$  as discussed in the above section. To study the hadronic transverse momentum  $p_t^{had}$  dependence of a DIS process, the differential distribution as a function of  $p_t^{had}$  can be written as:

$$\frac{d\sigma}{dp_t^{had}} = \int \int dx dy \delta(p_t^{had} - \sqrt{sxy(1-y)}) \varphi(x, y | \vec{p}) \quad (2.54)$$

Here the relation  $P_t^2 = sxy(1-y)$  as indicated in formula (2.30) is used. The sensitivity of the cross section relative to the input electroweak parameters is studied in [27], where the results show that the integrated unpolarized cross section  $\sigma^{NC}$  ( $Q^2 > 500 \text{ GeV}^2$ ) and  $\sigma^{CC}$  ( $Q^2 > 1000 \text{ GeV}^2$ ) are very insensitive to the values of  $M_H$  which varies from 60 GeV to 1000 GeV.  $\sigma^{CC}$  is more sensitive to the input electroweak parameters and has a variation at the level of 1% or more.

The NC cross section includes the contributions from both  $Z$  boson and photon exchange, the latter dominates at low  $Q^2$  ( $< 1000 \text{ GeV}^2$ ). The available statistics of NC is about 7 to 12 times larger than CC for  $e^\pm p$  interactions for the  $p_t^{had} > 25 \text{ GeV}$  range as predicted by the electroweak theory. In the high  $Q^2$  region one gets high sensitivity to electroweak physics, but the statistical precision decreases.

The kinematic range chosen is either the region of  $Q^2 > Q_{min}^2$  with  $Q_{min}^2$  around typically  $1000 \text{ GeV}^2$ , or a region above a cut on the transverse momentum of the total hadronic system ( $p_t^{had}$ ). The latter choice is more favoured experimentally, since  $p_t^{had}$  can be measured directly and the lines of constant  $p_t^{had} = \sqrt{Q^2(1-y)}$  in the  $x-y$  plane (as shown in Fig.2.8) allow as well as  $Q^2$  to characterize the region of interest. Further it excludes automatically the regions of large Bjorken- $y$  and of small  $x$  which are subject to experimental problems.

The shape of the differential cross section of CC process  $\sigma^{CC}$  can be exploited to extract the  $W$  mass. An analysis performed in [25] predicted that assuming an integrated luminosity of  $1000 \text{ pb}^{-1}$  (the systematic effects being kept under control), and setting the  $p_t^{had}$  cut to 15 GeV, a  $\pm 500 \text{ MeV}$  constraint on the  $W$  mass can be derived from the  $Q^2$  distribution analysis of the charged current data, which is almost independent of the top mass.

However, using absolute cross section of CC and NC to test electroweak SM or to get informations on the electroweak parameters is limited by the systematic uncertainties. Using the NC/CC ratio as the experimental observable will give rise to some advantages.

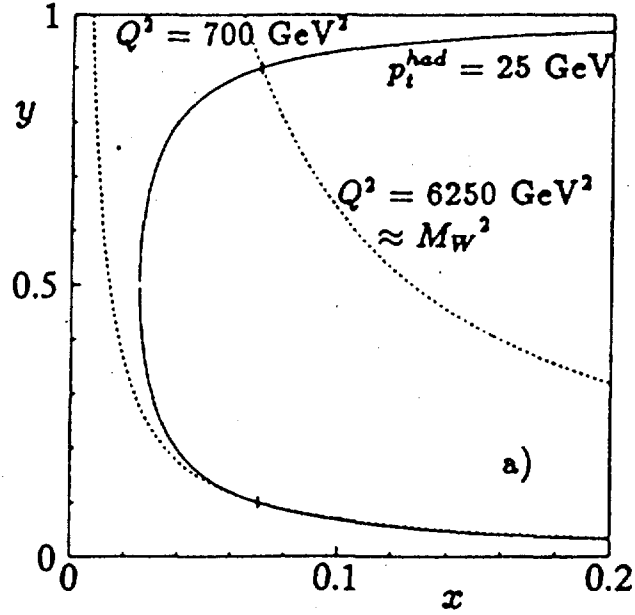


Fig.2.8 Kinematics distribution in the  $x, y$  plane. The  $p_t^{had} = 25$  line is indicated.

- Integrated NC/CC ratio

In order to reduce the large systematic errors in the overall normalization of the cross section caused by the uncertainty in the luminosity  $\mathcal{L}$  measurement, the integrated cross section ratio of NC and CC is considered:

$$R = \frac{\sigma^{NC}(e^-p \rightarrow e^-X)}{\sigma^{CC}(e^-p \rightarrow \nu_e X)} \quad (2.55)$$

where  $\sigma^{NC}$  and  $\sigma^{CC}$  are obtained after a cut on the hadronic transverse momentum  $p_t^{had}$ . This way any systematic uncertainty coming from the luminosity measurement is eliminated. The accepted kinematic region by the high  $p_t^{had}$  cut excludes events in low  $x$  region. This turns out to be of advantage when the dependence of  $R$  on the nucleon structure is investigated [25].

The cross section is determined essentially by  $M_W$  as the relevant electroweak parameter in the  $W$  propagator. The dependence of  $R$  on  $M_W$  mainly comes from  $\sigma^{CC}$ . By the normalization of  $\sigma^{CC}$  to  $\sigma^{NC}$ , the systematic uncertainties in the cross section measurements are partially suppressed. On the other hand, the  $M_W$  dependence of  $\sigma^{CC}$  in the ratio  $R$  is partly compensated by the very weak  $M_W$  dependence of  $\sigma^{NC}$  via the form factors [10]. Thus, compared to the sensitivity of  $\sigma^{CC}$  with respect to  $M_W$ , the sensitivity of  $R$  to  $M_W$  is slightly diminished. By forming the ratio, the effect of the initial state radiation is also decreased. This is confirmed by the study of the QED radiative effects in the leading log approximation in [28].

The  $p_t^{had}$  cut should be chosen high enough such that the integrated cross section is sensitive to the electroweak parameters, nevertheless a reasonable statistics of the NC and CC process should be guaranteed. Actually  $p_t^{had} > 25$  GeV is chosen in our analysis, which corresponds to  $Q^2 > 625$  GeV<sup>2</sup>. From the experimental point of view, a directly measured  $p_t^{had}$  is sufficient to decide whether a NC or CC events is counted or not, this will simplify the events selection procedure. The requirement of large  $p_t^{had}$  values leads to event topologies which are easy to detect. At large  $p_t^{had}$  a reliable separation of NC and CC events is possible.

- Physics implications of  $R$  measurement

From the expressions of the NC and CC cross sections in the above sections, the interdependence of the integrated ratio  $R$  and  $M_W$  can be obtained straightforwardly, with  $M_H$  and  $m_t$  as the input parameters. The result in [27] shows that, for two values of  $M_H$  (which was chosen to be 60 GeV and 1 TeV), the two curves generated in the  $R - M_W$  plane by varying  $m_t$  at fixed  $M_H$  are not separable, which yield a unique dependence of  $R$  on  $M_W$ . A shift in  $R$  by  $\Delta R/R = 0.011$  is observed by a variation of  $m_t$  from 90 to 200 GeV, which corresponds to  $\Delta M_W = 675$  MeV. The error  $\delta R$  can inversely be converted into a range for  $M_W$ .  $\delta R/R = 1\%$  will lead to  $\delta M_W = 630$  MeV [27].

Fig.2.9 shows the implications of a 1% uncertainty on the measurement of  $R$ , where  $R$  is interpreted as a function of  $M_W$  in the minimal SM with  $m_t$  as a parameter and  $M_H$  fixed to 300 GeV. The direct measurement from  $p\bar{p}$  collider provide a band  $M_W = 80.26 \pm 0.16$  GeV on the  $M_W$  scale, which restricts the allowed values for the top mass to an accuracy of  $\pm 30$  GeV, almost as stringent as the low  $Q^2$  constraint from  $G_F$ . In both cases the fit value of  $m_t$  is correlated with  $M_H$ .

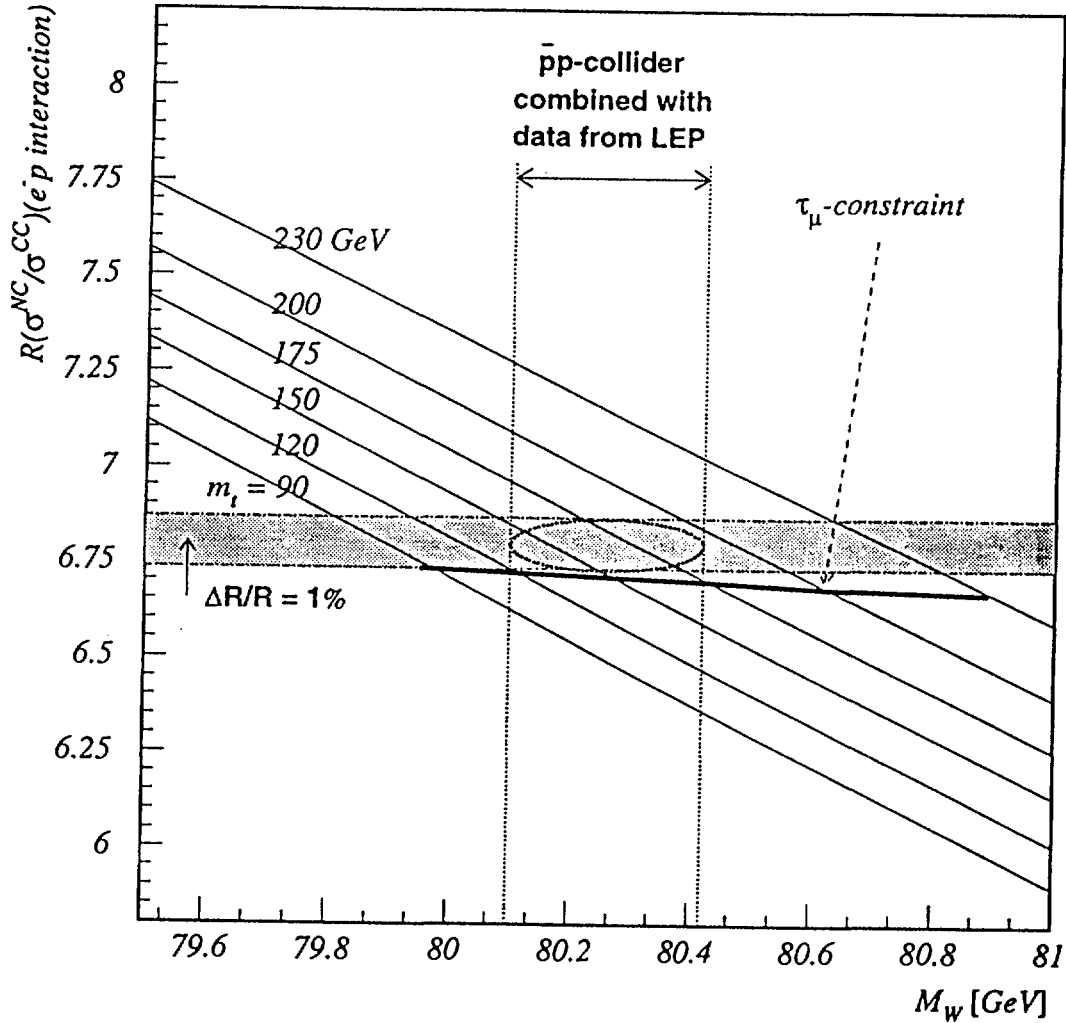


Fig.2.9 The correlation of  $R$  and  $M_W$  as a function of  $m_t$  for fixed  $M_H = 300$  GeV. The world average of the present direct  $M_W$  measurement from  $p\bar{p}$  collider is indicated. A possible 1%  $R$  measurement from HERA results in the shaded area. The combination of low  $Q^2$  data (muon lifetime) with  $M_Z$  from LEP give rise to the  $\tau_\mu$  constraint (solid line).

The above information on  $M_W$  is extracted from the  $W$  propagator, thus it can be interpreted as a “direct”  $W$  mass measurement. Although the coupling strength given by  $G_F$  contains indirect information of  $M_W$  (see equation (2.50) and (2.52)), but even the most precise measurement of  $G_F$  from muon lifetime can not be regarded as a measurement of  $M_W$ , since the relation between  $M_W$  and  $G_F$  is model dependent. In electroweak SM this relation depends on  $m_t$ , and at least one additional parameter (besides  $\alpha$  and  $M_Z$ ) is required to get a bound

on  $M_W$ . At HERA this independent experimental input can be provided in terms of the ratio  $R$ .

Confronted with low  $Q^2$  constraint from the muon lifetime, the combined high  $Q^2$  measurements of  $R$  and  $M_W$  at HERA provide a non-trivial test of the electroweak SM.

- Systematics due to structure function

The theoretical prediction of  $R$  not only depends on the electroweak parameters, but also on the knowledge of the proton structure functions. The systematic effect in  $R$  due to the latter dependence is studied in [25], where the dependence of  $R$  on quark distribution functions is derived in the following way. First, a few notations are introduced in terms of the individual quark and antiquark cross section:

$$\sigma_q^{NC}(eq \rightarrow eq) = \int \frac{dx}{x} dQ^2 xq(x, Q^2) C^{NC}(x, Q^2) = \epsilon_q \cdot \mathcal{Q} \quad (2.56)$$

$$\sigma_q^{CC}(eq \rightarrow \nu q) = \int \frac{dx}{x} dQ^2 xq(x, Q^2) C^{CC}(x, Q^2) = \eta_q \cdot \mathcal{Q} \quad (2.57)$$

where the function  $C(x, Q^2)$  is independent of the quark distribution function but directly related to the electroweak amplitudes. The integration is performed over the relevant domain in  $x$  and  $Q^2$  defined by the  $p_t^{had} > 25\text{GeV}$  cut.  $\epsilon_q, \eta_q$  and  $\mathcal{Q}$  are defined as:

$$\epsilon_q = \frac{\int \frac{dx}{x} dQ^2 xq(x, Q^2) C^{NC}(x, Q^2)}{\int \frac{dx}{x} dQ^2 xq(x, Q^2)} \quad (2.58)$$

$$\eta_q = \frac{\int \frac{dx}{x} dQ^2 xq(x, Q^2) C^{CC}(x, Q^2)}{\int \frac{dx}{x} dQ^2 xq(x, Q^2)} \quad (2.59)$$

$$\mathcal{Q} = \int \frac{dx}{x} dQ^2 xq(x, Q^2) \quad (2.60)$$

Hence the dependence of  $\sigma_q$  on the structure functions is separated into two parts:  $\mathcal{Q}$  is the integral of the quark distribution, while  $\eta_q$  and  $\epsilon_q$  contain the electroweak physics weighted over the quark distribution. Since the quark distribution enter both in the numerator and in the denominator of  $\eta_q$  and  $\epsilon_q$  expressions, the uncertainties are somewhat reduced.

Thus the ratio  $\sigma^{NC}/\sigma^{CC}$  can be expressed in terms of individual quark contributions:

$$R = \frac{\sigma_u^{NC} + \sigma_d^{NC} + \sigma_{\bar{u}}^{NC} + \sigma_{\bar{d}}^{NC} + \sigma_s^{NC} + \sigma_{\bar{s}}^{NC} + \sigma_c^{NC} + \sigma_{\bar{c}}^{NC} + \sigma_b^{NC} + \sigma_{\bar{b}}^{NC}}{\sigma_u^{CC} + \sigma_d^{CC} + \sigma_c^{CC} + \sigma_s^{CC} + \sigma_b^{CC}} \quad (2.61)$$

To see more clearly the contributions from different quarks to ratio  $R$ , the above formula can be rewritten in the following form:

$$R = \frac{\epsilon_u}{\eta_u} \left(1 + \frac{\sigma_d^{NC}}{\sigma_u^{NC}}\right) \frac{1 + \Delta NC}{1 + \Delta CC} \quad (2.62)$$

Thus the contributions to  $R$  from  $u$  and  $d$  quarks are represented only in the first two terms, while the third term accounts for a small modification to  $R$  value due to sea quarks and antiquarks. As an example, from KMRS parameterization one gets [25]:

$$\frac{1 + \Delta NC}{1 + \Delta CC} = 1.153 \quad (2.63)$$

A 1% difference in  $R$  is predicted for a change of 10% in  $\bar{D}/U$ , little effect on  $R$  is expected for even large uncertainties in  $\bar{S}/U$ ,  $\bar{C}/U$  and  $\bar{B}/U$ . In particular, the influence of the strange quark distribution is strongly suppressed

in the ratio  $R$ .

In the  $u$  and  $d$  quarks contributions, the first term  $R_u \equiv \epsilon_u/\eta_u$  in equation (2.62) depends on the shape of the up quark distribution, since the  $NC$  and  $CC$  couplings cause a different weighting via their propagator. The second term is determined by  $\sigma_d^{NC}/\sigma_u^{NC}$  and thus sensitive to  $D/U$  ratio, to keep the uncertainty of  $R$  lower than 1% requires the  $D/U$  ratio to be known to better than 10%.

Using this strategy, a large variety of the structure functions available in [29] has been tested, and the resulting uncertainties on  $R$  are found to be about 0.5%[25].

In our analysis, the CC and NC events are selected from 1993  $e^-p$  and 1994  $e^\pm p$  data at HERA in parallel, i.e., the same criteria are applied to the final hadronic system of the CC and NC events. The NC/CC ratio after the  $P_t^{had} > 25$  GeV cut is calculated and the physics implications are investigated. The CC and NC integrated and differential cross sections are also calculated and compared with the theoretical predictions from the Standard Model.

**NEXT PAGE(S)  
left BLANK**

# Chapter 3

## HERA And H1 Experiment

The  $e - p$  collider HERA at the DESY laboratory in Hamburg is a unique facility for the study of elementary particle physics using high energy electron-proton interactions. Many new interesting physics topics which are crucial in understanding the fundamental forces and the structure of the nucleon can be studied at HERA [30]. The H1 detector [31] measures the energy and the direction of the produced particles in the  $ep$ -interaction, which are used later for the study of the experimental distributions.

### 3.1 The HERA $ep$ Collider

HERA consists of two storage rings designed for 820 GeV proton beams and 30 GeV electron (positron) beams, which has the highest collision energies for lepton-proton interactions ever attained in the world. The high momentum transfer  $Q^2$  ( $\leq 4 \times 10^4 \text{GeV}^2$ ) at least two magnitudes more than before and low Bjorken  $x$  down to  $\sim 10^{-5}$  are achieved at these high energies. Fig.3.1 shows the kinematic domain extended by HERA in terms of  $Q^2$  and  $x$ , together with the kinematic ranges covered by some other experiments and by experiments foreseen in the future.

For the study of the photo-production ( $Q^2 \approx 0$ ), the center of mass energy realized at HERA is approximately one order of magnitude larger than in the fixed target experiments. At this high energy, a clean separation of the *direct* (photons interacting directly with proton through the point-like coupling) and *resolved* component (via

the so called hadronic or resolved component of the photon) can be achieved, and clear jet production and jet structures similar to high energy hadronic interaction become visible. Thus the photo-production interaction at HERA can be used for detailed QCD tests and to investigate the partonic structure of the photon. In the deep inelastic scattering (DIS) region ( $Q^2 > \text{few } \text{GeV}^2$ ), the proton structure can be studied at  $x$  values down to  $\sim 10^{-5}$ , where new physics is expected to be observed. Besides the extended tests of the Standard Model to regions of high  $Q^2$  and to higher families of quarks and leptons, the kinematic region reached at HERA opens up a fresh regime for many topics in particle physics study, such as super-symmetric particles, leptoquarks, lepton and quark substructures, massive new bosons, heavy leptons and quarks associated with right-handed currents.

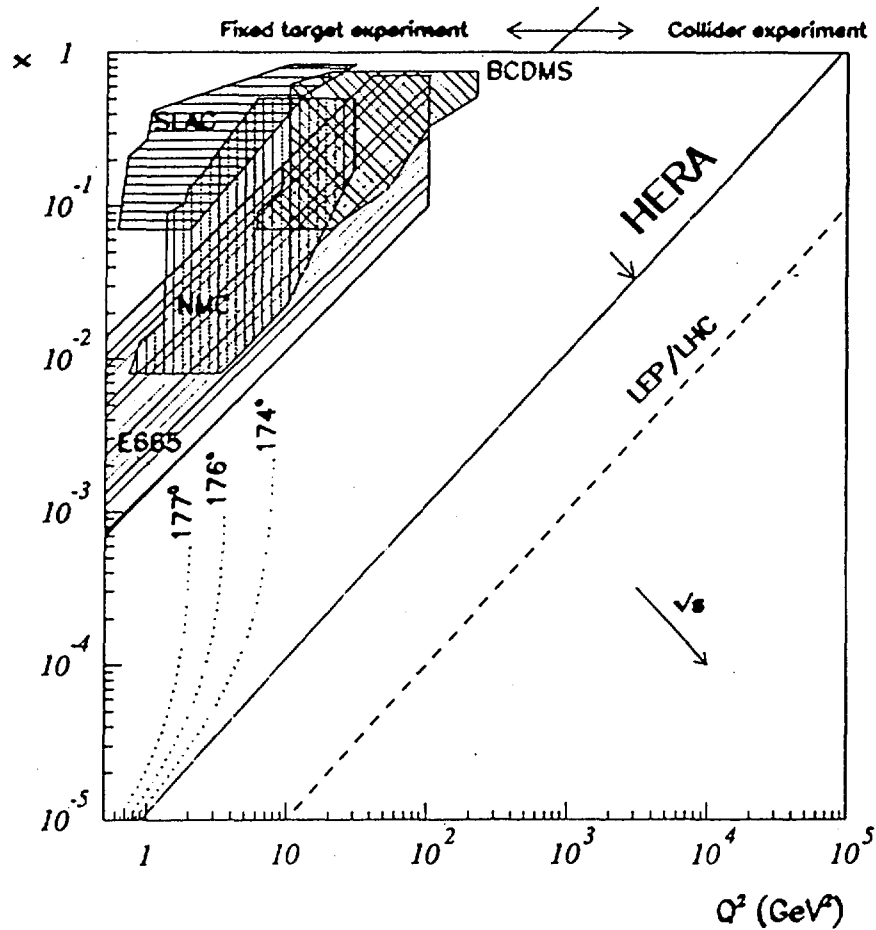


Fig.3.1 The kinematic ranges of current particle physics experiments. The excluded domains due to the beam hole size in HERA are also indicated.

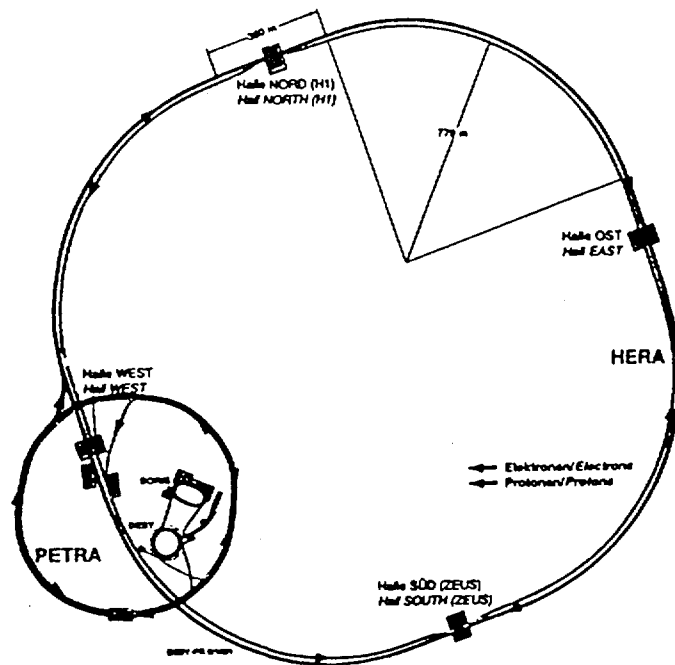


Fig.3.2(a) The layout of HERA.

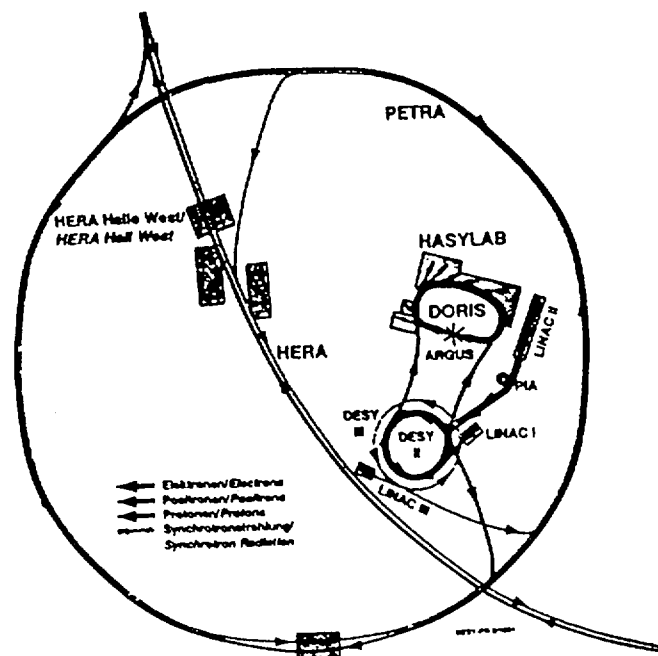


Fig.3.2(b) The layout of HERA pre-accelerators.

HERA also has a rich potential in the study of electroweak physics. For the first time, the weak interaction can be investigated through charged current ( $ep \rightarrow \nu X'$ ) processes in the high energy kinematic region where the  $W$  propagator plays a prominent role. The charged current process is actually the inverse neutrino-nucleon scattering, where the electron energy at HERA corresponds to a 50 TeV beam energy if considered as fixed target experiment. This energy is more than two orders of magnitude higher than in  $\nu N$  experiments.

As shown in Fig.3.2(a), the two counter-rotating proton and electron beams may collide head on in four interaction points spaced uniformly around the 6.3 km circumference of the ring. Two large detectors, the H1 detector in North Hall and the ZEUS detector in South Hall, are currently in operation. Fig.3.2(b) shows the pre-accelerators, where the electron (positron) beams are produced and pre-accelerated in LINAC II, PIA, DESY II and PETRA II, then injected to the main storage ring of HERA. Due to the limit of the maximum available RF voltage [32], for 1993 running period the actual electron beam energy is 26.7 GeV, and for 1994 running periods the electron and positron beam energies are 27.6 GeV. The proton beams are produced and pre-accelerated in LINAC III, DESY III and PETRA II before injected to HERA ring. A multi-bunch mode of running is adopted to deal with the low  $ep$  physics cross section (about one genuine  $ep$ -interaction every  $10^5$  bunch crossing). The designed total beam currents for the 210 circulating  $p$  and  $e^\pm$  bunches are  $I_p = 160mA$  and  $I_e = 60mA$ . The time interval between two successive bunches is 96 ns. There is always at least one bunch for each type without collision partner (pilot bunches) for background suppression purpose.

## 3.2 The H1 Detector

The H1 detector was designed for the detection and measurement of the energetic particles and jets emitted in the reaction taking place in collisions between electron (positron) and protons. It is devoted for the advanced study of the internal structure of the proton and for the search of hitherto unobserved particles. Such purposes put some requirements on the design and construction of the H1 detector: it should have a good hermeticity to absorb all of the energetic particles emitted from the  $ep$  scattering; the dead material and cracks between sub-detector parts have to be minimized to get a good homogeneity and to ensure a precise measurement of the energy; and it should have good granularity to ensure a precise measurement of the direction of the emitting particles and jets.

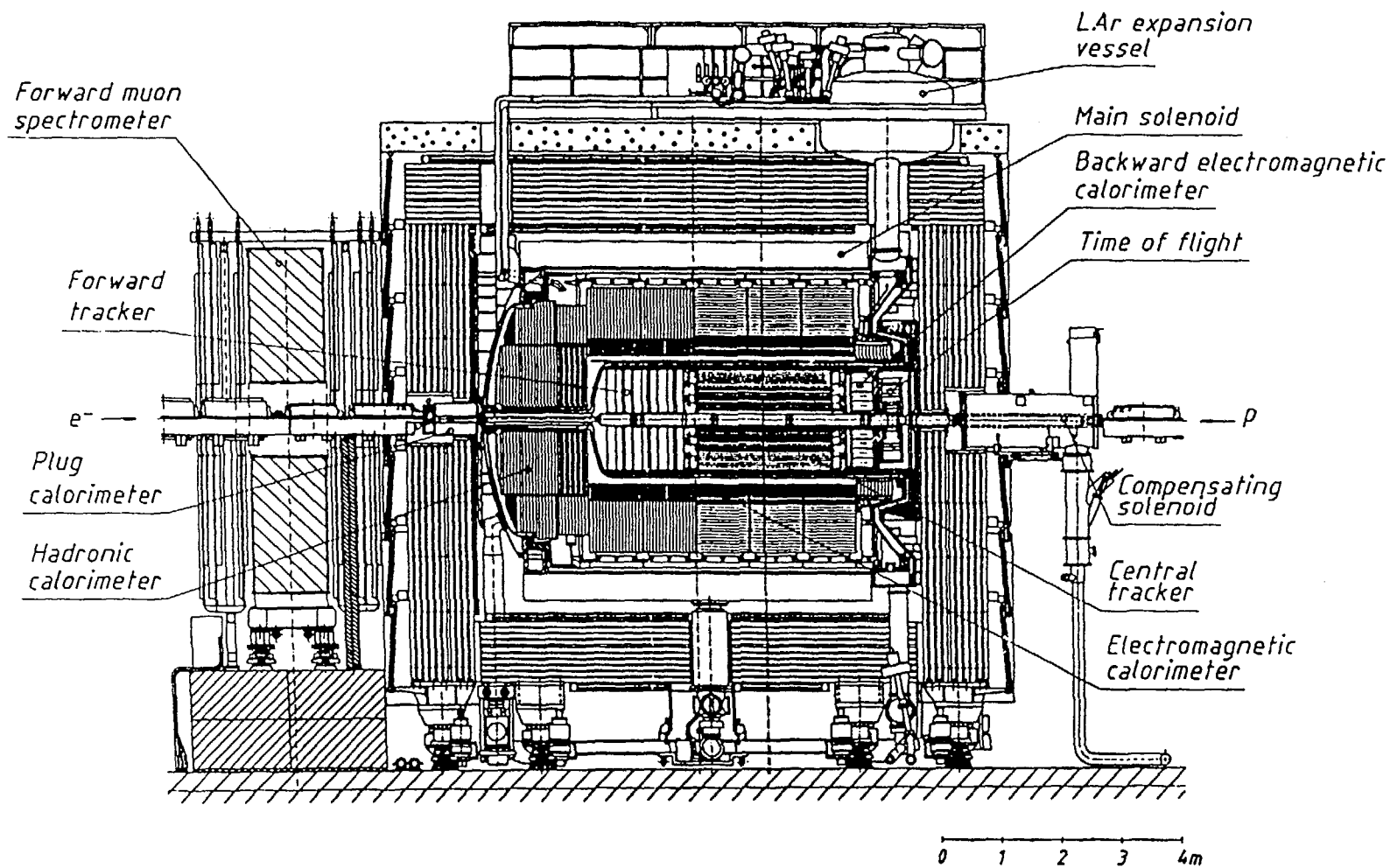


Fig.3.3 Longitudinal view of the H1 detector.

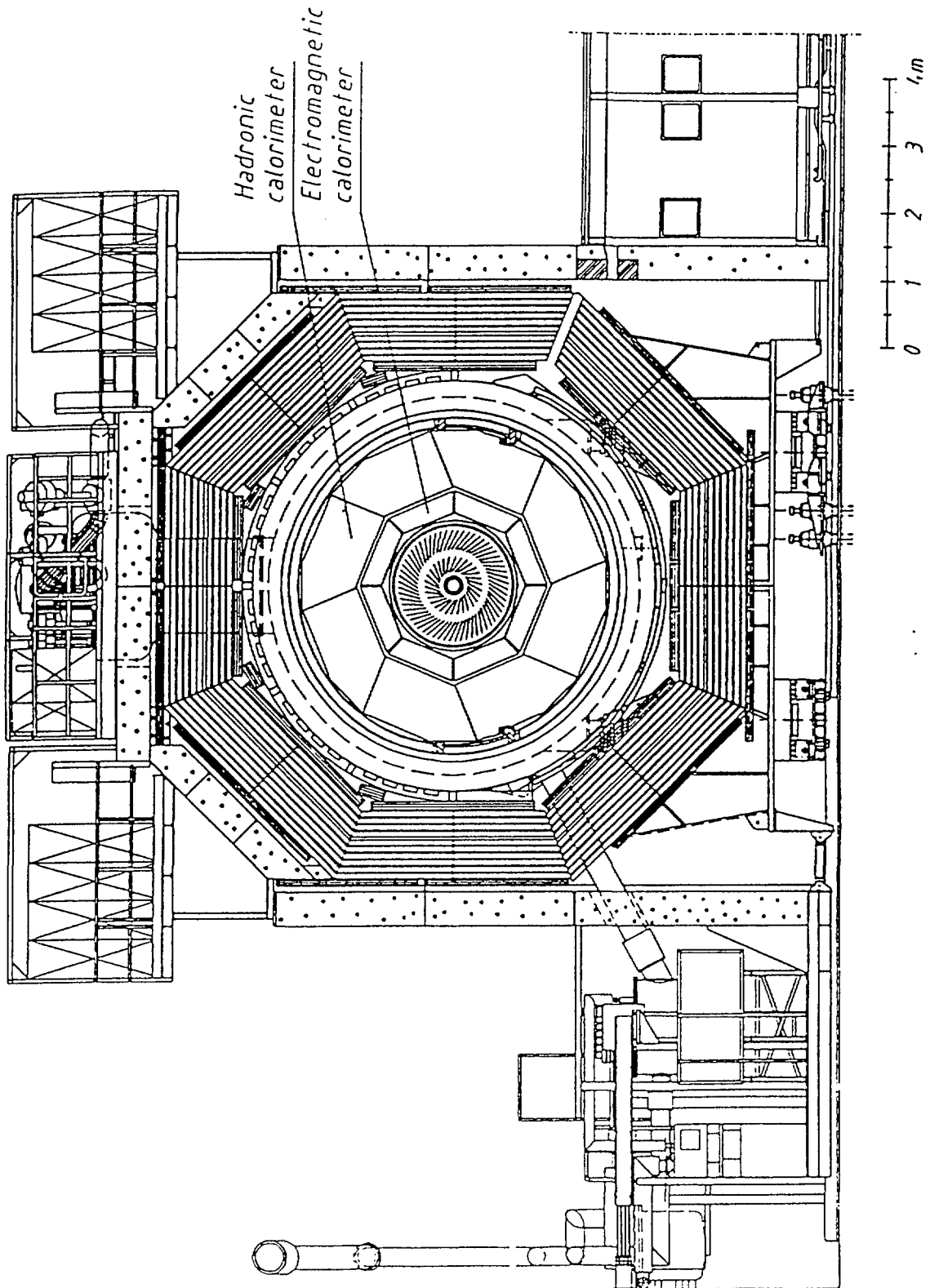


Fig.3.4 Transverse view of the H1 detector.

The general structure of the H1 detector is shown in Fig.3.3 and Fig.3.4, which give the longitudinal and the transverse sections of the H1 detector respectively. Taking into account the forward boost of the center-of-mass system of the interaction due to the asymmetry of the beam energies, the H1 detector is asymmetrical and more massive and highly instrumented in the proton direction, in order to provide a smooth and homogeneous detector response from small forward angles up to backward angles.

As shown in Fig.3.3 and Fig.3.4, H1 detector consists of a number of sub-detectors which are complex systems by themselves. The particles emitted from the  $ep$  interaction point traverse subsequently the beam pipe; the inner tracking system consisting of multi-wire proportional chambers (MWPCs) and the drift chambers for charged particle measurement; the liquid argon calorimeter (LAr) with 45,000 physical channels, surrounded by a super-conducting coil of 6 m diameter that provides a field of 1.2 T parallel to the beam direction. The iron return yoke is instrumented with a 160,000 channel streamer tube system for the identification of escaping muons, and also serves as a tail catcher (TC) for hadronic showers. An electromagnetic backward calorimeter (BEMC), a forward plug (PLUG) calorimeter and a forward muon spectrometer further cover most of the remaining solid angles thus complete the detection of the asymmetrical  $ep$  interaction events. These detector parts will be introduced in next sections.

The raw data size of one event amounts to 3 MBytes. After front end data compression, 50 to 100 kBytes per event are logged. The full data from all components allow a detailed reconstruction of the physics quantities of the  $ep$  interaction final state, i.e. the precise energies and flight directions of particles and jets.

### 3.2.1 Calorimeter

As shown in Fig.3.3, the complete solid angle range is covered by four parts of the calorimeters: the liquid argon calorimeter which is composed of an electromagnetic part with Pb absorber plates and a hadronic part with stainless steel absorber plates, covers most of the solid angle  $4^\circ < \theta < 153^\circ$  in a single cryostat. The backward lead-scintillator sandwich electro-magnetic calorimeter (BEMC) situated in the electron beam direction covers the remaining backward space of  $151^\circ < \theta < 177^\circ$ . The beam hole in the proton beam direction ( $\theta < 4^\circ$ ) is partly covered by a small plug calorimeter with copper-silicon sandwich structure. The tail catcher in the outmost position, which is composed of iron plates interleaved with plastic streamer tubes, provides a rough estimation of hadronic energy leaking out of the LAr as well as a measurement of muon tracks.

### The liquid argon calorimeter

The liquid argon technique was chosen for its advantages of good stability and ease of calibration, fine granularity for  $e/\pi$  separation and energy flow measurements, also for its good hermeticity and homogeneity of response.

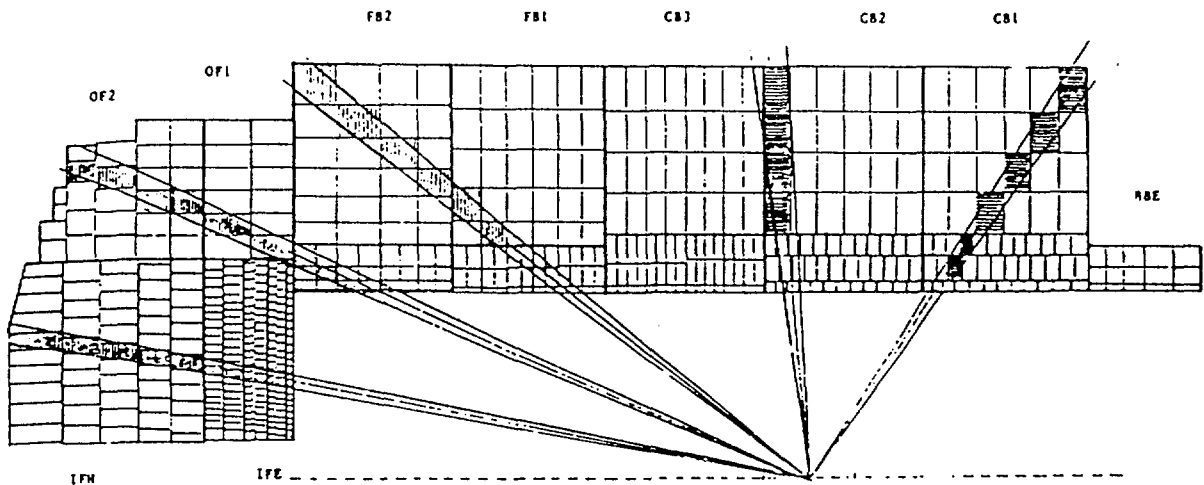


Fig.3.5 The segmentation of the LAr.

- Segmentation

The segmentation of the LAr is shown in Fig.3.5. There is no dead material between the fine grained layer of the electromagnetic part and the coarser outer layer of the hadronic part. The whole LAr is segmented into eight self supporting “wheels” along the beam axis named according to their position with respect to the proton beam; i.e. BBE in backward barrel region (this wheel only contains electromagnetic part since the chance of the hadronic jets produced in  $e-p$  interaction emitted in this direction is small), CB1, CB2, CB3 in central barrel region, FB1, FB2 in forward barrel region, OF1, OF2 (outer forward) and IF1, IF2 (inner forward) in forward region. Except BBE wheel which is electromagnetic and OF2(IFH) wheel which is hadronic, CB, FB and OF1(IFE) wheels contain both electromagnetic parts and hadronic parts. The LAr are segmented in  $\phi$  into eight

identical octants in the six barrel wheels (FB,CB,BBE), and into two half rings in the two forward wheels (OF,IF).

Throughout the calorimeter, the  $\phi$  cracks in electromagnetic parts are pointing to the beam line while the cracks in hadronic parts are strongly non-pointing as shown in Fig.3.4. This way a good containment is achieved and the energy deposited around the crack region can be corrected on an event-by-event basis. In order to obtain good hermeticity and homogeneity, a great effort has been made to minimize the cracks between stacks of LAr, which includes the  $z$ -cracks (between different wheels), the  $\phi$ -cracks (between octants in a wheel) and  $r$ -cracks (between electro-magnetic and hadronic parts of a wheel).

In the hadronic stacks of LAr, the signals are readout from independent cells inserted between welded stainless steel absorber plates, which are oriented in such a way that the incident particles cross them with angles not smaller than  $45^\circ$  [33][34] (shown in Fig.3.3 by vertical plate lines in FB, OF, BBE and horizontal plate lines CB). The hadronic showers are fully contained in hadronic stacks with the help of tail catcher for very energetic jets. Each electromagnetic stacks is composed of piled up sandwiches of G10(epoxy- fiberglass)-Pb-G10 separated by spacers defining the liquid argon gaps. The electromagnetic showers are fully contained in this part. The granularity of the cells is determined to clearly separate the electromagnetic and hadronic showers and to precisely reconstruct the emitting angles. The general  $\theta$ -granularity of the readout pads is shown in Fig.3.5.

- Trigger, electronics and DAQ

The LAr trigger system is illustrated in Fig.3.6, and is divided into an analog part and a digital part. In the analog part, the signals from 45000 LAr readout channels are reordered and combined in an analog form into 256 projective towers ("big tower"(BT)), which are divided into electromagnetic and hadronic sections. Various energy sums employing programmable threshold functions are yielded from the digital summing electronics which is fed by the digitized signals from these  $2 \times 256$  big towers, providing the trigger bits for the central trigger logic. The quantities derived from these energy sums include topological energies in various parts of the calorimeter (forward, barrel etc.) and the transverse energy and missing transverse energy. Further, the electron trigger can be derived by comparing the energy depositions in electromagnetic section and hadronic section of a given big tower, applying a minimum and a maximum threshold for these two sections respectively. The exact bunch crossing of the energy deposition ( $t_0$ ) should also be decided by the trigger, which is done in the analog part by a pulse delay and crossing technique [34].

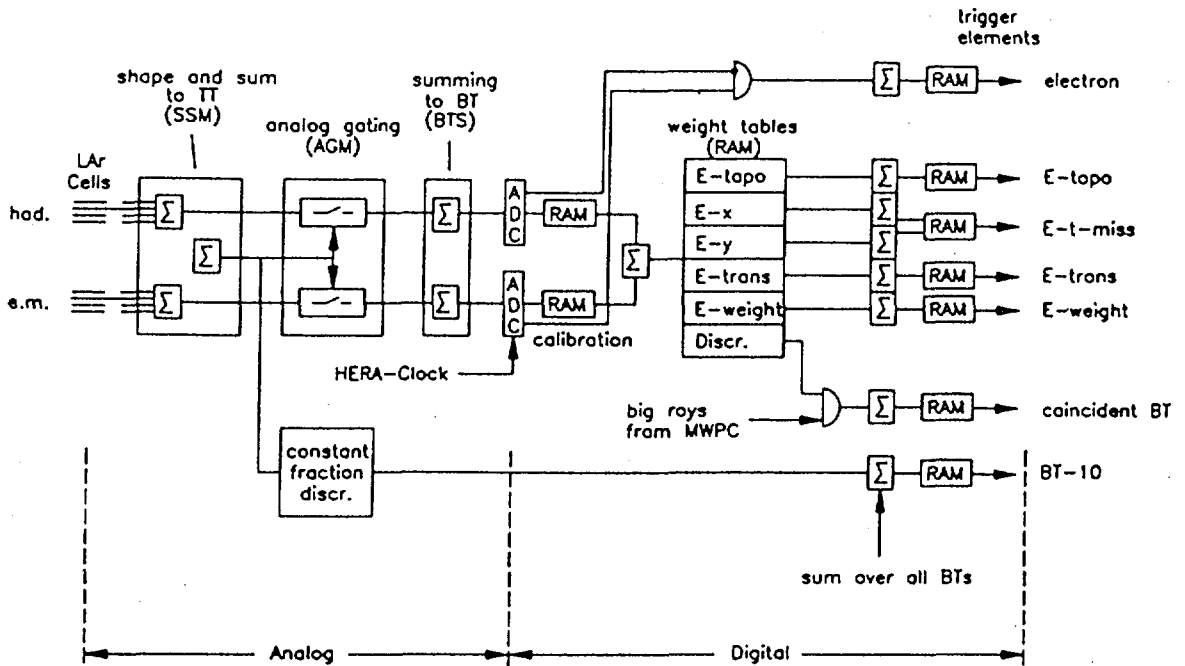


Fig.3.6 Schematic layout of the LAr trigger system.

The calorimeter trigger is built from sums of the neighboring segments. To ensure that the calorimeter trigger of large collected energies belong to a unique bunch crossing  $t_0$  with short time intervals (96 ns), the capacities of these segments should be equal within  $\pm 5\%$  [34].

The situation of large energies being deposited at short time intervals into detectors with large capacitances and long charge collection times is also the major concern in the design of the electronic system, together with the requirements that the information has to be stored until the arrival of the trigger signal ( $\sim 2.9\mu s$ ) and that the LAr has to be operated in a large magnetic field. Two electronic calibration systems have been built into the calorimeter: a "cold" system with the calibration capacitors in the LAr close to the stacks and a "warm" one with the calibration capacitors at the preamplifier level, to ensure that the calibration of the electronic chain is known and to keep the electronics system to be stable at a few per thousand level.

Most of the data readout by the calorimeter data acquisition system comes from LAr. At the preamplifier level, the LAr readout data is split into a data path (the outputs of slow shapers are processed) and a trigger path (the outputs of fast shapers are processed), where the first level trigger (L1) (and a planned level 2 trigger (L2)) decision is made. Two event builders collect the formatted data for both paths within independent VME branches. A third processor is planned to reject background events by running a fast trigger L3 algorithm. Finally, a level 4 filter farm based on the calorimeter information together with the informations coming from other sub-detectors is performed, and the data size is further reduced. The maximum data taking rate of 200 Hz is achieved with event size of 20 Kbyte in calorimeter and 1.2 ms first order dead time.

The front end electronics and the electronic calibration system is situated as close as possible to the H1 detector [34]. The charge collection efficiency of the LAr calorimeter stacks depends on the actually applied high voltage as well as on the purity change of the liquid argon due to pollution. The calorimeter output ADC counts are also affected by the electronic effects such as pedestal drift. A high precision determination of the calorimeter response curves is done whenever the current calibration constants are no longer valid due to the changes in the hardware or electronics. The signal in each cell after pedestal offset correction is converted to charge using a third order polynomial. The necessary offline corrections to resulting charge converted from ADC counts are then performed. In 1994 running period, about 13% of high voltage supply channels of BBE calorimeter have not functioned properly, which severely affected the homogeneity of the energy measurement, and needed to be corrected accordingly [35].

The calibrated charges for each LAr cell are then fed into LAr reconstruction program, where the noise cells are suppressed, the charges are converted to energies for both electromagnetic and hadronic showers, the dead material effect is also corrected, and the clusters are formed from groups of cells, which correspond closely to the particle showers.

- Energy measurement

The LAr calorimeter is a non-compensating one, i.e. the signals from electrons are on average higher than those from pions of the same energy, thus the hadronic energy has to be reconstructed by applying weighting functions to the measured signals.

The energy is first given at electromagnetic scale in cell level for both electromagnetic and hadronic sections of LAr, which is performed by applying an electron calibration constant to the charge signal on the cell level as described below.

The calibration constant has been determined for the electromagnetic sections by calibration measurements with electron beams at CERN, and corrected for dead material using detailed Monte Carlo simulation [36].

**Electromagnetic energy scale:** Several factors determine the scaling from the charge to energy in individual cells: a charge to energy calibration constant determined for each stack in the calibration runs at CERN [36], the correction for the charge collection efficiency of the calorimeter at operating high voltage of 1500 V, and the correction factors for local variations of gap and absorber thicknesses measured during the stack construction [34].

The absolute electromagnetic calibration constant  $c_{exp}$  for each module is defined by:

$$E_{rec} = c_{exp} \cdot \sum_i Q_i \quad (3.1)$$

where  $E_{rec}$  is the reconstructed energy in electromagnetic scale, and the sum runs over the channel  $i$  with charge  $Q_i$  which remains after electronic noise suppression cuts. In the CERN calibration test beam runs,  $c_{exp}$  was extracted iteratively by equalizing the reconstructed energy from measurements and from detailed Monte Carlo simulation [36].

The energy equivalents at electromagnetic scale of the standard electronic noise deviation  $E_i^\sigma$  for a channel  $i$  is obtained from random events. The noise level depends on the region of the detector, it varies from 10 MeV in IFE module to 30 MeV in CB wheels, from the measurement during the electron calibration. The signal in a cell is only kept if it exceeds a noise threshold  $2 \times E_i^\sigma$ . To further suppress noise cells, the negative noises presented in the Gaussian shaped noise signals after pedestal subtraction are used for an automatic compensation to the positive noise contribution to the measured signals. The cells above  $+4E_i^\sigma$  are kept as “signal seed”, all neighboring cells exceeding the  $2 \times E_i^\sigma$  threshold in a  $3 \times 3 \times 3$  cube around the signal seed are also kept in order to cover small signals at the fringe of the showers. The noise picked up in this step is automatically compensated by keeping also the signals from the cells below  $-2E_i^\sigma$  around the signal seed. Cells below  $-4E_i^\sigma$  are kept to compensate  $+4E_i^\sigma$  seed cell from noise, while no signal from the cells around  $-4E_i^\sigma$  cell is kept since they are purely noise [34].

The cells passing cell level reconstruction are subject to clustering. Firstly, a search for connected regions in the energy distribution of the two-dimensional (2D) longitudinal section of each calorimeter module is performed, and several separated maximum in this region are found; then these 2D clusters

are merged into three-dimensional (3D) clusters step by step, i.e. first inside calorimeter module, then across the module boundaries, finally the 3D clusters are formed. This merging is based on the dispersion in direction seen from the interaction point. The energy distribution pattern of the clusters in the electromagnetic part is firstly checked before merging them with clusters in hadronic calorimeters. By checking the fraction of the energy deposited in the first layer for early shower development, and checking four most energetic cells for compactness [37], the clusters which show obvious characteristics of an electromagnetic shower will not be merged further. The clustering gives an additional information to further reduce the noise in the hadronic part of the calorimeter: the scattered small signals far away from the prominent clusters (a cluster is called prominent when the significance  $\sqrt{\sum (E_i/\sigma_{noise})^2}$  is above 8) are suppressed.

Another important uncertainty in energy measurement of the calorimeter is the energy loss in dead material in front of the calorimeter and in cracks between the calorimeter stacks, which account for  $\approx 10\%$  of the energy deposited in low  $Q^2$  DIS events. About 90% of the missing energy is lost in the dead material in front of the calorimeter. This loss is corrected using Monte Carlo simulations. The correction is done by adding the lost energy to the cells in the first inner layer of LAr or to the pair of cells in the layers nearest to the crack and at both sides of the crack, according to the locations of the cells, the geometry and property of the dead material, and the energy deposited in the cells.

**Hadronic energy scale:** The energy derived in electromagnetic scale as described above has to be corrected for the 30% loss for hadrons due to the non-compensating response of LAr. The correction is to equalize the response to the electromagnetic and pure hadronic components of a hadronic shower, and therefore to suppress the influence of the large fluctuations in the hadronic shower composition on the reconstructed energy. A linear hadronic response to the energy is also desirable. The hadronic energy scaling is done by applying a weight to signals in individual cells within a hadronic object. The primary electromagnetic clusters which already have correct energy scale are filtered, according to their characteristics such as the containment in electromagnetic calorimeter, the early shower development and the compactness. Then the hadronic object is formed by cells not included in electromagnetic cluster and located around the direction defined by the barycenter of the hadronic cluster (a cluster is called hadronic if it is prominent and if it is not classified as electromagnetic in the filtering, or if

it penetrates deeply into the calorimeter for lower energies) and the nominal interaction point.

A software weighting technique which was initially proposed by the CCFR Collaboration and further developed by H1 in CERN test runs is applied. The weighted energy  $E_{rec}^i$  in cell  $i$  is given as a function of the cell energy on the electromagnetic scale  $E_0^i$  [38]:

$$E_{rec}^i = \{a_0 + a_1 \exp(-\alpha E_0^i/V^i)\} E_0^i \quad (3.2)$$

where  $V^i$  is the cell volume. The weighting parameters  $a_0$ ,  $a_1$ , and  $\alpha$  are different for electromagnetic and hadronic parts and should be determined respectively. These parameters are determined using the response to the hadrons in Monte Carlo simulated jets, and expressed as functions of the reconstructed jet energy. The same results are obtained using simulated single pion response. The formula can be simplified for jets with energy less than 7 GeV to  $E_0^i$  multiplied by a simple factor corresponding to effective  $e/\pi$  ratio in EMC and HAC. In energy range between 7 and 10 GeV, the correction was done with both methods to ensure a smooth transition between the two weighting expressions.

The absolute electromagnetic scale constants  $c_{exp}$  of different calorimeter modules were carefully calibrated using  $e^-$ ,  $\mu^-$  and  $\pi^-$  test beam at CERN. For electromagnetic part of LAr, the calorimeter response turns out to be uniform in space within  $\pm 1\%$  and linear with energy within  $\pm 1\%$ , a total systematic uncertainty of about 2% of the electromagnetic scale is expected [36]. For the hadronic part, the electromagnetic energy scale are derived from the ones measured in the electromagnetic sections, corrected for the difference in the sampling fractions by detailed electron shower simulation [38]. After the weighting procedure, the hadronic scale in LAr calorimeter is estimated up to  $\pm 4\%$ .

The dependence of the relative resolution  $\sigma(E)/E$  on the energy can be expressed by

$$\frac{\sigma(E)}{E} = \sqrt{\frac{a^2}{E} + \frac{b^2}{E^2} + c^2} \quad (3.3)$$

with a stochastic term  $a/\sqrt{E}$ , a noise term  $b/E$  and a constant term  $c$ . The energy resolution for electron was found to be 10% to 13%/  $\sqrt{E}$  for various stacks and amounts to about 11.5%/  $\sqrt{E}$  on average, with the constant term below 1%. The resolution for pions are determined by a Gaussian fit to the reconstructed

energy distribution after the weighting procedures, thereby the low energy tails are excluded. The same resolution function as above is used to fit the data points, which yields a hadronic energy resolution after weighting of about  $50\%/\sqrt{E}$ , with the energy independent term below 2% which indicates a good compensation is achieved [38]. The tail catcher is included for beam energy larger than 80 GeV in deriving this value to cover the energies leaking out of LAr. The transverse momentum  $p_t$  balance of DIS events can be used as a direct check of the electromagnetic and hadronic energy measurement.

### Tail catcher

The iron yoke of the main solenoid magnet encloses the H1 detector. It has an octagonal barrel made up of ten 75 mm thick laminations separated by 25 mm air gaps except one of 50 mm, and both flat endcaps made up of ten 75 mm thick laminations separated by 35 mm air gaps except one of 50 mm. The iron is interleaved with 16 layers of limited streamer tubes (LST) to catch the energetic hadronic jets leaking out of the calorimeters, as well as to detect the tracks of penetrating muons.

Eleven of the sixteen LST layers are equipped with readout electrodes (pads) to measure the hadronic energy. The front (back) tower signals are formed by summing up the analog pad signals from five inner (six outer) layers with tower builders, then grouped, amplified, integrated and stored. The hadronic energy  $E_{had,i}$  in a tower  $i$  is given as a function of the measured charge  $Q_{had,i}$  [40]:

$$E_{had,i} = c_1 c_{3,i} \frac{Q_{had,i}}{c_2} \quad (3.4)$$

The general calibration constant  $c_1$  is determined using test beams of pions and muons at CERN [41]. The parameter  $c_2$  gives the tower charge of an average minimum ionizing particle (muons) at an incident angle of  $0^\circ$  with respect to the normal of the LST chamber. The parameter  $c_{3,i}$  describes the tower to tower variations of the charge measurement, it is determined together with parameter  $c_2$  using cosmic muons triggered by opposite pairs of barrel or endcap modules. An energy resolution of  $100\%/\sqrt{E}$  is obtained using 10 to 80 GeV  $\pi$  and  $\mu$  test beams at CERN [41].

The energy lost in dead material outside calorimeter should be taken into account when combine the hadron clusters in tail catcher and LAr. The lost energy  $E_{loss}$  is described as a function of  $E_{LAr,last}$  (energy deposited in the last layer of LAr) and  $E_{TC,first}$  (energy deposited in the first layer of tail catcher):

$$E_{loss} = \alpha(\theta)E_{LAr,last} + \beta(\theta)E_{TC,first} \quad (3.5)$$

where  $\alpha$  and  $\beta$  depend on the thickness of the dead material between the two calorimeters, and were determined using CERN test beams [42]. This calculated  $E_{loss}$  is then distributed among the cells in proportion to their energy. Similar procedure is applied when linking the TC cluster with non-electromagnetic cluster in BEMC.

### BEMC and PLUG calorimeter

The solid angle near the beam hole left out by LAr calorimeter are further partially covered by a backward electromagnetic calorimeter and a forward plug calorimeter.

The DIS events with  $Q^2 < 100 \text{ GeV}^2$  dominate the cross section observed in H1 detector. The energy and direction of the electrons scattered in small angle in these events are measured by BEMC (up to 1994 data taking runs, replaced by 'SPACAL' from 1995), which also contributes to the measurements of hadronic final states with medium to low- $x$ , high  $y$  and of the hadrons emerging from photo-production. BEMC is a conventional electromagnetic lead-scintillator sandwich calorimeter, located 144 cm upstream from the nominal interaction point in electron direction, and segmented into 88 multi-layer lead-scintillator sandwich stacks aligned parallel to the beam axis. The entire structure corresponds to 22.5 radiation lengths or 0.97 hadronic absorption lengths.

Two contributions are taken into accounts in the calibration of BEMC. The first contribution, the electronics gain is determined using a pulser system. The testpulse is injected at the preamplifier level on the BEMC stacks, and each stack is connected to an individual pulser channel, the pulser system measures the response of the entire electronics chain including all cables. The entire electronics is calibrated once per week during the data taking period, and a good stability of the electronics at a few per thousand level is achieved. To calibrate another contribution, the light collection and detection in the stacks, first the absolute energy scale for individual stack is determined using testbeams at the DESY synchrotron, then this scale is confirmed and improved in situ using electrons scattered under small angle in the kinematic peak.

An energy resolution of  $10\%/\sqrt{E}$  has been found using testbeams with 1 GeV to 80 GeV electrons, the constant term for a single stack is well below 1%. Using DIS events with electrons scattered in BEMC, the cluster position reconstructed in BEMC is linked with the track reconstructed in tracking detector. A 1.3 cm resolution in

position is achieved according to the attenuation properties of light in the scintillator plates.

The main task of plug calorimeter is to catch the energy of hadrons emitted close to the beam pipe to minimize the loss in total transverse momentum measurement. It is also used to separate the proton jet and to veto beam gas and beam wall background events. Due to the limited available space and the physical requirements, PLUG is made of nine copper absorber plates interleaved by eight sensitive layers of large area silicon detector [43].

In energy calibration of PLUG calorimeter, the ADC output in units of visible energy is calibrated based on an absolute energy measurement using  $\alpha$ -particles, then converted into total absorbed energy using detailed Monte-Carlo simulation in comparison with test measurements. The coarse sampling and lateral and longitudinal leakage restrict the energy resolution of PLUG calorimeter to be about  $150\%/\sqrt{E}$ , which is nevertheless sufficient for the goals within H1 experiment.

### 3.2.2 Tracking System

According to the event topology particular to HERA electron-proton collisions, and the asymmetry of the forward boost of the emitting jets to the incident beam proton direction, the H1 tracking system, which composed of a central tracker (CTD) and a forward tracker (FTD), provides simultaneous track triggering, reconstruction and particle identification over the whole solid angle. The general layout of the H1 tracking system is given in Fig.3.7.

#### CJC1 and CJC2

Central jet chambers provides an accurate measurement of the charged track parameters in the  $(x, y)$ -plane, and the  $z$ -coordinate measurement with moderate resolution and  $dE/dx$  measurement. As shown in Fig.3.8, the track reconstruction in the central region is realized through two large concentric drift chambers CJC1 and CJC2. The wires in the CJC chambers (about 2200 mm long) strung parallel to the beam axis are read out at both ends yielding a  $z$ -measurement via charge division. The resolution of this  $z$ -measurement is achieved at 1% of the wire length in  $z$ . This  $z$ -measurement gives a link between CJC tracks and  $z$ -chamber hits, which gives a much more accurate  $z$ -coordinate. The drift cells are tilted by about  $30^\circ$  with respect to the radial

direction, which allows for compensation of the Lorentz angle. This tilt optimizes the track resolution, since in the presence of the magnetic field the ionization electron drift approximately perpendicular to stiff, high momentum tracks from the center. A space point resolution of  $170\mu\text{m}$  in the drift coordinate ( $r\phi$  plane) has been measured.

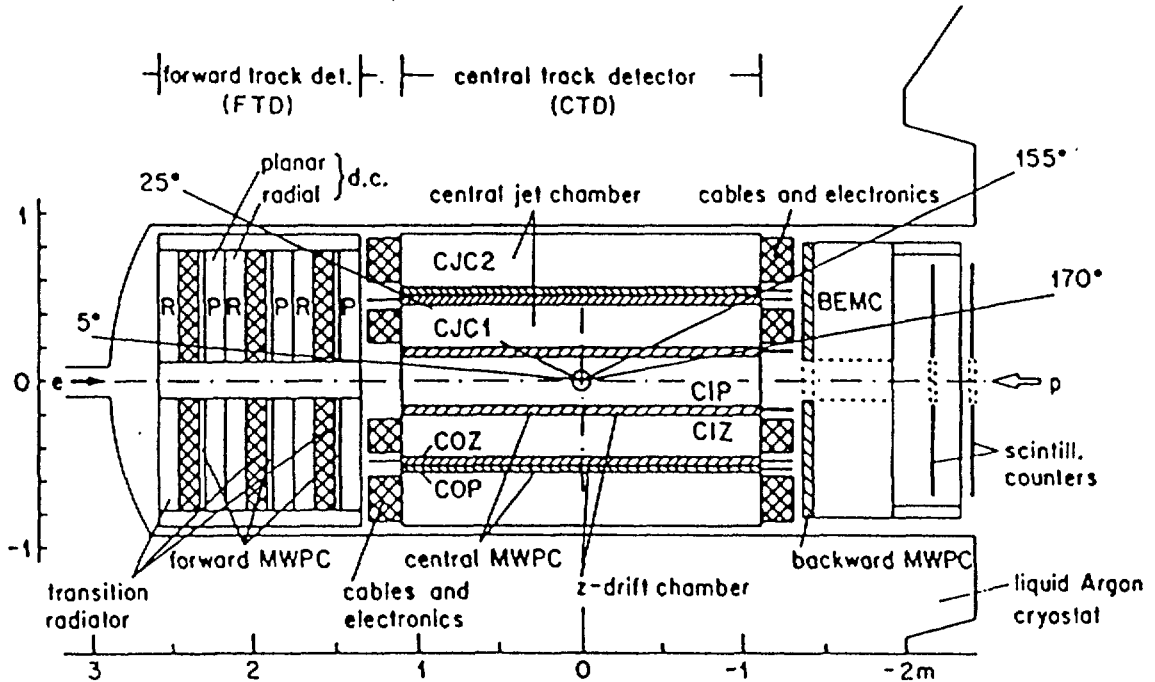


Fig.3.7 The H1 tracking system ( $r - z$  view).

In the track reconstruction, five helix parameters are used to describe the tracks of charged particles in the magnetic field: the signed curvature  $\kappa \equiv \pm 1/r$  (where  $r$  is the radius of the track circle in  $(x, y)$ -plane, the positive sign means the direction  $\phi$  coincides with a counter-clockwise propagation along the circle), the signed closest distance  $d_{ca}$  from the  $z$ -axis in the  $(x, y)$ -plane (positive means the vector from the  $z$ -axis to the point of closest approach and the trajectory direction form a right handed system), the  $z$ -position at the point of closest approach, and azimuthal angle  $\phi$  and polar angle  $\theta$ . The parameters  $\kappa, d_{ca}$  and  $\phi$  are fitted using the non-iterative algorithm of Karimäki [44] for the fitting of circular arcs, and  $\theta$  and  $z$  are fitted using a linear least-squares fit.

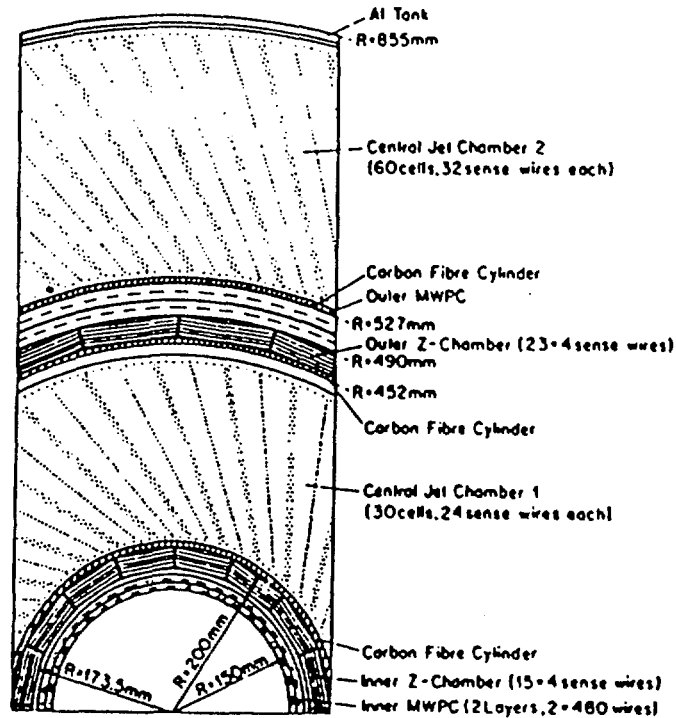


Fig.3.8 Central tracking system (transverse view).

The drift time data in the  $xy$ -plane is used to find tracks. Two versions are used in the track finding and fitting:

- 1) For background rejection and fast event classification on the fourth trigger level farm (L4), a fast version which is efficient for tracks originating from the primary vertex and with a momentum larger than 100 MeV/c is used. The bunch crossing time  $t_0$  is determined from the threshold in the drift time histogram. Firstly, the hit triplets with a wire distance of two within angular cells as track elements are searched, and curvature  $\kappa$  and track angle  $\phi_m$  at a mean radius  $r_m$  of CJC1 or CJC2 are defined. Then by sorting and clustering the hit triplets according to  $\phi_m$  and  $\kappa$ , the tracks are defined, and the standard track parameters are calculated from the coordinates of triplets. Further the track candidates are checked in the order of decreasing number of

triplets to resolve drift sign ambiguities and to discard mis-fitted tracks.

2) The standard version, which is about a factor of ten slower than the fast one, is efficient for all kinds of tracks and used in general reconstruction. It starts from the time reference  $t_0$  and tracks determined in the fast track finding. To improve  $t_0$  measurement, a special fits to the drift length values of long tracks is performed. This is done by comparing and fitting the difference of the expected drift length values calculated from the circular parameters in the  $(x, y)$  plane and the measured drift length values. The fit parameterizes the effect of a  $t_0$  difference and yields an accurate value of  $t_0$ . Meanwhile, by performing another circular fit, the track definition is also improved. At the first phase, the hit triplets are also searched as in fast version, but at adjacent wires instead of two wires distance. Chains of hits are extracted and checked by a fit to drift time after all hits within an angular cells are analyzed, then stored as track elements. Those track elements are merged step by step, from the same or the neighboring cell, to the whole ring (CJC1 or CJC2), finally the whole CJC (CJC1 and CJC2). The algorithm is similar in different step, which starts from a comparison of pairs of track element. By performing a  $\chi^2$ -fit to track elements with similar helix parameters and combining two acceptable elements, longer and more accurate track elements are formed. To further improve the quality of track fitting, the expected drift length values on all possible wires calculated from the circular parameters are compared with the measured values, by a simple fit to the difference, the hits not compatible with a track are discarded. The fits to determine track parameters are repeated using all acceptable hits. As last track parameter the mean energy loss  $dE/dx$  are determined from the single-hit value of the amplitudes, which could help in identifying electron, or in identifying proton to reject beam-gas events.

The mean vertex coordinates  $(x_v, y_v)$  in  $(x, y)$ -plane is quite stable for a sequence of runs, and can be fitted using long high momentum tracks with small  $d_{ca}$  from many events. This is done by minimizing the sum of squares of the distance  $b$  of the tracks to the vertex ( $b = x_v \sin\phi - y_v \cos\phi - d_{ca}$ ). The fitted  $x_v, y_v$  are then stored in the data base, which can be used to improve the track parameters originating from the primary vertex.

### CIZ and COZ

Another two thin drift chambers, the central inner  $z$ -chamber (CIZ) positioned inside CJC1 and the central outer  $z$ -chamber (COZ) positioned in between CJC1 and CJC2, provide a precise  $z$  measurement and a complementary measurement of the charged track momenta.

CIZ has an average radius of 180 mm and covers the polar angle  $16^\circ < \theta < 169^\circ$ , while COZ has an average radius of 460 mm and covers the polar angle  $25^\circ < \theta < 156^\circ$ . In some angular regions ( $16^\circ < \theta < 25^\circ$ ,  $156^\circ < \theta < 169^\circ$ ), the polar angle measurement can only be realized through accurate CIZ track segment information. The sense wires in these chambers are perpendicular to the beam axis, thus the drift direction of CIZ and COZ are perpendicular to the drift direction of CJC. In CIZ the sense wire plans are tilted by  $45^\circ$  from the normal to the chamber axis according to the tracks crossing the respective cells.

Typically the resolutions of  $300 \mu\text{m}$  in  $z$  and 1 to 2 % of  $2\pi$  in  $\phi$  are achieved in these two chambers. By linking the track elements with accurate  $r\phi$  from CJC and accurate  $z$  from  $z$ -chambers, the final accurate longitudinal as well as transverse momentum components are obtained.

### Forward tracking detector

When charged tracks are produced at direction close to beam axis (forward  $\theta < 30^\circ$ , backward  $\theta > 150^\circ$ ), the track length and the number of hits in CTD will decrease, which consequently cause the deterioration of accuracy in track pattern recognition. To compensate this loss, the forward tracking detector provides a higher radial density of accurate space points measurement. The layout of the forward tracking detector is displayed in Fig.3.9. It consists of three nearly identical super-modules, each super-module includes three planar wire drift chambers rotated at  $60^\circ$  to each other in azimuth  $\phi$  for the accurate measurement of  $\theta$ , a multi-wire proportional chamber (FWPC) for fast triggering, a passive transition radiator consisting of 400 polypropylene foils and a radial wire drift chamber to measure the accurate  $r\phi$  (drift coordinate) information.

The transverse view of the sense wire arrangements of each drift chamber is shown in Fig.3.10. All drift chambers in forward tracking detector have sense wires strung perpendicular to the beam axis, while the planars contain parallel wires and the radial wires radiate outward from the beam pipe. Each planar drift chamber has 32 cells with wire length between 460 mm and 1410 mm. Typically  $150 - 170 \mu\text{m}$  for the single point spatial resolution and  $< 2\text{mm}$  for the double track resolution are achieved in planers. The radial drift chamber which has 48 separate sectors of  $7.5^\circ$  width is situated at the most forward (positive  $z$ ) position in each super-module, each drift cell has 12 parallel wires staggered alternatively  $287 \mu\text{m}$  each side of a plane which bisects the sector and separated 10 mm to each other. A resolution of  $150 - 200 \mu\text{m}$  is achieved in the radial drift chamber. The radial drift chamber is also designed and operated for optimal

efficient X-ray detection. The combination of the radial drift chamber and the passive transition radiator can be used to for electron-pion discrimination.

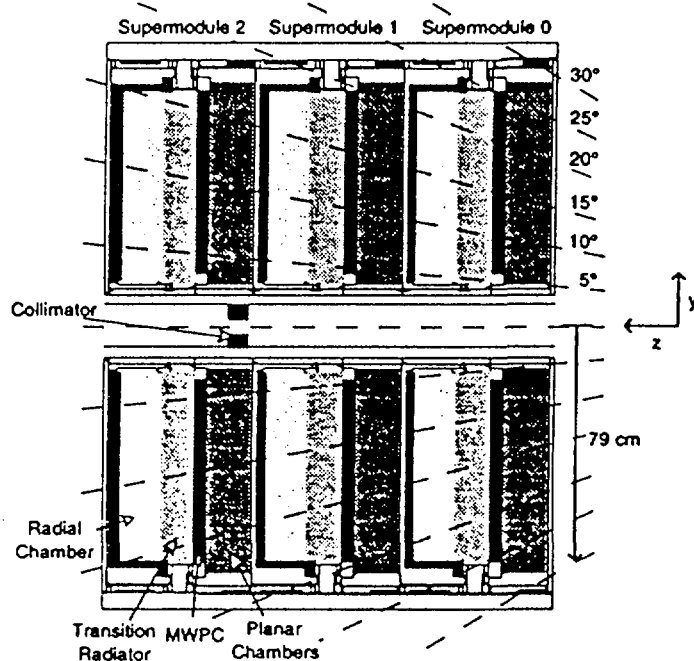


Fig.3.9 Schematic view of the H1 forward tracking detector.

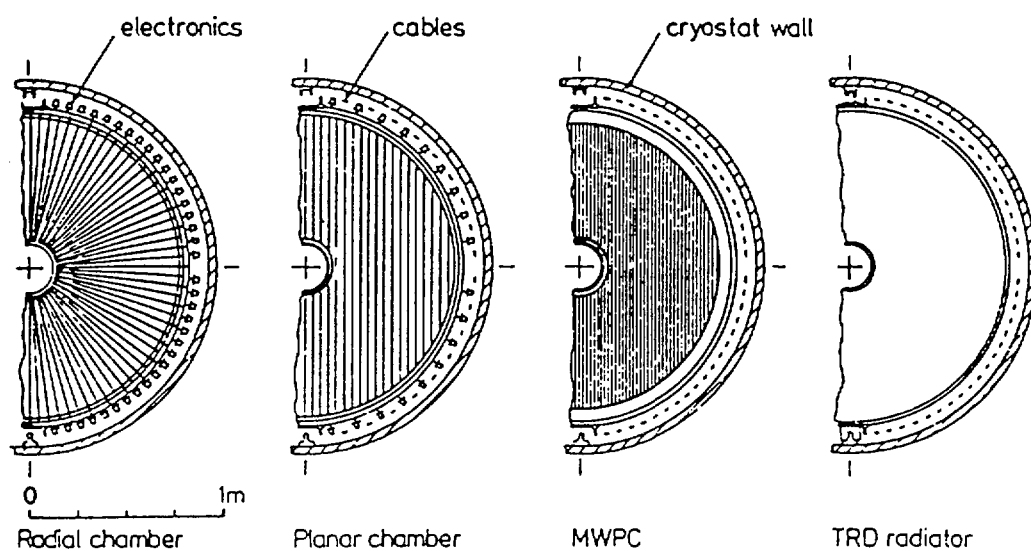


Fig.3.10 Axial view of one sense wire plane of the components in a super-module.

The pattern recognition in the forward tracking detector starts by finding line segments after the  $Q$ (charge)  $t$ (time) analysis of the raw data [45] in the drift chambers. This is done independently in the planar and radial chambers due to their different geometries.

In the planar chambers, first one finds as many candidates for tracks (referred to as "clusters") as possible in each of the three orientations. These clusters should be disconnected, i.e. they don't share the same digitization. Each of the clusters can only define a plane instead of a line due to the one end readout of the wires. It is found that about 70% of digitizations are assigned to clusters after a full search, the remaining 30% are due to track related noise arising. The next step is to find segment of tracks in a module. If three planes defined by clusters from each orientation intersect to the same line within measurement tolerances, this is a line segment candidate. Most of the false candidates are removed by selecting the disconnected line segments (i.e. no shared digitizations).

The line segment finding in the radial chambers is done by searching for straight line segments by joining the triplets of adjacent points in each wedge which satisfy the criteria  $|(d_1 + d_3)/2 - d_2| < P_1$ , where  $d_1, d_2, d_3$  are signed distances to the wire plane and  $P_1$  is a parameter ( $\sim 1$  mm). The joining is done if the triplets have points in common with the same drift sign, and lie within a certain tolerance along a straight line by linking the first and last point of the group. Then these triplets are fitted to a straight line. The searching switches to next wedge if the remain digitizations are insufficient to form a line.

An approximate track model representing a helix is used in linking the line segments to save computer time. The tracks are formed through four steps: first linking the tracks from the merging of the line segments in the planar chambers to radial line segments, second linking the tracks from the merging of the line segments in the radial chambers to planar line segments independently, then the best tracks found in above two steps are stored, finally a try to join the unlinked planar and radial line segments is performed. This procedure reduces the loss of tracks due to chamber inefficiency and two-track limited resolution.

To determine the optimum track parameters, a Kalman filtering technique [46] is used. This technique fits the parameters gradually by adding the measurements successively to an initial set of track parameters. The helix representation  $x, y, q/p, \tan\theta, \phi, z$  is chosen in track fitting.

### Multi-wire proportional chambers

The forward multi-wire proportional chambers (FWPC), the central inner proportional chamber (CIP) and the central outer proportional chamber (COP) provide a fast first level (L1) trigger decision over all the solid angle from  $5^\circ$  to  $175^\circ$ , which can be used to distinguish between successive bunch crossings. They also provide moderately accurate space point for charged tracks at L1, and give an accurate track element in the backward region where the drift chamber fails.

The FWPC's provide a fast ( $\Delta t < 96ns$ ) signal for bunch crossing timing and trigger decision by the coincidence of two planes of pad readout. Each of the FWPC's has two wire planes interleaved with three cathode planes with 4 mm spacing. For a track which cross all three or at least two FWPC modules, an effective timing resolution of 20 ns (FWHM) and 47 ns (base width at 10% of the maximum) was achieved, which is better than the separation of two successive bunch crossings. The double layers of chambers of CIP consists of three concentric cylinders: the inner cylinder serves as the inner cathode of the inner chamber and provides the electromagnetic shielding, the middle cylinder forms the outer cathode of the inner chamber and the inner cathode of the outer chamber, and the outer cylinder forms the outer cathode of the outer chamber. COP has similar structure and similar behavior, the time resolution is slightly larger than CIP but well below the required separation of two bunches. The combinations of pad hits in CIP, COP and FWPC in the central and forward region are also used to trigger on tracks coming from a nominal interaction vertex.

In backward region, BWPC which covers the front surface of BEMC has four differently oriented anode planes and five graphited cathode planes, with wires rotated  $45^\circ$  to each other in four layers. It has the same magnitude of time resolution as other MWPC and gives an accurate track element in angular range of  $155.5^\circ < \theta < 174.5^\circ$ . This information can be used to reconstruct electron in low  $Q^2$  events, as well as to discriminate electrons and photons.

### Scintillators

The scintillator arrays TOF(time-of-flight counters) and the veto wall are located in the backward region to reject proton beam associated background at L1 level. This background showers of energetic hadrons and halo muons are produced by proton beam gas and beam wall interactions, and hit H1 sensitive detector at a frequency of a few MHz.

Two planes of TOF are made of 3 cm NE102A plastic scintillator, mounted perpendicular to the beam pipe and situated at  $z = -1.95$  m (TOF1) and  $-2.25$  m (TOF2) respectively. The inner plane has 16 butted counters and the outer plane has 8 larger counters. The counters measure the time structure and the radial distribution of the beam related background. According to the time of flight difference between the arrival of the background particles (distance to the interaction point  $\sim 2.2$  m) and the bunch crossing time given by the RF system, the signals are collected and discriminated in three time windows: background, interaction and global, based on the logical OR of the signals from each of the two walls. Any coincidence gives a corresponding trigger which will be sent to the central trigger logic (CTL) for use in L1. The background trigger is used to suppress triggers from other sub-detectors, it effectively reduces 99% of the overall trigger rate, and subsequently reduces the dead-time.

Further upstream from the interaction region, two double scintillator veto walls with 4 and 10 scintillation counter pairs each, were installed at  $z = -6.5$  m and  $-8.1$  m respectively. The information on the amplitudes, signal arrival times, rates and efficiencies of all counters is used to study the background condition after each filling of the beams and during runs. Two trigger signals with HERA clock timing from each of the two veto walls are sent to the trigger logic, which can be used to trigger on real or veto on background events.

### 3.2.3 H1 Trigger And Data Acquisition System

H1 adopted a multilevel trigger system to allow decisions of increasing complexity. A very sophisticated deadtime free first level trigger (L1) has been built with the calorimeter which allows the selection of the physics events, and with the tracker which is used essentially to reject the background. Following L1 two synchronous trigger systems L2 and L3 are foreseen to operate during the primary deadtime of the front end readout, and one asynchronous event filter system L4 which collects the full event information and reconstructs event online is operational from the beginning.

To discriminate  $ep$  interactions from background, the most important feature that the physical events originate from the nominal fiducial volume of the  $ep$  interaction region is exploited. This origin position information is obtained from time of flight wall, the CJC tracks and the MWPC tracks. The energy deposition pattern also indicates the class of the physics events: the charged current event has imbalanced transverse momentum while the neutral current event has an electron candidate present which deposits energy in the electromagnetic part of LAr or BEMC; the low  $Q^2$  photo-production has an electron scattered under small angle into electron tagger of the

lumi-system; and a heavy quark or exotic physics candidate has muons penetrated into instrumented iron or forward muon system.

In the first trigger level, the fast trigger data from sub-detectors are fed into a centrally clocked front end pipeline, and the fast information is sent to the central trigger logic [47] where the global decision on acceptance for readout of the whole event is made and distributed again to the sub-detectors to stop the pipelines. The trigger data are encoded in the so-called trigger elements after pre-processed in the trigger subsystem [48]. These trigger elements consist of quantities depicting the character of the event, such as the interaction vertex coordinate reconstructed from MWPC system, multiplicity and momenta of drift chamber tracks, topological quantities like the imbalance of transverse momentum observed from the calorimeter, and even some combined information from several detector components in the form of “big rays” from MWPC system, which matched locally to the energy deposition given in “big tower” calorimeter granularity. The final L1 trigger decision is available about 24 bunch crossing interval (BC) after the  $ep$  interaction time, where the delay is caused by long detector response time in LAr or CJC, the processing times in trigger subsystems, and the experimental and electronic trailer. Further time is needed to distribute this signal around to stop the various subdetector pipelines. Such long response time can be tolerated since the interaction probability per BC is less than  $10^{-3}$  at design luminosity. The chosen concept of a pipelined front end system makes the L1 trigger decision completely deadtime free. A trigger element called  $t_0$  bit is available for most trigger subsystems, which identifies the bunch crossing that trigger the event.

Two trigger elements enter our selection of the charged current events: the  $Z_{vtx} - t_0$  trigger and  $E_{t-miss}$  trigger. To form  $Z_{vtx} - t_0$  trigger, first the cathodes pads signals from CIP, COP or FWPC which lie on a straight line are combined into a “ray”, which is treated separately in 16 fold sectors in azimuth  $\phi$ . A particle originating from nominal interaction point should pass through four layers of chambers in CIP, COP and FWPC. The  $z$ -positions of the rays are then filled into a histogram with sixteen 5.4 cm wide bins along beam axis, the  $Z_{vtx} - t_0$  trigger is activated if there is at least one entry in this histogram. As mentioned in previous section,  $E_{t-miss}$  is from the calorimeter trigger system, where the analog signals from each stacks are added to trigger towers (TT), which segments LAr into 23 vertex oriented  $\theta$  bins and  $\leq 32$   $\phi$  bins. The big tower (BT) is formed by summing up 1,2 or 4 TT depending on the  $\theta$  region. The total missing transverse energy is build by weighting BT energy with  $\sin\theta$ , i.e.  $E_x, E_y$  are obtained by multiplication with  $\sin\theta\sin\phi$  and  $\sin\theta\cos\phi$ . The  $E_{t-miss}$  is activated if the total missing transverse energy surpass the threshold.

The so-called subtrigger conditions are formed in central trigger based on the logical

combination of the 128 trigger elements (1993) using RAM look-up tables:

$$s_i = \prod_0^{15} f_j(\vec{t}_j) \quad (i = 0, 127) \quad (3.6)$$

where the  $f_j$  are arbitrary Boolean expressions of 11 trigger elements  $\vec{t}_j$ . The trigger elements are synchronized at the input to the central trigger logic before the formation of subtriggers. At least one  $t_0$  bit must be included in every condition in order to uniquely assign the correct bunch crossing. A L1 keep decision can be made from each single subtrigger to stop the pipelines and prepare the event readout. Three types of subtriggers are formed: the physics trigger for a given physical event class, the monitor trigger for needed experimental data such as efficiency measurement, and the cosmic trigger for calibration.

Considering the data size and transfer speed, some triggers with high rate for monitoring purposes need to be downscaled, also some desired physics processes can only be recorded with prescaled rate. Beam information is also used to gate the logic, for example, to distinguish cosmic triggers and physics triggers. Only the rising edge of a subtrigger condition leads to subtrigger, if it is not suppressed by prescaling or gating. The level 1 trigger accept is constituted of the logical OR of all subtriggers after prescaling:

$$level\ 1\ keep = \sum_0^{127} s_i \quad (3.7)$$

This set of conditions is optimized iteratively by analyzing the results from actual running, taking into account the background rejection power, the robustness with respect to varying beam condition and the implications to the system load in terms of trigger rate or average event size.

Two intermediate trigger levels are proposed to further reduce the primary event rate: the L2 decision based on more detailed trigger data which will actually start the front end readout processor ; and a parallel flexible L3 system with software algorithms which will refine the trigger and aborts the readout operation if necessary. L2 and L3 will operate during primary deadtime which begins when L1 keep signals are sent to the front end electronics of all sub-detectors to stop the pipeline. The events pass these intermediate trigger levels will be taken over by the central data acquisition system. These trigger levels are studied carefully and are foreseen to be operational in the future.

H1 data acquisition proceeds in several partly parallel stages. Primary readout takes about 1-2 ms, then the front end pipelines are released again. Further subsystem readout and formatting is done in a parallel and asynchronous manner [49]. Data are placed in multi-event buffers. The so-called “event builder” processor collects the data from each subsystem over an optical fiber ring and assembles the full event.

As shown in Fig.3.11 [50], the system is composed of three logical components. The role of the central trigger is twofold: to provide the decision on acceptance of each event based on the trigger elements, and to distribute the synchronized timing signals that control the subsystem readout such that data in the pipelines are properly assigned to the correct bunch crossing.

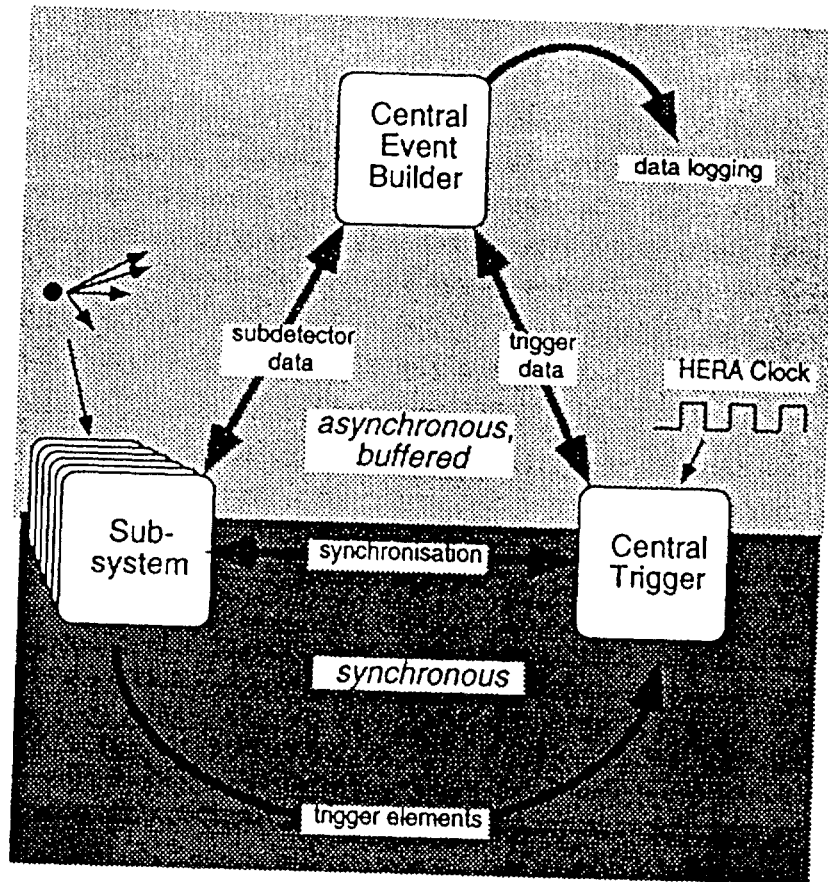


Fig.3.11 The three logical components of the H1 trigger and data acquisition system. While synchronization between central trigger and subsystems is vital, the event building is allowed to proceed asynchronously, since the event parts have already been marked with a common identification from the central trigger [50].

The level 4 processor farm integrated into the central DAQ system acts asynchronously as a filter on the full data to reduce the logging volume. The sub-trigger 66 and 77 for the electroweak processes entering our analysis will be reset by the L4 filter farm in some situations; such as, no reconstructed track was found in CJC ( $d_{ca} < 4$  cm) or in the forward tracker (1 planar segment) (for ST 77 only), there is only one significant peak in the CJC  $z$ -vertex histogram and situated at  $z > 60$  cm or  $z < -100$  cm; the transverse energy  $E_t$  measured in LAr is less than 1 GeV; the  $E_{t.miss}$  measured in LAr is less than 5 GeV, there is at least 1 upstream ( $z < -80$  cm) track and no good track ( $d_{ca} < 2$  cm,  $|z| < 40$  cm).

The characteristics of the events filtered by L4 farm indicates the non- $ep$  interaction origin of the events. An average of 70% of the input events are rejected as background by L4 filter based mainly on the technical quantities. Typically, 5 events/second are sent to permanent storage [51].

The trigger level 1 and 4 have been operational since the beginning of H1. Under the background rate of about 10 kHz, the physics selection power of the first level trigger information alone has made it possible to limit the acquisition rate such that second order deadtime effects could be avoided. On average, the system runs with 30~40 Hz level 1 input rate and deadtime around 10-15% while maintaining efficiency for physics.

H1 trigger and DAQ system has been successfully and reliably operated during the running period of 1992 - 1994.

**NEXT PAGE(S)**  
**left BLANK**

# Chapter 4

## Selection of The Charged and Neutral Current Events

Our analysis is based on the  $e^-p$  and  $e^+p$  interaction data taken during 1993 and 1994 luminosity runs in H1 detector at HERA.

In the neutral current process  $ep \rightarrow eX$ , a scattered electron will be detected in the LAr electromagnetic calorimeter or BEMC calorimeter, its transverse momentum  $P_t^{el}$  will balance that of the hadronic system  $P_t^{had}$ . The differences between energy and longitudinal momentum ( $E - P_z$ ) for electron and hadronic system satisfy the following relation:

$$(E - P_z)^{el} + (E - P_z)^{had} = 2E_e \quad (4.1)$$

where  $E_e$  is the incident electron beam energy. For the charged current  $ep \rightarrow \nu X'$  process, only the hadronic system can be recorded by the calorimeter, the most prominent observable feature being the imbalance of the total transverse momentum due to the emitted neutrino.

In the selection of the charged current events, the  $P_{t,miss} > 25GeV$  cut is used as the major criteria, which will strongly suppress the contaminations from the  $P_t$  balanced neutral current,  $\gamma p$  and beam gas events. The events are also required to be triggered by a charged current trigger, and to have an interaction vertex within the nominal interaction region. More selection cuts based on the topologies of the CC process are

applied to remove the contamination from various sources of background.

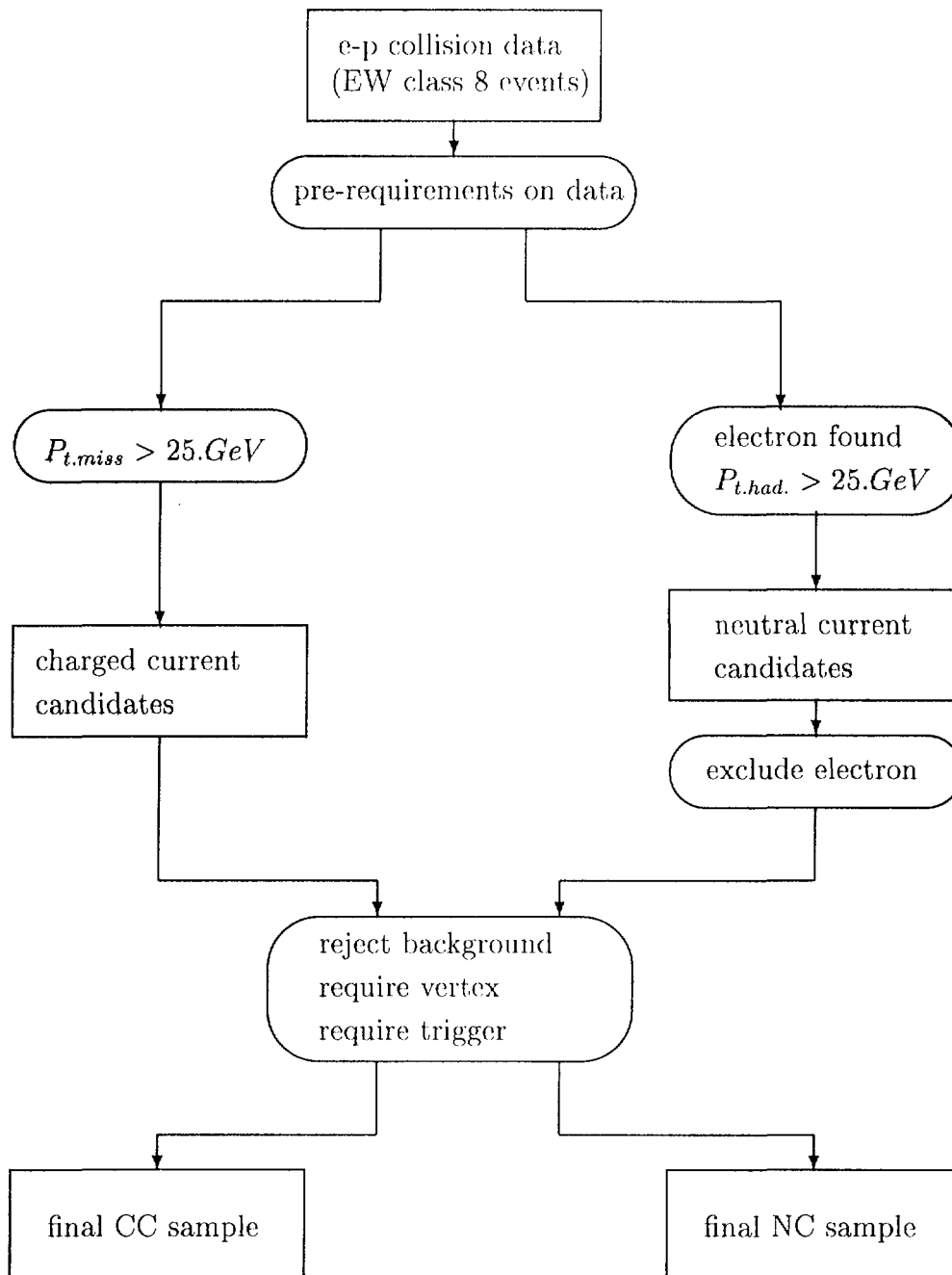


Fig.4.1 Process flow in event selection.

Considering the coherence of the electroweak physics analysis, the neutral current events are selected in parallel to the charged current events, i.e. with the same luminosity and technical requirements for data runs. For NC events, the  $P_t^{had} > 25\text{GeV}$  is required and the same selection cuts as in CC selection are applied to the hadronic systems after removing the scattered electrons (its energy and track informations removed).

The general program flow in the CC and NC event selection is illustrated in Fig.4.1. The basic selection procedures are the same for 1993  $e^-p$  and 1994  $e^\pm$  runs, while for the 1993 data we have done a pre-selection and obtained a pre-selected data sample. The conditions applied in this step include: events are classified as EW class (class 8) and satisfy the technical requirements, the missing transverse momentum of the event  $P_{t.miss}$  should be larger than 15 GeV, or there exists a cluster (electron candidate) which has transverse momentum  $P_{t.el.cand.}$  larger than 15 GeV. All further selection are based on this sample. The reason was to avoid staging large amount of tapes each time because of the limited computer power.

Four Monte Carlo simulation samples, the CC and NC samples for  $e^-p$  and  $e^+p$  interactions respectively, are used to study the event topology in data selection and to calculate the correction factor for various selection steps. Each Monte Carlo sample contained 5000 generated events. These MC events are generated using the generator DJANGO21 where the parton distribution parameterization MRS-H is used. For NC events the generated transverse momentum of electron is cut at 14 GeV. The energy and track information deposited in the H1 detector by the outgoing particles are carefully simulated according to the performance of the detector during the running time.

We will describe both 1993 and 1994 selections at the same time in the following sections, only mentioning the difference when it is necessary.

## 4.1 Technical requirements on luminosity runs

The integrated luminosity during the 1993 and 1994 data taking at HERA is shown in Fig.4.2(a) and Fig.4.2(b) respectively. The H1 data runs are classified as “good”, “medium” or “poor”, according to the operational sub-detectors, and the situation of the energy calibration and of the data reconstruction. Only “good” and “medium” runs has been chosen in our analysis.

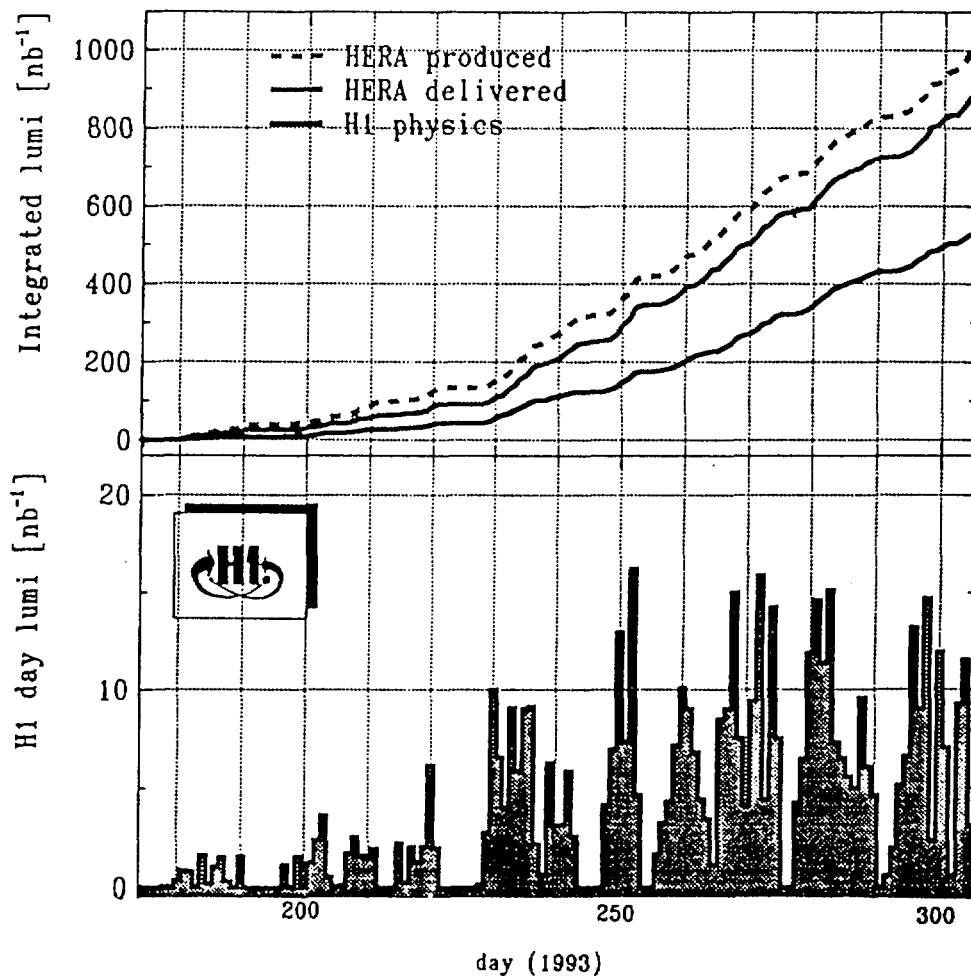


Fig.4.2(a) Luminosity of 1993 data.

### 4.1.1 Event Classification

In order to provide a fast access to the interesting events for different physics analysis, an event classification based on well measured and well understood quantities is performed after the full reconstruction of H1 data. The event class for electroweak processes is the class 8, which consists of high  $Q^2$  charged current and neutral current candidates satisfying the following requirements:

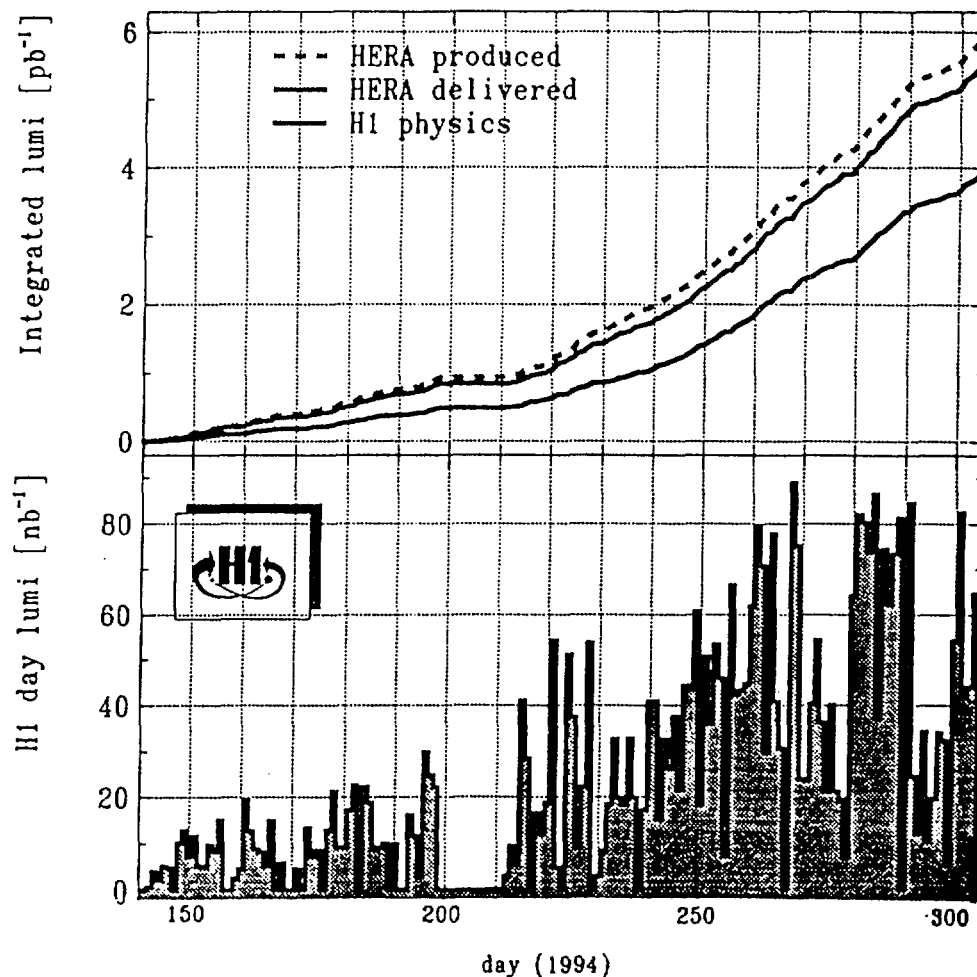


Fig.4.2(b) Luminosity of 1994 data.

- The missing transverse momentum  $P_{t,miss}$  from the energies deposited in LAr and BEMC is calculated. The electron candidate with transverse momentum  $P_t$  greater than 5 GeV is found and excluded, then the “modified” missing transverse momentum  $P_{t,miss,mod}$  of the remaining particles in LAr and BEMC is recalculated. If more than one electron candidate is found, more than one  $P_{t,miss,mod}$  values will be obtained. Event is accepted on POT sample if  $P_{t,miss}$  (CC candidate) or the largest of  $P_{t,miss,mod}$  is greater than 10 GeV (NC candidate).

- An additional requirement on track for DST selection is added: at least one “good” central track ( $|z|$  position  $< 100\text{cm}$ , radius at track beginning  $< 30\text{cm}$ , track length in  $x - y$  plane  $> 10\text{cm}$ , at least one CJC hit and  $d_{ca} < 5\text{cm}$ ) or “good” forward track (at least one planar segment) exists.

We use class 8 in our analysis, which is composed of a CC subclass ( $P_{t.miss} > 10$  GeV) and a NC subclass ( $P_{t.miss.mod} > 10$ ) GeV as indicated above.

### 4.1.2 Technical requirements

To ensure the data quality in the electroweak analysis, several more technical requirements related to the running conditions are applied. These conditions include:

- All of the runs with shifted interaction vertex are excluded. The run periods with noise and other operational problems in the sub-detector’s analog boxes, trigger or readout systems are excluded in 1994 data. For 1993 data, the runs without magnetic field during summer period are excluded.
- The trigger phase should be set up to normal luminosity running conditions and the charged current subtrigger (subtrigger 77) should be enabled. The events are also required to be detected during the colliding bunch for 1994 data, while the events in pilot or empty bunches are excluded.
- An event which has a high voltage failure in sub-detectors LAr, CJC, CIP, COP or  $\mu$  systems will be discarded, in order to get a reliable measurement of the energy, of the direction and vertex, as well as trigger information. The high voltage information could be got from the slow control system, which checks and records the HV situation of each sub-detector every time interval of 10 seconds during the running period. The luminosity for each run is adjusted according to the percentage of the HV tripped events (typically about 10%) discarded in this run.
- The runs with “coherent noise” events due to analog boxes problem in 1994 data were excluded online. This kind of events in 1993 data were subject to an offline treatment of the noisy cells and were kept in the sample previously. Here we remove them to treat the 1993 and 1994 analysis coherently. However, a quite large fluctuation of CC event number is observed when removing these events due to the poor statistics.

The luminosity of the data sample is affected by these requirements, thus should be corrected. The following table summarizes the integrated luminosities of different periods in 1993 and 1994 data:

Table 4.1 Integral luminosities (unit in  $nb^{-1}$ ):

luminosity[ $nb^{-1}$ ]	1993	1994	
	$e^-p$ runs	$e^-p$ runs	$e^+p$ runs
$\mathcal{L}(HERA.total)$	998.4	938.2	4977.4
$\mathcal{L}(H1.runs)$	699.8	714.23	4111.7
$\mathcal{L}(H1.physics)$	528.6	492.51	3424.0
$\mathcal{L}(H1.ew.physics)$	330.	360.	2700.

In the above table, a part of the luminosity accepted by the H1 detector were used in monitor mode for detector study, or in cosmic ray mode to take background data. The luminosity used in our electroweak analysis only accounts for about a half of the total luminosity accepted by the H1 detector for 1993 and 1994  $e^-p$  runs, and about two third for 1994  $e^+p$  runs. The conditions applied when choosing the luminosity runs for electroweak analysis will be discussed in the following section.

## 4.2 Selection of Charged current events

The main characteristics of a charged current  $ep$  interaction recorded by the H1 detector are: a large missing transverse momentum and no isolated electromagnetic energy deposition with large  $P_t$ , both measured in LAr. As an example, Fig.4.3 shows the longitudinal and transverse view of a CC events in 1994 data recorded by the H1 detector.

### 4.2.1 $P_{t.miss}$ cut

The essential quantities for this analysis, the scalar sum ( $S$ ) the vector sum ( $V$ ) of the transverse momentum of the individually observed final state particles, are defined as:

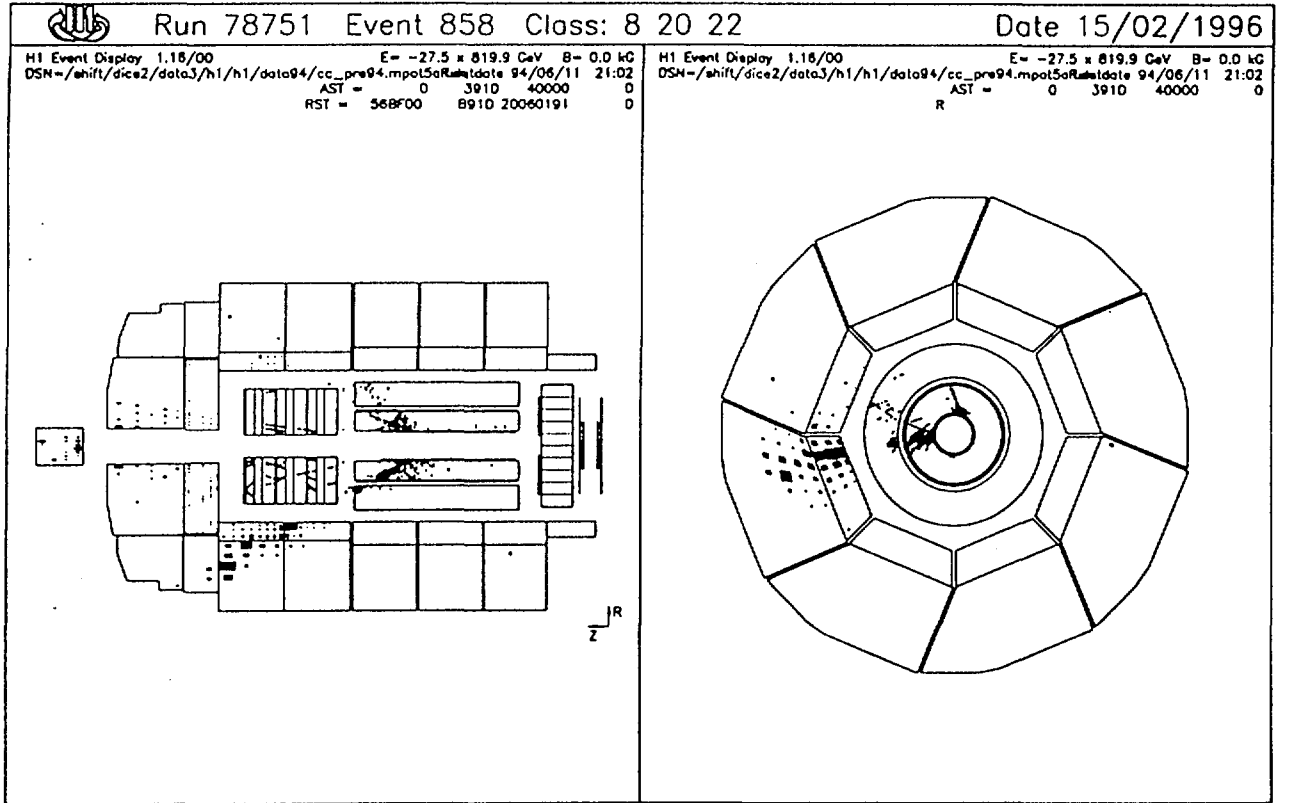


Fig.4.3 An example of CC event in H1 detector.

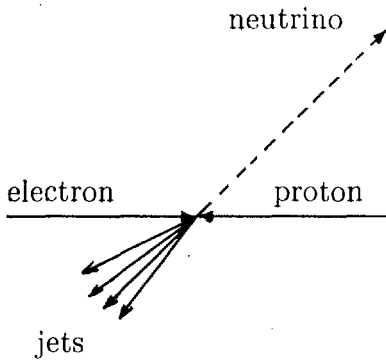
$$S = \sum_i |\vec{p}_i| \quad (4.2)$$

$$V = \left| \sum_i \vec{p}_i \right| \quad (4.3)$$

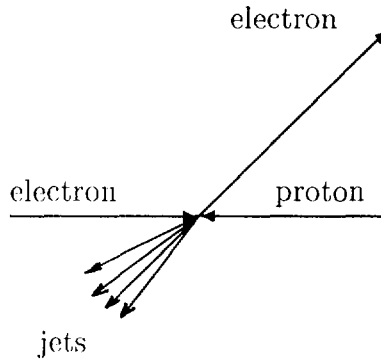
where the momentum  $\vec{p}_i$  is calculated from the energies measured in all calorimeter cells taking the direction with respect to the primary interaction vertex. All final state particles (hadrons, leptons and photons) contribute to the summation. As illustrated by the diagram, for a charged current event,  $S \approx V = p_t^{had} = P_{t,miss}$ , since the momentum

carried by the neutrino in direction opposite to the jets can not be observed; while for neutral current and  $\gamma p$  events,  $V \approx 0$  and  $S \approx 2p_t^{had}$  since the measured scattering lepton balances the transverse momentum.

CC process



NC process



As in some old neutrino experiments, the transverse momentum  $p_t^{had}$  is chosen as the criteria to select the CC and NC samples. For CC candidates, we require  $p_{t.miss} > 25$  GeV, which corresponds to  $Q^2 > 625 \text{GeV}^2$ . The distribution of  $S$  vs.  $V$  for CC and NC Monte Carlo are shown in Fig.4.4, the  $p_{t.miss} > 25$  GeV cut is also indicated. Note that since the generated NC events have an electron  $P_t$  cut at 14 GeV, most of the NC events have  $S$  larger than  $2P_t$ , i.e.  $S > 28$  GeV. Although the energy resolution of the detector causes the non-zero value of  $V$  for NC events, the  $p_{t.miss}$  cut at 25 GeV clearly separates the NC from CC events, as can be seen from the plot.

Most of the hadronic energy from the  $ep$  interaction is deposited in the LAr calorimeter. Some very energetic jets may have small part of energy leak out of LAr and deposit in Tail Catcher.

In the selection, we only use the energy in LAr calorimeter in  $P_t^{had}$  calculation, in order to avoid the noise signal founds in Tail Catcher. The measured value of  $P_t^{had}$  is calculated from the direction of the LAr calorimeter cell and the energy deposited in it. Assuming  $\theta_i$  and  $\phi_i$  are the polar angle and the azimuth angle of the cell  $i$  respectively,  $E_i$  is the energy deposited in it, then

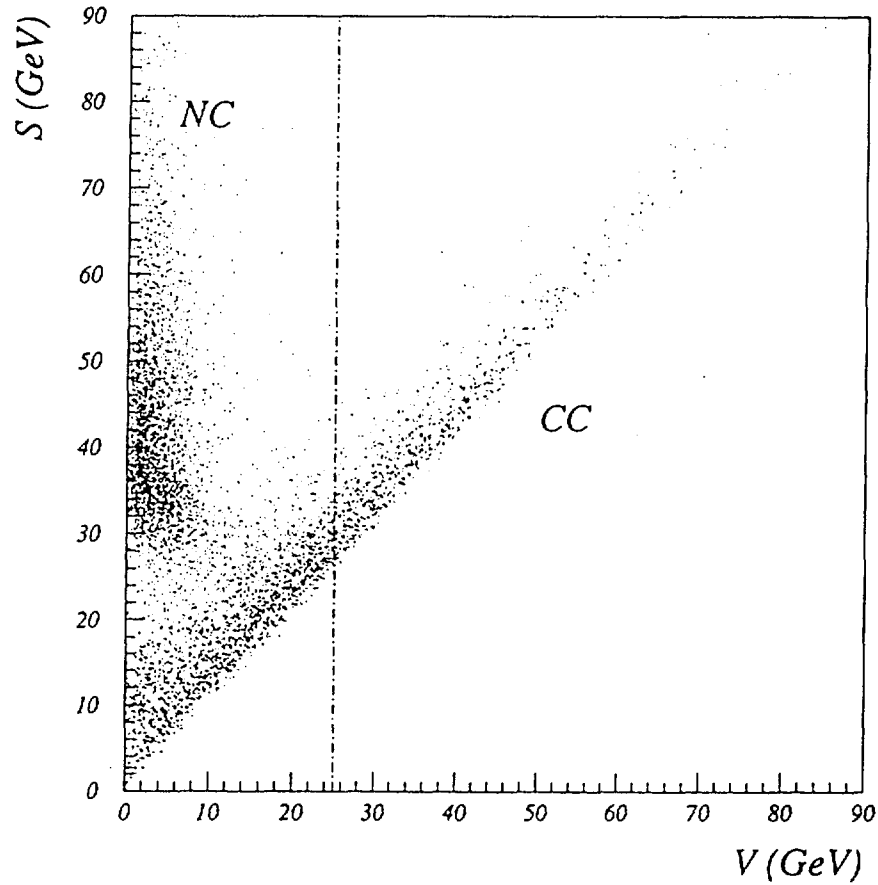


Fig.4.4 The  $S$  vs.  $V$  distribution for CC and NC Monte Carlo. The NC sample has  $P_{t,el}^{gen} > 14$  GeV.

$$P_t^{had} = \left| \sum_i (\vec{P}_t)_i \right| = \sqrt{\left( \sum_i E_i \sin\theta_i \cos\phi_i \right)^2 + \left( \sum_i E_i \sin\theta_i \sin\phi_i \right)^2} \quad (4.4)$$

where the summation runs over all LAr cells with energy deposited. The direction is determined from the geometrical bary-center of the cell position and the interaction vertex.

The event selection strongly depends on the value of  $P_t^{had}$ , which is the only kinematic variable used in the selection. We use several different checks to estimate the effect of the different calculation of  $p_t^{had}$  on the selection results. Since  $p_t^{had}$  is calculated only from the LAr calorimeter cells, inevitably, part of the energy from very energetic

jets leaking out of LAr calorimeter is lost, although there is some energy compensated to the outmost layer of cells in LAr for the dead material correction.

We have compared  $P_t^{had}$  calculated from three different method: from LAr cells, from clusters which include the energies in all of the calorimeters, and from electron, to study the effect on the event selection.

- Different approaches in  $P_t^{had}$  calculation

The “official” H1 reconstruction package has done a clustering of the energies deposited in the calorimeter cells, where the energetic cells from different calorimeters (LAr, BEMC, PLUG or Iron) are merged together to form a “cluster” according to the geometrical position of the fired cells and of the interaction vertex. For each event a list of the clusters is produced, and the total transverse momentum  $P_t^{had}(cluster)$  can be calculated by a summation of  $P_t$  over all of the reconstructed hadronic clusters. This way the energy escaping LAr is included, but the  $P_t$  value may get an additional bias due to the imperfect energy calibration in Iron.

We also use a compromised method to estimate the systematic effect in  $P_t^{had}$  measurement, where we try to include the escaped energy in the Tail Catcher from energetic jets and reject the noise energy. In this method, firstly the directions of the five most energetic clusters are determined, then the cones from the interaction point with the axis in these directions are built. The energy deposited in the cells of TC located within these cones will be counted in the  $P_t^{had}$  calculation, and the scattered energy cells outside these cones which being more likely to be noise are excluded.

Using Monte Carlo simulation, we have compared the reconstructed  $P_t^{had}$  with the true one (generated  $P_t^{had}$ ) for CC, NC and for  $e^-p$ ,  $e^+p$  interactions respectively. These comparisons are done for the above mentioned three methods, namely, only from LAr cells, from clusters which comprise all calorimeters, and from LAr cells and cells in jet directions in Tail Catcher.

In order to get a reasonable statistics, we also use the selected NC 1994  $e^+p$  data for comparison here.

Fig 4.5 shows the distribution of  $P_t^{had}$  calculated from these three methods using NC  $e^+p$  Monte Carlo with a cut at  $P_t^{had}(LAr) > 25$  GeV, where we see a good agreement. The  $P_t^{had}$  distribution from 1994  $e^+p$  NC data using these three different methods are displayed in Fig.4.6, which is in good agreement with the Monte Carlo. Fig.4.7 gives the distributions of the ratio  $\rho$ , defined as  $\rho \equiv (P_t^{had})_{mea.}/(P_t^{had})_{gen.}$  which describes the precision of the calculation method, for

these three methods and for  $e^+p$  and  $e^-p$  NC Monte Carlo respectively. The  $P_t^{had}(LAr) > 25$  GeV cut is applied in these plots.

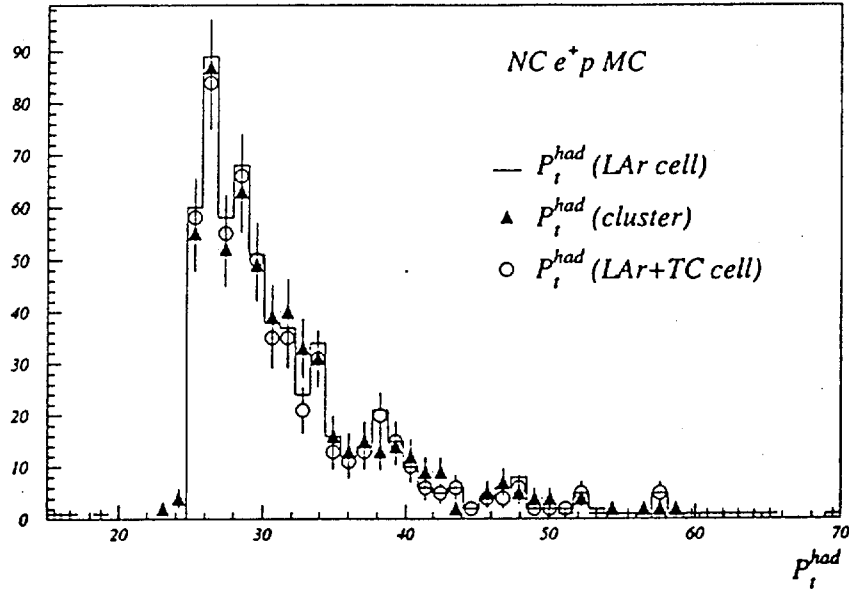


Fig 4.5 The distributions of  $P_t^{had}$  calculated from three different methods using NC  $e^+p$  Monte Carlo.

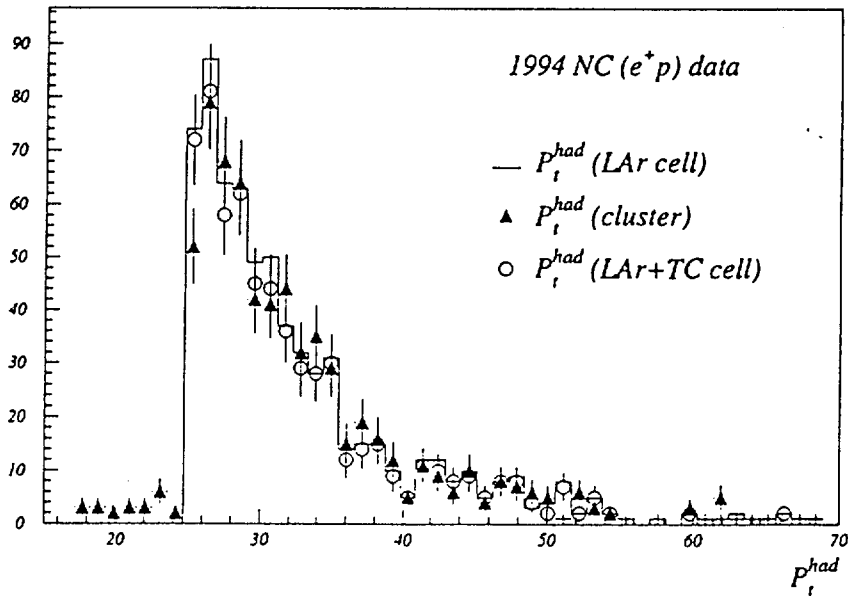


Fig 4.6 The distributions of  $P_t^{had}$  calculated from three different methods using 1994 NC  $e^+p$  data.

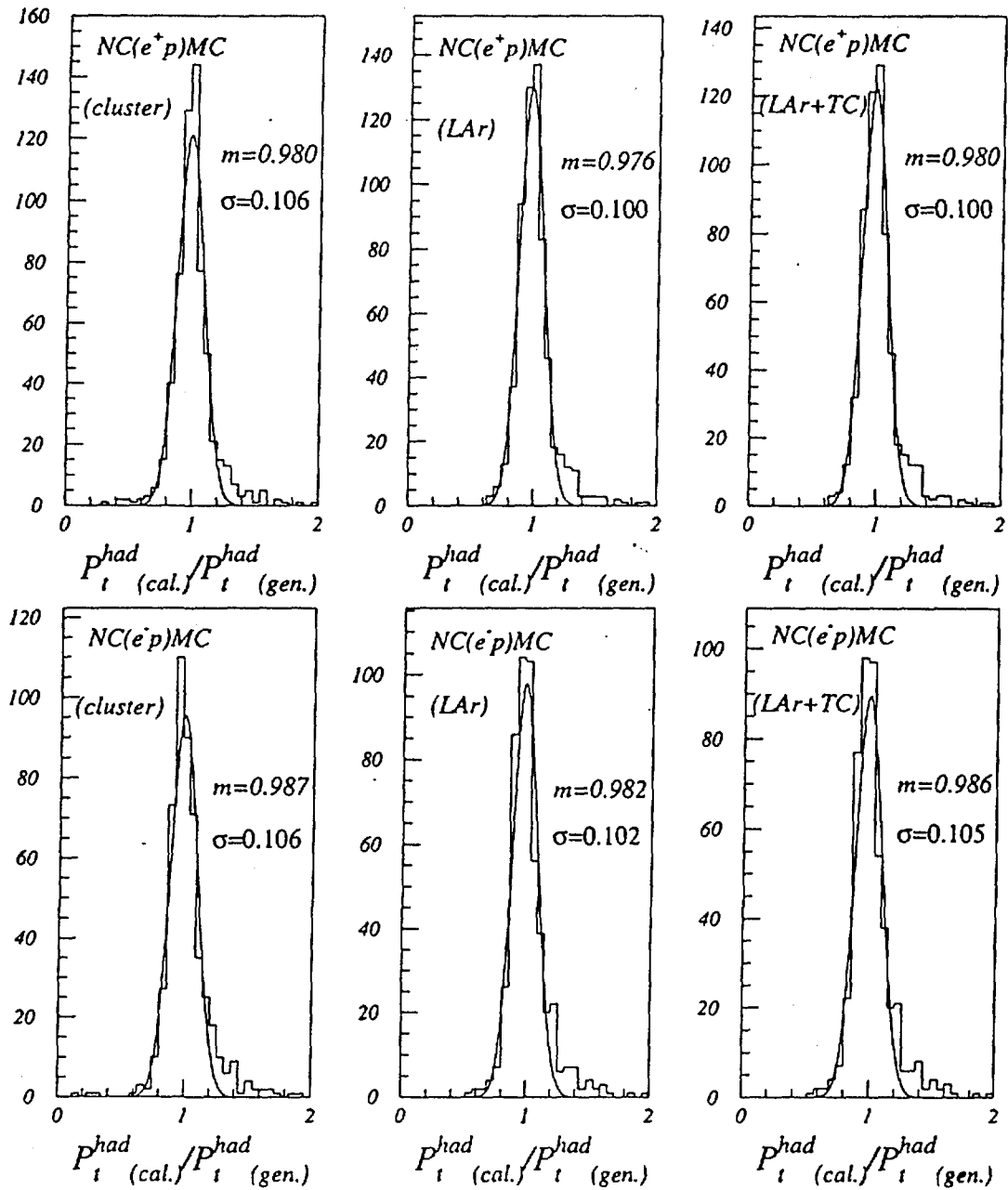


Fig 4.7 The ratio between measured and true  $P_t^{had}$  using three different calculation methods, for  $e^+p$  NC Monte Carlo (a) and for  $e^-p$  NC Monte Carlo respectively.

By a Gaussian fit to the distributions of  $\rho = \frac{(P_t^{had})_{mea.}}{(P_t^{had})_{gen.}}$  for the three methods, we see that the resolutions in these calculations are of the same magnitude of about 10%, and the mean value of shifts from the measured  $P_t^{had}$  to true value are about 2%. From CC Monte Carlo we got similar results on the resolutions and shifts of the measured  $P_t^{had}$  using these three methods. The comparisons of the two  $P_t^{had}$  calculations, from the LAr cell or from the cluster, are displayed through the ratio  $(P_t^{had})_{LAr}/(P_t^{had})_{cluster}$  in Fig 4.8 for CC  $e^+p$  Monte Carlo and 1994 CC  $e^+p$  data respectively. The two distributions are in good agreement.

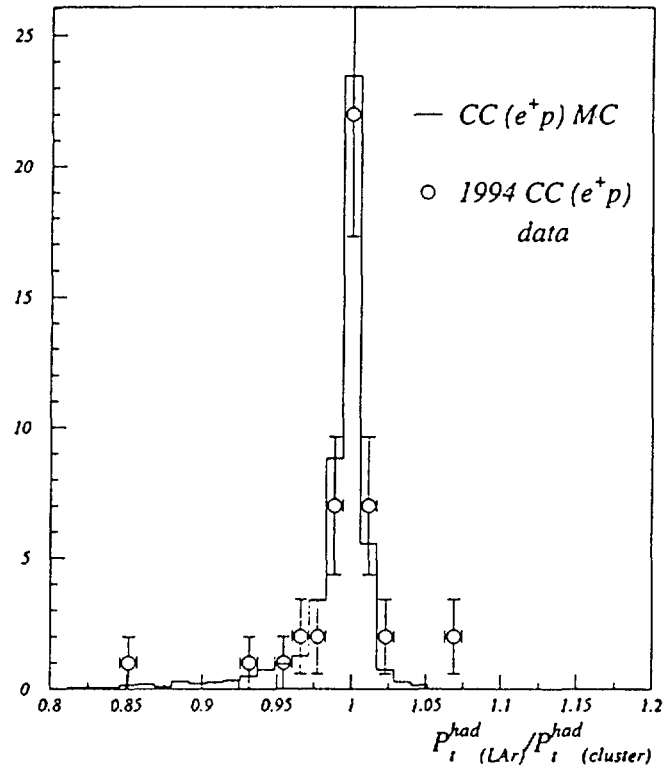


Fig.4.8 The comparison of  $P_t^{had}$  calculated from LAr cells and from cluster, for 1994 CC  $e^+p$  data and Monte Carlo respectively.

- $p_t$  measurement from electron and from hadrons for NC events

In the neutral current process, the balance of the transverse momentum provides a good check of the systematic effect of the hadronic energy absolute calibration, since the energy and the position of the electron are well measured in the calorimeter. By a careful study on the  $P_t$  measurement in the data and Monte Carlo, a 2.5% increase of energy scale is applied to the hadronic jet energy for 1994 data in order to obtain a best  $P_t$  balance between the electron and the

hadronic system.

The distribution of the ratio  $p_t^{had}/p_t^{el}$  for 1994 NC  $e^+p$  data and Monte Carlo are compared in Fig.4.9, for two  $p_t^{had}$  calculation methods (cluster and LAr cell) respectively.

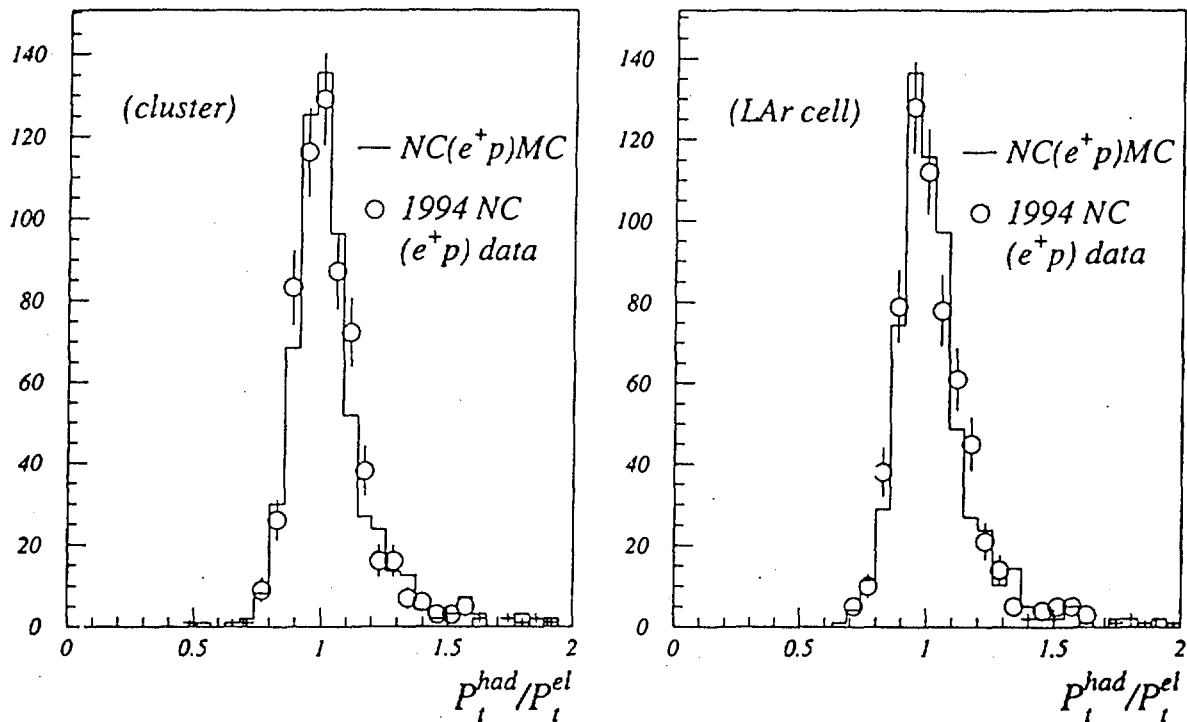


Fig 4.9 The comparison of the distribution of the ratio  $P_t^{had}/p_t^{el}$  between 1994  $e^+p$  data and Monte Carlo, using cluster and LAr cells to calculate  $P_t^{had}$  respectively.

After the 2.5% hadronic energy rescaling, the Gaussian fit to the  $p_t^{had}/p_t^{el}$  ratio distributions ( given in Fig.4.10) shows the mean shift value are within 1% for both NC data and Monte Carlo, and the resolutions are about 10%. The different  $p_t^{had}$  calculation methods give the same magnitude of the uncertainties.

We can conclude that using LAr cells only to calculate  $P_t^{had}$  didn't bring any additional systematic shift or worsen the resolution, and the effect is correctly simulated by the Monte Carlo, thus the correction factor for the efficiency and the migration effect can be calculated, which will be discussed in next chapter.

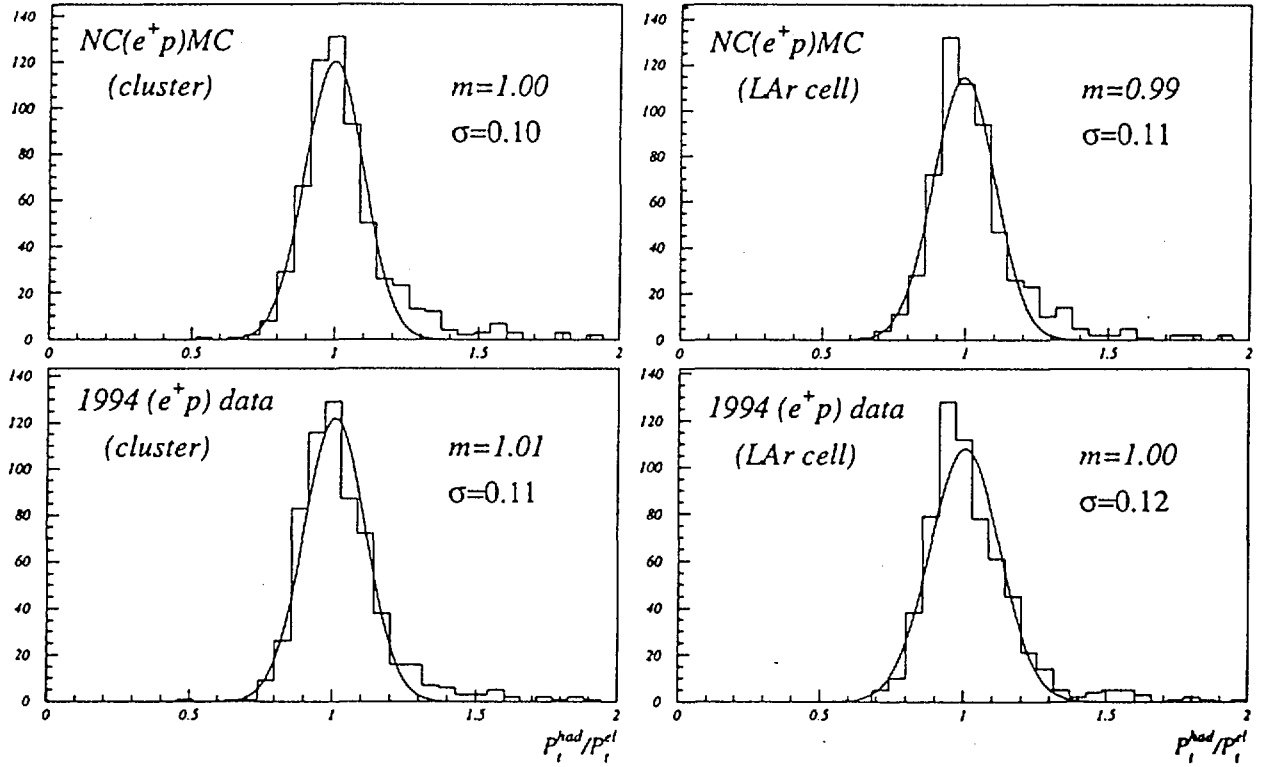


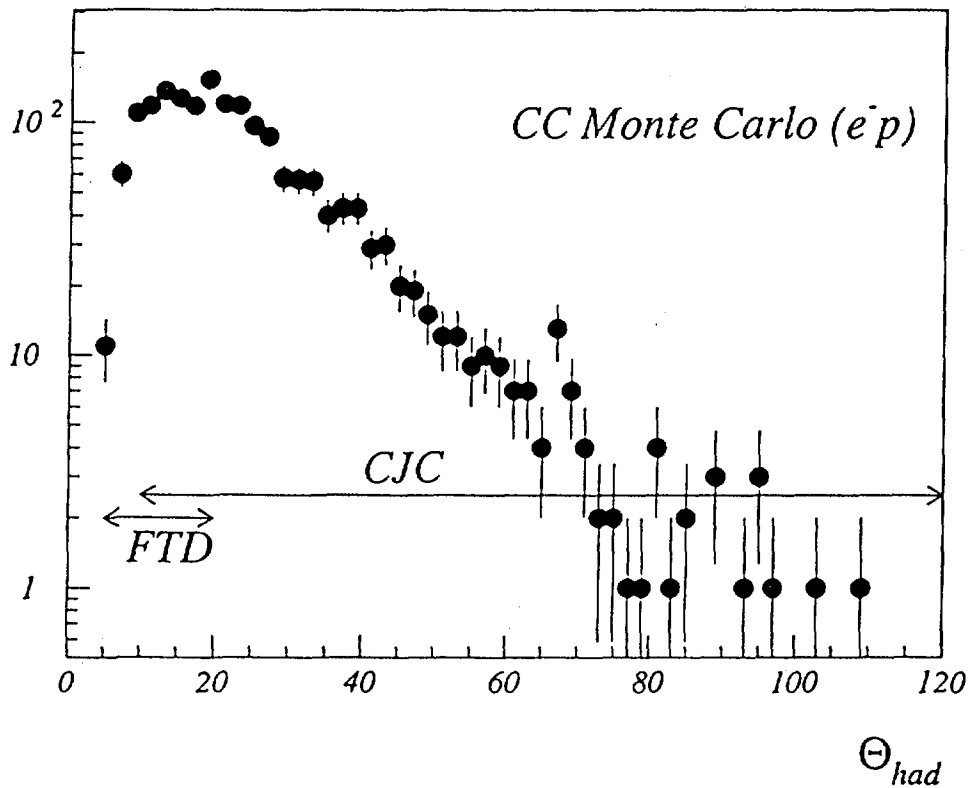
Fig 4.10 The Gaussian fit to the  $p_t^{had}/p_t^{el}$  ratio, for 1994  $e^+p$  data and Monte Carlo and using two  $p_t^{had}$  calculation methods.

### 4.2.2 Vertex requirement

A primary vertex requirement is a clear indication of the  $ep$  interaction origin of the individual event, and suppresses a considerable amount of contaminations from halo muon and cosmic muon induced background. The position of the interaction vertex is also important for the determination of the direction of the energetic particles deposited in the calorimeter, thus it is important for the calculation of the kinematic variables.

The vertex is reconstructed from the tracks in the drift chambers induced by charged particles, which are produced in the  $ep$  interaction, or products of the secondary interactions or from electromagnetic showers caused by the penetrating muons. For the

charged current process, most of the final state hadrons are emitted in forward and barrel direction and leave tracks in the central drift chamber (CJC) or forward tracking detector (FTD). The jets emitted near the beam pipe ( $\theta < 5^\circ$ ) are totally lost. CJC covers most of the polar angle ( $10^\circ < \theta < 140^\circ$ ) and provides a good measurement of track parameters for vertex finding, while the quality of the tracks reconstructed in FTD is not so good. However, as shown in Fig 4.11, the CC process which have quark emitted in the forward region covered by FTD ( $5^\circ < \theta < 20^\circ$ ) makes up to 15% of the total cross section in our high  $Q^2$  ( $P_t < 25\text{GeV}$ ) CC selection, thus can not be neglected.



polar angle of the final hadronic jets  $\theta$

Fig.4.11 The polar angle distribution of the final hadronic jets for CC event ( $P_t > 25\text{GeV}$ )

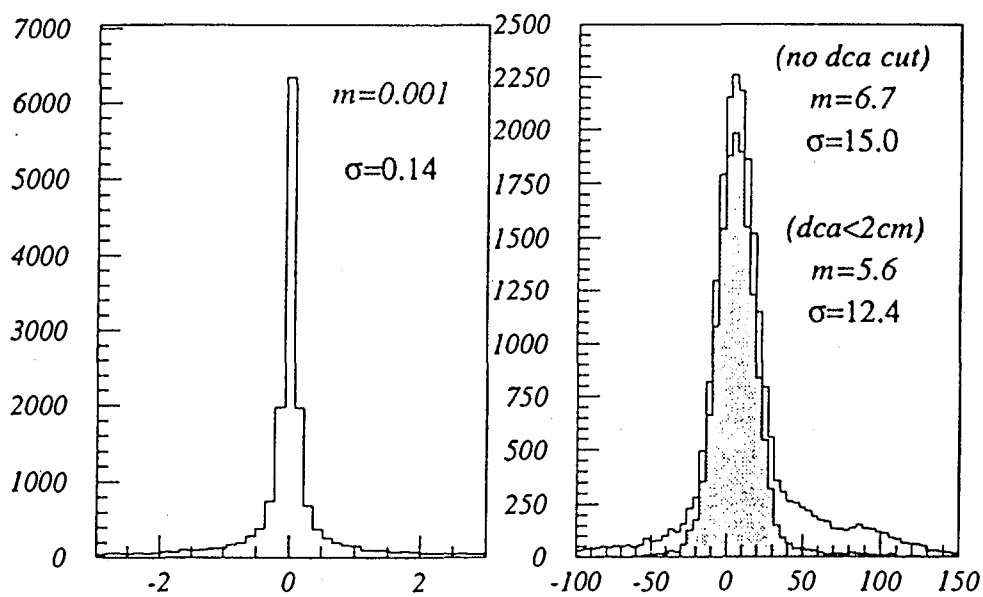
By studying the track characteristics and distribution pattern in CJC and FTD using Monte Carlo and real data, we propose a simple method to estimate the position of the primary vertex combining the tracks reconstructed from CJC and FTD, which has been proved to be quite efficient. It has moderate precision and offers an easy way to remove the electron contribution in the vertex decision demanded in parallel in the NC selection.

### Selection of good tracks in CJC and FTD

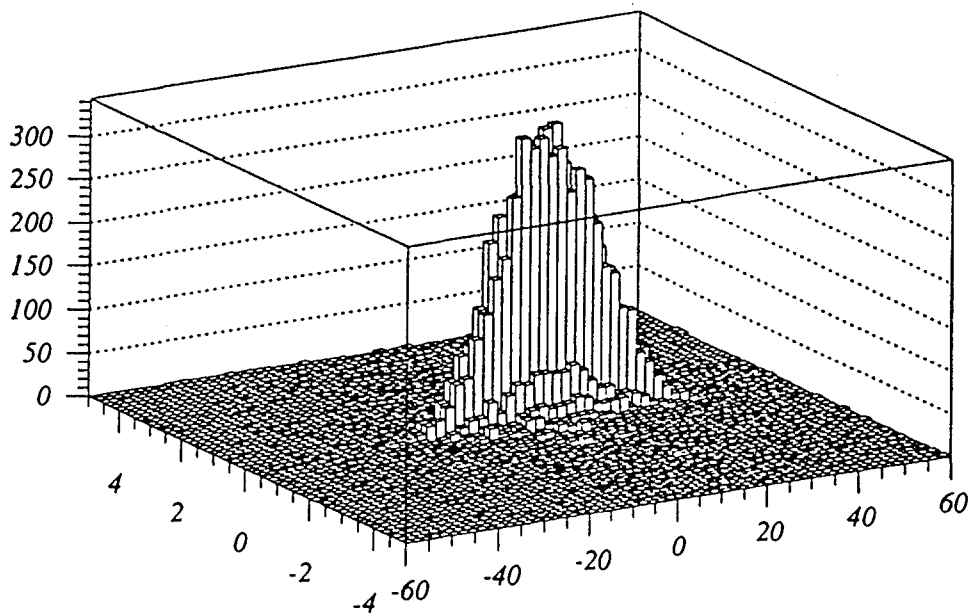
The principle of this method is quite straightforward: the  $z$  position of the primary vertex is defined as the weighted average of the  $z$  position of all “good” tracks in CJC or FTD. The criteria for “good” track is defined from the track parameters measured in the drift chambers.

For CJC track, the H1 reconstruction package gives a series of track parameters to describe the geometrical position ( $d_{ca}$ ,  $z_{dca}$ ,  $\theta$ ,  $\phi$ ,  $\kappa$ , track starting and ending position etc.) and reconstruction quality (errors, covariance,  $\chi^2$  in the fit, number of hits on the track etc.). The most relevant parameters are:

- $d_{ca}$ , the closest distance in  $r\phi$  plane from the beam line to the track. This is an important quantity to discriminate the tracks from primary vertex and from background tracks (i.e. tracks from secondary interaction such as  $\gamma \rightarrow e^+e^-$  and  $K_s^0 \rightarrow \pi^+\pi^-$ , or from charged particles in electromagnetic showers induced by incoming muons etc.), since the latter don't necessarily come from the beam axis. Fig.4.12(a) shows the distribution of  $d_{ca}$  in CJC, the mean value and  $\sigma$  of the distribution from a Gaussian fit is also indicated. We see that  $d_{ca}$  for most of the CJC tracks are near 0, the mean error is less than 0.2 cm.
- The  $z$  position of the track at  $d_{ca}$ . The nominal interaction point is at  $z = 0$ , the actual primary vertex lays in  $|z_{vtx}| < 50$  cm range. Considering the error in the measurement, the  $z$  of the track from the primary vertex should not be too far away from this range. The tracks from upstream direction ( $z < -80$ cm) with small  $d_{ca}$  most probably originate from beam-gas interactions. Fig.4.12.(b) shows the  $z$  distribution of the tracks in CJC, where the shadowed histogram shows the  $z$  distribution after requiring  $d_{ca} < 2$  cm. The mean values and  $\sigma$  before and after the  $d_{ca}$  cut are also indicated in the plot. Fig.4.12.(c) shows the relationship between  $d_{ca}$  and  $z$  of the tracks in CJC.



(a). dca distribution in CJC (cm)      (b). z distribution in CJC (cm)



(c). dca .vs. z in CJC

Fig.4.12 Distributions of  $z_{dca}$  and  $d_{ca}$  of the tracks in CJC (from  $e^+p$  CC Monte Carlo).

- The track length which is calculated from

$$L_{track} = \left| \frac{R_{end} - R_{start}}{\sin\theta} \right| \quad (4.5)$$

where  $R_{start}$  and  $R_{end}$  are the radius at track starting point and track ending point. A short track may come from background such as low momentum secondary particles or from wrong matching of hits in pattern recognition. As shown in Fig.4.13 the track length  $L_{track}$  is also correlated to other parameters such as the number of hits on the track, the momentum of the track etc., thus a cut on track length has an effect on other parameters.

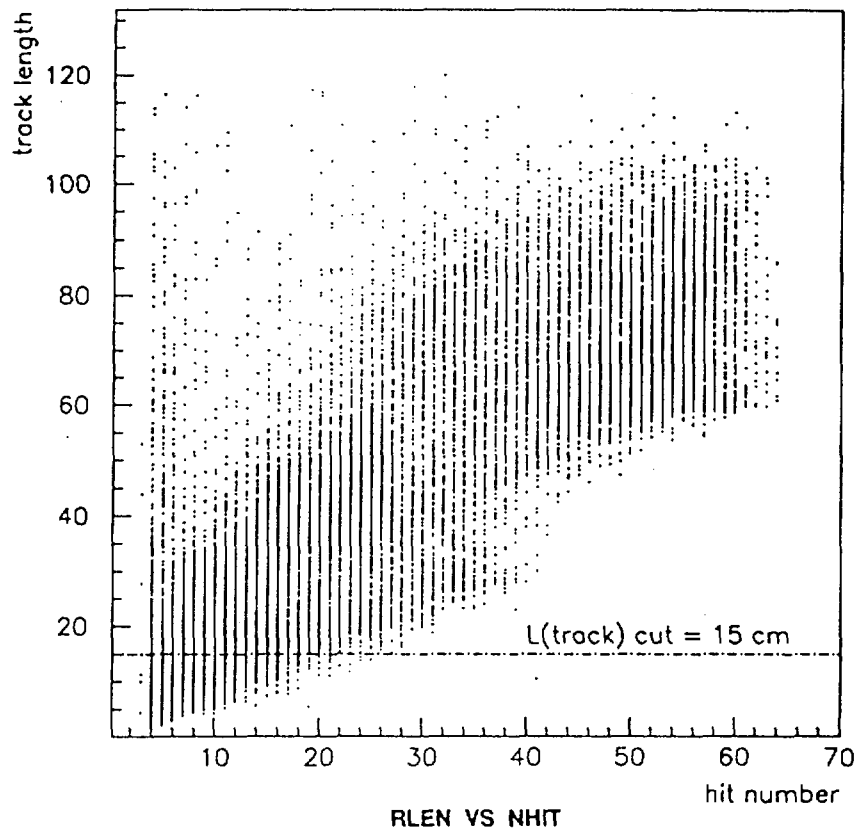


Fig.4.13 The relationship of track length to hit number in CJC (from  $e^+p$  CC Monte Carlo)

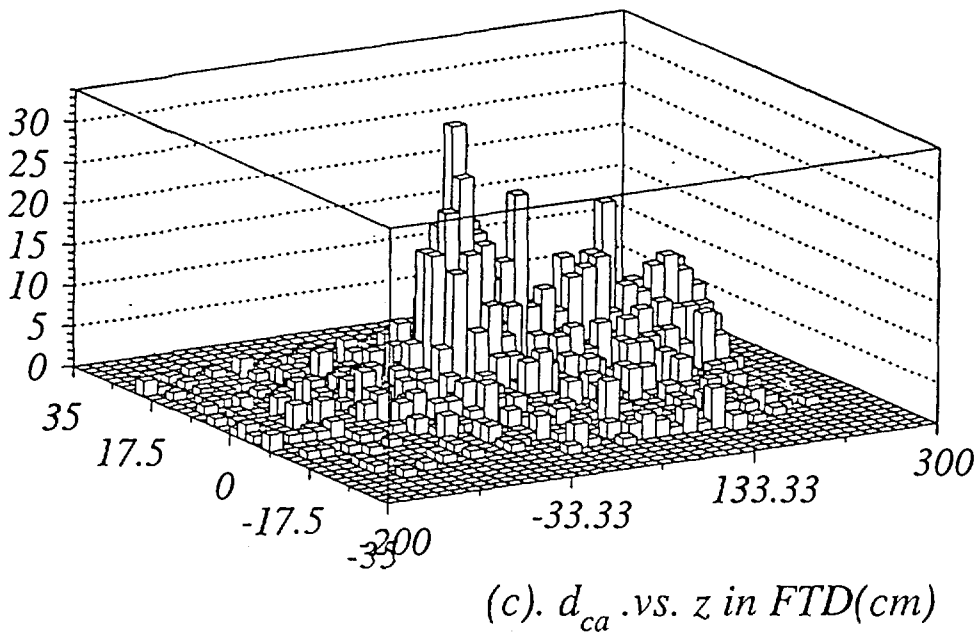
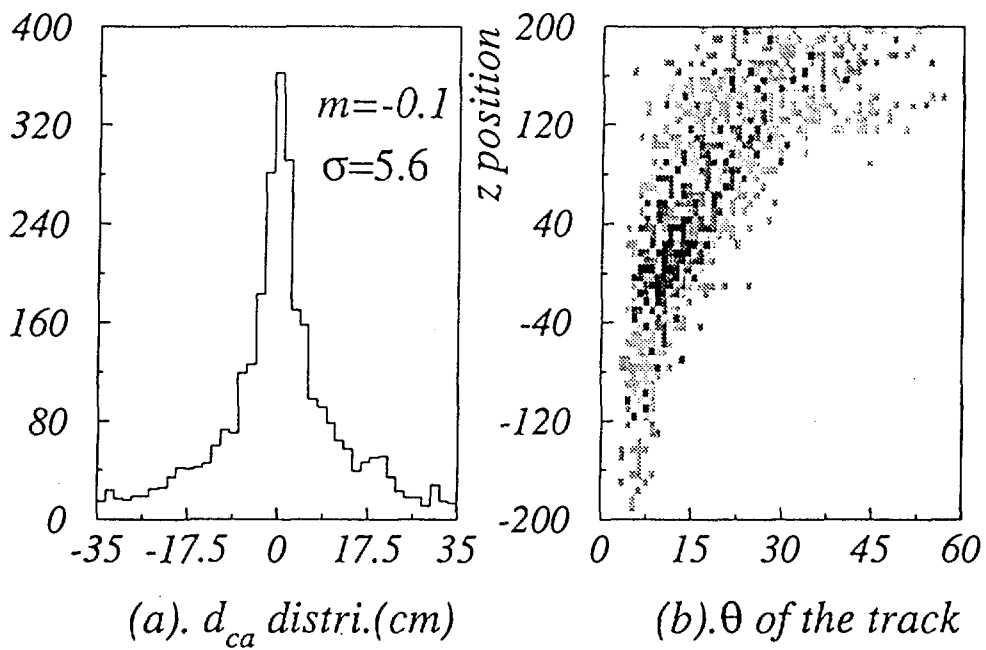


Fig.4.14 Distributions of  $z_{dca}$  and  $d_{ca}$  of the tracks in FTD (from  $e^+p$  CC Monte Carlo).

For forward tracks, a different set of parameters ( $\kappa, \theta, \phi$  at first and last point,  $(x, y, z)$  at first and last point etc.) are adopted in the track reconstruction (chapter 3),  $d_{ca}$  and  $z_{dca}$  are not given explicitly, thus they must be calculated from the original set of parameters.

Compared to CJC tracks, there are more background tracks present in the forward tracker due to multiple scattering in the housing material of FTD. The reconstruction of tracks is more difficult in FTD than in CJC due to its geometrical location, for example, the  $z_{dca}$  of a track has to be extrapolated more than 1 m. The  $d_{ca}$  and  $z_{dca}$  of the forward tracks are more dispersed than in CJC as shown in Fig.4.14(a) and Fig.4.14(c), where the mean value and  $\sigma$  from a Gaussian fit to the central part of the  $d_{ca}$  distribution is indicated. From these distributions we see there are a lot of background tracks with large  $d_{ca}$  and  $z_{dca}$ , a considerable amount of these background tracks have large polar angle  $\theta$  and have  $z_{dca}$  at very forward region ( $z > 100\text{cm}$ ) (as shown in Fig.4.14(b)). Most likely these tracks are from the multiple scattering in the C4 collimator situated in the beam pipe region [52]. Here an important parameter to describe the quality of the reconstructed tracks is the number of planar segments  $N_{planar}$  of the track. The tracks from C4 collimator are often quite steep and don't pass any planar segment ( $N_{planar} = 0$ ). By requiring at least one planar segment, most of these tracks are discarded and the tracks coming from the interaction vertex with more forward polar angle are kept.

Based on the observations described above, a set of simple criteria for selecting good tracks has been chosen considering both the efficiency of vertex finding and the precision of the vertex calculation. For CJC tracks, we require:

- $d_{ca} < 2$  cm,
- $|z_{dca}| < 60$  cm,
- track length  $> 15$  cm.

For forward tracks, we require:

- at least one planar segment existing,
- $d_{ca} < 5$  cm,
- $|z_{dca}| < 60$  cm.

Fig.4.15 shows the distributions of  $z_{dca}$  of forward tracks after the  $N_{planar} \geq 1$  and  $d_{ca} < 5$  cm requirements. Together with  $|z_{dca}| < 60$  cm requirement, the tracks selected are more likely coming from the primary vertex.

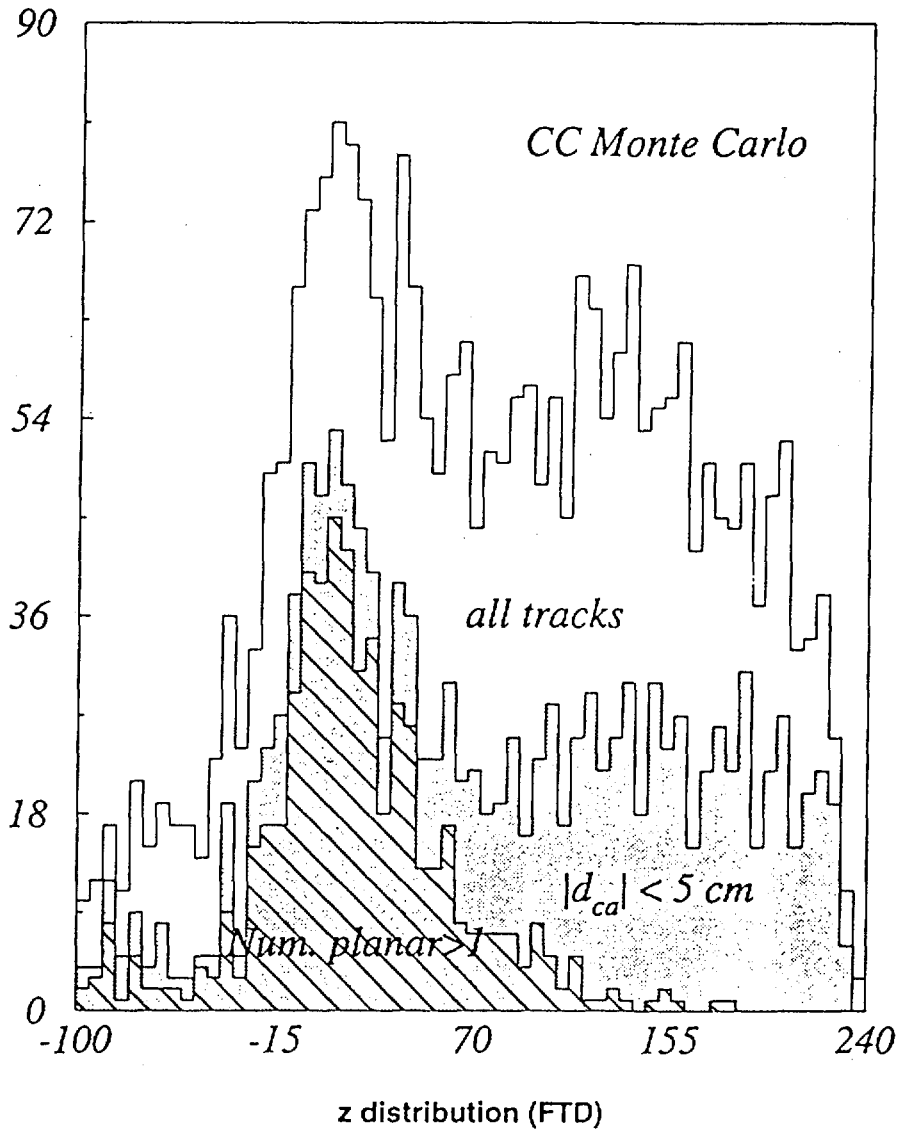


Fig.4.15  $z_{dca}$  Distributions of the tracks in FTD ( from  $e^+p$  CC Monte Carlo), require a). $d_{ca} < 5$ cm and b).at least one planar.

### Vertex calculation

As a first order approximation, we suppose that all the tracks which passed the good track criteria are coming from the primary vertex and have the same weight. The difference in  $z$  position of the tracks reflects the error in the track parameter measurement. Thus the “true”  $z$  position of the interaction point is simply the average of  $z$  over all good tracks:

$$z_{vtx.mean} = \frac{\sum_{good.tracks} z_{i,good}}{N_{good.track}} \quad (4.6)$$

where  $N_{good.track}$  is the number of good tracks. The vertex calculated using the above formula gives a good approximation of the true vertex. The efficiency and background rejection power are also quite satisfactory. However, the assumption of all good track coming from primary vertex is not always true, thus it is needed to suppress the contribution from the tracks not coming from the primary vertex (background tracks) in the vertex calculation, this can be done by introducing a weight to every good track according to their  $d_{ca}$  and  $z_{dca}$ .

For the good tracks in the individual event, there are some correlation of  $d_{ca}$  and  $z_{dca}$ . Fig.4.16 gives some examples of the  $d_{ca}$  and  $z_{dca}$  distributions for several typical events in central and forward tracker respectively. We see that for CJC tracks, the  $d_{ca}$  and  $z_{dca}$  distributions for good tracks are more probably concentrated in a unique cluster which may come from the primary vertex, the scattering background tracks are easily identified. But for the forward tracker, the good tracks are more dispersed in  $d_{ca}$  and  $z_{dca}$  and the number of good tracks is lower, which makes the vertex calculation more difficult. However, some unique clusters of good tracks can still be found in those events, which are likely to come from a primary vertex.

From the distributions of  $d_{ca}$  and  $z_{dca}$  of good tracks, we assume  $d_{ca}$  and  $z_{dca}$  have Gaussian distributions around their mean value. The probability of  $d_{ca}$  to have a value at  $d$  can be represented by

$$P_{dca} \Delta d_{ca} = \frac{1}{\sqrt{2\pi}\sigma_{dca}} \exp\left(-\frac{d^2}{2\sigma_{dca}^2}\right) \Delta d_{ca} \quad (4.7)$$

here  $\sigma_{dca}$  is the standard deviation of  $d_{ca}$ , and the mean value of  $d_{ca}$  is 0.

The probability of  $z_{dca}$  has a value at  $z$  is:

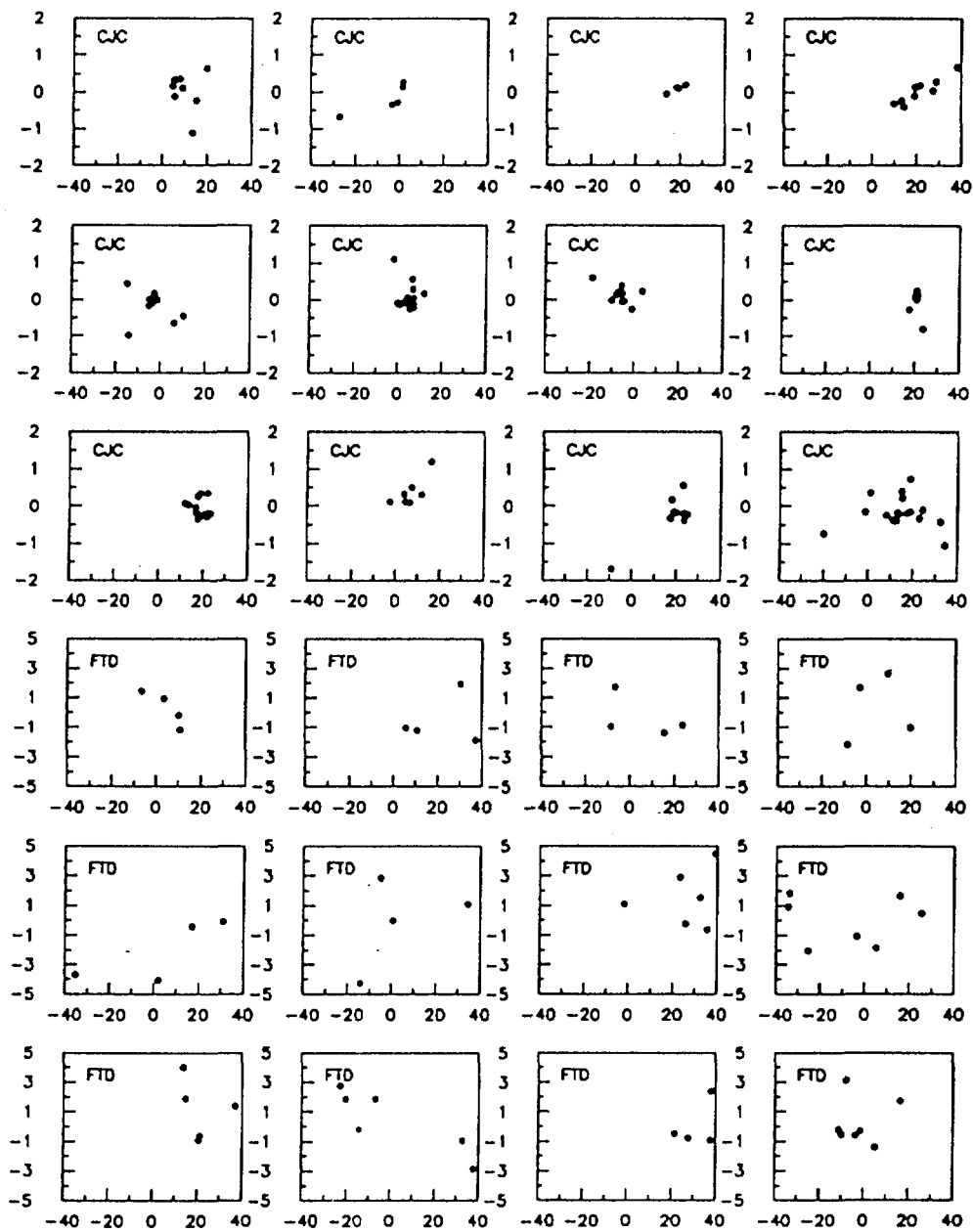


Fig.4.16 The distributions of  $d_{ca}$  and  $z_{dca}$  for some events in CJC and FTD (CC Monte Carlo). The vertical coordinate is  $d_{ca}$  in cm, the horizontal coordinate is  $z$  in cm.

$$P_z \Delta z = \frac{1}{\sqrt{2\pi}\sigma_{dca}} \exp\left(-\frac{(z - z_{mean})^2}{2\sigma_z^2}\right) \Delta z \quad (4.8)$$

here  $\sigma_z$  is the standard deviation of  $z_{dca}$ , and  $z_{mean}$  is the mean value of the measured  $z_{dca}$ . Actually  $z_{mean}$  is the event vertex calculated in our first order approximation, for different event  $z_{mean}$  are different. Note that  $\sigma_{dca}$  and  $\sigma_z$  are different in the central tracker and in the forward tracker, as demonstrated in Fig.4.12 and Fig.4.14. The values of  $\sigma_{dca}$  and  $\sigma_z$  can be obtained by doing a Gaussian fit to the distributions of  $d_{ca}$  and  $z_{dca} - z_{mean}$  for good tracks. This was done using CC Monte Carlo as well as data, the results for  $e^+p$  Monte Carlo are given in Table 4.2 for CJC and FWD respectively, together with the "Pseudo-CC" data, i.e. the  $e^+p$  NC data with only hadronic tracks being taken into account. We also give the results from finally selected CC data for reference, since the statistics of good tracks of CC data in FTD is too low to get a reasonable distribution, only the results in CJC are given in the table. For  $e^-p$  run we got similar results.

Table 4.2  $\sigma_{dca}$  and  $\sigma_z$  for data and MC (cm):

Sample		$e^+p$ CC Monte Carlo	$e^+p$ Data	
			CC	PsCC
CJC	$\sigma_{dca}$	0.13	0.15	0.15
	$\sigma_z$	4.6	8.7	9.3
FTD	$\sigma_{dca}$	2.7	3.9	(statistic too poor)
	$\sigma_z$	12.8	14.3	

We see that while  $\sigma_{dca}$  are quite in agreement for data and Monte Carlo simulation, the  $z$  distribution in data is more dispersed. The  $\sigma_{dca}$  and  $\sigma_z$  fitted from the tracks in data will be used in the selection.

The  $d_{ca}$  and  $z$  measurements are independent, thus these two probability functions are not correlated. The weight  $P_{tk}$  assigned to each track can be written as:

$$P_{tk} \Delta d_{ca} \Delta z = P_{dca} \cdot P_z = \frac{1}{2\pi\sigma_{dca}\sigma_z} \exp\left(-\frac{(z - z_{mean})^2}{2\sigma_z^2} - \frac{d_{ca}^2}{2\sigma_{dca}^2}\right) \Delta d_{ca} \Delta z \quad (4.9)$$

and the event vertex is calculated from the weighted good tracks:

$$z_{vtx.weighted} = \frac{\sum_{good.tracks} z_{i,good} P_{tk}}{\sum_{good.tracks} P_{tk}} \quad (4.10)$$

The precision of the calculated vertex is improved after this weighting procedure.

A more general treatment of the weighting is proposed [53], where a maximum likelihood approach is used to fit the event vertex. In this approach, a flat distribution in  $z, d_{ca}$  plane defined by the good track selection criteria is used to approximate probability for the badly measured tracks or the background tracks:

$$P_b \Delta d_{ca} \Delta z = \frac{\Delta d_{ca} \Delta z}{4 d_{max} z_{max}} \quad (4.11)$$

where  $d_{max}$  and  $z_{max}$  are the criteria for  $d_{ca}$  and  $z_{dca}$  in the selection of good tracks, having different values in central and forward tracker. A probability  $b$  ( $0 < b < 1$ ) is assumed for the tracks with flat distribution, and the probability for a track to have the measured values is:

$$P = (1 - b)P_{tk} + bP_b \quad (4.12)$$

Using maximum likelihood approach, and defining the likelihood as  $W = -2 \times \sum_{(good\ tracks)} \log(P)$ , the best estimation for the event  $z$  vertex position is given by:

$$z_{max.lik} = \frac{\sum_{good.tracks} z W_{tk}}{\sum_{good.tracks} W_{tk}} \quad (4.13)$$

where

$$W_{tk} = \frac{1}{\sigma_z^2 (1 - b (1 - \frac{\pi \sigma_{dca} \sigma_z}{2 d_{max} z_{max}} \exp(\frac{(z - z_{max.lik})^2}{2 \sigma_z^2} + \frac{d^2}{2 \sigma_{dca}^2})))} \quad (4.14)$$

The vertex  $z_{max.lik}$  and the factor  $b$  can be obtained iteratively, and they converge very fast after a few iterations. The value of  $b$  is different for central and forward tracks due to their different track parameters, thus should be treated separately. We use the  $b$  values obtained from data, which are 0.14 and 0.4 for central and forward tracks respectively.

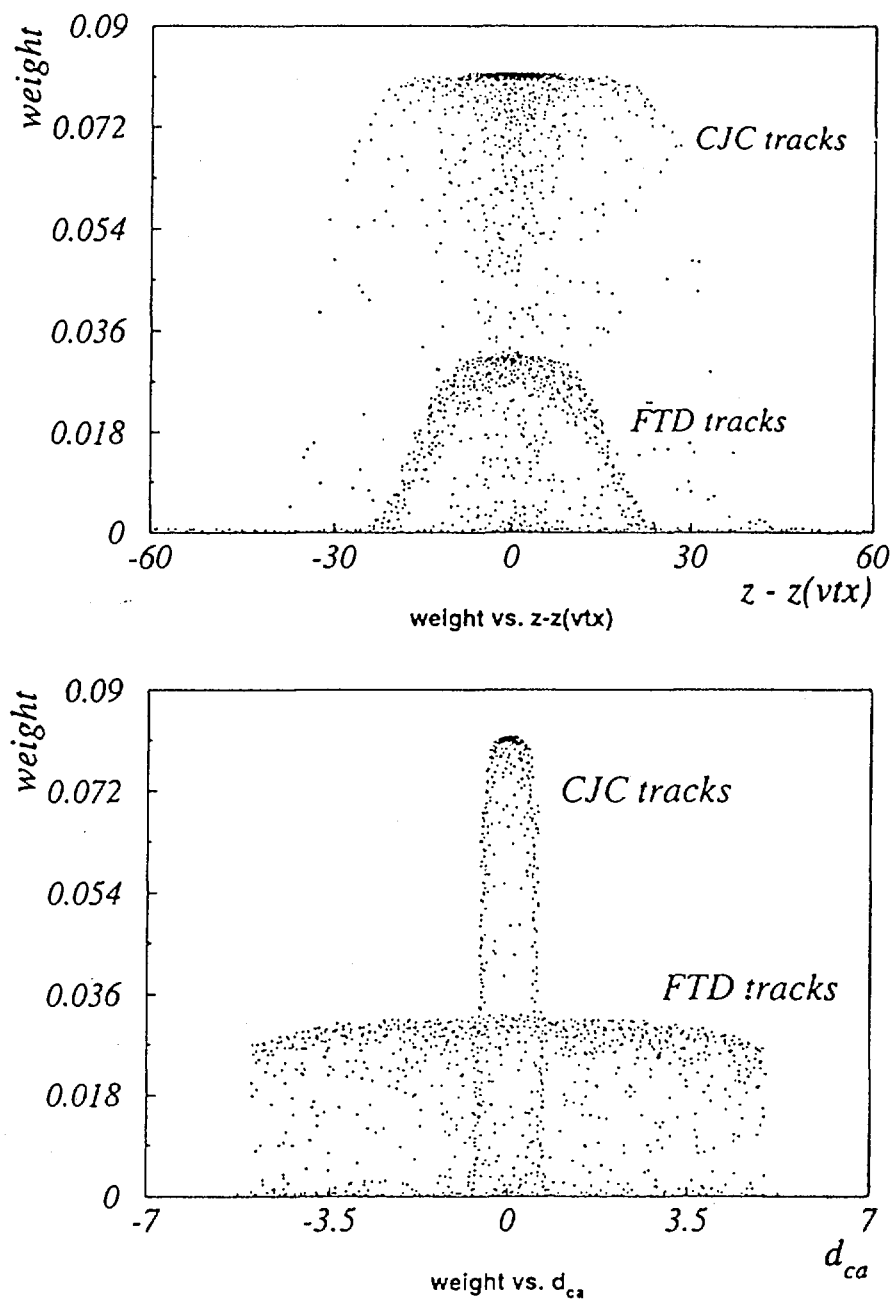


Fig.4.17 The track weight distribution as a function of a).  $z - z_{vtx}$  and b).  $d_{ca}$

The weight in this approach of vertex fitting is not only a function of the uncertainties of  $z_{dca}$  and  $d_{ca}$ , but also a function of the fitted vertex value. Thus the weight for a track is different in different iteration steps. Fig.4.17 shows the weight value distributions as functions of  $(z_{dca} - z_{vtx})$  and  $d_{ca}$  in the last iteration loop, i.e.  $z_{vtx}$  is the fitted vertex. It should be noted that the weight is not normalized in the plots.

Fig.4.18 shows the distribution of the simulated vertex (true vertex) and calculated vertex using mean method and maximum likelihood method respectively. The distribution of true vertex is well reconstructed by both methods. As to the precision of the vertex calculation, Fig.4.19 gives the difference between the calculated vertex and the true vertex, where we can see an obvious improvement on the precision of the vertex calculation after the weighting using maximum likelihood method.

The comparison of vertex calculation between data and Monte Carlo is given in Fig.4.20, where the CC data sample is 48 CC events selected from 1994  $e^+p$  runs, and the Monte Carlo is normalized to the same luminosity of 1994  $e^+p$  data. Also given in the plot is the vertex from the H1 reconstruction package, where a  $\chi^2$  multi-vertex fit is performed in the early stage of data reconstruction. Large fluctuations are shown in the distributions due to the limited statistics of the CC data.

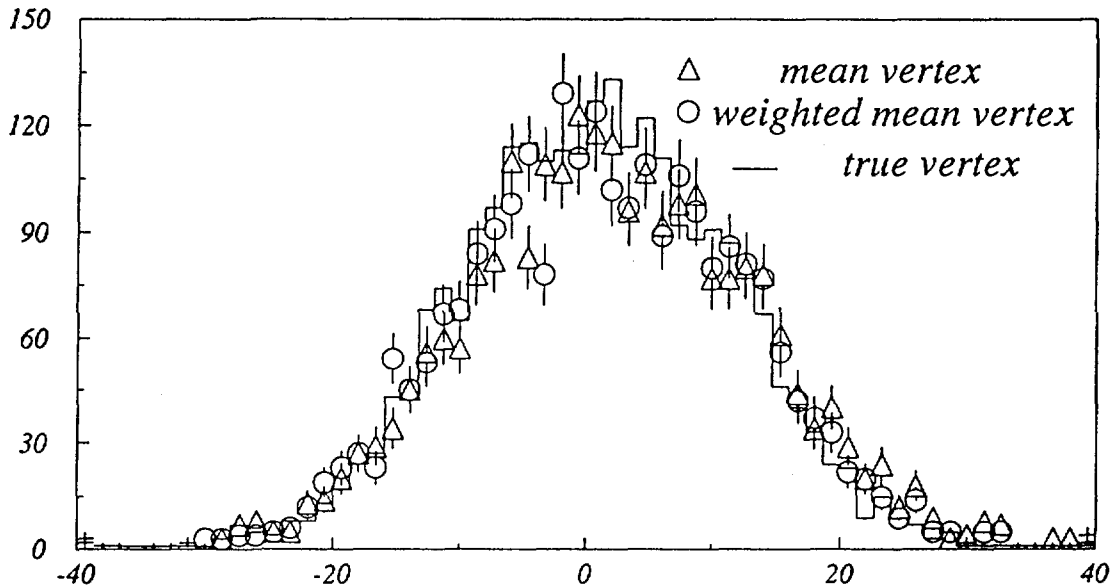


Fig.4.18 The distribution of calculated vertex and the true vertex (CC Monte Carlo). "Mean vertex" is calculated using equation (4.6); "weighted mean vertex" is calculated using equation (4.13).

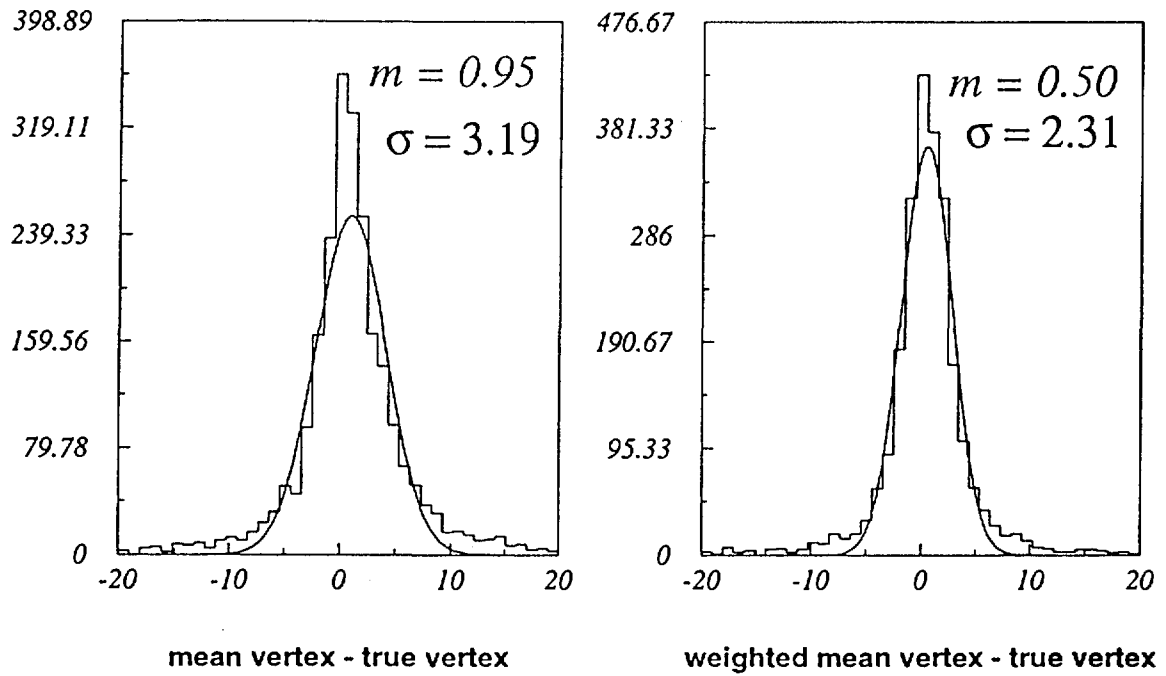


Fig.4.19 Comparison of calculated vertex with true vertex (CC Monte Carlo).

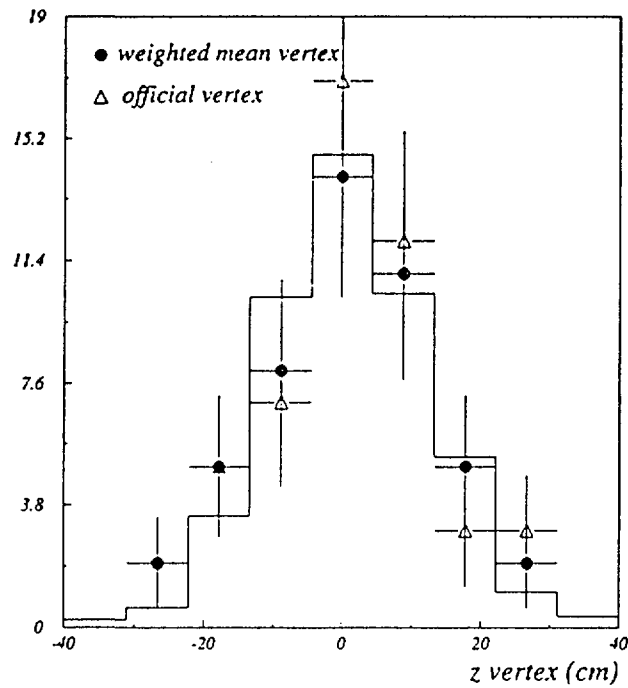


Fig.4.20 Comparison of the reconstructed vertex (weighted and "official") from 1994 CC  $e^+p$  data (points) and Monte Carlo (histogram).

The calculation of the transverse momentum  $P_t$  depends on the direction of the final state jets, which is determined by the barycenter of the energy cluster of the jet and by the position of the interaction point. Using CC Monte Carlo, we can compare how the values of the  $z$  vertex defined by different approaches affect the  $P_t$  calculation, thus affect the event selection. This is discussed in detail in the next chapter. The conclusion is that, compared with the generated  $P_t$  value, the  $P_t$  calculated from the vertex defined by the maximum likelihood and the vertex given in H1 package have the same magnitude of uncertainties.

Based on the knowledge of the vertex distribution of  $ep$  interaction data at HERA, the vertex criteria is given by:

$$|z_{vtx} - z_m| < 35 \text{ cm} \quad (4.15)$$

here  $z_m$  is the difference between the actual average  $z$  position of the  $ep$  interaction point in 1993 and 1994 runs and the nominal interaction vertex. The value of  $z_m$  depends on the beam conditions. For 1993 and 1994 runs  $z_m$  is determined to be 5 cm.

The  $z$  vertex calculated from a maximum likelihood method are used in our event selection. We also use the “official” vertex in the selection procedures for comparison. As to background rejection power, our vertex method removes 30% more background than the “official” vertex after the  $P_{t,miss} = 25 \text{ GeV}$  cut, if no other cut (trigger, background filter) is applied. The same background rate is kept after applying all of these selection cuts for the two vertices.

### 4.2.3 Trigger requirement

Based on the topology of the high  $Q^2$  CC events, a special hardware trigger is applied in charged current event selection. This CC trigger requires two conditions to be satisfied simultaneously:

- The missing transverse momentum  $P_{t,miss}$  evaluated at the first level of the trigger should exceed a minimum threshold. The  $P_{t,miss}$  is the vector sum of momentum of the final state jets from the coarsely segmented LAr calorimeter big tower trigger readout. The threshold is 6 GeV, which is just above the noise level and well below the 25 GeV cut in the physics analysis such that the good CC events are not lost due to the error in the estimation of  $P_{t,miss}$  from LAr big tower.

- The time of the event should be identified by the fast track trigger from the multi-wire proportional chambers, which requires hits in at least 3 out of 4 proportional chamber layers, and the  $z$  position of the tracks are restricted to  $\pm 80cm$  around the nominal interaction point which is very loose compared to the expected interaction region ( $\pm 35cm$ ) to ensure no good event will be lost.

These two conditions can be fulfilled accidentally by the overlapped background: the energy deposited by a cosmic or halo muon induced showers fulfill the  $P_{t,miss}$  requirement, and a underlying beam-gas event provides the  $t_0$  trigger. A cosmic muon passing the interaction point can also fire the CC trigger. Thus these kinds of backgrounds can not be rejected by the CC trigger.

#### 4.2.4 Background rejection

The background at HERA comes from three major sources: the synchrotron radiation from the electron beam, which produces about 10 low energy photons per beam crossing in the central region of the interaction; the interactions between primary protons or electrons with the residual gas in the beam pipe; and the particle showers produced by off momentum beam particles hitting the beam tube and other apparatus. The background coming from these sources has been already efficiently suppressed by the H1 trigger system.

#### Source of background in data samples

Most of the non- $ep$  interaction background events presented in the data sample for CC and NC event selection are of two major sources: the cosmic ray muon induced background where  $\mu$  enters the detector from all the directions, and the upstream produced halo muon induced background where the trajectory of  $\mu$  is always parallel to the beam axis. Other insignificant sources include the noise due to technical reasons, such as the abnormal energy signals caused by the failure of an analog box or readout system.

For cosmic or halo muon background events, the energy deposited in LAr calorimeter by the interacting  $\mu$  induces an electromagnetic shower which is localized and concentrated along the trajectory of the incoming  $\mu$ . The momentum of these events are not balanced with respect to the nominal interaction point. The tracks of the incoming  $\mu$ 's are usually detected in the muon system and in LAr, which do not necessarily

pass through the nominal interaction point. A considerable amount of background is excluded by the vertex requirement. However, the tracks from the charged particles from the secondary interaction or from the overlapped beam-gas events may accidentally provide a vertex for the muon induced background events.

The CC sample is also contaminated by the backgrounds from the beam interactions, such as the interactions of beam-gas, beam-wall,  $\gamma p$ , or neutral current event with electron not well measured due to technical reasons. These events are balanced in the transverse momentum, i.e.  $V = 0$ . The  $P_t$  loss due to energy measurement is well below 25 GeV. Most of these backgrounds are removed by the  $P_{t,miss} > 25\text{GeV}$  cut, the remaining background like bad measured NC is discarded by visual scan in the final step.

Some of the background events are from different sources which overlap to each other, and satisfy accidentally the  $P_{t,miss}$ , trigger and vertex requirements, therefore more selection criteria are needed to remove them. The longitudinal view and transverse view of a typical overlapped halo-muon event and a cosmic-muon event in the H1 detector is shown in Fig.4.21(a) and Fig.4.21(b) respectively.

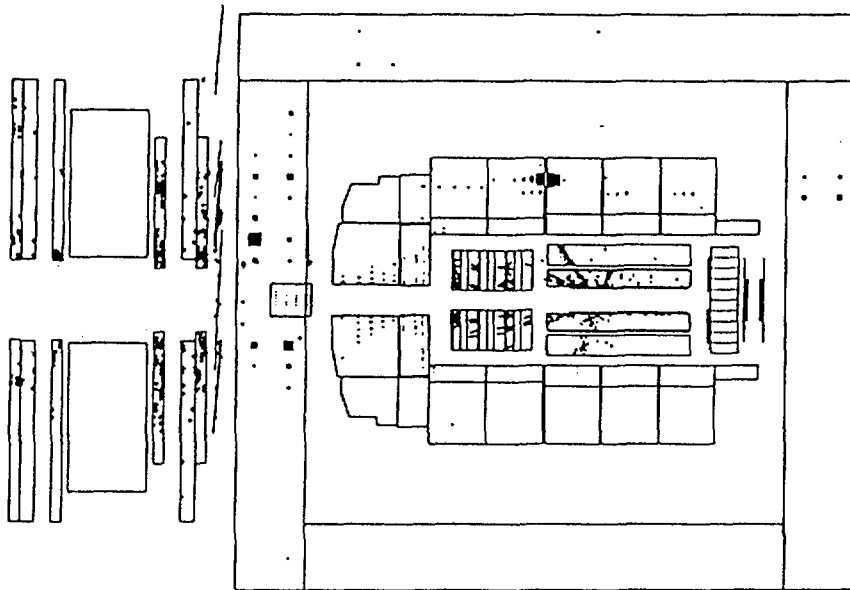


Fig.4.21(a) A typical halo-muon event overlapped with beam-gas interaction in H1 detector.

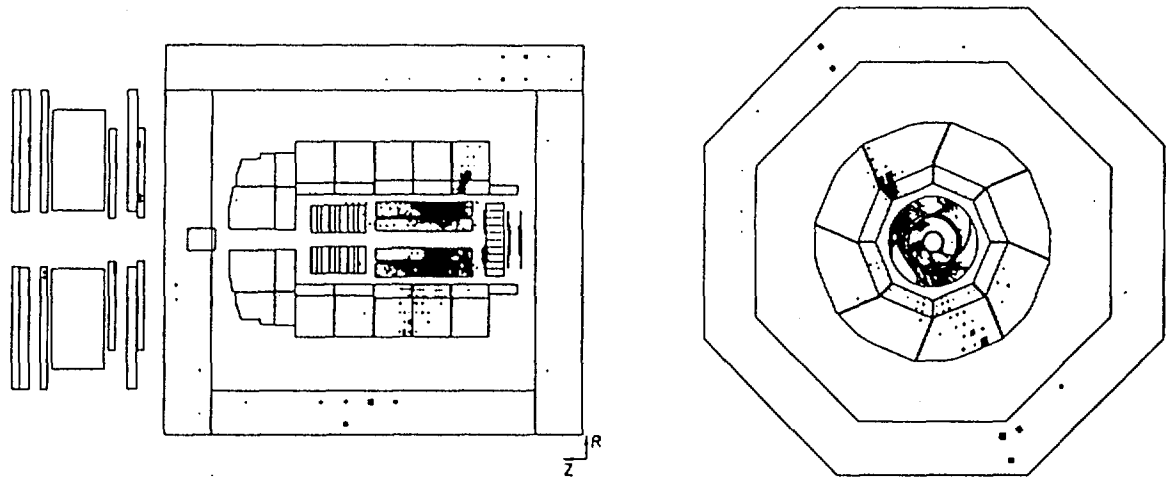


Fig.4.21(b) A typical cosmic-muon event overlapped with beam-gas interaction in H1 detector.

### Selection cuts for background suppression

At the first step, for the straight forward cosmic muon and halo muon induced events with their unique energy deposition patterns and track characteristics, a primary background filter 100% transparent for good CC event with loose cut criteria is applied [54]

This filter exploits the localized energy deposition pattern of the background. For halo muon background rejection, first the cluster in calorimeter which has the largest transverse momentum  $P_t$  is found, and the position of its barycenter in  $r\phi$  plane is determined. Then a cylinder parallel to the beam axis with a radius of 15 cm around the barycenter position is built, and the total energies deposited inside and outside of the cylinder are calculated. For simple halo muon event, most of the energy of the  $\mu$  induced shower will be deposited inside this cylinder. The event which has the energy

deposited outside the cylinder  $E_{out}$  less than 10 GeV will be discarded.

To discard cosmic muon events, a similar “tube building” technique is used: first the positions of all muon candidates in the muon tracking system surrounding the LAr calorimeter are found, then by combining the muon candidates one by one, a set of axis is defined by two point positions of these muon candidates. A tube is constituted around these axes, and the energies deposited inside and outside the tube are calculated. If the energy deposited inside the tube accounts for more than 90% of the total energy deposited in LAr, the event is rejected. Special care is taken in the very forward region to avoid mistaking the hadronic jets as cosmics.

However, different sources of background are often superimposed to each other and mimic topologically a charged current event, which make the background recognition difficult. The criteria based on the localized energy deposition are not effective any more due to dispersed energy from different sources. By studying further the difference of the topological structure between genuine CC event and background from experimental data and Monte Carlo simulation, we developed several more criteria of the selection cuts, which are efficient for these kinds of background applied finally to the selected data sample.

- As described above, for charged current event, the scalar momentum sum  $S \approx$  vector momentum sum  $V (= P_{t.miss})$ , Due to the dispersion of the directions of the final state jets and the energy resolution,  $S$  is larger than  $V$  but within certain limit. Some of the noise events has  $S$  much greater than  $V$ , a criteria of  $S < 3V$  is a safe cut to remove these events.
- Two quantities  $y_{exp}$  and  $R_{zp}$  defined as following (where  $E_{el.beam}$  is the energy of incident electron)

$$y_{exp} = \frac{\sum_i (E_i - p_{z,i})}{2E_{el.beam}} \quad (4.16)$$

$$R_{zp} = \frac{\sum_i p_{z,i}}{\sum_i p_i} \quad (4.17)$$

are used to reject background. Actually, for genuine CC events,  $y_{exp}$  equals to the scaling variable Bjorken- $y$  (Jacquet-Blondel method, see chapter 6), and  $R_{zp}$  is the normalized longitudinal hadronic momentum. Fig.4.22 gives the distribution of  $y_{exp}$  and  $R_{zp}$  for Monte Carlo and for 1994 data. We see that most of good CC events have  $0 < y_{JB} < 1$  and  $R_{zp} > 0$ . There is also a correlation between

these two quantities, all good events are situated above the solid line drawn in the plots. Due to the energy resolution and the error in direction measurement,  $y_{exp}$  of some events may exceed the  $[0,1]$  range a little, but for non-physical backgrounds it may be situated far beyond the range. Finally the safe cuts at  $y_{JB} < 1.2$ ,  $R_{zp} > -0.1$  and  $y_{JB} > (0.66 - 0.7R_{zp})$  (the solid line in the plot) are applied. The finally selected CC events in 1994 data are also plotted in Fig.4.22.

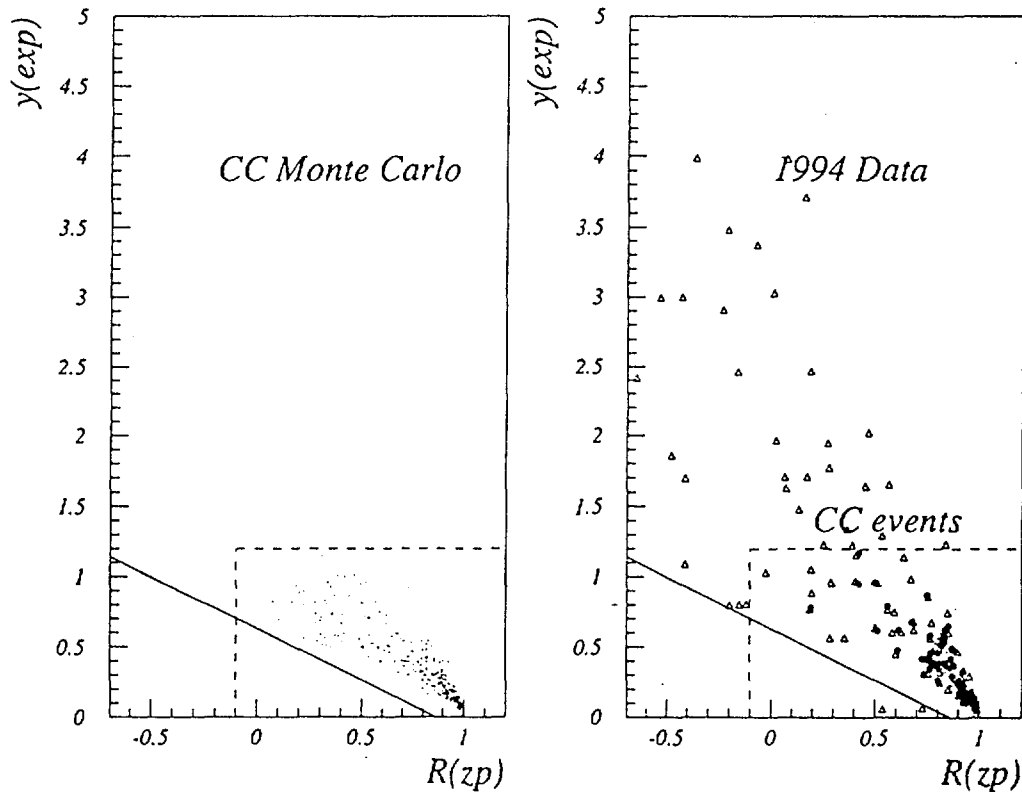


Fig.4.22 The distributions of  $y_{exp}$  vs.  $R_{zp}$  for Monte Carlo and 1994  $e^+p$  data.

- Another two distinct features distinguishing halo muon or cosmic muon events from genuine CC events concern the track-cluster link and the position of the energy cluster with respect to the inner surface of the LAr calorimeter. We always pay attention to the energy cluster with the largest  $P_t$ : for genuine CC events, the charged particles within the jets always leave some tracks in drift chambers which point from the interaction vertex to the energy cluster deposited in LAr. In some occasions there may not exist any track pointing to the largest  $P_t$  cluster. These occasions include: the failure of the tracker, the direction of the

jet is in some special angular region where the tracker has low efficiency, or the largest  $P_t$  cluster happened to be a photon. Nevertheless, from data and Monte Carlo study, these possibilities are very small and well below 1%. For background events, the logical link of track-cluster does not exist necessarily, a requirement on the link effectively removes many of them. However, for overlapped background, the track from beam-gas interaction may incidentally point to the energy cluster of halo or cosmic  $\mu$ s, thus can not be removed by this requirement.

Another criteria uses the energy deposition pattern: for the highest  $P_t$  jet emitted from the interaction vertex of the CC event, it traverses the tracker, the electromagnetic and hadronic part of LAr calorimeter successively, the energy deposited in LAr calorimeter distributed within a cone with respect to the vertex. The innermost layers of LAr along the trajectory of the jets where the jets enter the LAr calorimeter always have some energy deposition. For halo and cosmic muon backgrounds, the trajectory of  $\mu$  do not necessarily pass the primary vertex, if a cone is built with the direction of the axis defined by the vertex and the barycenter of the highest  $P_t$  cluster, there may not be any energy deposited between the inner surface of LAr and the first fired cell of the cluster along the cone.

To reject background exploiting this feature, a distance  $d$  is calculated as follows (Fig.4.23): first a cone from the interaction point along the direction from the vertex to the barycenter of the highest  $P_t$  cluster is constituted, then the position of the first fired cell within this cone to the inner surface of LAr is located, Thus, there is no any energy deposition between this cell and the inner surface of LAr. The distance  $d$  is calculated depending on the position of the cluster in LAr: in the barrel region (CB1,CB2,CB3,FB1,FB2),

$$d = r_{1st.cell} - r_{innerLAr} \quad (4.18)$$

is the radius difference between the first cell and LAr inner surface. In the inner forward region (lower part of IFE,IF1,IF2),

$$d = z_{1st.cell} - z_{innerLAr} \quad (4.19)$$

is the  $z$  difference between the first cell and LAr inner surface. In the outer forward region (OF1,OF2,OF3, and upper part if IFE,IF1,IF2),

$$d = \sqrt{(z_{1st.cell} - z_{innerLAr})^2 + (r_{1st.cell} - r_{innerLAr})^2} \quad (4.20)$$

is the distance in  $r\phi$  plane between the first cell and the intersection of barrel and forward region.

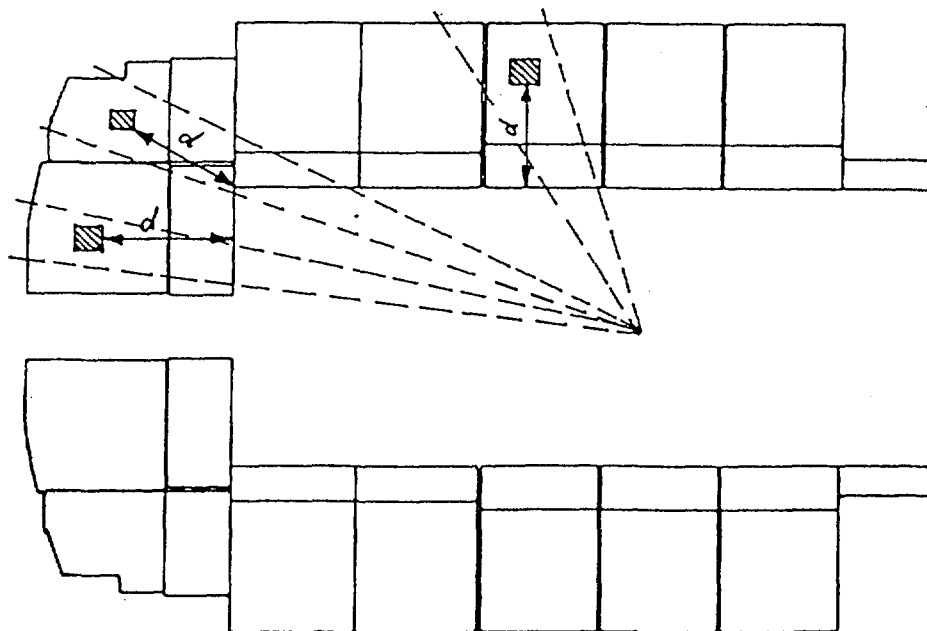


Fig.4.23 The definition of the distance  $d$  in the calorimeter.

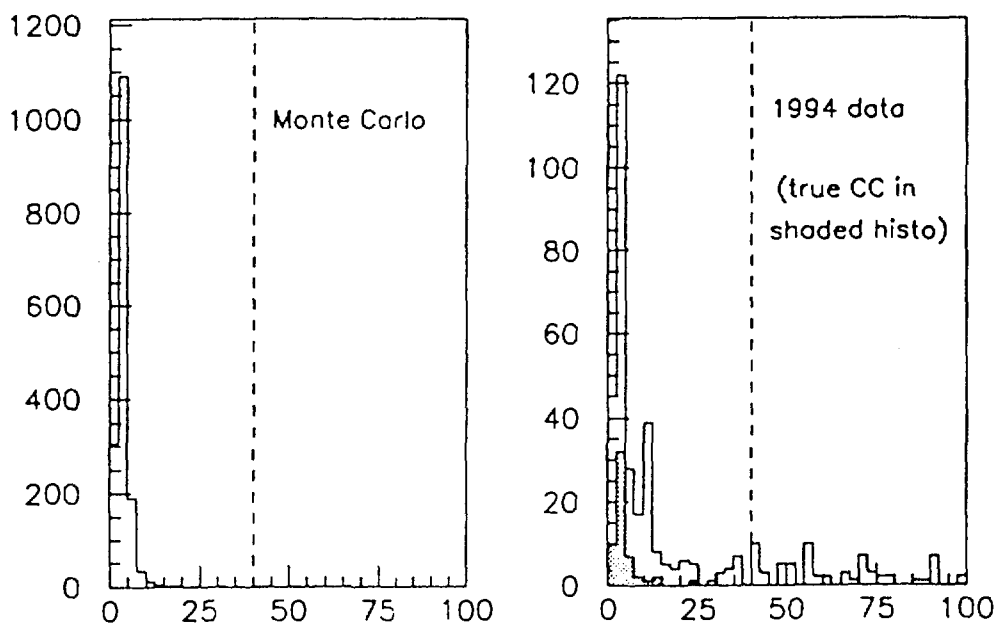


Fig.4.24 The distribution of the distance  $d$  for CC Monte Carlo and 1994 data. The selected CC events from data are also shown.

Fig.4.24 shows the distance  $d$  for 1994 data and for Monte Carlo respectively. The true CC events found in 1994 data are also plotted in the shaded histogram. It is clear that  $d$  for most of CC event is near Zero, some has larger  $d$  due to energy or position resolution of LAr, but well below 40 cm. We choose a safe cut  $d < 40\text{cm}$  to remove the backgrounds.

- For halo muon and beam gas overlapped events which escaped the above filter based on energy deposition pattern ( a typical event is shown in Fig.4.21(a)), a simple and effective criteria can be applied: for a large part of the halo muon events, there is a muon cluster or track in the backward instrumented iron, and its position in  $r\phi$  plane is in coincidence with the barycenter of the energy cluster of halo  $\mu$  induced shower deposited in LAr calorimeter, since the trajectory of the halo  $\mu$  is parallel to the beam axis.

For CC event, it is unlikely to find a  $\mu$  candidate in the backward endcap corresponding to the high  $P_t$  cluster, there exist the possibility of random coincidence due to technical noise, but the chance is very rare. This is confirmed by studying CC Monte Carlo and real data, the coincidence possibility for good CC event is nearly zero. The rejection procedure is to find first the barycenter position in  $r\phi$  plane of the energy cluster in LAr which has the largest  $P_t$ , then to check if there is a  $\mu$  candidate present in the backward iron endcap corresponding to this position; only events without such  $\mu$ 's are accepted.

After this set of selection cuts, most of the background surviving the simple cosmic and halo muon filter are removed. However, there are still some overlapped background which has very similar topology as real CC event and escaped the above cuts. They will be removed by visual scan in the final step.

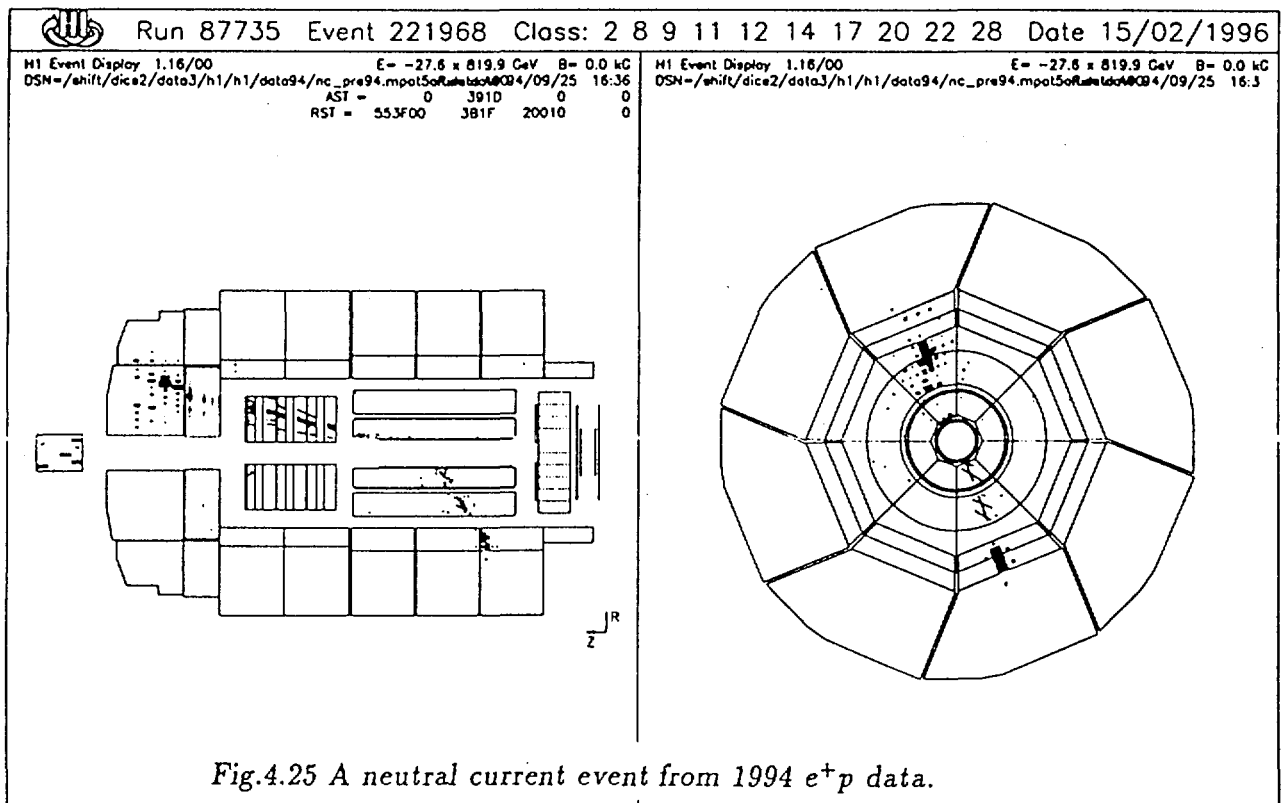
### 4.3 Selection of Neutral current events

A neutral current event is defined as a  $ep$  interaction which leaves a clearly identified electron in H1 detector. The observed transverse momentum of a NC event is balanced, and the  $P_t$  of hadrons should be high enough to pass the 25 GeV cut in our high  $Q^2$  analysis. A typical NC event recorded by the H1 detector is shown in Fig.4.25.

The neutral current events are selected from the same luminosity data and the same class of event for electroweak process (class 8) as in charged current selection. To ensure a parallel selection of CC and NC events, the same criteria applied in the

CC selection as described above were applied to the final state hadronic system of NC events.

The selection procedure is: first the scattered lepton (electron or positron) should be found, then the energy deposited by the lepton in the LAr calorimeter and the tracks from the lepton in drift chamber will be removed, and the vertex should be reconstructed from the remaining hadronic tracks. The hits from the lepton in the MWPC trigger system are also removed, and the trigger conditions are re-simulated. The remaining final hadronic system has the same topology as the CC event. The same set of criteria as in CC selection are then applied to these “pseudo-CC” events. The selected “pseudo-CC” event sample from data is also used to calculate various efficiencies since the Monte Carlo may not give a precise simulation of the detector response.



### 4.3.1 Electron identification

The essential task in neutral current event selection is to find the scattered lepton. An electron finder should be as efficient as possible to increase the statistics of the

selected data sample, and should have low mis-identification rate, i.e. to find the true electron to avoid the wrong calculated kinematics due to mis-identification.

The LAr calorimeter has a fine granularity and good  $e - \pi$  separation power. Most of the energy of the scattering electron is deposited in the electromagnetic part of the LAr calorimeter, or in BEMC for low  $Q^2$  event. Because of the momentum balance of the neutral current process, the electromagnetic shower from electron is isolated and in the opposite direction of the final state jet system in  $r\phi$  plane, and concentrated in several adjacent LAr cells. These characteristics are exploited by our electron finder.

The basic strategy of the electron finder is quite simple and straightforward: the electron candidates are searched from all the energy clusters reconstructed from the energy deposited in H1 calorimeter system, where individual cluster may have energy contribution from several sub-calorimeters. The searching procedure is described step by step in the following:

- Firstly, from all the energy clusters reconstructed in this event, the clusters which deposited most of their energies in LAr or BEMC calorimeter are found. For high  $Q^2$  electroweak process which we are interested in, most of the electrons are scattered in the barrel region of the detector and are recorded in LAr calorimeter. The fraction of NC events with scattered electrons in a polar angle not covered by LAr is negligible.
- Secondly, if the energy cluster is in LAr, only the clusters which have 75% of the energy deposited in the electromagnetic part of the calorimeter are kept. Other clusters are excluded as being hadronic jets candidates.
- Then the cluster which has the largest transverse momentum  $P_t$  from the clusters passing through the above two steps was found. Most likely the true electron always has the largest  $P_t$  since it should balance the transverse momentum from the final state hadronic jets.
- Finally the calorimeter cluster mass  $m_{CL}$  was used to further remove the wrong-identified electron candidates. It is defined as follows:

$$m_{CL} = \sqrt{(\sum_i E_i)^2 - (\sum_i \vec{p}_i)^2} \quad (4.21)$$

where the summation is done over all the calorimeter cells within the cluster, i.e. within a cone around the axis defined by the interaction point and the barycenter of the cluster. Actually the quantity  $m_{CL}$  reflects the compactness of the cluster.

Fig 4.26 shows  $m_{CL}$  as a function of the transverse momentum of the electron candidate  $P_{t,el}$  from neutral current Monte Carlo and real data. We see that  $m_{CL}$  of true electron cluster always lie below the line represented by the function

$$m_{CL} = 1\text{GeV} + (p_{t,el} - 15\text{GeV}) \cdot 3/35, \quad (4.22)$$

where the mis-identified electron from background events are situated beyond this region. By applying the  $m_{CL}$  cut, the backgrounds from mis-identification are strongly suppressed.

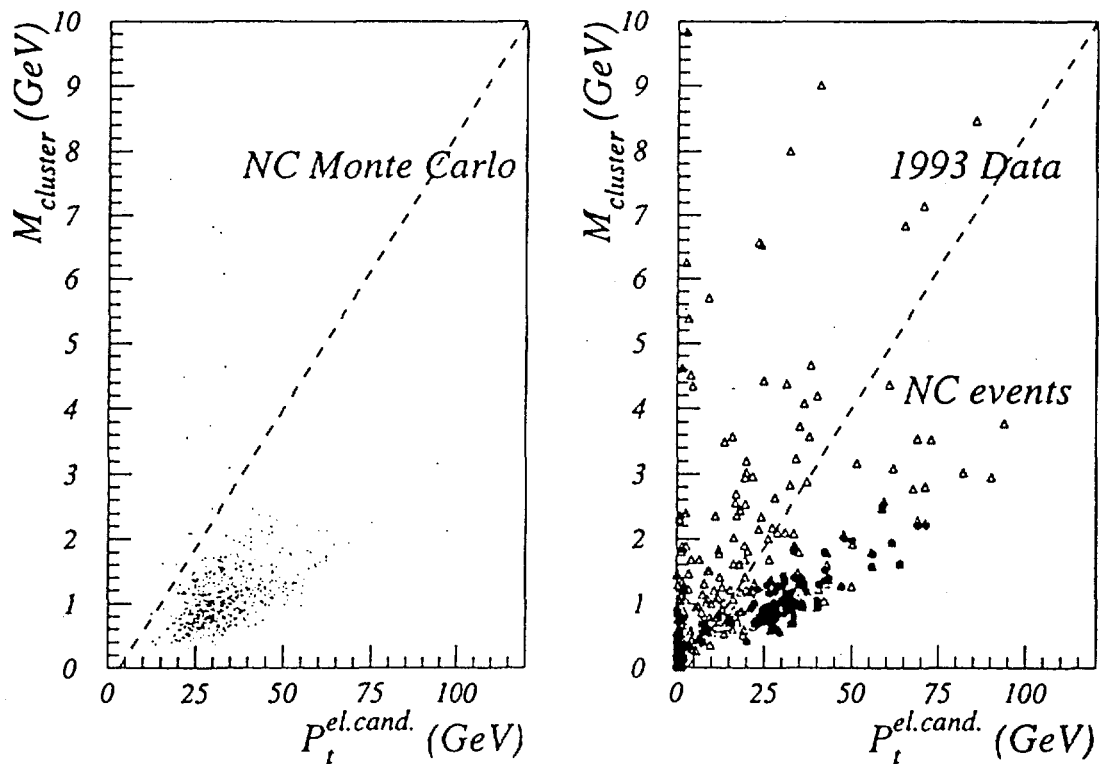


Fig.4.26 The cluster mass  $m_{CL}$ , as a function of the transverse momentum of electron candidate  $P_{t,el}$ , for Monte Carlo and 1994 data respectively.

This simple electron finder works satisfactorily and gives a good efficiency ( $\sim 97\%$ ) and very low mis-identification rate ( $< 0.1\%$ ). However, there is still room for further increase of the efficiency, which is demanded by the low cross section of the high  $Q^2$

process. By checking the characteristics of the lost NC events using Monte Carlo, we found there are two major reasons causing the loss, namely the scattered electron happens to be emitted in a  $\phi$  crack between the LAr calorimeter stacks, as the NC event shown in Fig.4.27, and the largest  $P_t$  cluster is not the true electron but hadrons. Thus the following treatments are applied:

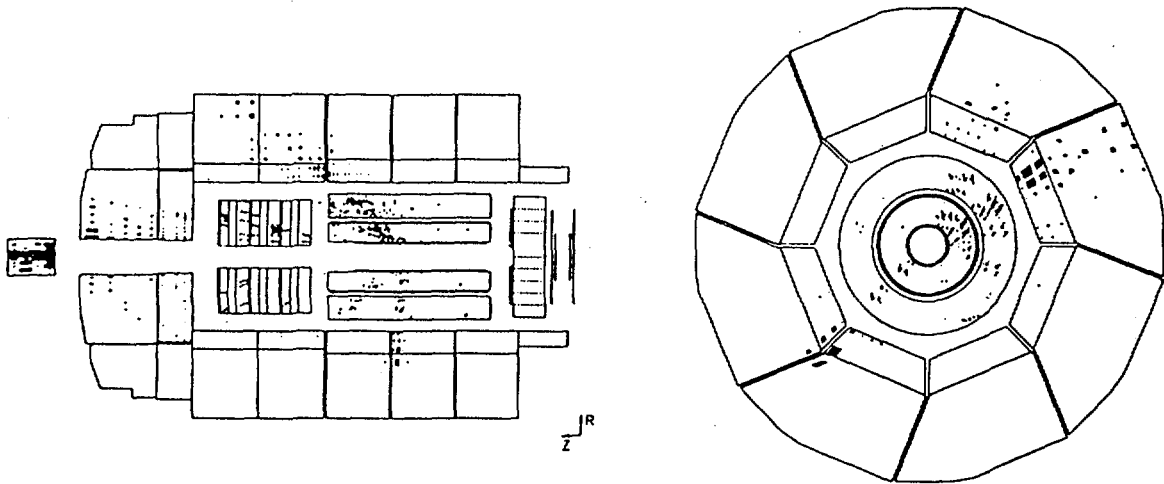


Fig.4.27 A NC event with an electron scattered in the  $\phi$  crack region of the calorimeter.

- In the second step described above, if the cluster points to a  $\phi$  crack ( $|\phi_{cluster} - \phi_{crack}| < 3^\circ$ ), then we only require that 10% of the energy should be deposited in the electromagnetic part of LAr calorimeter instead of 75%, since most of the energy of this cluster may leak out of the electromagnetic part and be deposited in the hadronic part of LAr. Since this kind of events only account for a small fraction of the total NC events, the background rate will not be increased by this procedure.
- The two largest  $P_t$  clusters are kept in step 3. In case the largest  $P_t$  cluster didn't satisfy the  $m_{CL}$  cut, the second to largest  $P_t$  cluster will be taken, thus the possibility of loss due to the largest  $P_t$  requirement is reduced.

These modification indeed increase the efficiency. Table 4.3 gives the efficiency and misidentification rate calculated from NC Monte Carlo (the  $P_{t.had.}$  cut at 25 GeV is applied):

Table 4.3 Efficiency and misidentification rate of electron finder:

Monte Carlo	$e^-p$ Neutral Current	$e^+p$ Neutral Current
efficiency of $e$ finding	99.0%	99.0%
mis-identification rate	0.009%	0.007%

These values show that our electron finder has good efficiency.

### 4.3.2 $P_{t.had.}$ cut

After the electron is found and discarded, the topology of the NC (so-called “pseudo-CC”) is similar to that of the CC event. Let’s denote the electron as particle “ $e$ ”, then the scalar and vector sum of the transverse momentum are:

$$S_{no.e} = \sum_{i \neq e} |\vec{p}_{t_i}| \quad (4.23)$$

$$V_{no.e} = \left| \sum_{i \neq e} \vec{p}_{t_i} \right| \quad (4.24)$$

here we have  $V_{no.e} = P_{t.had.}$  and  $S_{no.e} \approx V_{no.e}$  as in the charged current case. The  $P_t$  balance requires  $P_{t.el.} = P_{t.had.}$ , the measured values may differ a little due to the energy resolution and the detector response. This is also a way to check the hadronic energy scale.

We applied the same 25 GeV cut on the transverse momentum of the hadronic system  $P_{t.had.}$  in our NC selection. The procedure is, first the direction of the electron candidate is found using the electron finder described above, then a cone of half angular size  $7.5^\circ$  from the interaction point is built around the electron direction. The  $P_{t.had.}$  is calculated by summing over all the energy cells in LAr calorimeter except the energy cells located in the cone., using the formula (4.4). Here the vertex position fitted from

the hadronic jets is used to determine the direction of the fired cell. As in  $P_{t,miss}$  calculation in CC selection, the energy deposited in tail catcher is not used due to technical reasons. Fig.4.28 shows the relationship between the reconstructed  $P_{t,el.}$  and  $P_{t,had.}$  for NC Monte Carlo and 1994 data respectively, note that a  $P_{t,had.} > 25$  GeV cut is applied to data.

Unlike in CC selection, the  $P_{t,had.} > 25$  GeV cut has significantly suppressed the background events. In fact, after this cut, the background ratio of the NC sample is about 5%. The remaining background events are further removed by the  $P_t$  balance requirement, i.e.  $P_{t,miss} < 25$  GeV.

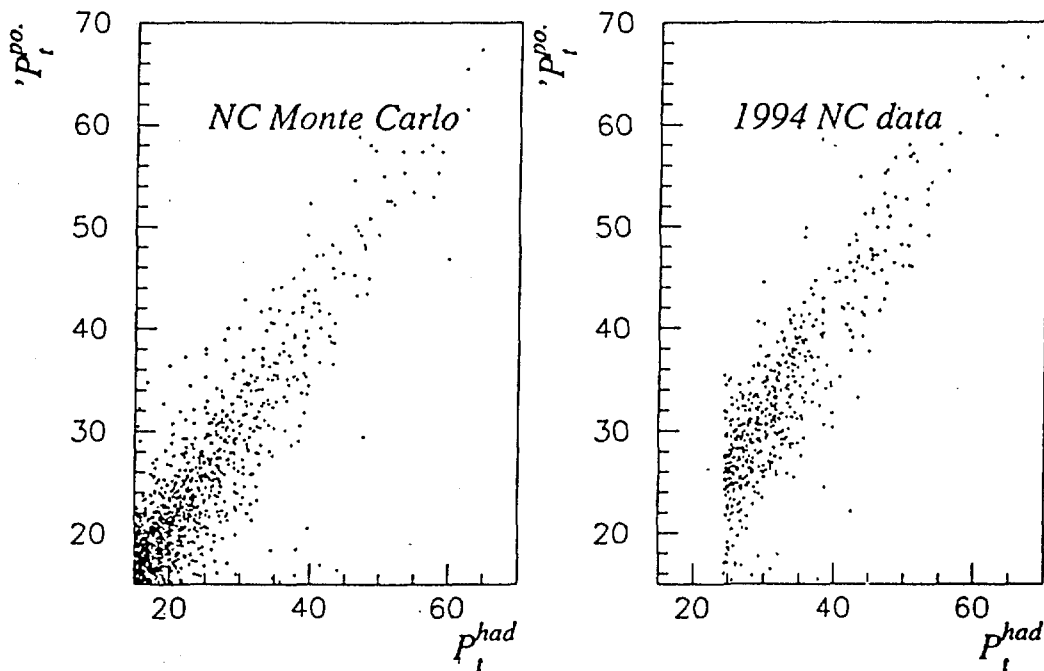


Fig.4.28 The transverse momentum from positron and from hadron for NC events. A  $P_{t,had.} > 25$  GeV cut is applied to data.

### 4.3.3 Vertex requirement

As described in CC selection, here we use the same simple method to calculate the event vertex position. The difference with NC events is that, the track of the electron should be excluded in the vertex calculation in order to get vertex only from the hadronic system as in CC case.

The high  $Q^2$  NC events always have a reconstructed vertex if the electron track is included. In most of the cases, the tracks of scattered electrons in high  $Q^2$  NC event are well defined due to their isolated high momentum and long trajectories in the drift chambers, which point directly to the primary interaction point. It can be expected that after the electron track has been excluded, the precision on the reconstructed vertex will deteriorate. In some cases, the jets in NC events emitted in very forward region can not provide any good tracks, thus no vertex can be reconstructed after the electron tracks were excluded. The vertex requirement is the same as in CC selection:

$$|z_{vtx.had} - z_m| < 35 \text{ cm} \quad (4.25)$$

where  $z_m = 5 \text{ cm}$  for 1993 and 1994 runs. Fig.4.29 shows the calculated vertex compared to the true vertex for NC Monte Carlo with electron tracks or without electron tracks. Compared with the true position of vertex, the calculated vertex are more spread after the electron tracks are excluded. The vertex can not be reconstructed for less than 2% of NC events after electron tracks are excluded, thus these events are lost after the vertex requirement.

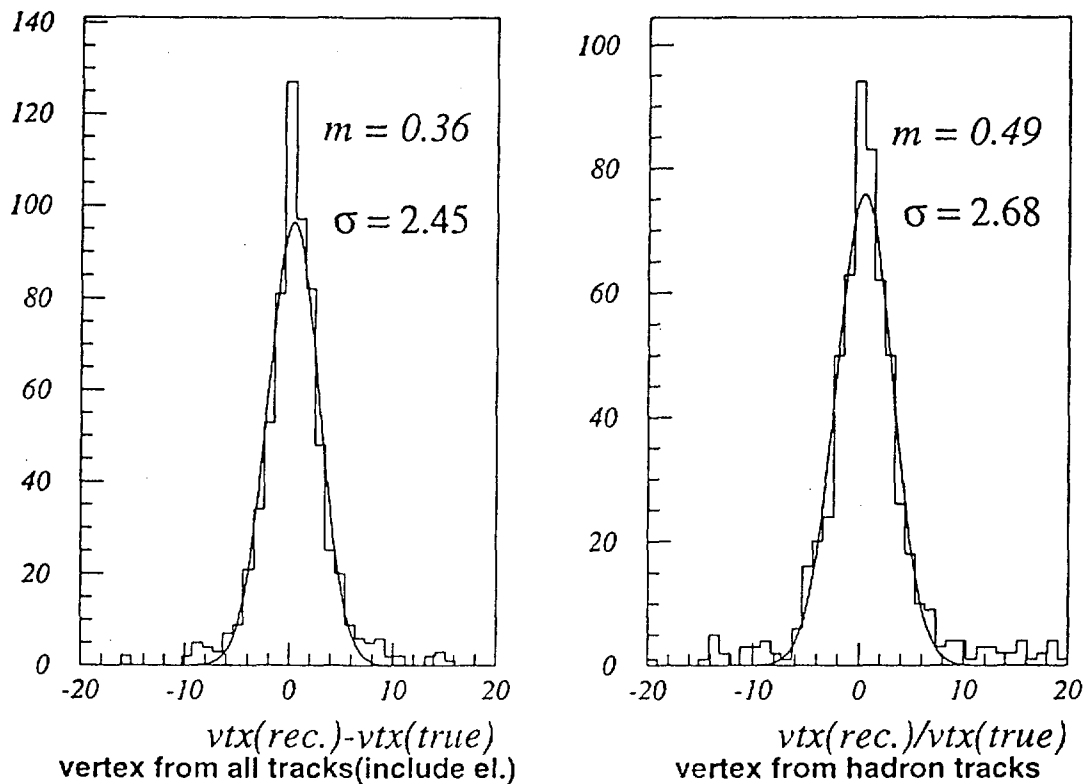


Fig.4.29 The effect of electron track in the vertex reconstruction.

### 4.3.4 Trigger requirement

To see if the hadronic system of a neutral current event could fire the CC trigger, firstly the electron contribution to the trigger elements should be removed and the trigger elements should be re-simulated. This procedure includes: the removal of the energy deposition from the electron candidate in the LAr big tower trigger readout, and the recalculation of the missing transverse momentum  $P_{t,miss}$ ; also the removal of the track of the electron candidate in  $z$ -vertex histogram of MWPC trigger readout and the re-simulation of the event  $t_0$ . Then the same CC trigger condition is applied to the “pseudo-CC” event.

In the same kinematic range of  $P_{t,had} > 25\text{GeV}$  as for the CC events, the hadronic system of NC events is more boosted to the forward direction where the CC trigger efficiency is a little lower than in the barrel region, thus it is expected that the percentage of NC events discarded by the CC trigger requirement after removing the electron contribution will be higher compared to the CC events.

### 4.3.5 Background rejection

Unlike the situation in CC selection, the contamination in high  $Q^2$  NC sample is very small. The electron finder, which requires the existence of an isolated high  $P_t$  electromagnetic energy cluster, has already strongly suppressed the background from incoming interacting muons and from beam induced background. Actually, after the  $P_t$  balance requirement ( $P_{t,miss} < 25\text{GeV}$ ) was applied to the NC sample selected by the electron finder, the remaining background events are all filtered out.

However, in order to get a NC sample selected parallel to CC selection, the selection criteria used to suppress background in CC selection are applied to the hadronic system of NC events. This procedure will cause the loss of good NC events, and will be compensated by an efficiency factor which will be discussed in the next chapter.

## 4.4 Final CC and NC sample

In order to check the quality of our selected sample and to remove the residual background events surviving the above selection procedure, we have performed the visual scan on the selected samples at the final step of the selection. While the NC sample is very clean, the CC sample is contaminated by some background events.

110 CHAPTER 4. SELECTION OF THE CHARGED AND NEUTRAL CURRENT EVENTS

These background include the non- $ep$  background such as superimposed events from halo  $\mu$ , cosmic  $\mu$  and beam-gas interactions, the high  $P_t$  NC events with badly measured electron and noise events which have similar topology as CC events due to technical problems such as hot analog boxes.

Table 4.4 Result in Charged Current Selection:

Selection Procedure	1993 $e^-p$ Data	1994 $e^-p$ Data	1994 $e^+p$ Data
Total Number of Class 8 Event	3193 (pre-selected sample)*	12408	71356
After Technical Requirements		8366	53719
Require $P_{t,miss} > 25GeV$	793	2301	14871
Apply a Loose Cos. & Halo Filter	710	869	4996
Require Vertex $ z_{vertex}  < 35cm$	285	235	1288
Require CC Trigger	133	138	639
Apply Selection Cuts	21	23	75
Scan Results	13 CC ( + 3 Cosmic + 5 Halo )	12 CC ( + 4 Cosmic + 6 Halo + 1 Noise )	48 CC ( + 8 Cosmic + 15 Halo + 3 NC + 1 Exotic)

Table 4.5 Result in Neutral Current Selection:

Selection Procedure	1993 $e^-p$ data	1994 $e^-p$ data	1994 $e^+p$ data
Total Number of Class 8 Event	3193 (pre-selected sample)*	12408	71356
After Technical Requirements		8366	53719
electron finding, Require $P_{t.had.} > 25 GeV$	108	92	631
Require Vertex $ z_{vertex}  < 35cm$	90	88	595
Apply selection cuts	86	84	580
Require CC Trigger	81	76	530
Scan Results	81 NC	76 NC	530 NC

\* : Requirements: 1) EW class (class 8), 2) satisfy the technical requirements, 3)  $P_{t.miss} > 15 GeV$  or  $P_{t.el.cand.} > 15 GeV$ .

Six final samples are obtained after all these selection procedures, i.e. the charged current and neutral current samples for 1993  $e^-p$  data, 1994  $e^-p$  data and 1994  $e^+p$  data. We summarize the event numbers after each selection criteria in table 4.4 and table 4.5 for CC and NC selection respectively.

The next pages show some comparison between the 1993 and 1994 data and Monte Carlo distribution. Fig.4.30 shows the comparison of the distributions of  $P_t^{had}$  between the final CC (NC) data and Monte Carlo. Fig.4.31 shows the comparison of the polar

angle of the hadronic system between CC (NC) data and Monte Carlo. Fig.4.32 shows the comparison of the polar angle and the transverse momentum of the electron of the NC events between data and Monte Carlo. All these distributions are in good agreement.

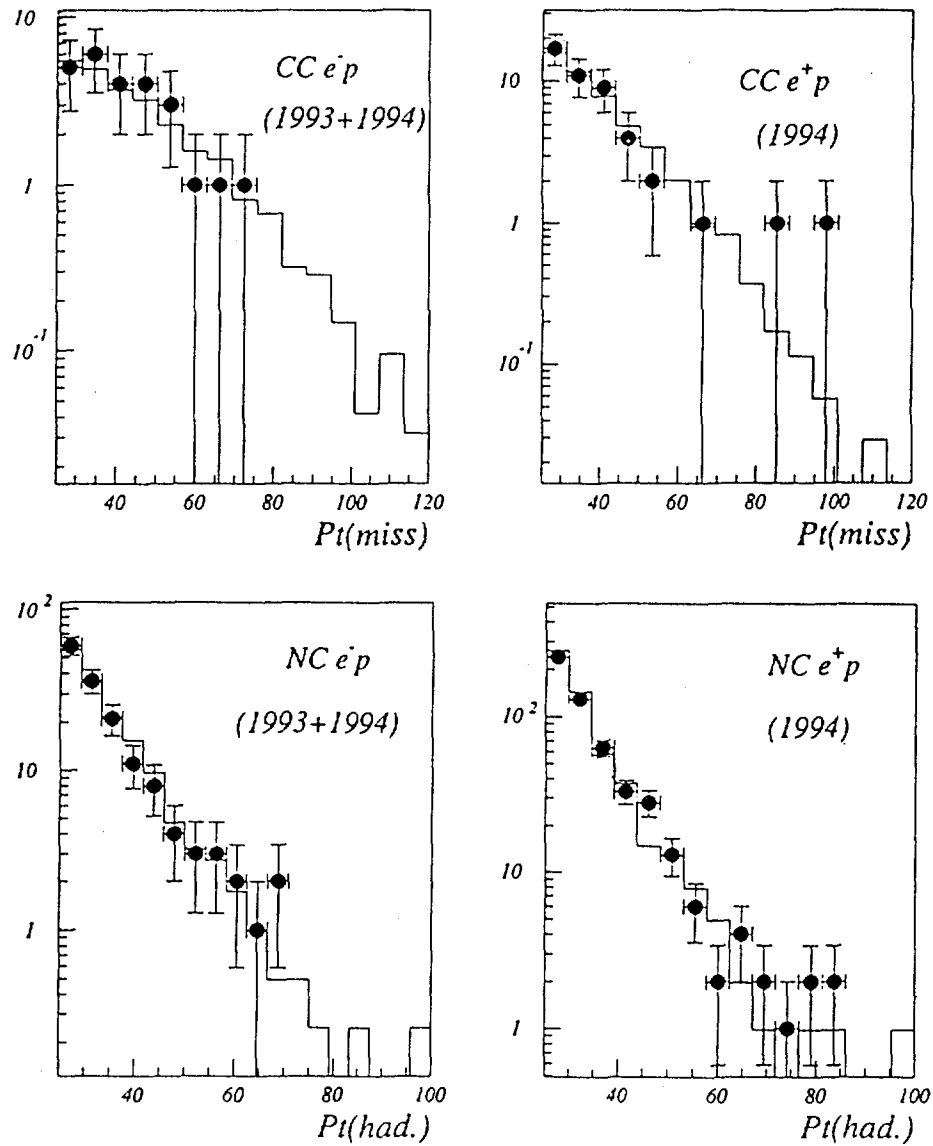


Fig.4.30 The distributions of  $P_t^{\text{had}}$  of the final CC and NC sample for 1993 and 1994 data. data

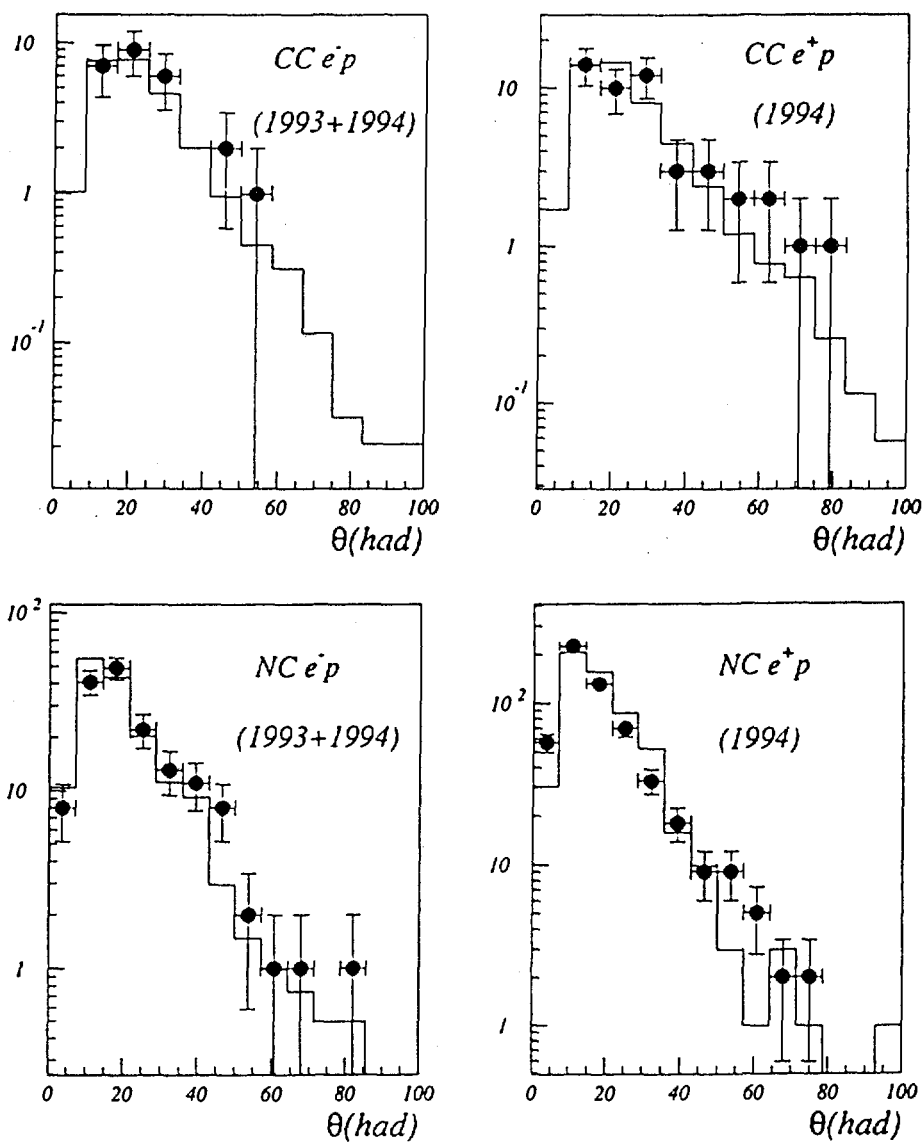


Fig.4.31 The distributions of  $\theta^{quark}$  of the final CC and NC sample for 1993 and 1994 data. data

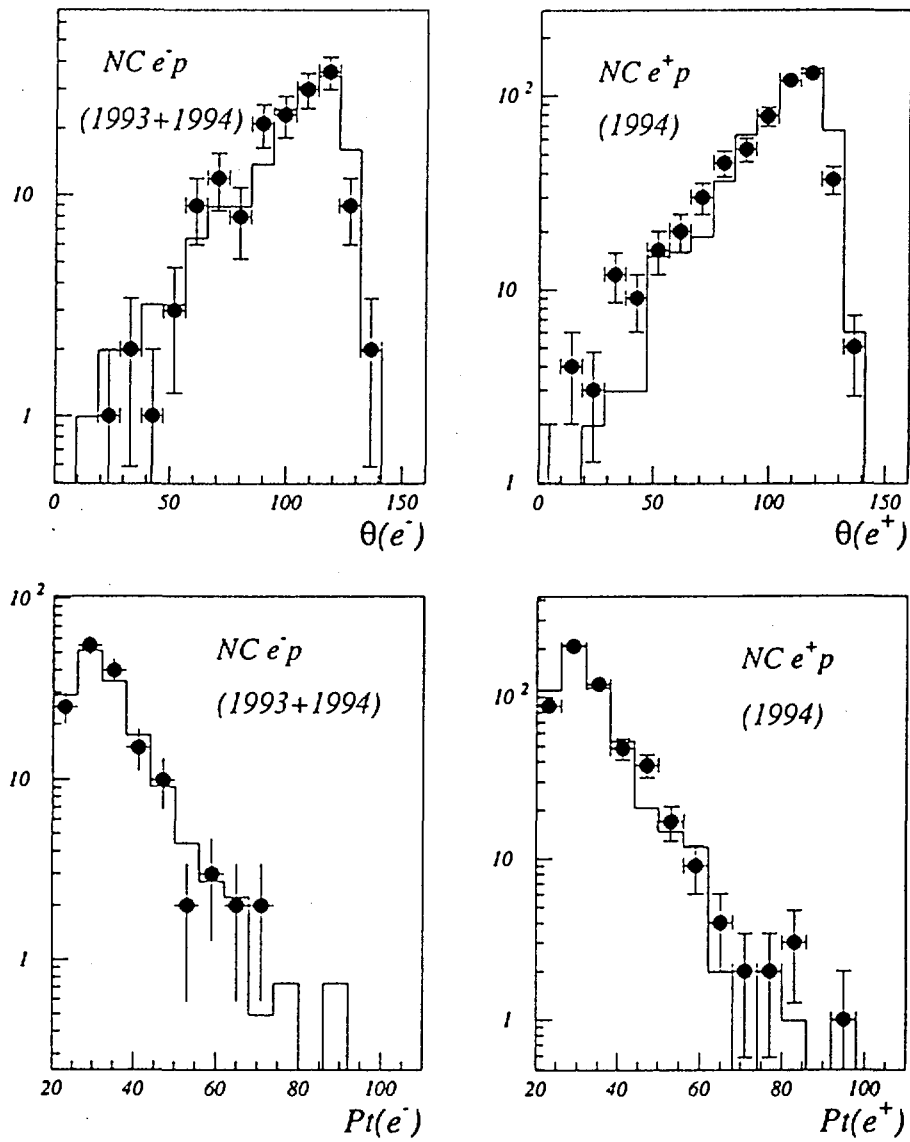


Fig.4.32 The distributions of  $\theta^{el}$  and  $P_t^{el}$  of the final NC sample for 1993 and 1994 data. data

We have compared the CC and NC samples obtained with those selected using different procedures by other groups, and found a good agreement. Our final samples have 1 more CC event in 1993 data, and 1 more CC in 1994  $e^+p$  data than the DESY samples. The reason is the difference in vertex calculation giving a different efficiency. For NC samples, the total number of events is in agreement, while there are some differences in the composition of the final sample. By checking event by event, we found out that more than 90% of events are in common, the different events are due to mainly the  $P_{t,had}$  calculation which depends on the  $z$  position of the interaction vertex. Other reasons are the different efficiencies of the electron finder, the vertex definition and the background filter.

**NEXT PAGE(S)**  
**left BLANK**

## Chapter 5

# Measurements of NC/CC Ratio And CC Integrated Cross Sections

The calculation of the NC/CC Ratio and the CC integrated cross sections are based on the numbers of final selected charged current and neutral current events, for 1993  $e^-p$  data and 1994  $e^\pm p$  data. The  $P_t^{had} > 25$  GeV cut is used in the selection to get an optimum between the sensitivity to electroweak physics and reasonable statistics, also this cut excludes automatically the regions of large Bjorken- $y$  and of small  $x$  which present additional difficulties in theoretical interpretation. The  $P_t^{had}$  is measured directly in the experiment which makes the selection straightforward, and at  $P_t^{had} > 25$  GeV the CC and NC events are clearly separated and the backgrounds in the selection are strongly suppressed.

In this chapter we will calculate the NC/CC ratios and the CC integrated cross sections for 1993  $e^-p$  and 1994  $e^\pm p$  H1 data at HERA. First, the procedures in the calculation are described, then the efficiencies in various selection steps are studied and the numbers of events in the final selected CC and NC samples are corrected. The statistical and systematic uncertainties in the selection and calculation are estimated afterwards. Finally the results of NC/CC ratios and the CC integrated cross sections are given, and their physics implications are investigated.

## 5.1 Measurement of NC/CC Ratio

The NC/CC ratio is interesting for electroweak physics study, since it cancels the systematic uncertainties from the luminosity measurement, and partially suppresses the systematic uncertainty from the absolute energy calibration. The NC and CC events are selected in parallel as described in the previous section. The number of NC and CC events should be corrected for the efficiency and migration effects. The main sources of the error in the ratio come from the poor statistics of the CC events and the systematic effect of energy calibration in NC samples.

### 5.1.1 The NC/CC Ratio Calculation

#### Procedure

The measured number of events  $N_{obs.}$  in a certain kinematic region is affected by several factors: the limited acceptance of the detector response, the resolutions in energy and direction measurements, the selection criteria applied in different steps, and the contamination of background events in the final sample.

Some effects, like wrong absolute energy calibration or misalignment of the detector, generate a systematic shift in the  $P_t^{had}$  calculation and limit the accuracy of the measurement. These effects are not known a priori and the uncertainties will be estimated in the next section. Other effects, such as the acceptance of the detector, the migration of events due to the resolution of momentum measurement, or loss of events due to different cuts, can be corrected by studying the Monte Carlo or real data. The true number of events  $N_{true}$  in a kinematic range can be obtained by applying a correction factor  $\epsilon$  which corrects for these effects:

$$N_{true}(P_t^{had} > 25GeV) = \frac{N_{obs.}(P_{t,obs.}^{had} > 25GeV, \text{ other cuts})}{\epsilon} \quad (5.1)$$

In our selections of CC and NC events, each criteria applied introduces a loss or migration of the events due to detector efficiency or measurement resolution. The  $\epsilon$  in above formula actually includes all these individual correction factors:

$$\varepsilon = \prod_i \varepsilon_i \quad (5.2)$$

the multiplication runs over all the selection procedures and  $\varepsilon_i$  is the efficiency in each step as described in the previous chapter.

The pre-requirements of data runs where the technical cuts are applied do not cause any inefficiency, since the luminosities are corrected according to those requirements. As to the inefficiency due to class 8 requirement in NC selection, we have done NC selection from class 9 in 1993 data and reached the same number of events. The NC selected from data sample of exotic physics group of 1994 data do not give additional events either. Thus we concluded that the efficiency in this step is 100%, i.e.:

$$\varepsilon_{pre.} = \varepsilon_{cls} = 1. \quad (5.3)$$

The loose cosmic and halo muon filter used in the early stage of selection should not cause any loss of good event. This is confirmed by both Monte Carlo and data. The more strict selection cuts applied later to further reject overlapping background (see Chapter 4) cause a small inefficiency, which should be corrected by a factor  $\varepsilon_{filt.}$ . Thus, the correction factor  $\varepsilon$  can be written as:

$$\varepsilon = \varepsilon_{mig.} \cdot \varepsilon_{vtx.} \cdot \varepsilon_{trig.} \cdot \varepsilon_{filt.} \quad (5.4)$$

where  $\varepsilon_{mig.}$  is the correction factor for the migration due to  $P_t^{had} > 25\text{GeV}$  cut, which depends on the energy and direction measurements,  $\varepsilon_{vtx.}$  is the vertex efficiency which compensates the loss due to vertex requirement;  $\varepsilon_{trig.}$  is the efficiency of the CC trigger requirement. For NC event, the efficiency of the electron finder  $\varepsilon_{el.id.}$  is given in Table 4.3, the correction for the inefficiency of electron finder is included in the migration correction factor  $\varepsilon_{mig.}$ , since we should first identify the electron in order to calculate  $P_t^{had}$ .

Once the correction factor is determined, the NC/CC ratio  $R$  for  $p_t^{had} > 25\text{ GeV}$  can be calculated as:

$$R = \frac{\sigma_{NC}}{\sigma_{CC}} = \left( \frac{N_{true}^{NC}}{\mathcal{L}} \right) / \left( \frac{N_{true}^{CC}}{\mathcal{L}} \right)$$

$$= \frac{N_{obs.}^{NC}}{N_{obs.}^{CC}} \times \left( \frac{\varepsilon_{mig.}^{CC} \cdot \varepsilon_{vtx.}^{CC} \cdot \varepsilon_{trig.}^{CC} \cdot \varepsilon_{filt.}^{CC}}{\varepsilon_{mig.}^{NC} \cdot \varepsilon_{vtx.}^{NC} \cdot \varepsilon_{trig.}^{NC} \cdot \varepsilon_{filt.}^{NC}} \right) \quad (5.5)$$

here  $N_{obs.}^{CC}$  and  $N_{obs.}^{NC}$  are the numbers of the CC and NC events selected from the data. The correction factors will be discussed in next sections.

### Correction factors in various selection steps

The correction factors can be calculated from Monte Carlo simulation or from real data. The correction factor  $\varepsilon_{mig.}$  for the migration effect due to  $P_t^{had}$  cut can only be calculated from Monte Carlo, since the true momentum of the particles (generated values) are given there. For other correction factors the data samples can be used. The statistics of the CC and NC events from data is limited by the relatively small cross sections at high  $Q^2$  values, while Monte Carlo can provide a larger number of simulated events which greatly reduce the statistical uncertainties in efficiency calculation. However, sometimes it can not give a very precise simulation of the detector response and of the actual experimental situation, thus using real data to calculate these factors is needed, especially in the calculation of trigger efficiency.

To reduce the statistical uncertainties in correction factor calculation, the "pseudo-CC" (see Chapter 4) event sample are constructed from the NC events in which the electron is removed, and the same selection criteria are applied to the remaining hadronic system. The statistics of these 'pseudo-CC' events are higher than the CC events by a factor of  $\sigma^{NC}(P_t > 25\text{GeV})/\sigma^{CC}(P_t > 25\text{GeV})$ , roughly 7 and 12 times higher for  $e^-p$  and  $e^+p$  interactions respectively. Although the energy deposition pattern and the track information of the hadronic system in the individual "pseudo-CC" event are similar to the CC event, the kinematic distributions of the "pseudo-CC" sample are different from the CC sample in the  $P_t^{had} > 25$  GeV range owing to the different differential cross sections of NC and CC processes. Thus a weighting procedure for the different differential cross sections is needed to get the integrated correction factor for CC in  $P_t^{had} > 25$  GeV range from 'pseudo-CC' (NC) sample. A weighting factor  $\xi_{CC/NC}$  is assigned to each 'pseudo-CC' event which has the kinematic values  $x, Q^2$ :

$$\xi_{CC/NC} = \frac{\sigma_{CC}(x, Q^2)}{\sigma_{NC}(x, Q^2)} \quad (5.6)$$

where  $\sigma_{CC}(x, Q^2)$  and  $\sigma_{NC}(x, Q^2)$  are the differential cross sections at  $(x, Q^2)$  for

CC and NC processes respectively. The uncertainty caused by the assumption in the differential cross sections calculation is small and will be taken as a systematic error.

In our analysis, the migration factor  $\epsilon_{mig.}$  is calculated from the Monte Carlo simulation, the trigger efficiency  $\epsilon_{trig.}$  for CC selection is calculated from the 'pseudo-CC' data sample. The vertex efficiency  $\epsilon_{vtx.}$ , the background filter efficiency  $\epsilon_{filt.}$  and the electron finder efficiency  $\epsilon_{el.id.}$  for NC events are calculated from Monte Carlo simulation, and are verified with data samples. A good agreement between these factors from data and Monte Carlo is found, which indicates that the real detector response is successfully simulated by the Monte Carlo.

The value of the correction factor is affected by the statistical error due to the limited number of events of the Monte Carlo samples and pseudo-CC data samples, and the systematic uncertainties mainly coming from the imperfect knowledge of the energy resolution and absolute calibrations. These effects both from Monte Carlo and from data are checked and compared.

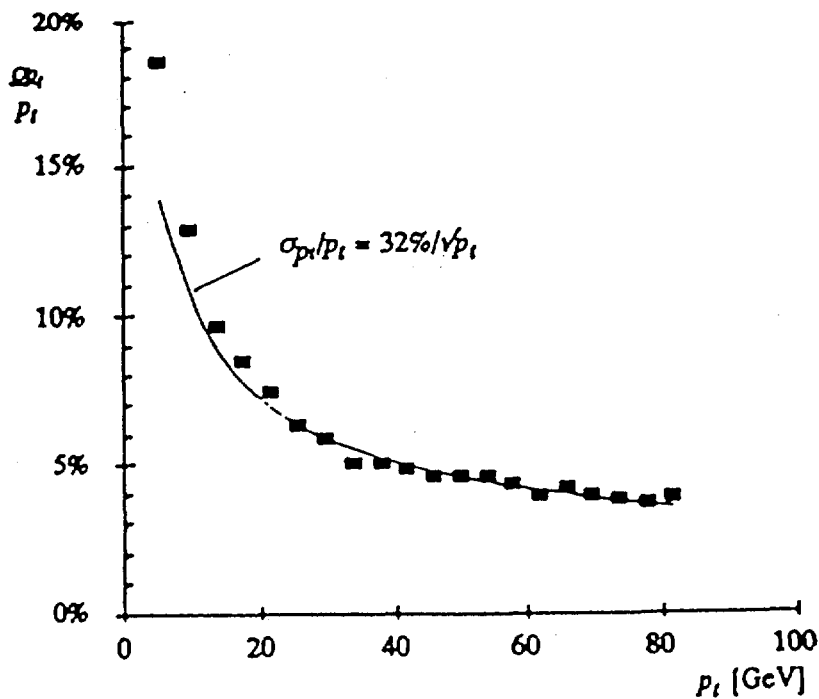


Fig 5.1 The resolution of  $P_t^{had}$  measurement ([25]).

- The  $P_t^{had}$  migration factor

The main migration effect comes from the transverse momentum  $p_t^{had}$  measurement which is dominated by the energy resolution of the LAr calorimeter. The  $p_t^{had}$  resolution has been estimated in [25] where the average polar angle  $\theta$  of the hadronic jets was taken into account, and an approximation of  $\sigma_{p_t^{had}}/p_t^{had}$  was given to be  $32\%/\sqrt{p_t^{had}}$ . Fig.5.1 ([25]) gives the  $p_t^{had}$  resolution with respect to  $p_t^{had}$ , where we see a 7% resolution for  $p_t^{had}$  is obtained at  $p_t^{had} = 25$  GeV, and the resolution becomes smaller when  $p_t^{had}$  increases, and finally reaches about 4% at very high  $p_t^{had}$ .

Theoretically, the total number of the charged current events  $N_{true}^{CC}$  with  $P_t^{had}$  greater than 25 GeV is:

$$N_{true}^{CC}(P_t^{had} > 25\text{GeV}) = \mathcal{L} \int_{P_t^{had} > 25}^{\infty} \frac{d\sigma_{CC}}{dP_t^{had}} dP_t^{had} \quad (5.7)$$

where  $\mathcal{L}$  is the integrated luminosity, and  $\frac{d\sigma_{CC}}{dP_t^{had}}$  is the differential cross section for CC process with respect to  $P_t^{had}$ . The actually measured  $P_t^{had}$  deviates from the true one due to the resolution in  $P_t^{had}$  measurement. Fig 5.2 gives the difference between the measured hadronic transverse momentum and the true one from the  $e^+p$  CC Monte Carlo, where plot (a) shows the difference with respect to the measured value of  $P_t^{had}$ , and plot (b) gives a Gaussian fit to the difference for CC events with  $P_t^{had}$  greater than 25 GeV.

The number of observed CC events with measured  $P_t^{had}$  greater than 25 GeV  $N_{obs.}(P_{t,obs.}^{had} > 25 \text{ GeV})$  depends on the energy resolution of the detector which causes the migration of events across the  $P_t^{had}$  cut, and of the acceptance of the detector which causes the loss of events. These effects are corrected by the correction factor  $\varepsilon_{mig.}$ :

$$\varepsilon_{mig.} = \frac{N_{obs.}(P_{t,obs.}^{had} > 25\text{GeV})}{N_{true}(P_t^{had} > 25)} \quad (5.8)$$

Four Monte Carlo samples, the CC and NC Monte Carlo for  $e^-p$  and  $e^+p$  interactions respectively, are used in the calculation of  $\varepsilon_{mig.}$ . Each of them has 5000 simulated high  $Q^2$  DIS events. The true hadronic  $P_t^{had}$  is the generated value, i.e. the vector sum of the transverse momentum of all generated stable particles except the scattering lepton and the radiative photons. The measured value of  $P_{t,obs.}^{had}$  is calculated from LAr calorimeter cell using formula (4.4), where

the vertex position used in direction determination is only fitted from the tracks of hadronic particles.

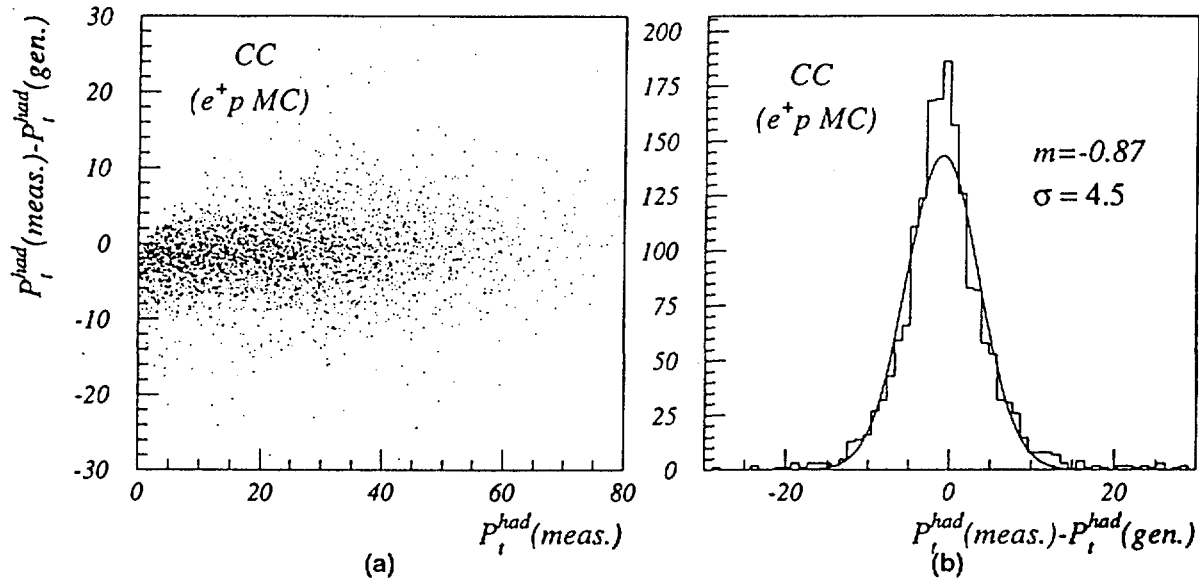


Fig 5.2 (a) The difference between measured and generated  $P_t^{had}$  with respect to the measured  $P_t^{had}$  for CC events; (b) a Gaussian fit to the difference for CC events with  $P_t^{had}$  greater than 25 GeV.

The migration of the events around the  $p_t^{had}$  cut can be seen from Fig 5.3, where the distributions of the measured  $P_t^{had}$  and true  $P_t^{had}$  are given for CC and NC events with a cut at measured  $P_t^{had} > 25$  GeV. The slope of the original  $p_t^{had}$  distribution also affects the amount of migrated events. As shown in the plots, the steeper the distribution around the  $p_t^{had}$  cut, the larger the migration across it. For neutral current process, the cross section for  $Q^2 \ll M_Z^2$  falls off very rapidly with  $1/Q^4$ , thus roughly with  $1/p_t^4$  since  $p_t^2 = Q^2(1-y)$ . On the other hand, the cross section of the charged current process falls with  $1/(1+Q^2/M_W^2)^2$ , therefore the  $p_t^{had}$  distribution is flatter than the neutral current case. As a consequence, more migration effect is observed in NC process.

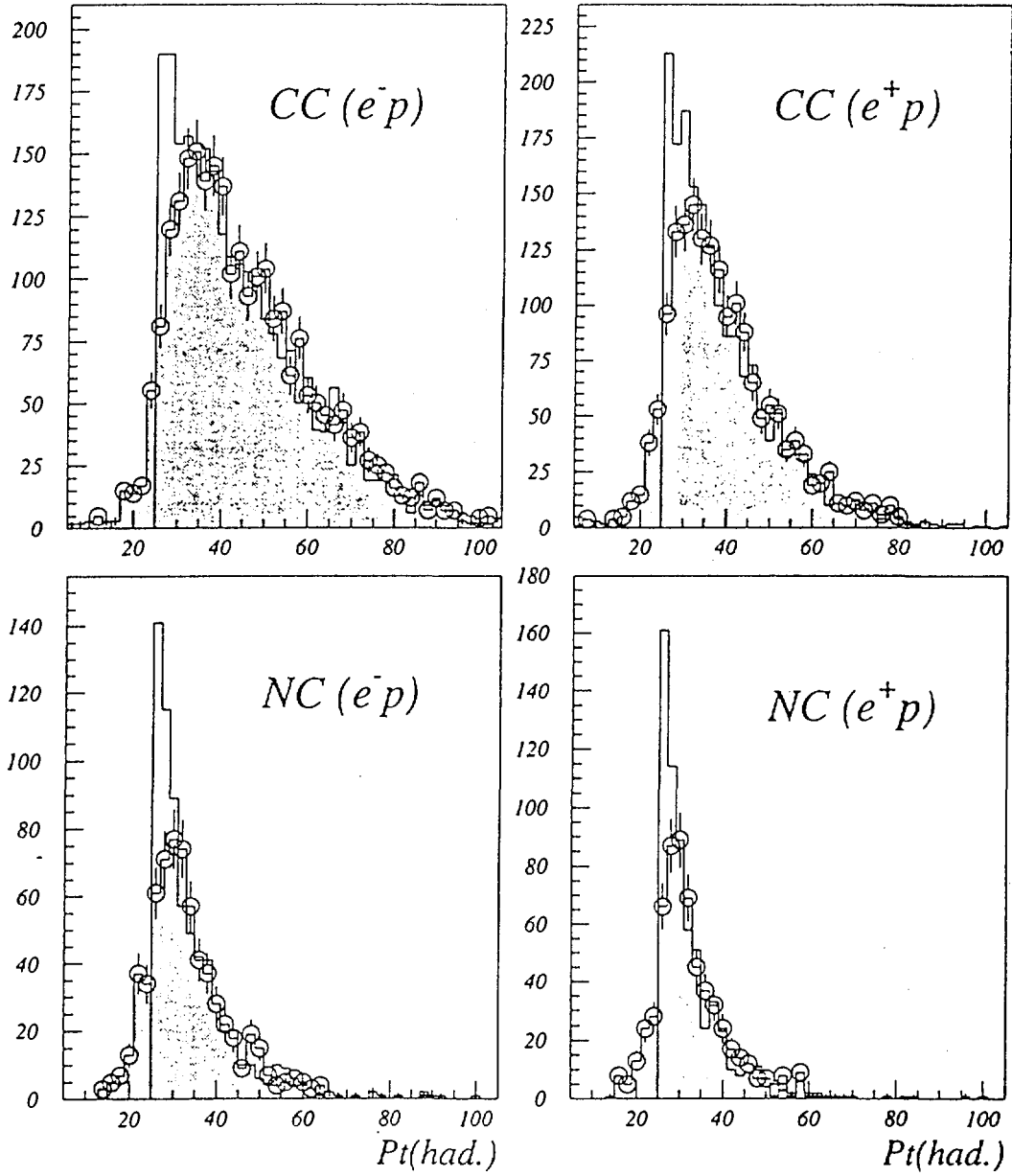


Fig 5.3: The distribution of the  $p_t^{\text{had}}$  for CC and NC events with a cut at measured  $p_t^{\text{had}} > 25$  GeV. The corresponding true  $p_t^{\text{had}}$  are given by the shaded histograms.

Fig.5.4 gives the distribution of the true  $p_t^{had}$  versus the measured  $p_t^{had}$ . Two different flows of events contribute to the migration: a "gain" of events when the measured  $P_t^{had}$  is larger than the true one, and a "loss" of events when the measured  $P_t^{had}$  is smaller than the true one. The resolution in energy and direction measurement contributes to both "gain" and "loss". The limited acceptance of the detector also causes a "loss" of events. The factors of "gain" and "loss" are calculated from the event numbers according to the value of measured and true  $p_t^{had}$ .

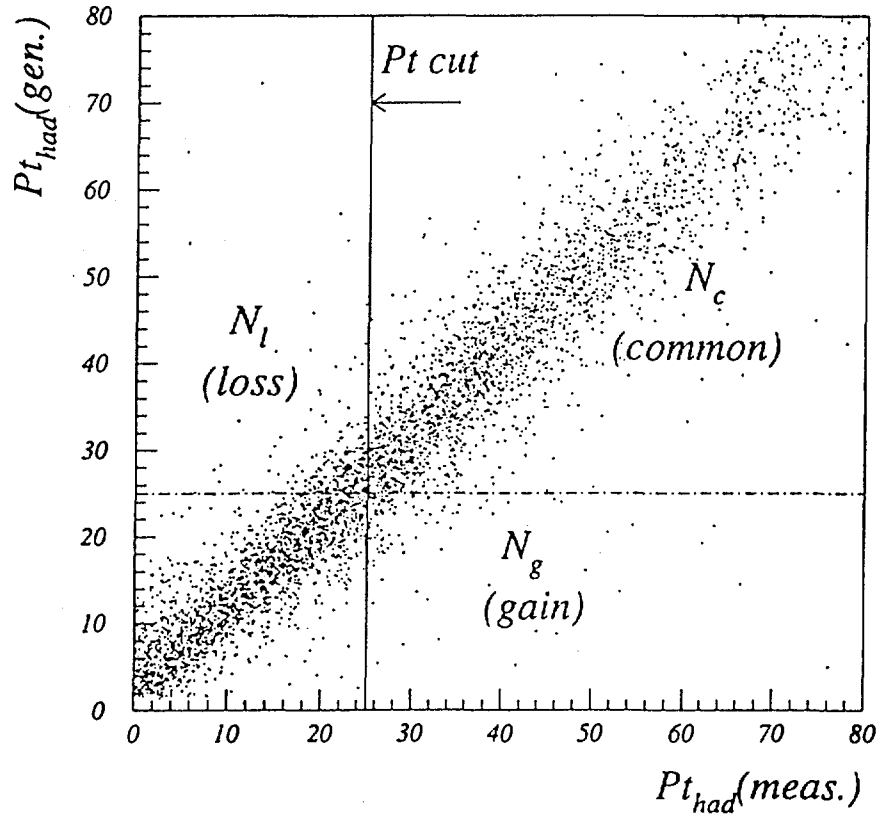


Fig 5.4: The distribution of the true  $p_t^{had}$  versus measured  $p_t^{had}$  and the definition of the events in different  $p_t^{had}$  range.

Using the number of events  $N_g$ (gain),  $N_l$ (loss) and  $N_c$ (common) in different  $P_t^{had}$  ranges as defined in Fig.5.4, we have

$$N(P_{t,true}^{had} > 25) = N_c + N_l; \quad N(P_{t,obs.}^{had} > 25) = N_c + N_g \quad (5.9)$$

$$\eta_{gain} = \frac{N_g}{N(P_{t,true}^{had} > 25)} = \frac{N_g}{N_c + N_l} \quad (5.10)$$

$$\eta_{loss} = \frac{N_l}{N(P_{t,true}^{had} > 25)} = \frac{N_l}{N_c + N_l} \quad (5.11)$$

The smearing correction factor is obtained from formula (5.8), which comprises the migration effect caused by the inaccuracy of the energy reconstruction and the acceptance effect caused by the detector inefficiency:

$$\varepsilon_{mig.} = \frac{N(P_{t,obs.} > 25)}{N(P_{t,true}^{had} > 25)} = \frac{N_c + N_g}{N_c + N_l} \quad (5.12)$$

From these definitions, we have:

$$\varepsilon_{mig.} + \eta_{loss} - \eta_{gain} = \frac{(N_c + N_g) + N_l - N_g}{N_c + N_l} = 1 \quad (5.13)$$

To estimate the statistical error, it should be noted that there are three independent event samples entering the  $\varepsilon_{mig.}$  calculation, namely, the  $N_l$  lost events, the  $N_g$  gained events, and  $N_c$  common events which have both  $P_{true}^{had}$  and  $P_{t,obs.}^{had} > 25$  GeV. Assuming the errors in these samples are  $\Delta N_l$ ,  $\Delta N_g$  and  $\Delta N_c$  respectively, the statistical error of  $\varepsilon_{mig.}$  is given by:

$$(\Delta\varepsilon_{mig.})_{sta}^2 = \left(\frac{\partial\varepsilon_{mig.}}{\partial N_l}\right)^2(\Delta N_l)^2 + \left(\frac{\partial\varepsilon_{mig.}}{\partial N_g}\right)^2(\Delta N_g)^2 + \left(\frac{\partial\varepsilon_{mig.}}{\partial N_c}\right)^2(\Delta N_c)^2 \quad (5.14)$$

By a simple derivation we get,

$$(\Delta\varepsilon_{mig.})_{sta} = \frac{1}{N_c + N_l} \sqrt{\left(\frac{N_l - N_g}{N_c + N_l}\right)^2 \cdot N_c + \left(\frac{N_c + N_g}{N_c + N_l}\right)^2 \cdot N_l + N_g} \quad (5.15)$$

here we assume that the statistical error for a sample with  $N$  selected events is  $\sqrt{N}$ . The estimated statistical errors  $\Delta\varepsilon_{mig.}^{sta}$  for the four Monte Carlo samples are in the magnitude of 1 to 2 %.

The values of the ‘‘gain’’, ‘‘loss’’ and migration factor  $\varepsilon_{mig.}$  calculated from the four Monte Carlo samples are summarized in table 5.1, together with their statistical uncertainties.

Table 5.1 The migration factors:

Monte Carlo	$e^-p$ interaction		$e^+p$ interaction	
	CC	NC	CC	NC
$\eta_{gain}$	0.046	0.126	0.071	0.104
$\eta_{loss}$	0.086	0.259	0.129	0.283
$\epsilon_{mig.}$	$0.960 \pm 0.007$	$0.853 \pm 0.021$	$0.942 \pm 0.010$	$0.799 \pm 0.021$

For CC or NC processes, there are some difference between the correction factors for  $e^-p$  and  $e^+p$  interactions, which mainly come from the different  $p_t^{had}$ -dependences of the cross section for  $e^-p$  and  $e^+p$  processes, as shown in Fig.5.3.

- Vertex efficiency

The vertex criteria requires that there exist a vertex reconstructed from CJC or FTD tracks within  $\pm 35$  cm from the nominal interaction point along the beam line. Two reasons cause the inefficiency of the vertex: the event has no “good” track because of the final hadronic jets emitted near the beam pipe outside the acceptance range of the tracker or some tracker parts is temporarily dead, or the event has reconstructed vertex outside the  $\pm 35$  cm range because of the uncertainties in track fitting and vertex calculation, or the  $e^\pm p$  interaction has actually happened outside the  $\pm 35$  cm range.

For the CC event which has the final state jets emitted in the barrel region well covered by CJC, the vertex can always be constructed from the tracks left by hadrons in the drift chambers. However, about 10% of CC events in the  $P_t^{had} > 25$  GeV region have very forward jets and don't leave any “good” track in the CJC. Most of these CC events are in low  $Q^2$  and small  $y$  region. The vertex can only be constructed from the tracks in the forward tracker in this case. Compared with the central vertex, the precision of forward vertex deteriorates due the large uncertainties in track fitting in FTD as explained in Chapter 2. The probability of the calculated vertex situated outside the  $\pm 35$  cm range is larger in FTD comparing to CJC.

For NC events the vertex is also reconstructed from the hadronic tracks. In the same  $P_t^{had} > 25$  GeV range, the final hadronic system of NC event are more boosted in forward direction than in CC case, which can be seen in Fig 4.25. This implies that more NC events have vertex (without electron tracks) only from forward tracks than CC events. Fig 5.5 gives the precision of hadronic vertex in CJC and FTD from  $e^-p$  NC Monte Carlo, where the distributions of the differences between reconstructed vertex and simulated vertex (true vertex)

are given. Plot (a) shows the difference for vertex from CJC or from both CJC and FTD, which is more precise than vertex only from FTD (plot (b)).

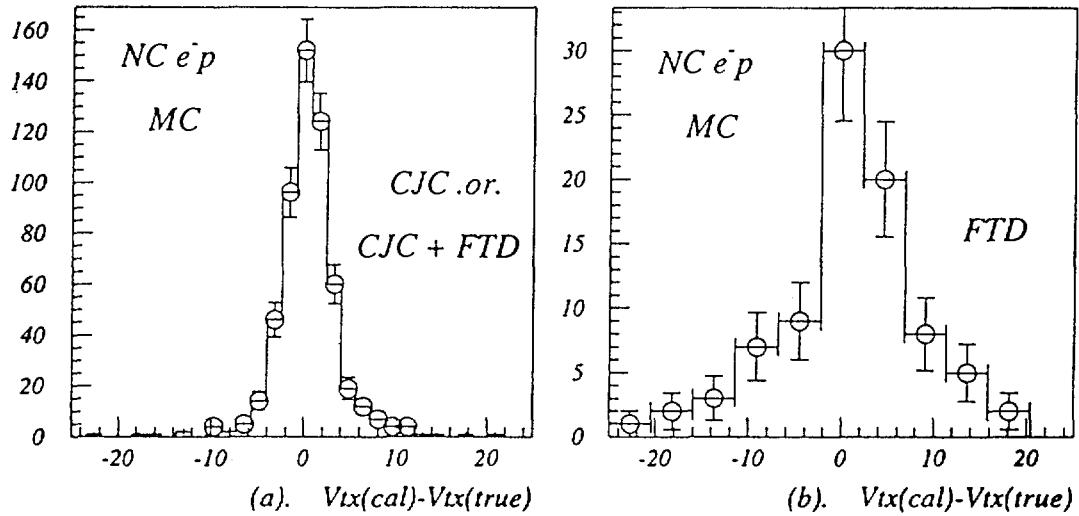


Fig 5.5 The distributions of the differences between reconstructed vertex and simulated vertex (true vertex). (a). vertex from CJC or from both CJC and FTD, (b). vertex only from FTD.

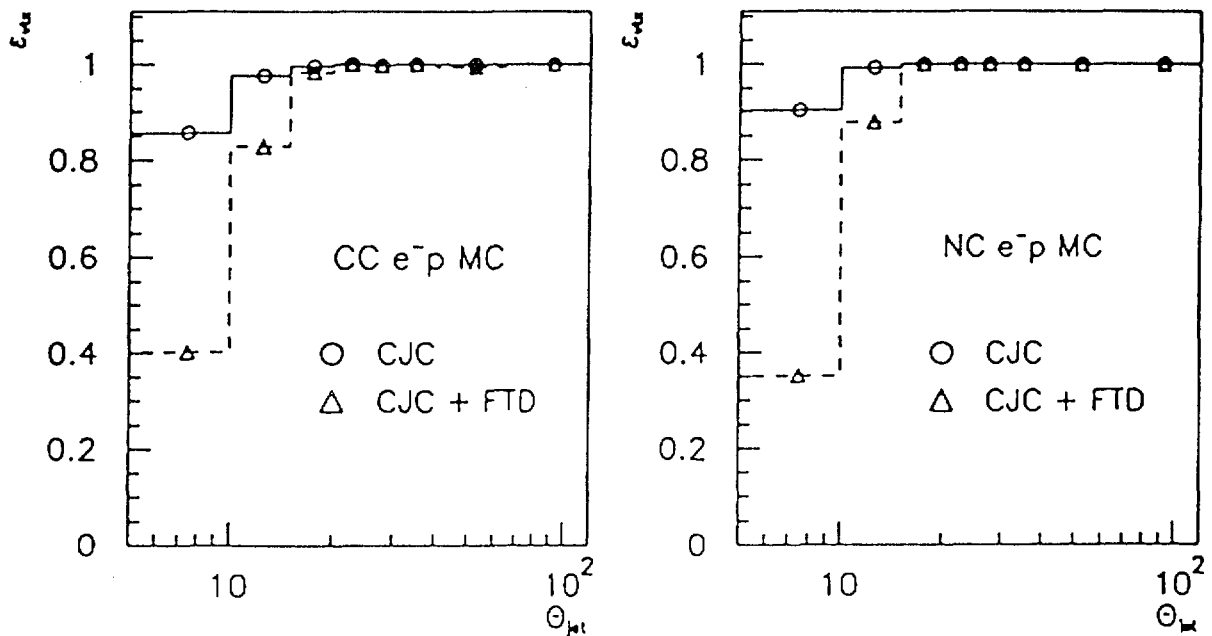


Fig 5.6 The vertex efficiency for (a) CC and (b) NC as a function of the polar angle of the final hadronic jets, for CJC only or for both CJC and FTD.

The vertex efficiency can be calculated from

$$\epsilon_{vtx.} = \frac{N(z_{vtx.} < 35cm)}{N(all)} \quad (5.16)$$

Fig 5.6 shows the vertex efficiency as a function of the polar angle of the final hadronic jets, for CJC only or for both CJC and FTD. We see that the vertex efficiency is always near 1 at large jet angle, while decreases at small jet angles. The loss in very forward angle is mostly compensated when FTD tracks are included in vertex calculation.

Fig 5.7 shows the comparison of the hadronic vertex efficiency of the 1994  $e^+p$  NC data and NC Monte Carlo using CJC and CJC+FTD tracks respectively. The vertex efficiency is about 100% for NC events if the electron tracks are included in the vertex calculation in  $P_t^{had} > 25$  GeV range. For data the vertex efficiency is calculated by comparing the number of events with vertex from hadronic tracks and the the number of events with vertex from all tracks. We see a good agreement between the data and Monte Carlo.

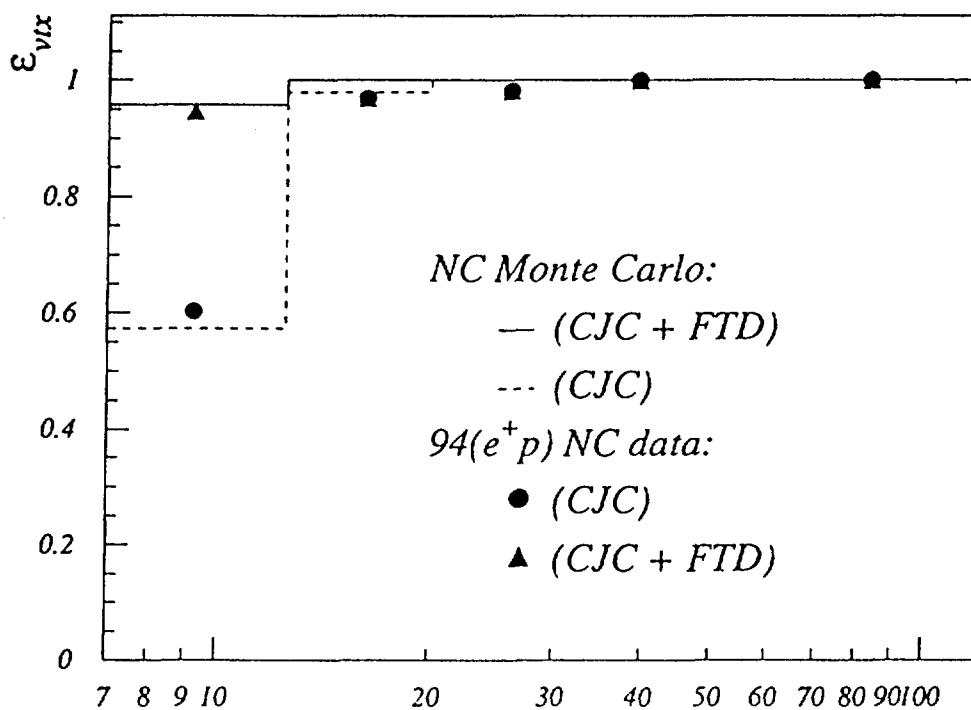


Fig 5.7 The comparison of the vertex efficiency as a function of  $\theta_{jet}^{had}$  between 1994  $e^+p$  NC data and NC Monte Carlo, for CJC and CJC+FTD respectively.

The overall vertex efficiency for  $P_t^{had} > 25$  GeV is listed in table 5.2, together with their statistical uncertainties. As a comparison, the efficiencies for vertex only from CJC tracks are also given in the table.

Table 5.2 The vertex efficiency:

Monte Carlo	$e^-p$ interaction		$e^+p$ interaction	
	CC	NC	CC	NC
$\varepsilon_{vtx.}(CJC)$	$0.910 \pm 0.006$	$0.827 \pm 0.015$	$0.918 \pm 0.007$	$0.825 \pm 0.002$
$\varepsilon_{vtx.}(CJC + FTD)$	$0.984 \pm 0.003$	$0.965 \pm 0.007$	$0.990 \pm 0.002$	$0.970 \pm 0.007$

- Trigger efficiency

The efficiency for CC trigger is calculated from the “pseudo-CC” (NC) data in order to avoid the Monte Carlo dependence in the simulation of the trigger response. The statistics of the NC final sample in 1993  $e^-p$  and 1994  $e^\pm p$  data made it feasible to get a reliable results. Firstly the tracks and energies from an identified electron are removed from the two trigger elements of the CC trigger: the “ $Z_{vtx}-t_0$ ” and “ $E_{t-miss}$ ” trigger. Then the trigger conditions are simulated for the “Pseudo-CC” events. In the trigger efficiency calculation, we use a reference sample which was selected from the “Pseudo-CC” sample requiring the “LAr – electron – 1” trigger fired. This trigger, which requires that the energy deposited in the electromagnetic part of a Big-Tower of LAr is above some threshold and the energy in the hadronic part is below a threshold, is very efficient for high  $Q^2$  NC event. Suppose  $N_0$  is the number of the “Pseudo-CC” events in the reference sample before the CC trigger requirement, and  $N_t$  is the number of “Pseudo-CC” events having CC trigger fired, then the trigger efficiency is:

$$\varepsilon_{trig.}^0 = \frac{N_t}{N_0} \quad (5.17)$$

However  $\varepsilon_{trig.}^0$  is not the CC trigger efficiency since the kinematic distributions of CC and Pseudo-CC (NC) are different. The CC trigger efficiency can be obtained by a weighting according to this difference. Denoting the differential cross section in terms of  $x, Q^2$ :

$$\sigma^{NC}(x, Q^2) = \frac{d^2\sigma_{NC}(x, Q^2)}{dx dq^2}, \quad \sigma^{CC}(x, Q^2) = \frac{d^2\sigma_{CC}(x, Q^2)}{dx dq^2} \quad (5.18)$$

For a CC event at  $x, Q^2$ , one may assume the trigger efficiency to be  $\epsilon^{CC}(x, Q^2)$ , then the integrated efficiency  $\epsilon_{trig.}$  for CC events cut at  $P_t > 25$  GeV is:

$$\epsilon^{CC} = \frac{\int_{P_t > 25}^{\infty} \int \int \epsilon^{CC}(x, Q^2) \sigma^{CC}(x, Q^2) \delta(P_t - \sqrt{sxy(1-y)}) dx dQ^2 dP_t}{\int_{P_t > 25}^{\infty} \int \int \sigma^{CC}(x, Q^2) \delta(P_t - \sqrt{sxy(1-y)}) dx dQ^2 dP_t} \quad (5.19)$$

here we exploit the relation between  $P_t$  and  $Q^2, x, y$  as indicated in formula (2.29) ( $P_t^2 = Q^2(1-y) = sxy(1-y)$ ), and use  $\delta$  function  $\delta(P_t - \sqrt{sxy(1-y)})$  to represent the correspondence between  $x, y$  and  $P_t$  in order to convert the integration in terms of  $P_t$ . It can also be written as:

$$\epsilon^{CC} = \frac{\int_{P_t > 25}^{\infty} \int \int \epsilon^{CC}(x, Q^2) \rho_{NC}^{CC}(x, Q^2) \sigma^{NC}(x, Q^2) \delta(P_t - \sqrt{sxy(1-y)}) dx dQ^2 dP_t}{\int_{P_t > 25}^{\infty} \int \int \rho_{NC}^{CC}(x, Q^2) \sigma^{NC}(x, Q^2) \delta(P_t - \sqrt{sxy(1-y)}) dx dQ^2 dP_t} \quad (5.20)$$

where

$$\rho_{NC}^{CC}(x, Q^2) = \frac{\sigma^{CC}(x, Q^2)}{\sigma^{NC}(x, Q^2)} \quad (5.21)$$

For an individual Pseudo-CC event,  $\epsilon^{CC}(x, Q^2)$  either equals 0 (CC trigger not fired) or equals 1 (CC trigger fired). The above integration can be converted into the summations over all Pseudo-CC events:

$$\epsilon^{CC} = \frac{\sum_{i, trig.} \rho_{NC}^{CC}(x, Q^2)}{\sum_i \rho_{NC}^{CC}(x, Q^2)} = \epsilon_{trig.} \quad (5.22)$$

where the summation in numerator runs over only the Pseudo-CC events which have CC trigger fired. The kinematic variables  $x, Q^2$  for an individual Pseudo-CC event can be calculated using scattered electron energy and polar angle, or using Jacquet-Blondel method (see Chapter 6). The differential cross section  $\sigma^{CC}(x, Q^2)$  and  $\sigma^{NC}(x, Q^2)$  are calculated using the package HERACLES [20].

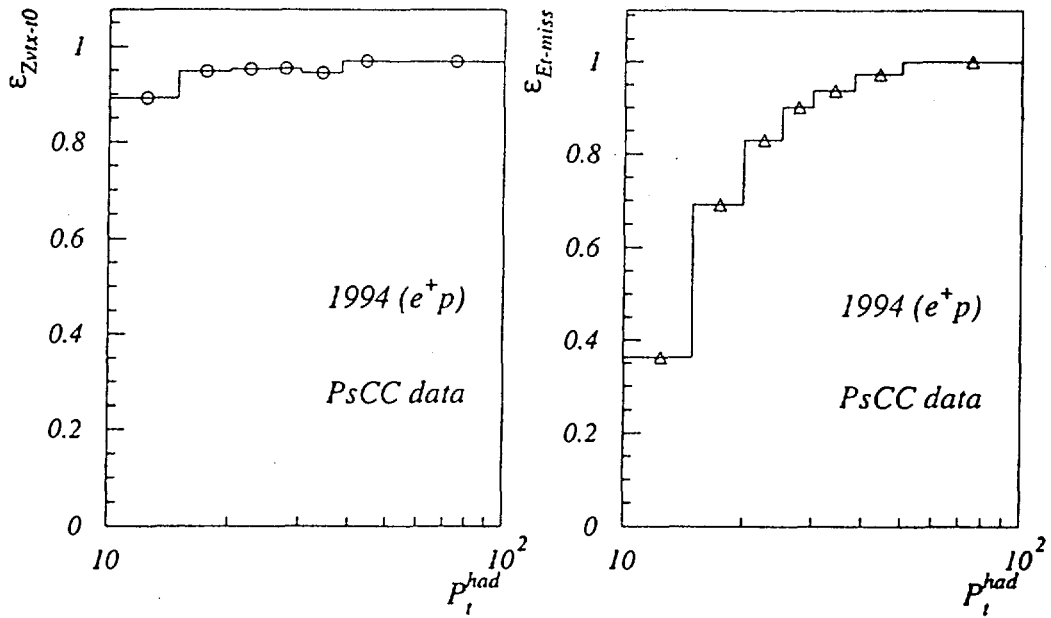


Fig 5.8 The efficiency for trigger element  $Z_{vtx} - t_0$  and  $E_{t-miss}$  as a function of the  $P_t^{had}$  of the Pseudo-CC events.

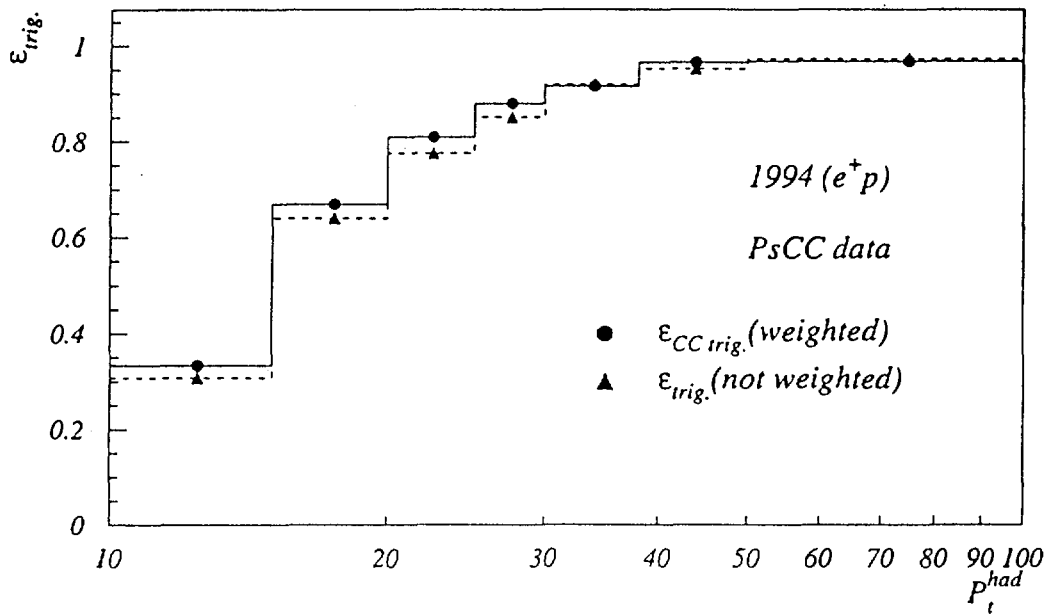


Fig 5.9 The CC trigger efficiency as a function of  $P_t^{had}$  for 1994  $e^+p$  Pseudo-CC data, with or without weighting.

Fig 5.8 shows the trigger efficiency as a function of  $P_t^{had}$  for “ $Z_{vtx} - t_0$ ” and “ $E_{t-miss}$ ” trigger element (see Chapter 4) respectively. We see that there is no obvious dependence of “ $Z_{vtx} - t_0$ ” trigger on  $P_t^{had}$ , while the “ $E_{t-miss}$ ” strongly depends on it. Fig 5.9 gives the efficiency of CC trigger, which is a combination of the above two trigger elements, as a function of  $P_t^{had}$  from 1994  $e^+p$  Pseudo-CC data. As a comparison, the efficiency before the weighting is also shown in the plot.

The CC trigger efficiency for 1993 and 1994  $e^\pm p$  data calculated from Pseudo-CC sample are summarized in Table 5.3. The efficiencies for CC and NC are from the same Pseudo-CC samples, but using formulae (5.19) and (5.17) respectively. We see that the weighting causes the increase of the efficiency as expected, since the hadronic system of NC events is boosted in more forward region where the CC trigger is less efficient than in the barrel region. The trigger efficiency for  $e^-p$  runs is more efficient than for  $e^+p$  runs.

Table 5.3 The CC trigger efficiencies from Pseudo-CC data:

Data sample	$\epsilon_{trig.}$	
	CC	PsCC
1993 $e^-p$	$0.934 \pm 0.028$	$0.932 \pm 0.028$
1994 $e^-p$	$0.957 \pm 0.029$	$0.904 \pm 0.029$
1994 $e^+p$	$0.920 \pm 0.014$	$0.886 \pm 0.014$

- Correction for loss due to the background filter

A small loss of events due to the background rejection cuts is found using NC and CC Monte Carlo, the results are listed in Table 5.4, together with their statistical uncertainties:

Table 5.4 The efficiency for selection cuts:

Monte Carlo	$e^-p$ interaction		$e^+p$ interaction	
	CC	NC	CC	NC
$\epsilon_{filt.}$	$0.981 \pm 0.003$	$0.995 \pm 0.003$	$0.973 \pm 0.004$	$0.990 \pm 0.004$

These results are in good agreement with the NC data. The statistics of CC sample is limited and no loss due to the selection cuts is found in CC data, which is also in agreement with the above values within statistical uncertainty.

### Results of NC/CC ratio

The following table summarizes the observed event numbers of six data samples, and the values of various correction factors. Here only statistical errors are indicated.

Table 5.5 CC and NC Event numbers and correction factors (in %):

Data sample	1993 $e^-$		1994 $e^-$		1994 $e^+$	
	CC	NC	CC	NC	CC	NC
$N_{obs.}$	13. $\pm$ 3.6	81. $\pm$ 9.	13. $\pm$ 3.6	76. $\pm$ 8.7	48 $\pm$ 6.9	530 $\pm$ 23.
$\epsilon_{mig.}$	96.0 $\pm$ 0.7	85.3 $\pm$ 2.1	96.0 $\pm$ 0.7	85.3 $\pm$ 2.1	94.2 $\pm$ 1.0	79.9 $\pm$ 2.1
$\epsilon_{vtx.}$	98.4 $\pm$ 0.3	96.5 $\pm$ 0.7	98.4 $\pm$ 0.3	96.5 $\pm$ 0.7	99.0 $\pm$ 0.2	97.0 $\pm$ 0.7
$\epsilon_{trig.}$	93.4 $\pm$ 2.8	93.2 $\pm$ 2.8	95.7 $\pm$ 2.9	90.4 $\pm$ 2.9	92.0 $\pm$ 1.4	88.6 $\pm$ 1.4
$\epsilon_{filt.}$	98.1 $\pm$ 0.3	99.5 $\pm$ 0.3	98.1 $\pm$ 0.3	99.5 $\pm$ 0.3	97.3 $\pm$ 0.4	99.0 $\pm$ 0.4
$\epsilon_{tot.}$	86.6 $\pm$ 2.7	76.3 $\pm$ 3.0	88.7 $\pm$ 2.8	74.0 $\pm$ 3.0	83.5 $\pm$ 1.6	68.0 $\pm$ 2.1

From the Table 5.5, we see that the overall factor  $\epsilon_{tot.}$  is smaller for the NC sample compared to the CC samples, which leading to a larger correction. This is due to the fact that for NC samples, the  $P_t^{had}$  distributions are steeper than for the CC samples which cause the  $\epsilon_{mig.}$  to be smaller, and the hadronic system in NC samples are boosted more forward which leads to a smaller trigger efficiency.

From the equation (5.4), the NC/CC ratios can be calculated for different data samples. The results for 1993  $e^-p$  data and 1994  $e^\pm p$  data are given in the following:

Data sample:	NC/CC ratio:
1993 $e^-p$	7.1 $\pm$ 2.1
1994 $e^-p$	7.0 $\pm$ 2.1
1994 $e^+p$	13.6 $\pm$ 2.0

The errors in the NC/CC ratios are the statistical only. The systematic uncertainties of the ratio measurements and the comparison with theory will be discussed in the next sections.

### 5.1.2 Systematic Effect In Ratio Measurement

In our analysis, the main source of the systematic effects comes from the  $p_t^{had}$  measurement, which in turn comes from the uncertainty in the hadronic energy calibration. Other sources of the systematic uncertainties are due to the imperfect Monte Carlo simulation and the limited statistics of the Monte Carlo used for the correction factor calculation, and the background contamination in the final data samples.

#### Systematic errors in $p_t^{had}$ measurement

The systematic shift in  $p_t^{had}$  measurement, which mainly comes from the absolute hadronic energy calibration, will cause the migration of events in or out of the  $p_t^{had} > 25$  GeV cut, as shown in Fig 5.10 for CC and NC events respectively. By doing a ratio of NC/CC, the systematic effect from the energy calibration is diminished than in the NC case, and only affected by the difference between the differential cross section distribution of NC and CC processes.

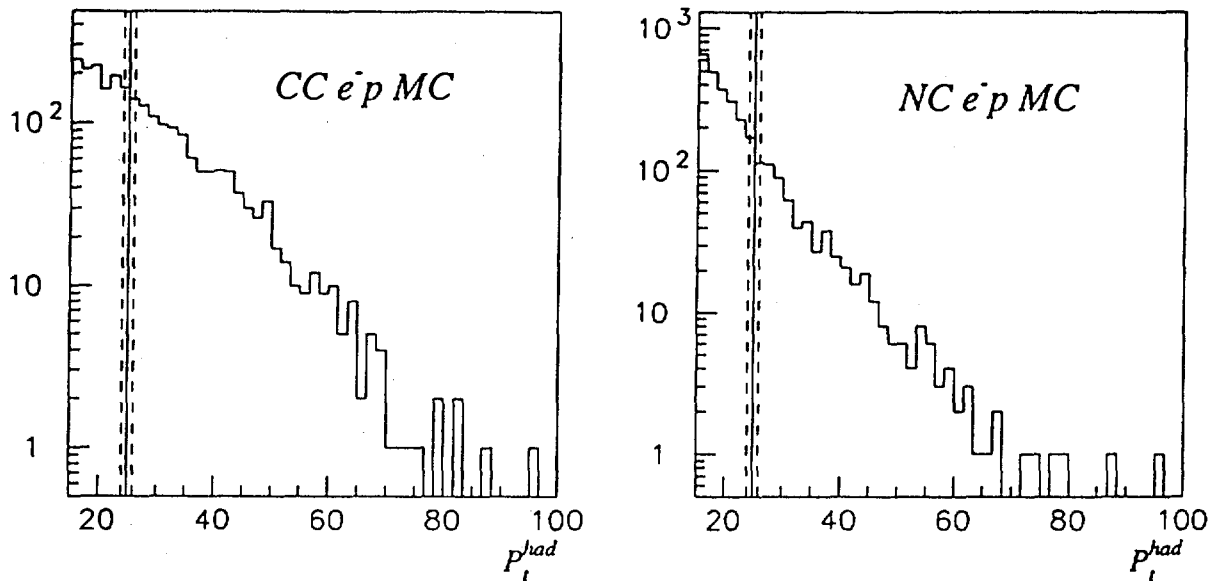


Fig 5.10 The migration of events due to the systematic uncertainty in  $p_t^{had}$  measurement. Solid line is the 25 GeV cut, dashed lines are  $\pm 4\%$  shift around the cut.

In Chapter 4, we have done several different checks to estimate the systematic effect of  $p_t^{had}$  measurement. As we have described before, the results from the study of  $p_t^{had}$  calculated using three different methods (from LAr cells, from clusters and from electron) show that: using LAr cells only to calculate  $P_t^{had}$  didn't bring any additional systematic shift, and the effect is correctly simulated by the Monte Carlo.

The value of  $p_t^{had}$  is also affected by the measurement of the direction of the jets, which in turn depends on the geometrical position of the calorimeter cells and the interaction vertex. Thus the precision in the alignment of the detector parts and the vertex calculation also affects the ratio measurement. This systematic effect is also studied by comparing the event migration using different type of vertices: from multiple vertex  $\chi^2$  fit (official vertex) or from the weighting of good tracks using maximum likelihood (used in our analysis). For NC events the migration using vertex fitted from all tracks or only from hadronic tracks are compared. The systematic effect from direction measurement is found to be minor compared with the effect from the energy calibration.

- Systematic effect from hadronic energy scale

It was foreseen that the H1 LAr calorimeter will provide the absolute energy calibration for electrons at the precision of  $\sim 1\%$ , and for hadrons at the precision of  $\sim 2\%$  [31]. At present, the hadronic energy scale is known at 4% [56]. This may cause a significant shift in the cross section calculation due to the migration of events above  $p_t^{had}$  cut, and also affect the ratio calculation.

We have calculated the corresponding migration of the event numbers in the NC and CC samples with  $P_t^{had} > 25$  GeV cut after the hadronic energy scale shifted by  $\pm 1\%$ ,  $\pm 2\%$ ,  $\pm 3\%$ , and  $\pm 4\%$  respectively. The results are shown in Fig.5.11.

We can see that the NC samples are affected much more severely by the hadronic energy scale than the CC samples, and this effect is not symmetric in  $+/-$  directions around the  $P_t^{had}$  cut. For  $\pm 4\%$  of hadronic energy scale shift, up to 15.8% of change in the event number of NC sample can be observed, while for CC events of corresponding event migration can reach 5%. Also the  $e^-p$  interaction is affected by the hadronic energy scale slightly more than  $e^+p$  interaction, which comes from the different  $P_t^{had}$  distributions of the  $e^-p$  and  $e^+p$  interactions. The same observations can be made for the data samples.

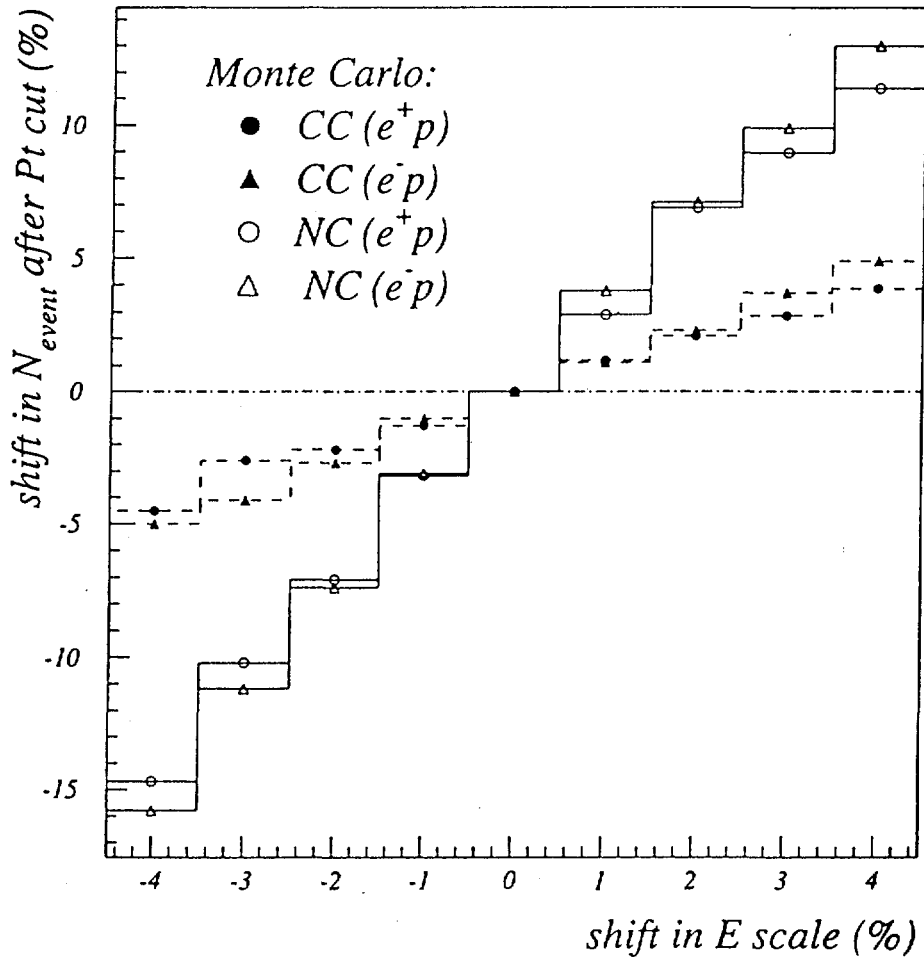


Fig 5.11 The percentage of the migration of the NC and CC event numbers corresponding to the percentage of the hadronic energy scale shift.

- Error estimation in  $p_t^{had}$  from vertex definition

$p_t^{had}$  is calculated from both energy and the direction of the jets, which is determined by the geometrical position of the fired calorimeter cell and the interaction point of the event. The effect of the reconstructed vertex position on the  $p_t^{had}$  calculation can be seen from Fig.5.12, where the precision of the measured  $p_t^{had}$  described by the ratio  $(p_t^{had})_{measure}/(p_t^{had})_{true}$  is plotted versus the precision of the reconstructed vertex which is represented by the difference between the reconstructed and the true vertex position.

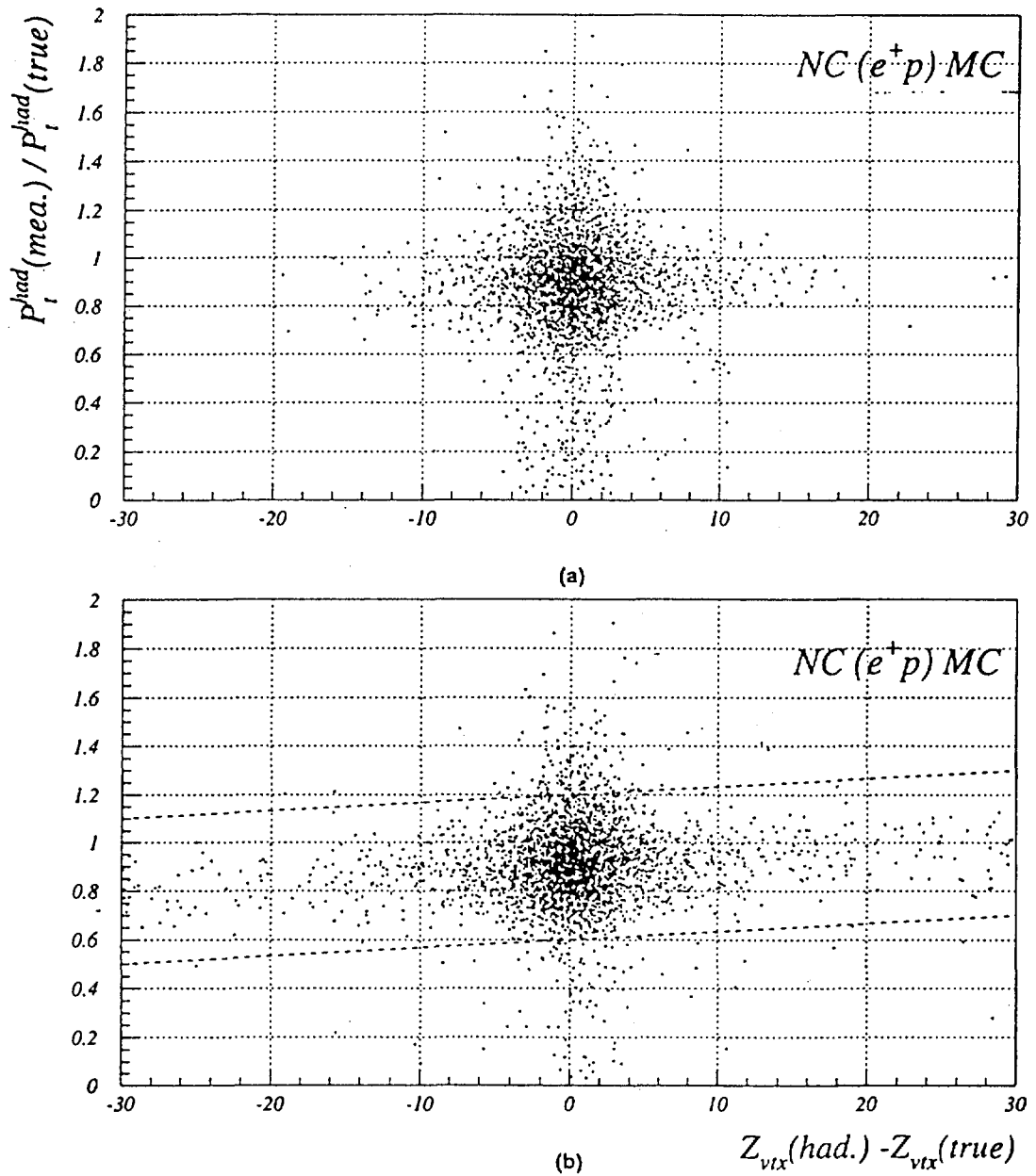


Fig 5.12 The precision of the  $p_t^{had}$  calculation  $(p_t^{had})_{measure}/(p_t^{had})_{true}$  with respect to the precision of the vertex calculation (the difference between the calculated vertex and the true vertex). (a) Using vertex from all tracks, (b) only from hadronic tracks.

In Fig.5.12, the  $e^+p$  NC Monte Carlo is used. We have two kind of vertices: the vertex fitted from all good tracks and the vertex fitted only from the hadronic tracks. The precision of the former is always better since the well measured electron tracks are included in vertex determination. From Fig.5.12 we see that the vertex in plot (b) (only hadronic tracks are used) are more dispersed than in plot (a), the corresponding  $p_t^{had}$  ratios are distributed in an inclined area between the two dashed lines in plot (b), while in plot(a) they are more concentrated. This can be understood that, in the region of the plot (b) where  $(Z_{vtx}(had.) - Z_{vtx}(true)) > 0$ , the reconstructed  $z$ -vertex position ( $Z_{vtx}(had.)$ ) is larger than the true  $z$ -vertex position ( $Z_{vtx}(true)$ ), which means that the reconstructed vertex is shifted to the proton beam direction. Since most of the outgoing hadronic particles are in the forward direction, this in turn causes the calculated polar angle of the hadrons  $\theta_{had}$  to be larger than the true one, thus the calculated  $p_t^{had}$  shift to the larger side ( $p_t^{had} = E^{had} \times \sin\theta_{had}$ ), and the ratio  $(p_t^{had})_{measure}/(p_t^{had})_{true}$  shifts to larger than 1 region in plot (b). The reverse effect can be seen in the left region of the plot (b), where the reconstructed  $z$ -vertex has position lower than the true position.

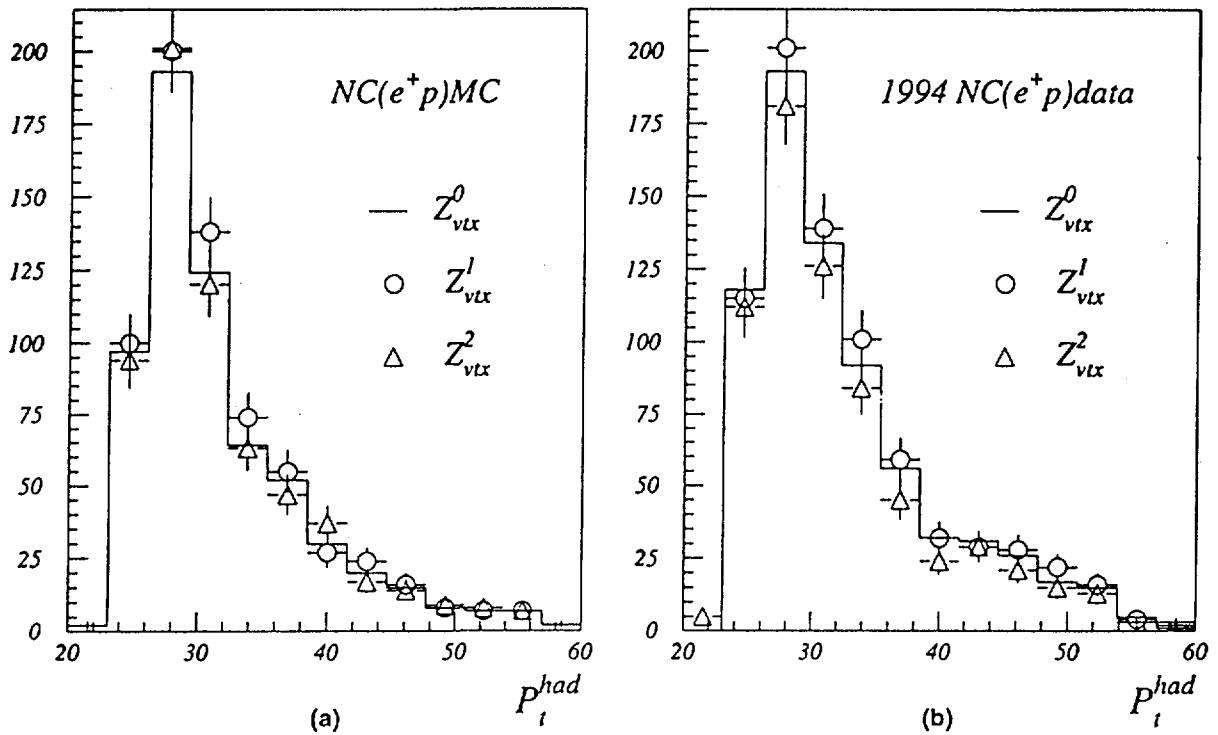


Fig 5.13 The distribution of  $p_t^{had}$  using three methods of the vertex calculation:  $Z_{vtx}^0$  is the weighted vertex including all tracks,  $Z_{vtx}^1$  is the weighted vertex using only hadronic tracks,  $Z_{vtx}^2$  is from multiple vertex  $\chi^2$  fitting. (a) 1994  $e^+p$  data,

(b) Monte Carlo. Cut at  $p_t^{had}$  (from  $Z_{vtx}(1)$ )  $> 25$  GeV.

The distribution of  $p_t^{had}$  calculated using different vertices for NC events are shown in Fig.5.13, for Monte Carlo and 1994  $e^+p$  data respectively. Here three reconstructed vertices are used:  $Z_{vtx}^0$  is the weighted vertex using all tracks,  $Z_{vtx}^1$  is the weighted vertex using only hadronic tracks,  $Z_{vtx}^2$  is from multiple vertex  $\chi^2$  fitting. A cut at  $p_t^{had}$  (calculated using  $Z_{vtx}^1 > 25$  GeV) is applied in these plots.

The distribution of the ratio  $(p_t^{had}(Z_{vtx}(0))/p_t^{had}(Z_{vtx}(1)))$  and  $(p_t^{had}(Z_{vtx}(2))/p_t^{had}(Z_{vtx}(1)))$  are shown in Fig.5.14. Compared with the difference between  $p_t^{had}$  calculated using different energy summation approach, these differences are much smaller. All of these ratios are well centered at 1, for both data and Monte Carlo, and we see that the distributions in data are slightly more dispersed than in the Monte Carlo.

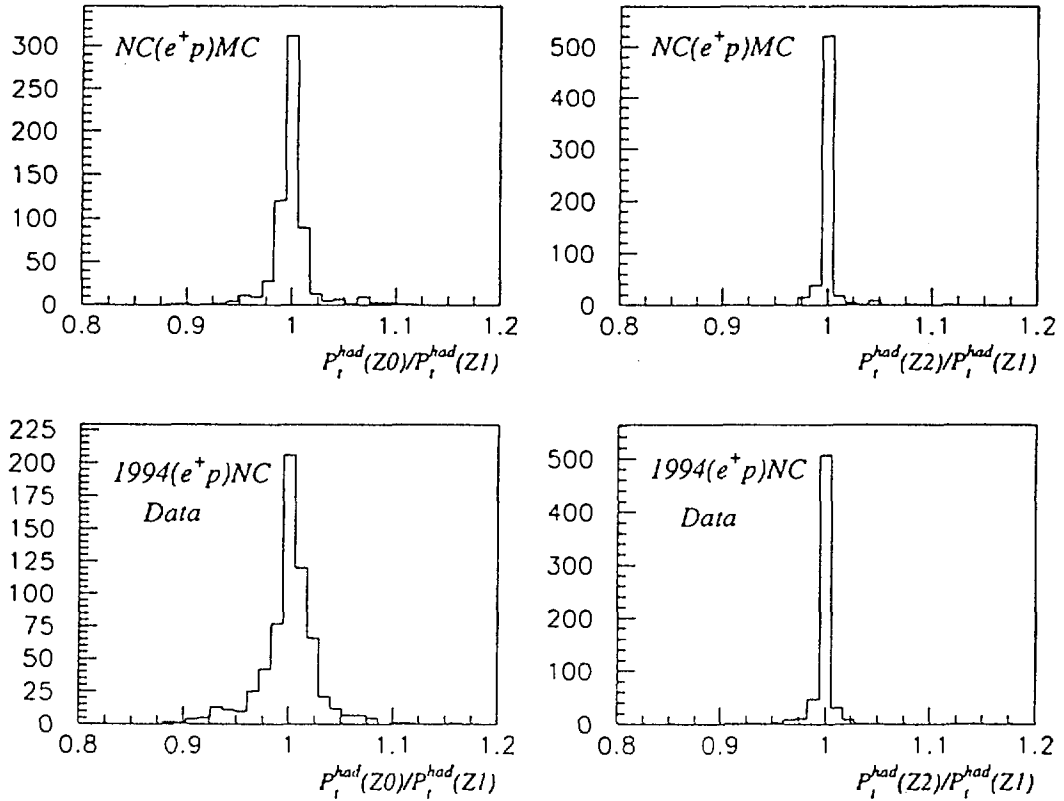


Fig 5.14 The distribution of the ratio  $p_t^{had}(Z_{vtx}(0))/p_t^{had}(Z_{vtx}(1))$  and  $p_t^{had}(Z_{vtx}(2))/p_t^{had}(Z_{vtx}(1))$ , for 1994  $e^+p$  Monte Carlo and data respectively.

The migration of events due to the cut at  $p_t^{had}$  calculated from different vertex are found to be very small (less than 0.2%), both data and Monte Carlo present good agreement. Thus compared to the hadronic energy scale effect on the event migration, the effect from the uncertainty on the vertex is negligible.

### Other sources of systematic errors

In the above analysis we have compared the effects on the migration from different  $p_t^{had}$  calculation methods, and the result shows that the data and Monte Carlo are consistent. No obvious systematic deviation from Monte Carlo simulation has been found with respect to the data. Therefore, different  $p_t^{had}$  calculation will give a slightly different observed event numbers, but can be corrected by a correction factor calculated from Monte Carlo which can successfully simulate the true data.

The CC trigger efficiency is calculated from the Pseudo-CC data sample by discarding the electrons and weighting by a factor  $\sigma^{CC}/\sigma^{NC}$ . The main uncertainty is the statistical error due to the limited event number, which was estimated above. The uncertainty from the different method of calculating the kinematic variables  $x, Q^2$  in the weighting procedure is found to be negligible.

The final CC data samples were visually scanned and the muon-induced background was removed. However, the  $\gamma p$  event, which is a NC interaction (at very small  $Q^2$ ) having a lepton scattered in the beam pipe not detected by the BEMC calorimeter, may have final hadronic jets simulating the CC process. Generally the missing transverse momentum of  $\gamma p$  events is near zero, thus it is suppressed by the  $P_t > 25$  GeV cut. The  $\gamma p$  events may enter the data sample if a large part of  $P_t$  carried by the forward jets escaped the detection, or  $P_t$  is incorrectly measured due to the the energy resolution of the detector. This effect was quantitatively studied: within present luminosity, the contamination from  $\gamma p$  events to the CC samples seems negligible [57].

From Fig.4.1 we see that the CC and NC events are well separated by the  $P_t > 25$  GeV cut. NC events contaminating the CC sample are mainly due to the semileptonic decays with energetic missing neutrinos producing a transverse momentum imbalance. This contamination is estimated as less than 0.1%. Several NC events were found in CC sample with the electron poorly measured in the LAr calorimeter, and were removed by the visual scan.

The cluster mass criteria in our electron finder allows to select events with a true electron with high efficiency. The effect of electron misidentification is well below 1% from the NC Monte Carlo study. The contamination of NC sample from the misidentified CC events due to a fake electron is estimated to be less than 0.01%. Actually, in the visual scan of the final NC data samples, no CC event were found, and no muon-induced background was found either.

### Systematic uncertainties on the NC/CC ratio

In summary, the conclusions on the systematic uncertainties in the CC and NC selections are:

- The main systematic error comes from the uncertainty in the hadronic energy scale. For a  $\pm 4\%$  shift of the hadronic energy scale, the changes in the number of NC events are  $+13.0/-15.8\%$  for  $e^-p$  interaction and  $+11.4/-14.7\%$  for  $e^+p$  interaction, while the changes in the number of CC events are  $-5.0/+4.9\%$  for  $e^-p$  interaction and  $-4.5/+3.9\%$  for  $e^+p$  interaction.
- $P_t^{had}$  calculated using different approach can cause several percent change in the event number with a  $P_t^{had}$  cut, which can be corrected by a correction factor calculated from Monte Carlo, and finally lead to the same values after the correction. The effects in the data and the Monte Carlo used are found to be consistent, which means that the Monte Carlo events correctly simulate the true data, thus no substantial systematic error is expected from this source.
- The effect of the different vertex calculation on the total number of events after  $P_t^{had}$  cut is negligible ( $< 0.2\%$ ), and correctly described by the Monte Carlo.
- The muon-induced or  $\gamma p$ -induced background contamination rates in the final CC and NC sample are negligible.
- Finally, the errors in the event numbers come also from the statistical uncertainties of the correction factors due to the limited number of Monte Carlo events, especially due to the the limited "Pseudo-CC" data samples when calculating trigger efficiency. These uncertainties are included here as another systematic effects.

The estimated relative systematic errors for the selected CC and NC event numbers and the NC/CC ratio measurement are listed below:

Table 5.6 The estimated relative systematic errors for Number of events  $((\Delta N)_{sys})$  and NC/CC ratio  $((\Delta R)_{sys})$ :

Data sample	1993 $e^-$		1994 $e^-$		1994 $e^+$	
	CC	NC	CC	NC	CC	NC
$(\Delta N)_{sys}$	+5.8%	+13.6%	+5.9%	+13.6%	+4.3%	+11.8%
	-5.9%	-16.3%	-5.9%	-16.3%	-4.9%	-15.0%
$(\Delta R)_{sys}$	+8.9%		+8.9%		+8.0%	
	-12.2%		-12.2%		-11.2%	

### 5.1.3 Conclusions and Physics Implications of NC/CC Ratio Measurement

Since the electron beam energies are slightly different for 1993  $e^-p$  runs ( $E_e = 26.7\text{GeV}$ ) and 1994  $e^-p$  ( $E_e = 27.5\text{GeV}$ ) runs, a very small difference (about 1.5%) on the predicated theoretical ratios is expected. Thus, a corresponding correction should be done when combining these two data samples.

The theoretical prediction for the NC/CC ratio in the frame of Standard Model is calculated using the package HERACLES [20], where the parton distribution parameterization MRSH is used, and the radiative effects are taken into account.

Here we have combined 1993  $e^-p$  data to 1994  $e^-p$  data and the theoretical predicted ratios are corrected according to the luminosities of 1993 and 1994. Table 5.7 gives the final results of the measured NC/CC ratios for 1993 and 1994 data with the estimated statistical errors and the systematic errors, together with the theoretical predictions from the Standard Model.

These results of NC/CC ratio from 1993 and 1994 data are in good agreements with the theoretical predications from the Standard Model. Fig 5.15 gives the predicted NC/CC ratio as a function of the propagator mass  $M_{prop}$  ( $M_W$  value in the propagator term  $1/(1+Q^2/M_W^2)^2$ ) for  $e^-p$  and  $e^+p$  interactions respectively. The measured NC/CC ratios from (1993+1994)  $e^-p$  data and 1994  $e^+p$  data are shown in the plots.

Table 5.7: The results of the NC/CC ratio measurement:

Data sample		$(NC/CC)_{measured}$	$(NC/CC)_{theory}$
$e^-p$	1993	$7.1 \pm 2.1(\text{stat.}) \begin{smallmatrix} +0.6 \\ -0.9 \end{smallmatrix}(\text{syst.})$	6.75
	1994	$7.0 \pm 2.1(\text{stat.}) \begin{smallmatrix} +0.6 \\ -0.9 \end{smallmatrix}(\text{syst.})$	6.85
	1993+1994	$7.0 \pm 1.5(\text{stat.}) \begin{smallmatrix} +0.6 \\ -0.9 \end{smallmatrix}(\text{syst.})$	6.80
$e^+p$	1994	$13.6 \pm 2.04(\text{stat.}) \begin{smallmatrix} +1.1 \\ -1.5 \end{smallmatrix}(\text{syst.})$	15.57

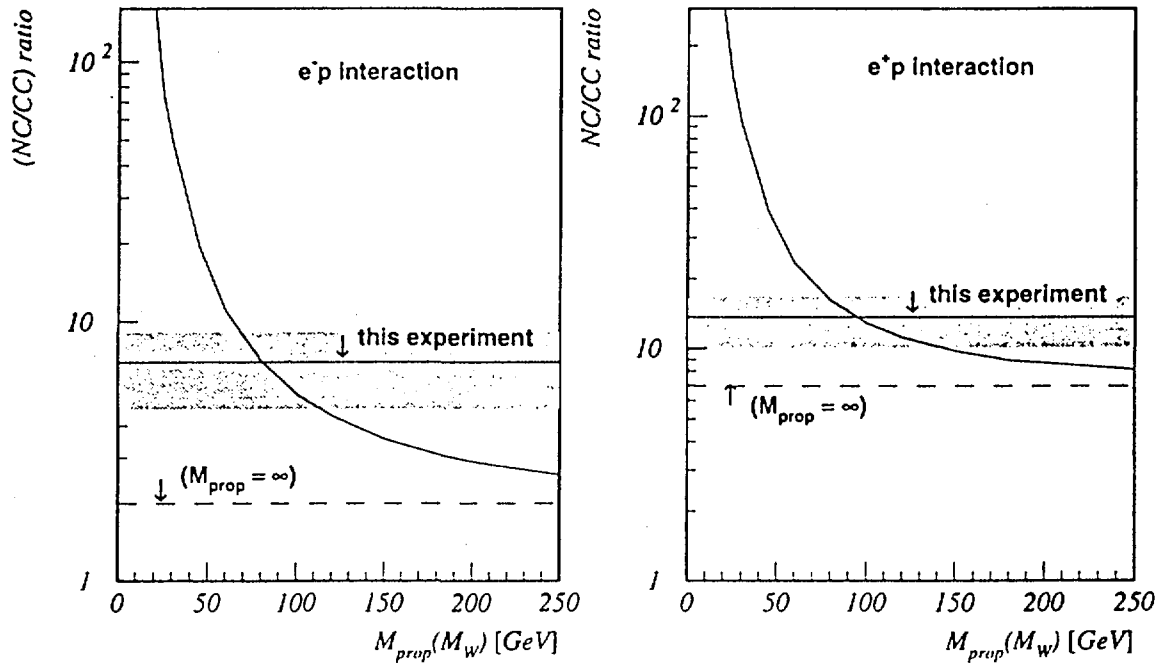


Fig.5.15 The predicted NC/CC ratio as a function of the propagator mass  $M_{prop}$  for  $e^-p$  and  $e^+p$  interactions. The measured NC/CC ratios from (1993+1994)  $e^-p$  data and 1994  $e^+p$  data and the  $1\sigma$  band are shown in the plot.

The NC/CC ratio is more sensitive to  $W$  mass in the  $e^-p$  interaction than in the  $e^+p$  interaction. From Fig.5.15, the  $W$  mass implied by the NC/CC ratios can be estimated to be  $81_{-12}^{+20}$  GeV for  $e^-p$  interaction, and  $93_{-13}^{+47}$  GeV for  $e^+p$  interaction. These results are in good agreement with the previous resonance mass measurements.

## 5.2 The Integrated Charged Current Cross Sections

The charged current process in deep-inelastic scattering is mediated by the exchange of the  $W$  vector boson. As discussed in Chapter 2, the  $W$  mass is the most sensitive Standard Model parameter that could be looked for in the deep-inelastic-scattering. Thus, the measurement of CC cross section provide a consistency check of the vector boson mass interdependence.

The integrated cross section for the charged current process with a cut at  $P_t^{had} > 25$  GeV is given by:

$$\sigma^{CC}(P_t^{had} > 25\text{GeV}) = \frac{N^{CC}(P_t^{had} > 25\text{GeV})}{\epsilon^{CC}\mathcal{L}} \quad (5.23)$$

where  $N^{CC}$  is the observed number of CC events which has  $P_t^{had} > 25$  GeV (Table 4.4),  $\mathcal{L}$  is the luminosity, and  $\epsilon^{CC}$  is the correction factor for the efficiencies in different selection steps and the  $P_t^{had}$  migration and detector acceptance effects (equation (5.4)), as given in the previous section (in Table 5.5).

The integrated luminosity  $\mathcal{L}$  is measured by a luminosity system using the rate of the small angle bremsstrahlung  $ep \rightarrow ep\gamma$  [58]. The electron and proton are detected in crystal calorimeters positioned at 33 m and 103 m, respectively, from the nominal interaction point along the incident  $e$  beam direction. The value of  $\mathcal{L}$  for 1993 and 1994 data is given in Table 4.1. The systematic error of  $\mathcal{L}$  arises predominantly from the uncertainty in the acceptance of the detector and its statistical error is negligible. The precision of the luminosity determination is 1.5% [58].

The integrated cross section of CC process with  $p_t^{had} > 25$  GeV for 1993  $e^-p$  and 1994  $e^\pm p$  data are given in the Table 5.8, together with the theoretical predictions from the Standard Model.

In combining 1993 and 1994  $e^-p$  data, the different luminosities are taken into account. In Table 5.8, the first error in  $\sigma_{measure}^{CC}$  is the statistical uncertainty of the

number of events, the second error comprises all known systematic effects as given in Table 5.6, and also includes the uncertainties in luminosity measurement.

The theoretical predictions are calculated using the HERACLES generator [20], as for the calculation of the theoretical prediction of the NC/CC ratio. The measured  $\sigma^{CC}$  for  $e^-p$  interactions are in good agreement with the theoretical predictions within the error limits, while  $\sigma^{CC}$  for  $e^+p$  interactions seems to be more than  $1\sigma$  higher than the theoretical prediction. Again, we see that the main source of the error in the cross section measurement is the limited statistics.

Table 5.8: The integrated cross section of CC process( $pb$ )  
(for  $P_t^{had} > 25$  GeV)

Data sample		$\sigma_{measure}^{CC}$	$\sigma_{theory}^{CC}$
$e^-p$	1993	$45.5 \pm 12.6(\text{stat.}) \begin{smallmatrix} +3.1 \\ -3.1 \end{smallmatrix}(\text{syst.})$	41.3
	1994	$40.7 \pm 11.3(\text{stat.}) \begin{smallmatrix} +2.8 \\ -2.8 \end{smallmatrix}(\text{syst.})$	42.1
	1993+1994	$43.0 \pm 8.4(\text{stat.}) \begin{smallmatrix} +2.9 \\ -2.9 \end{smallmatrix}(\text{syst.})$	40.7
$e^+p$	1994	$21.3 \pm 3.1(\text{stat.}) \begin{smallmatrix} +1.0 \\ -0.5 \end{smallmatrix}(\text{syst.})$	17.2

Fig.5.16 and Fig.5.17 show the sensitivity of the predicted CC cross sections to the propagator mass  $M_{prop}$  for  $e^-p$  and  $e^+p$  interactions respectively. The measure cross sections with  $1\sigma$  bands are shown in the plots. The  $W$  mass implied by the measured values can be estimated to be  $83_{-15}^{+17}$  GeV for  $e^-p$  and  $103_{-22}^{+30}$  for  $e^+p$  interactions. The result of  $e^-p$  experiment agrees well with with the known mass value of 80.35GeV [23], while the  $e^+p$  result seems to be  $1\sigma$  larger.

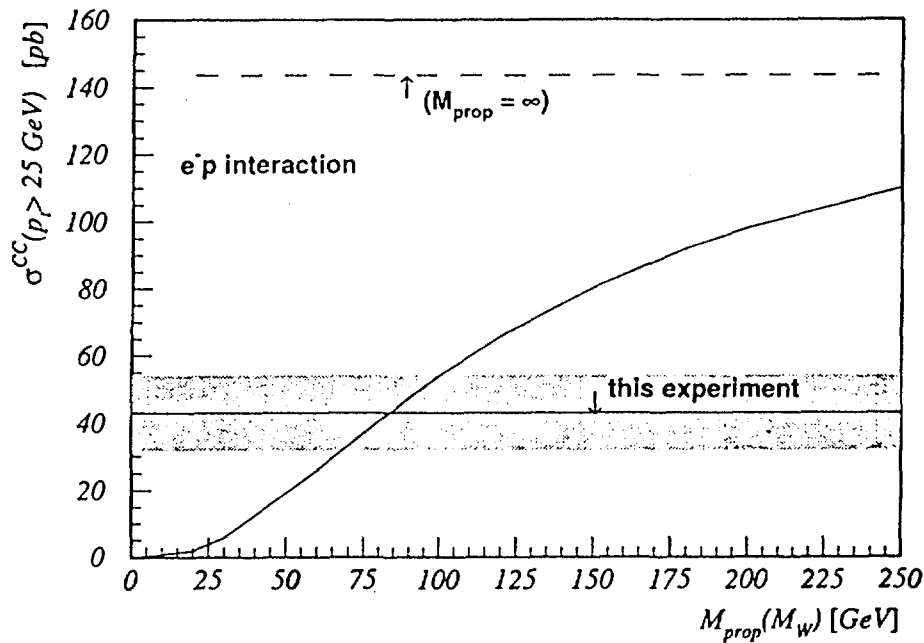


Fig.5.16 The CC cross section as a function of  $M_W$  for  $e^-p$  interaction. The measured  $\sigma^{CC}$  from (1993+1994)  $e^-p$  data and the  $1\sigma$  band is also shown in the plot.

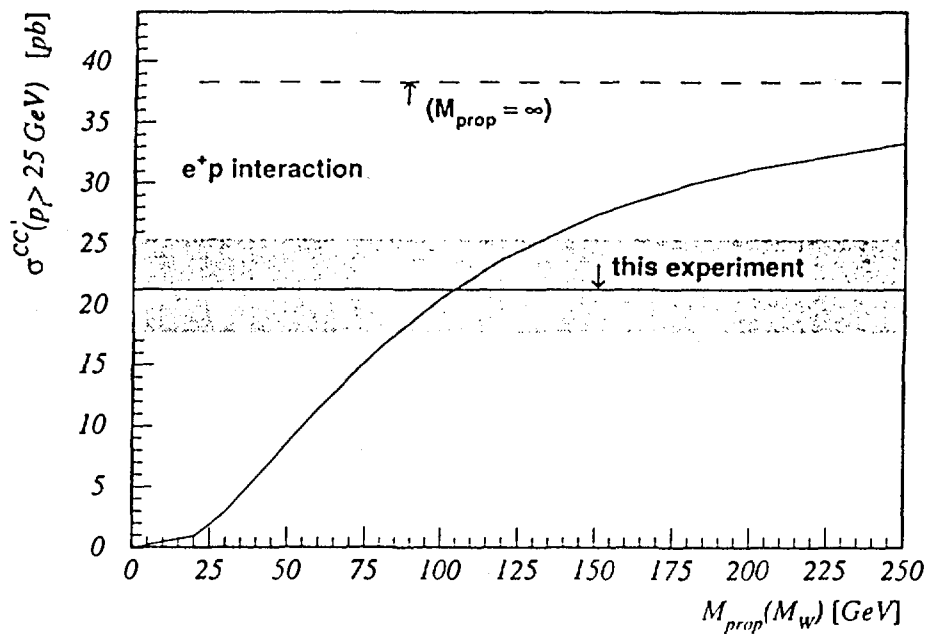


Fig.5.17 The CC cross section as a function of  $M_W$  for  $e^+p$  interaction. The measured  $\sigma^{CC}$  from 1994  $e^+p$  data and the  $1\sigma$  band is also shown in the plot.

The effect of the  $W$  propagator can also be seen when comparing our results to those measured at lower energy experiments. Fig.5.18 shows the deviation from the linear dependence extrapolated from the low energy data of the neutrino-nucleon experiments, where the two total cross sections at the corresponding  $E_\nu$  at HERA (by equalizing the invariant mass squared of  $e^\pm p$  and  $\nu N$  interactions) transformed from the two measured charged current cross sections of  $e^-p$  and  $e^+p$  interactions are shown, together with some measured values of the total cross sections  $\sigma_{\nu N}^{tot}$  in the neutrino-nucleon experiments.

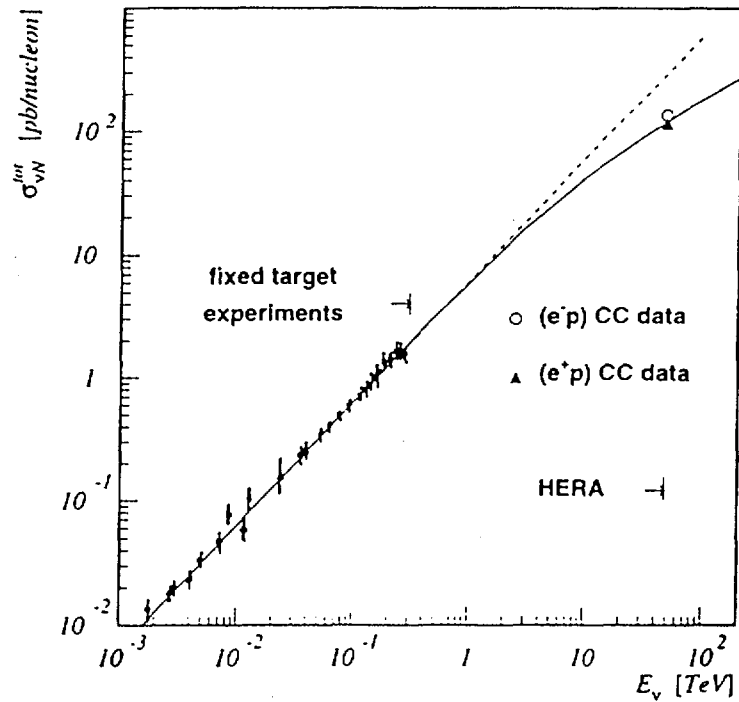


Fig.5.18 The two total cross sections transformed from measured CC cross sections for  $e^\pm p$  interactions compared with the linear extrapolation of the low energy data of neutrino-nucleon interactions.

The ratio between the  $e^-p$  and  $e^+p$  CC integrated cross sections is:

$$R_e = \frac{\sigma_{(e^+p)}^{CC}(P_t^{had} > 25\text{GeV})}{\sigma_{(e^-p)}^{CC}(P_t^{had} > 25\text{GeV})} = 0.50 \pm 0.12 \pm 0.01 \quad (5.24)$$

where the common systematic errors are canceled. The ratio  $R_e$  can be interpreted qualitatively in terms of the relevant  $e^\pm$  - *quark* and *antiquark* subprocesses mediated by the weak vector boson  $W^\pm$  in the quark-parton model. As a good approximation,

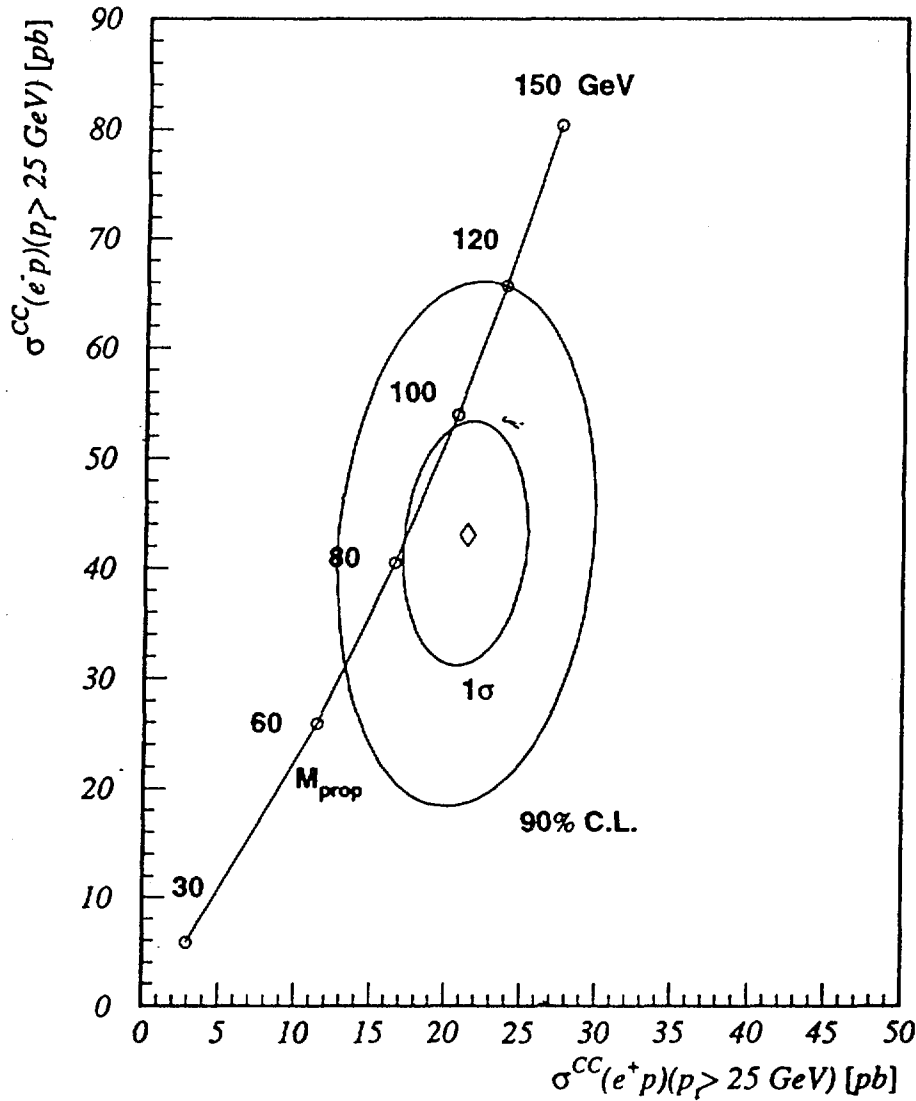


Fig.5.19 The CC cross section as a function of  $M_W$  for  $e^-p$  and  $e^+p$  interactions. The measured  $\sigma^{CC}$  from (1993+1994)  $e^-p$  data and 1994  $e^+p$  data are shown in the plot. The 39.4% ( $1\sigma$ ) and 90% CL contours are given by the two ellipses, which are tilted slightly due to the correlation of the systematic errors.

$$R_e \approx \frac{\sigma(e^+d) + \sigma(e^+\bar{u})}{\sigma(e^-u)} = \frac{D}{U} \left( \frac{a_1}{a_0} + \frac{\bar{U}}{D} \right), \quad (5.25)$$

where  $D/U$  and  $\bar{U}/D$  are the ratios of the corresponding integrated parton distributions,  $a_1 = \langle (1-y)^2 \rangle$  and  $a_0 = \langle 1 \rangle$  account for the  $W$  helicities averaged over the appropriate parton distributions. The sea in the proton contributes little to  $e^-p$  scattering, but it has the same size of contribution to  $e^+p$  scattering as the one of the valence  $d$ -quark. The effect of the  $W$  propagator on  $R_e$  is reduced although it strongly affects each CC cross section separately [31]. Fig.5.19 gives the the predicted  $\sigma^{CC}(e^-p)$  and  $\sigma^{CC}(e^+p)$  as a function of the  $W$  propagator mass, together with the measured values from 1993 and 1994 data.

In conclusion, the results from 1993  $e^-p$  and 1994  $e^+p$  data collected by H1 at HERA show, for the first time, the effect of the  $W$ -propagator in deep inelastic charged current interactions. The measured NC/CC ratio is consistent with the theoretical prediction of the Electroweak Standard Model. With present statistics, the  $W$  mass estimated from the NC/CC ratios are  $81_{-12}^{+20}$  GeV and  $93_{-13}^{+47}$  for  $e^-p$  and  $e^+p$  interactions respectively. Here, the  $W$  mass estimation comes indirectly from the measurement of the ratio of the coupling constant of the NC and CC cross sections.

The limited statistics of the selected Charged Current events is too poor to conclude on the higher order effect or measurable deviation from the Standard Model. The  $M_W$  values estimated from  $e^-p$  and  $e^+p$  charged current cross sections are  $83_{-15}^{+17}$  GeV and  $103_{-22}^{+30}$  GeV respectively. With increasing cumulated luminosity, more precise measurements of the electroweak parameters at HERA are foreseen in the future. However, with decreasing statistical error, more effort is needed to lower the uncertainty on the hadronic energy scale, this will become possible also with more NC events at high  $Q^2$ .

## Chapter 6

# The Cross Sections of CC and NC as a Function of $Q^2$

The inclusive cross sections of the Deep Inelastic scattering process are usually expressed in terms of kinematic variables  $Q^2, x, y$ , because of their simple interpretation in the electroweak theory and the Quark-Parton model. These variables can be calculated from the experimentally measurable quantities such as the energy and the direction of the scattered lepton (as indicated in formula (2.28)) or from the final hadronic energy flow (Jacquet-Blondel Method).

The differential cross sections for the Charged and the Neutral Current processes measured at HERA may provide information on the weak propagators, which is important for the electroweak study. Despite the limited statistics of the charged current data samples, the differential cross sections can still possibly be obtained in several kinematic bins. In this chapter, we will calculate the differential cross sections as a function of  $Q^2$  in 4 bins, for the Charged and the Neutral Current processes for 1993  $e^-p$  and 1994  $e^\pm p$  data collected by H1.

## 6.1 Experimental Measurement of the Kinematic Variables

### 6.1.1 Jacquet-Blondel Method

The kinematic variables  $Q^2$ ,  $x$ ,  $y$  can be calculated from the precisely measured energy and angle of the scattered electron (positron) in the Neutral Current process, while for the charged current process, these quantities can only be obtained from the measurement of the hadronic system, since the scattered neutrino cannot be recorded by the detector.

Using the method proposed by A.Blondel and F.Jacquet [59], the kinematic variables can be derived from the information of the final hadronic energy flow, without any jet identification or proton structure assumption. Denoting the energies of the incident lepton and proton as  $E_l$  and  $E_p$  respectively, this method gives:

$$y_{JB} = \frac{\sum_i (E_i - p_{zi})}{2E_l} \quad (6.1)$$

$$Q_{JB}^2 = \frac{(\sum_i \vec{p}_{ti})^2}{1 - y_{JB}} = \frac{(\sum_i p_{xi})^2 + (\sum_i p_{yi})^2}{1 - y_{JB}} \quad (6.2)$$

$$x_{JB} = \frac{Q_{JB}^2}{s \cdot y_{JB}} \quad (6.3)$$

where  $\vec{p}_{ti}$  is the transverse momentum of the outgoing hadronic particle  $i$ ,  $s = 4E_l E_p$  is the total invariant mass squared, and the sum runs over all observed hadronic final states. Equation (6.1) actually reflects the longitudinal energy conservation.

We use the Jacquet-Blondel method to reconstruct the kinematic variables of both Charged Current and Neutral Current events, to get a coherent analysis of the electroweak processes as well as to reduce various systematic effects. Meanwhile we also use the electron (positron) informations to reconstruct the kinematics, as a check to the precision of the Jacquet-Blondel method.

### 6.1.2 The Kinematic Distributions of CC and NC events

The precision of the reconstruction of the kinematic variables using Jacquet-Blondel method depends on the energy and angular resolutions of the final hadronic states, and of the size of the beam hole which causes the loss of energy flow in the forward direction. The later effect only has minor influence, since the hadrons emitted in the forward direction near the beam pipe contribute little to  $(E - p_z)$  and  $p_t$  (thus to  $y_{JB}$  or  $Q_{JB}^2$ ), as shown in equations (6.3) and (6.4).

Only the hadronic energy deposited in the LAr calorimeter cells are used in the calculation of  $y_{JB}$  and  $Q_{JB}^2$  in our analysis, as in the case of the  $P_t^{had}$  calculation (see Chapter 4). For both charged and neutral current events, the vertex used in the polar angle calculation is reconstructed only from the hadronic tracks.

The precision of the  $Q^2$  reconstructed using Jacquet-Blondel Method ( $Q_{JB}^2$ ) can be checked by a comparison to  $Q^2$  reconstructed from the scattered lepton ( $Q_{el}^2$ ). From equation (2.28), we have:

$$\frac{\partial Q_{el}^2}{Q_{el}^2} \Big|_{E'_i} = \frac{\Delta E'_i}{E'_i}; \quad \frac{\partial Q_{el}^2}{Q_{el}^2} \Big|_{\theta'_i} = -tg \frac{\theta'_i}{2} \Delta \theta'_i \quad (6.4)$$

where  $E'_i$  and  $\theta'_i$  are the energy and the polar angle of the scattered lepton. It is clear that the resolution of  $Q_{el}^2$  is determined by the resolution of the measured electron energy except in a very small  $\theta'_i$  range, where the angular resolution has decisive effect. Since  $E'_i$  is precisely measured, the resolution in  $Q_{el}^2$  is very good except for lepton scattered in very small angle.

Using a Neutral Current Monte Carlo simulation, we can see the precision of the  $Q^2$  reconstruction using these two methods. Fig.6.1 gives the ratio between the reconstructed  $Q^2$  and the generated  $Q^2$ , for  $Q_{el}^2$  and  $Q_{JB}^2$  respectively. We can see that the relative resolution of  $Q_{el}^2$  is much better than that of the  $Q_{JB}^2$ .

In the calculation of  $y_{JB}$  and  $Q_{JB}^2$  using formulae (5.1) and (5.2), the summation can also run over the clusters (where the cells from different calorimeters are grouped into a object pointing to the interaction vertex), instead of LAr calorimeter cells. Using clusters will include also the energy of hadrons deposited in other calorimeters (Tail Catcher, PLUG and BEMC). Fig.6.2 shows the comparison of these two approaches using the charged current Monte Carlo.

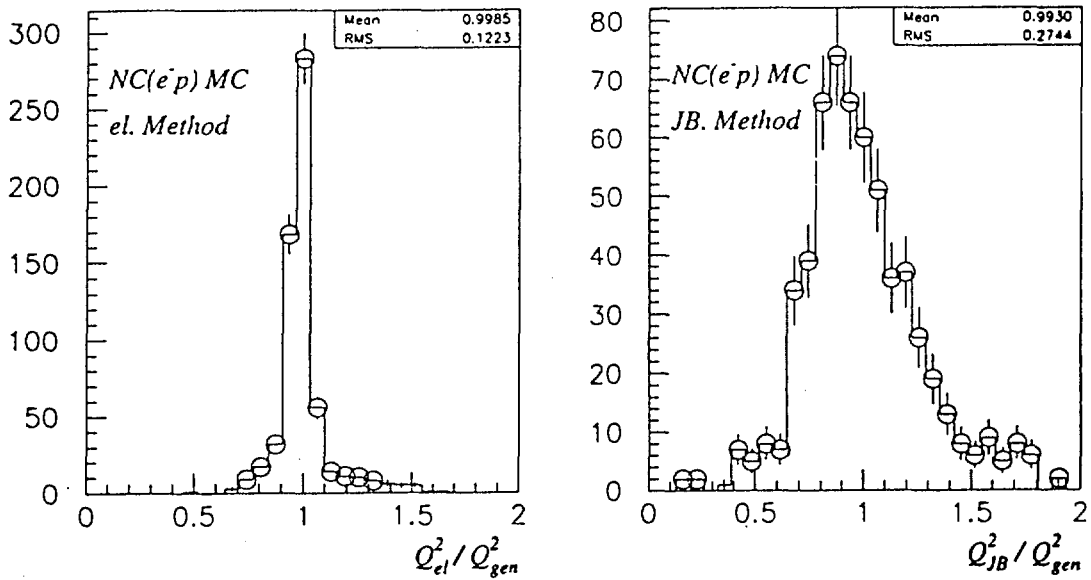


Fig.6.1 The distributions of the ratios between the reconstructed  $Q^2$  and the true  $Q^2$ , using informations from scattered lepton and from hadrons respectively. The statistic errors are also shown.

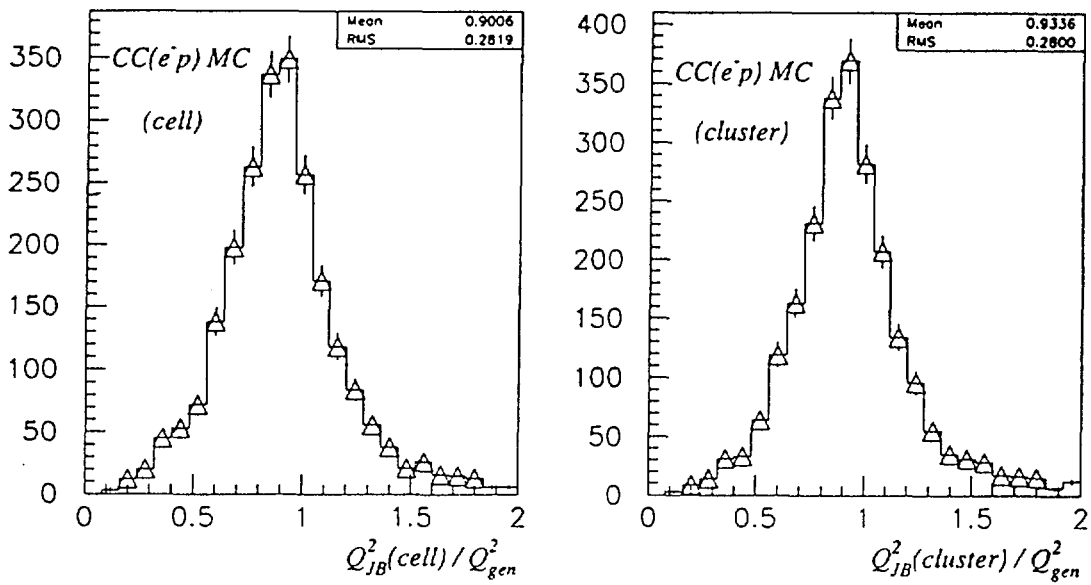


Fig.6.2 The distributions of the ratio between reconstructed  $Q^2$  and true  $Q^2$  using CC Monte Carlo, using clusters and cells in  $Q_{JB}^2$  calculation respectively. Also shown are the statistical uncertainties.

From the distribution of the ratio between the reconstructed  $Q^2$  and the true  $Q^2$ , we see that, the  $Q_{JB}^2$  calculated using cluster gives a slightly larger result than using cells (which can be seen from the mean values in the plots). From the study in the previous chapter, we know that the data are correctly described by the Monte Carlo, therefore this effect can be taking into account using the Monte Carlo simulation when calculating the cross sections. Little difference can be seen in terms of the resolutions between these two approaches, thus the precisions are the same.

Using the final selected data samples listed in Table 4.4, the  $y$  and  $Q^2$  distributions of the Charged Current events using Jacquet-Blondel method are displayed in Fig.6.3 and Fig.6.5 respectively, for (1993 + 1994)  $e^-p$  and 1994  $e^+p$  data. The similar distributions for the Neutral Current events (listed in Table 4.5) are displayed in Fig.6.4 and Fig.6.6. In these plots, no correction factors for the smearing and acceptance effects are applied. The errors indicated in these plots are statistical uncertainties, which is the dominant source of error in the Charged Current case. The systematic error (mainly comes from the energy scale) plays a more important role in the Neutral Current case. The distributions from the corresponding Monte Carlo simulations are also shown by the histograms in the plots. These Monte Carlo distributions are also reconstructed using the same conditions as in the data case.

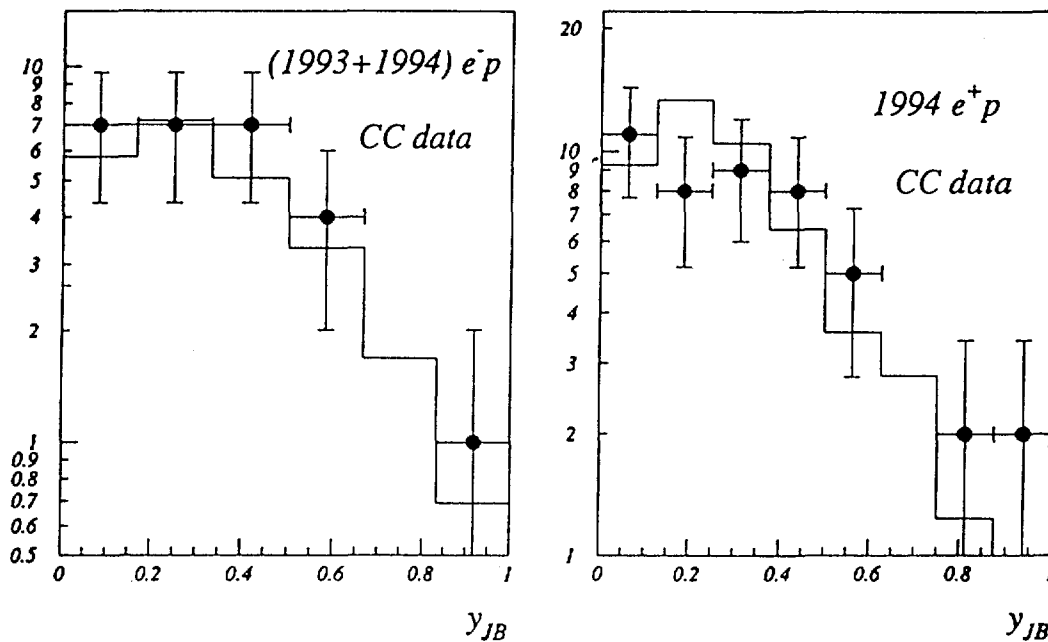


Fig.6.3  $y_{JB}$  distributions of the charged current events for (1993 + 1994)  $e^-p$  and 1994  $e^+p$  data, compared with the Monte Carlo distributions (histograms). The error bars in data points are statistical only.

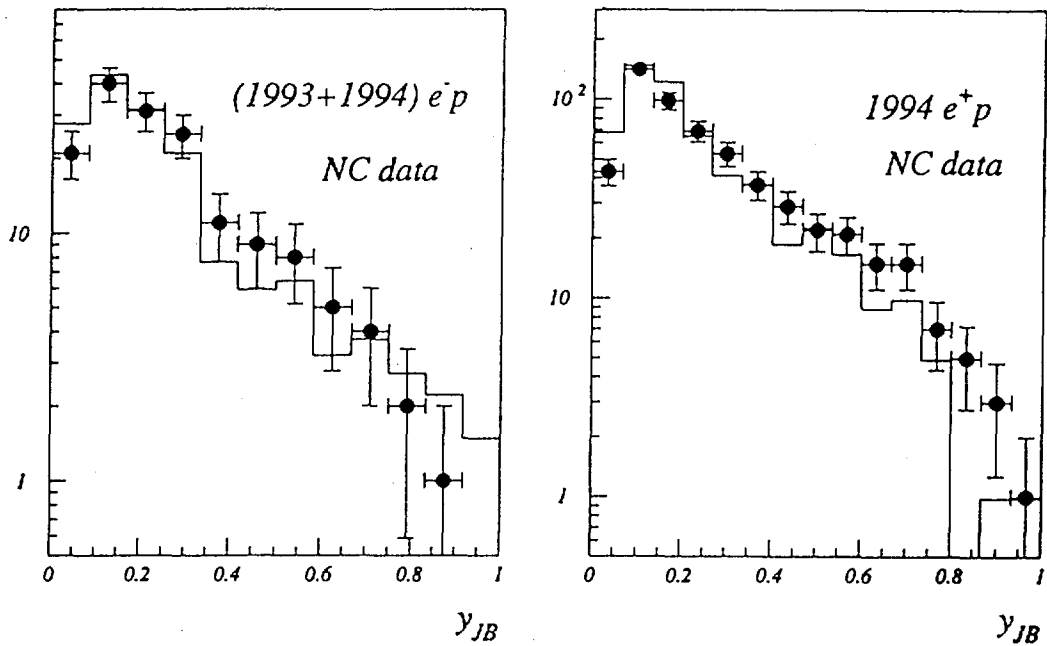


Fig.6.4  $y_{JB}$  distributions of the neutral current events for (1993 + 1994)  $e^-p$  and 1994  $e^+p$  data, compared with the Monte Carlo distributions (histograms). The error bars in data points are statistical only.

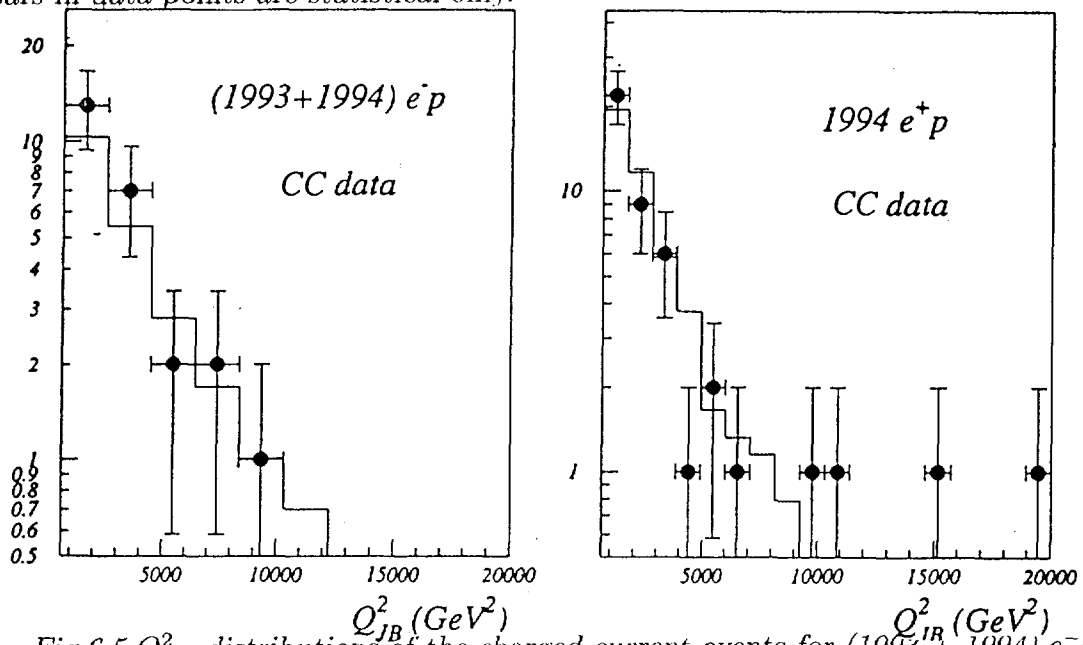


Fig.6.5  $Q_{JB}^2$  distributions of the charged current events for (1993 + 1994)  $e^-p$  and 1994  $e^+p$  data, compared with the Monte Carlo distributions (histograms). The error bars in data points are statistical only.

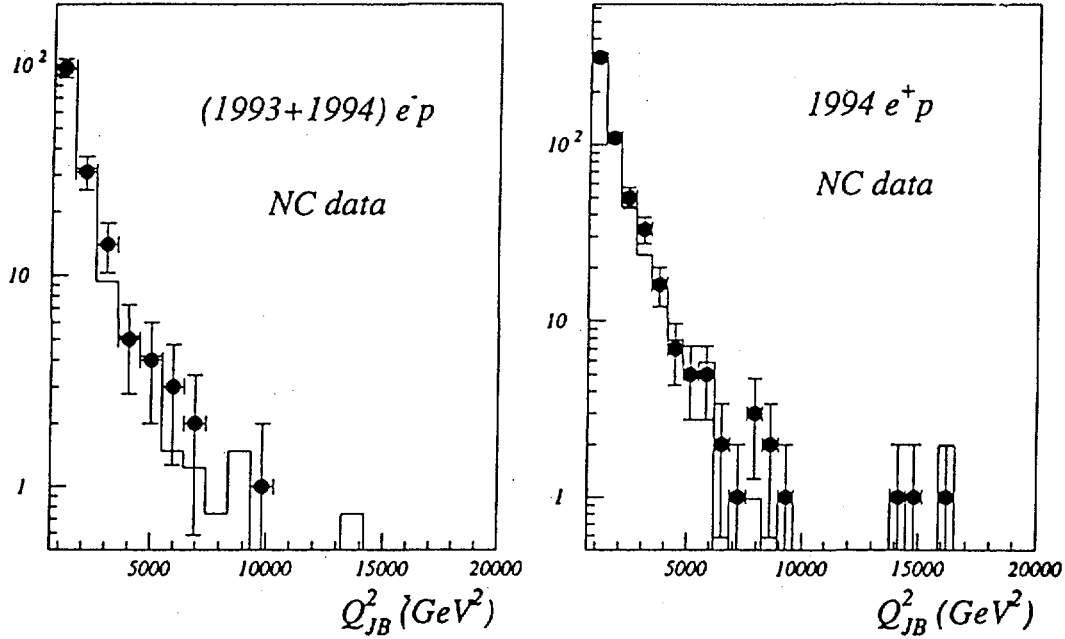


Fig.6.6  $Q^2_{JB}$  distributions of the neutral current events for (1993 + 1994)  $e^-p$  and 1994  $e^+p$  data, compared with the Monte Carlo distributions (histograms). The error bars in data points are statistical only.

Finally, the ratio between  $Q^2$  reconstructed using Jacquet-Blondel Method and using electron method ( $Q^2_{JB}/Q^2_{el}$ ) can be used as a consistency check between the data and Monte Carlo simulation. Fig.6.7 gives the ratio  $Q^2_{JB}/Q^2_{el}$  for the NC 1994  $e^+p$  data and for Monte Carlo respectively. We see that the systematic shift of this ratio in the data sample due to the hadronic energy measurement are correctly simulated by the Monte Carlo.

## 6.2 Differential Cross Sections

The differential cross sections for the high  $Q^2$  neutral current process have been measured precisely at HERA, using the informations from the scattered electron (positron) [60] or using also the informations from the hadrons [61]. We will calculate here the cross sections for both Charged Current and Neutral Current processes in four  $Q^2$  bins, using only the informations from the hadronic flow.

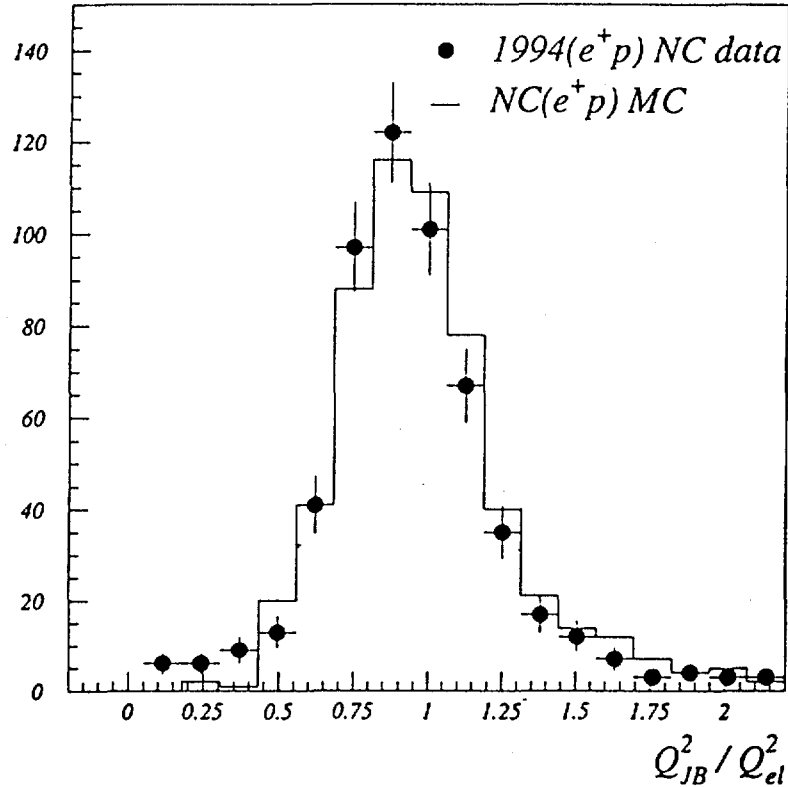


Fig.6.7 The distributions of the ratio  $Q_{JB}^2/Q_{el}^2$ , for 1994  $e^+p$  NC data and for Monte Carlo respectively. A good agreement can be seen from the plot.

- Binning

In the experimental measurement of the differential cross section, the kinematic range is divided into several bins, taking into account the precision in the measurement of the kinematics and the statistics of the data sample. Let  $(Q^2)_1^i$  and  $(Q^2)_2^i$  be the lower and upper limit of the bin  $i$ , the “bin center”  $(Q^2)^i$  is defined as the  $Q^2$  value where  $d\sigma/dQ^2$  equals to the average value over this bin:

$$\left(\frac{d\sigma}{dQ^2}\right)_{Q^2=(Q^2)^i} = \frac{1}{(Q^2)_2^i - (Q^2)_1^i} \cdot \int_{(Q^2)_1^i}^{(Q^2)_2^i} \frac{d\sigma}{dQ^2} dQ^2 \quad (6.5)$$

Thus once the binning is defined, the “bin center”  $(Q^2)^i$  can be calculated from the Monte Carlo using the above formula.

The observed event number in a certain bin is not the true one, since due to the error in the measurement of the kinematic variables, some of the events in the

neighboring bins may migrate across the bin limits. Besides the smearing effect, the limited detector acceptance and the efficiencies when applying the trigger, vertex requirements and the selection cuts also affect the number of events in each bin.

Considering all these effects, the measured differential cross section at  $(Q^2)^i$  can be expressed in terms of the measurable quantities:

$$\left(\frac{d\sigma}{dQ^2}\right)_{Q^2=(Q^2)_i} = \frac{\Delta N_i}{\mathcal{L} \cdot \varepsilon_i} \cdot \frac{1}{(Q^2)_2^i - (Q^2)_1^i} \quad (6.6)$$

where  $\mathcal{L}$  is the luminosity,  $N_i$  is the observed number of events in a given bin, and  $\varepsilon_i(Q^2)$  is the correction factor for the smearing effects, the limited detector acceptance and the efficiencies caused by various criteria applied in the event selection.

The  $Q^2$  range is divided into 4 bins in our calculation, namely:

$$[625 - 1900], \quad [1900 - 5000], \quad [5000 - 12000], \quad [12000 - s] \text{ (GeV}^2\text{)} \quad (6.7)$$

where  $s$  is the total invariant mass squared. The binning was chosen such that the majority of the Monte Carlo generated events in each bin remain in the same bin after reconstruction. The Charged and the Neutral current data samples selected in parallel from 1993  $e^-p$  and 1994  $e^\pm p$  interactions (summarized in Table 4.4 and Table 4.5 in Chapter 4) are used in the cross section calculation.

The bin center  $(Q^2)^i$  ( $i = 1, 2, 3, 4$ ) can be calculated using formula (6.5). However, since there are 4 distributions (CC, NC for  $e^-p$  and  $e^+p$  interactions), for each distribution we may get different bin center  $(Q^2)^i$ . In order to compare the differential cross section at the same fixed  $(Q^2)^i$  values, we chose the bin center  $(Q^2)^i$  a priori for each bin as follows:

$$1250, \quad 3400, \quad 7500, \quad 25000 \text{ (GeV}^2\text{)} \quad (6.8)$$

and apply a factor  $c_{bin}^i$  to the measured differential cross sections in each bin to correct for the effect of the cross section variation over the finite bin.  $c_{bin}^i$  is calculated from the Monte Carlo, for example, the correction factor for the first bin  $c_{bin}^1$  is:

$$c_{bin}^1 = \frac{(d\sigma/dQ^2)|_{Q^2=1250}}{[\int_{625}^{1900} (d\sigma/dQ^2)dQ^2]/(1900 - 625)} \quad (6.9)$$

- Correction for migration effect

The “true” number of events in each  $Q^2$  bin can be obtained from the observed number of events in this bin, by applying correction for the migration effect with a factor computed from the Monte Carlo simulation:

$$N_i^{true} = \frac{N_i^{obs.}}{\varepsilon_i}, \quad \varepsilon_i = \frac{(N_{gen.}^{MC})_i}{(N_{obs.}^{MC})_i} \quad (6.10)$$

where  $(N_{gen.}^{MC})_i$  is the number of MC events with the generated  $Q^2$  in bin  $i$ , and  $(N_{obs.}^{MC})_i$  is the number of MC events with the reconstructed  $Q^2$  in the same bin after all of the criteria in the selection procedure have been applied. The factor  $\varepsilon_i$  depends on the precision of the experimental measurement as well as on the cross section of the process.

Fig.6.8 shows the migration of the events between different  $Q^2$  bins due to the measurement error and detector acceptance. The effects from four Monte Carlo samples - the charged and the neutral current events for  $e^-p$  and  $e^+p$  interactions respectively - are shown, where the number of events in 4 generated  $Q^2$  bins (true  $Q^2$ ) are displayed versus the number of events in 4 reconstructed  $Q^2$  bins.

From the plots we see that, compared to the Charged Current events, the number of the Neutral Current events decreases drastically with the increasing  $Q^2$  and are mainly concentrated in the first two  $Q^2$  bins, due to the  $1/Q^4$  dependence (photon dominance) of the cross section for low  $Q^2$ .

- $d\sigma/dQ^2$  for CC and NC processes

The differential cross section at  $(Q^2)^i$  is calculated using equation (6.6), multiplied by the bin center correction factor  $c_{bin}^i$ . The results of the differential cross section calculation for charged and neutral current processes are summarized in Table 6.1 and Table 6.2, for (1993+1994)  $e^-p$  interaction and for 1994  $e^+p$  interaction respectively.

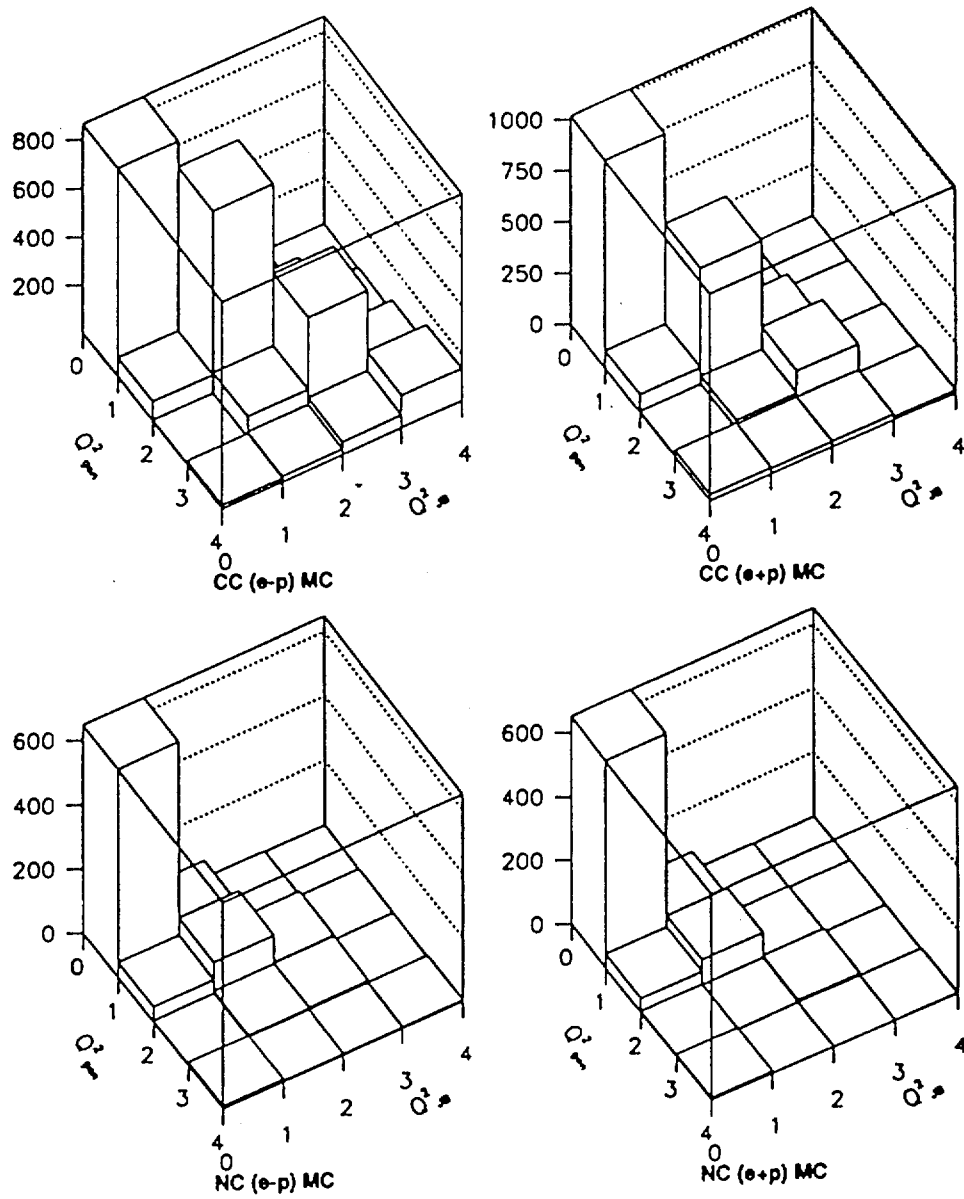


Fig.6.8 The migration of the charged and the neutral current events between different  $Q^2$  bins from Monte Carlo simulation, for  $e^-p$  and  $e^+p$  interactions respectively. The number of events in 4 generated  $Q^2$  bins versus 4 reconstructed  $Q^2$  bins are shown. The values of the  $Q^2$  of the bins are shown in equation (5.7).

Table 6.1 The differential cross sections for (1993+1994)  $e^-p$  interaction:  
(luminosity  $\mathcal{L} = 0.69 \text{ pb}^{-1}$ )

Process		CC	NC
$Q^2 = 1250 \text{ GeV}^2$ [625 – 1900] $\text{GeV}^2$	$N_{obs}^1$	7	105
	$\varepsilon_1$	0.937	0.705
	$c_{bin}^1$	1.191	0.956
	$(d\sigma/dQ^2) [\frac{\text{fb}}{\text{GeV}^2}]$	10.1	162.
	$\pm \Delta_{stat.}$	$\pm 3.8$	$\pm 15.8$
	$\pm \Delta_{syst.}$	$\pm 0.9$	$\pm 20.7$
$Q^2 = 3400 \text{ GeV}^2$ [1900 – 5000] $\text{GeV}^2$	$N_{obs}^2$	13	44
	$\varepsilon_2$	0.842	0.786
	$c_{bin}^2$	0.990	0.703
	$(d\sigma/dQ^2) [\frac{\text{fb}}{\text{GeV}^2}]$	7.1	18.4
	$\pm \Delta_{stat.}$	$\pm 2.0$	$\pm 2.8$
	$\pm \Delta_{syst.}$	$\pm 0.3$	$\pm 2.9$
$Q^2 = 7500 \text{ GeV}^2$ [5000 – 12000] $\text{GeV}^2$	$N_{obs}^3$	5	9
	$\varepsilon_3$	0.828	0.614
	$c_{bin}^3$	1.129	0.949
	$(d\sigma/dQ^2) [\frac{\text{fb}}{\text{GeV}^2}]$	1.4	2.9
	$\pm \Delta_{stat.}$	$\pm 0.6$	$\pm 1.0$
	$\pm \Delta_{syst.}$	$\pm 0.1$	$\pm 0.4$
$Q^2 = 25000 \text{ GeV}^2$ [12000 – s] $\text{GeV}^2$	$N_{obs}^4$	1	0
	$\varepsilon_4$	0.876	1.84
	$c_{bin}^4$	1.47	1.142
	$(d\sigma/dQ^2) [\frac{\text{fb}}{\text{GeV}^2}]$	0.03	0.
	$\pm \Delta_{stat.}$	$\pm 0.03$	0.
	$\pm \Delta_{syst.}$	$\pm 0.01$	$\pm 0.02$

In Table 6.1 and. Table 6.2, the systematic uncertainties for each bin include the errors in the luminosity measurements, the errors in the calculation of the correction factors for various selection criteria, and the uncertainties from the hadronic energy scale. The later is the main contribution to the uncertainties in the neutral current cross section measurements, while in the charged current case the statistical errors are predominant.

Table 6.2 The differential cross sections for 1994  $e^+p$  interaction:  
(luminosity  $\mathcal{L} = 2.7 \text{ pb}^{-1}$ )

Process		CC	NC
$Q^2 = 1250 \text{ GeV}^2$ [625 – 1900] $\text{GeV}^2$	$N_{obs.}^1$	25	375
	$\varepsilon_1$	0.873	0.669
	$c_{bin}^1$	1.213	0.95
	$(d\sigma/dQ^2)[\frac{1b}{\text{GeV}^2}]$	10.1	154.8
	$\pm\Delta_{stat.}$	$\pm 2.0$	$\pm 8.2$
	$\pm\Delta_{syst.}$	$\pm 0.3$	$\pm 19.3$
$Q^2 = 3400 \text{ GeV}^2$ [1900 – 5000] $\text{GeV}^2$	$N_{obs.}^2$	13	129
	$\varepsilon_2$	0.804	0.658
	$c_{bin}^2$	0.939	0.674
	$(d\sigma/dQ^2)[\frac{1b}{\text{GeV}^2}]$	1.9	15.8
	$\pm\Delta_{stat.}$	$\pm 0.5$	$\pm 1.4$
	$\pm\Delta_{syst.}$	$\pm 0.1$	$\pm 2.4$
$Q^2 = 7500 \text{ GeV}^2$ [5000 – 12000] $\text{GeV}^2$	$N_{obs.}^3$	6	20
	$\varepsilon_3$	0.768	0.768
	$c_{bin}^3$	1.099	0.894
	$(d\sigma/dQ^2)[\frac{1b}{\text{GeV}^2}]$	0.5	1.2
	$\pm\Delta_{stat.}$	$\pm 0.2$	$\pm 0.3$
	$\pm\Delta_{syst.}$	$\pm 0.1$	$\pm 0.2$
$Q^2 = 25000 \text{ GeV}^2$ [12000 – s] $\text{GeV}^2$	$N_{obs.}^4$	4	7
	$\varepsilon_4$	1.738	1.772
	$c_{bin}^4$	0.654	0.848
	$(d\sigma/dQ^2)[\frac{1b}{\text{GeV}^2}]$	0.007	0.02
	$\pm\Delta_{stat.}$	$\pm 0.004$	$\pm 0.01$
	$\pm\Delta_{syst.}$	$\pm 0.002$	$\pm 0.01$

The comparison of the results with the theoretical predictions are shown in Fig.6.9 and Fig.6.10, for  $e^-p$  and  $e^+p$  interactions respectively. The Standard Model predictions of  $d\sigma/dQ^2$  for charged and the neutral current process are calculated using the HERACLES generator [20], where the MRSH parton distribution parameterizations [62] are used. The predictions for neutral current cross section from photon exchange alone are also indicated in the plots.

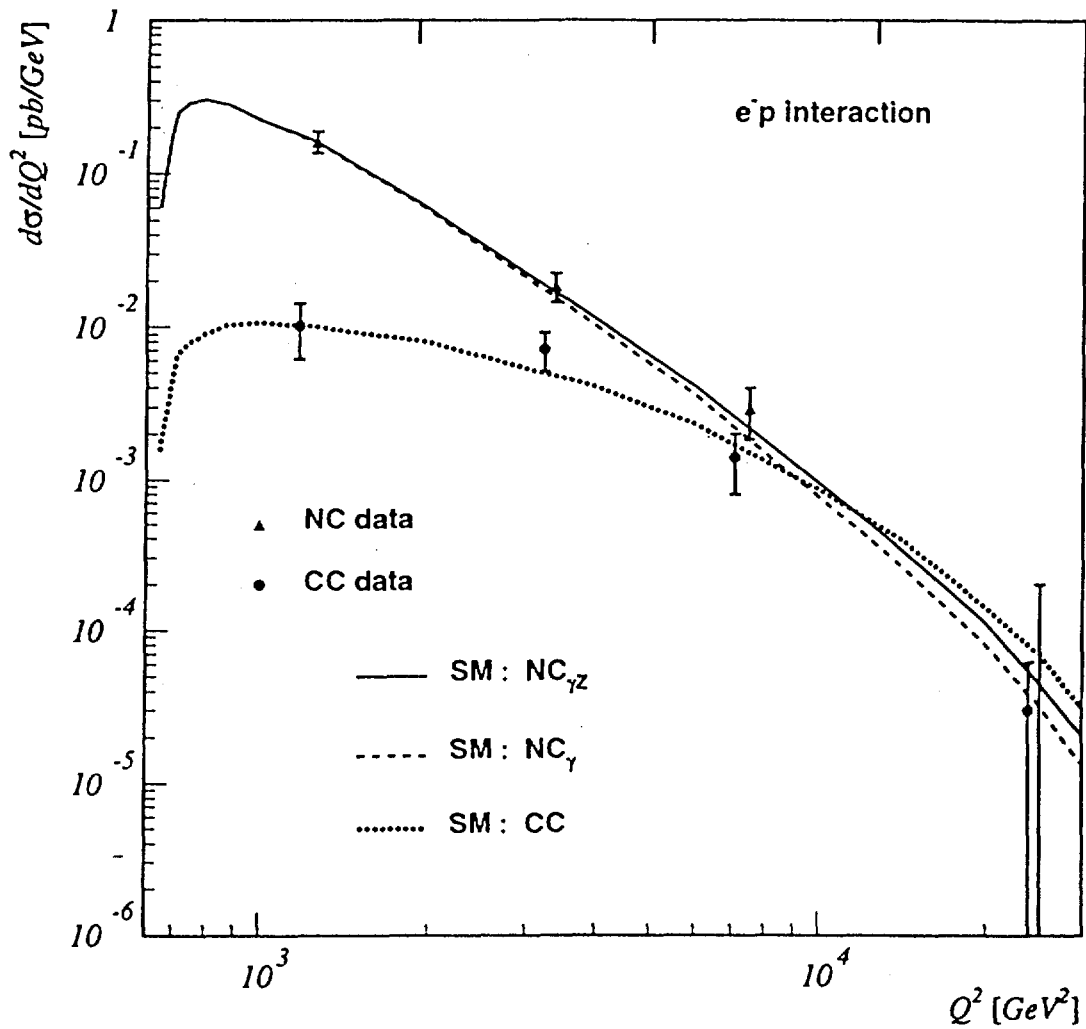


Fig.6.9 The differential cross sections  $d\sigma/dQ^2$  in four  $Q^2$  bins for (1993+1994)  $e^-p$  data, for charged and the neutral current processes respectively. The Standard Model predictions are also shown

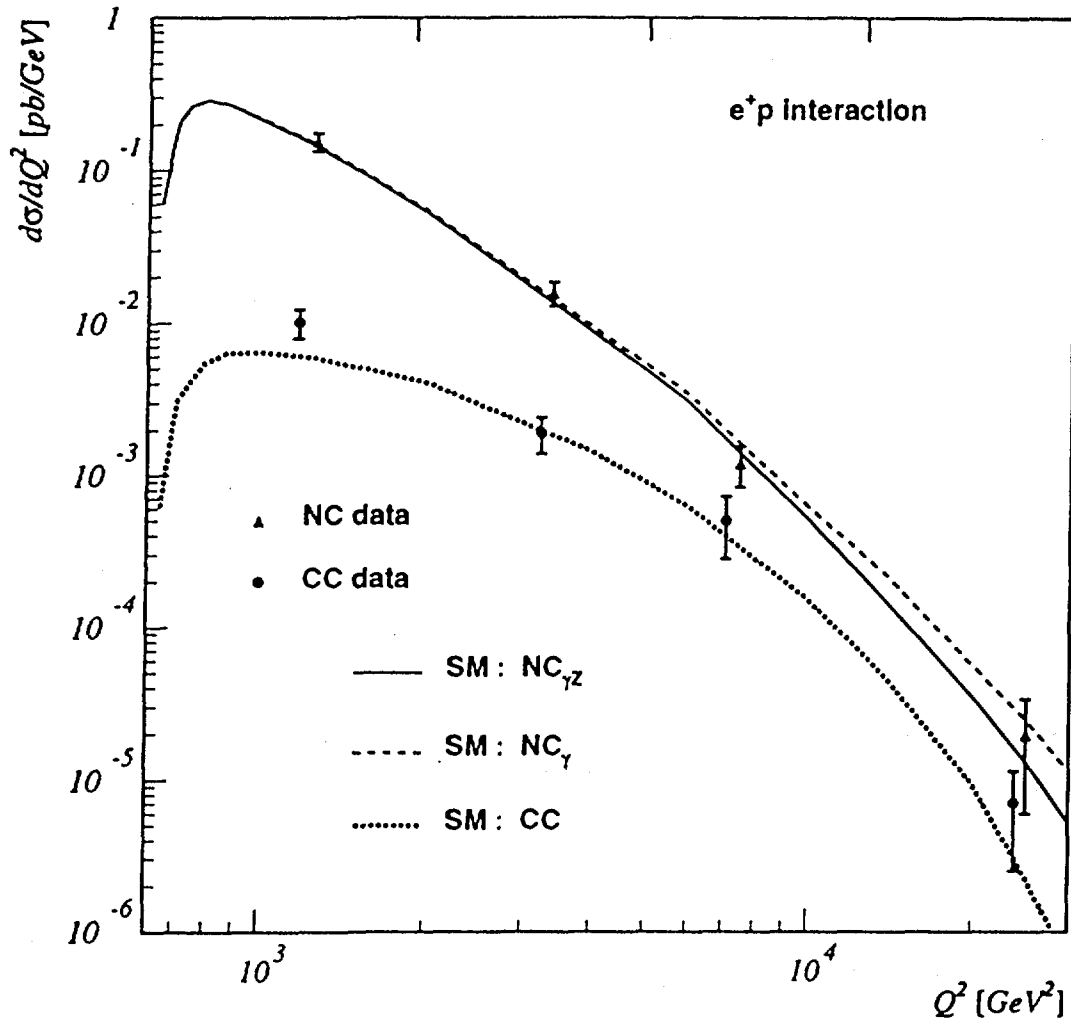


Fig.6.10 The differential cross sections  $d\sigma/dQ^2$  in four  $Q^2$  bins for 1994  $e^+p$  data, for charged and the neutral current processes respectively. The Standard Model predictions are also shown

From the plots we see that the cross sections of the Neutral and the Charged Current processes are of comparable magnitudes at the large  $Q^2$  range ( $Q^2 \geq 5000 \text{ GeV}^2$ ). The Charged Current cross sections are always lower than the Neutral Current cross section in the whole  $Q^2$  range for  $e^+p$  interactions, while they exceed the Neutral Current cross section at very large  $Q^2$  in  $e^-p$  interactions. This difference comes from that, in the  $e^+p$  interactions, the main contributions to the Charged Current cross sections come from the  $d$  and  $\bar{u}$  quarks in the proton scattering with  $e^+$ , while in  $e^-p$  interactions the main contribution comes from  $u$  quark scattering with  $e^-$ . The  $y$ -dependences of the contributions from these quarks in the cross section formula are different, as shown in equations (2.46) and (2.47).

A good agreement between the measured cross sections and the Standard Model predictions can be observed in the plots. The neutral current cross sections are also in good agreement with the previous measurements at HERA based on the informations from the scattered lepton [60]. Due to the limited statistics of the data sample, the contributions to the neutral current process from the dominant  $\gamma$ -exchange and from the  $\gamma-Z^0$  interference or  $Z^0$ -exchange can not be distinguished at present. Moreover, in the neutral current case we would expect variations due to the different weak interaction of the  $e^-$  and  $e^+$  via  $Z^0$ -exchange (see formula (2.38), Chapter 2). This effect will also be studied with the forthcoming increase of the HERA luminosity.

### 6.3 $W$ Mass from the Fit to the $Q^2$ -Distributions of the Charged Current

A  $\chi^2$  fit to the  $Q^2$ -distributions for the charged current processes can be used to derive the mass of the  $W$  boson. Assuming  $n_i$  ( $i = 1, 2, 3, 4$ ) is the observed number of CC events in bin  $i$ , the function  $\chi^2(M_W)$  can be constructed as following:

$$\chi^2(M_W) = \sum_{i=1}^4 \left[ \frac{n_i^{th}(M_W) - n_i}{\sqrt{n_i}} \right]^2, \quad (6.11)$$

where  $n_i^{th}(M_W)$  is the theoretical prediction of the number of events in the bin  $i$ , as a function of the propagator mass  $M_W$ :

$$n_i^{th}(M_W) = \mathcal{L} \cdot \varepsilon_i \cdot \sigma_i(M_W), \quad (6.12)$$

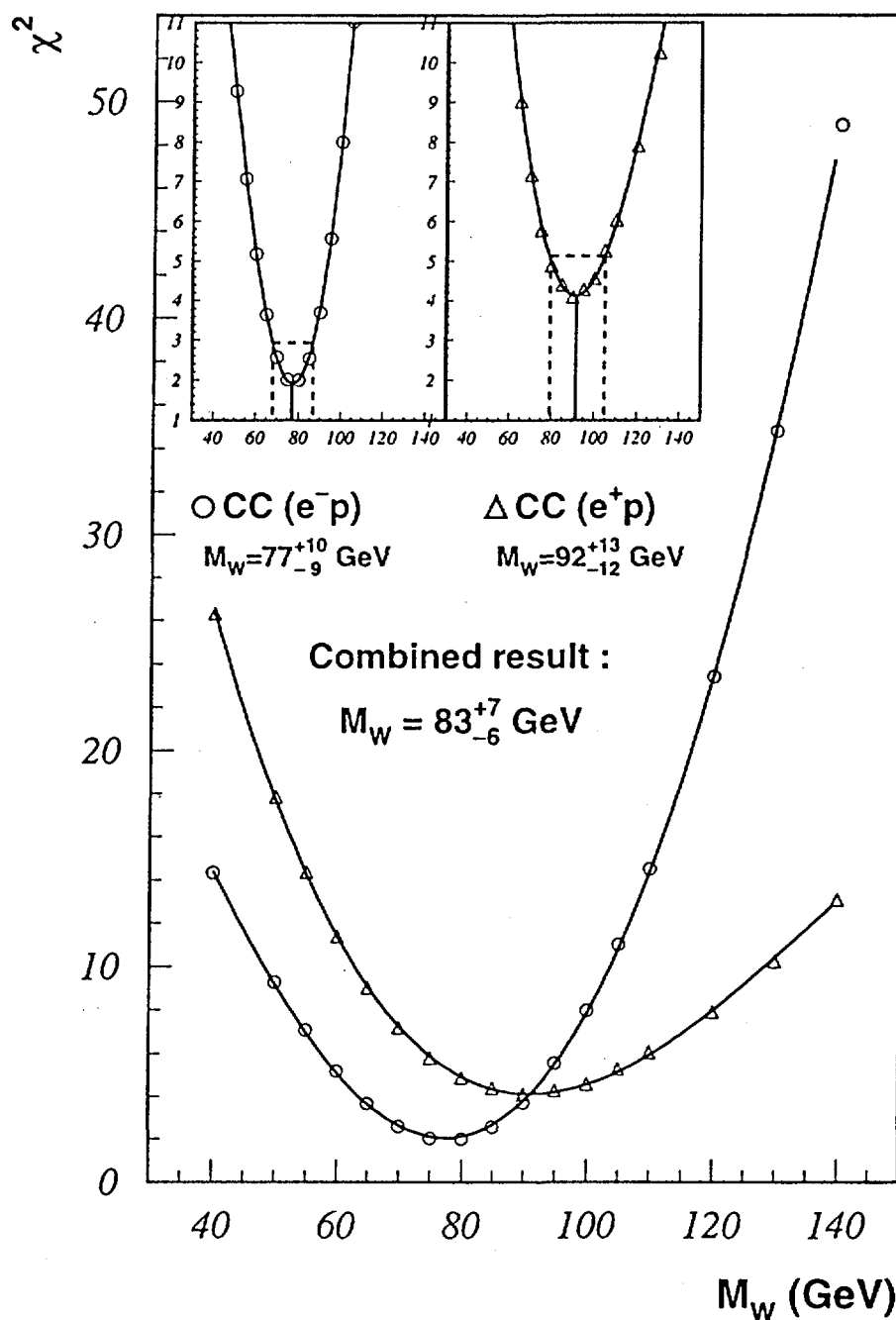


Fig.6.11 The  $\chi^2$  fit of the shape of the differential cross sections  $d\sigma/dQ^2$  for  $e^-p$  and  $e^+p$  interactions respectively. The masses of  $W$  derived from the fits are also indicated in the plots, where the errors statistical are only. The combination of the two fit gives  $M_W = 83^{+7}_{-6}$  GeV (with the statistical errors).

$\mathcal{L}$  is the luminosity,  $\varepsilon_i$  is the correction factor for the detector response in bin  $i$ , and  $\sigma_i(M_W)$  is the theoretical cross sections integrated over  $Q^2$  range of bin  $i$ .

The results of the  $\chi^2$ -fits performed for  $e^-p$  and  $e^+p$  interactions are shown in Fig.6.11 respectively. We see that the  $e^-p$  processes are more sensitive to the parameter  $M_W$ . The values of  $M_W$  corresponding to the minimum of the  $\chi^2$  curves ( $\chi^2_{min}$ ) are then obtained, the statistic uncertainties are determined from the increase of  $\chi^2$  by 1. We obtain:

$$M_W(e^-p) = 77^{+10+4}_{-9-3} \text{ (GeV)}, \quad M_W(e^+p) = 92^{+13+5}_{-12-10} \text{ (GeV)},$$

where the first error is statistical and the second error reflects the systematic uncertainties. These two results are compatible, and a combined fit result is

$$M_W = 83^{+7+5}_{-6-4} \text{ (GeV)}.$$

These  $W$  mass results are in good agreement with the previous measurements at HERA [58][57][64], with improved precision. The shape and the cross section analysis confirms that, the charged current processes in  $e^-p$  and  $e^+p$  interactions are both mediated by the exchange of the  $W$  boson with the same masses and different charge states.

# Chapter 7

## Conclusions

We have presented here the analysis of the electroweak part of the charged current  $e^\pm p \rightarrow \nu_e X$  and the neutral current  $e^\pm p \rightarrow e^\pm X'$  processes at high hadronic transverse momentum ( $P_t^{had} > 25$  GeV). The charged current and the neutral current events were selected in parallel, i.e. following the same vertex and trigger conditions, and the background rejection cuts were applied to the final NC and CC samples in the same way. The kinematic variables were calculated only using the informations from the hadronic energy flow.

The results from 1993 and 1994 data were combined. The  $e^+p$  interactions were only available in 1994. The measured integrated charged current cross sections  $\sigma^{CC}$  and the NC/CC ratios are summarized below, compared to the theoretical predictions from the Standard Model:

	(1993+1994) $e^-p$ -interaction	(1994) $e^+p$ -interaction
Integrated $\mathcal{L}[pb^{-1}]$ :	0.69	2.7
Num. of CC:	25	48
Num. of NC:	157	530
NC/CC:	$7.0 \pm 1.5(\text{stat.}) \pm_{-0.9}^{+0.6}(\text{syst.})$	$13.6 \pm 2.04(\text{stat.}) \pm_{-1.5}^{+1.1}(\text{syst.})$
$(\text{NC/CC})_{\text{theory}}$ :	6.80	15.57
$\sigma^{CC}[pb]$ :	$43.0 \pm 8.4(\text{stat.}) \pm_{-2.9}^{+2.9}(\text{syst.})$	$21.3 \pm 3.1(\text{stat.}) \pm_{-0.5}^{+1.0}(\text{syst.})$
$(\sigma^{CC})_{\text{theory}}[pb]$ :	40.7	15.2

The above results are in good agreement with the parallel work performed in other groups of H1 for the same analysis, with different strategy in data selection and kinematic variable reconstruction. The measured NC/CC ratios and the CC integrated cross sections agree well with the Standard Model predictions. The mass of the weak intermediate  $W$  boson implied by these results is also in good agreement with the Collider mass measurements, and excludes the asymptotic case where the propagator mass  $\rightarrow \infty$ . The effect of the  $W$ -propagator in the Deep Inelastic charged current process is observed, for the first time, in these measurements.

At present integrated luminosity, the statistics of the selected charged current events is poor and constitutes the main contribution to the measurement errors. The systematic uncertainties in the hadronic energy scale (4%) is also a significant source of error, and affects mainly the neutral current measurement due to its steep transverse momentum distribution.

The differential cross sections  $d\sigma/dQ^2$  at four  $Q^2$  values are also calculated, for the charged current and the neutral current processes and for  $e^-p$  and  $e^+p$  interactions respectively. The results agree well with the Standard Model predictions, and confirm that, at large momentum transfer, the weak and the electromagnetic interactions are of comparable strengths. The measured  $d\sigma/dQ^2$  for the neutral current process is also in good agreement with the early measurements at HERA based on the informations from the scattered lepton. A  $\chi^2$  fit to the shape of the charged current distribution gives the mass of  $W$  boson  $M_W = 83_{-6}^{+7+5}$  GeV, which is in agreement with the previous measurements at HERA, with improved precision. It is also in agreement with the values measured in  $\bar{p}p$  experiments or LEP.

The limited statistics of the selected data samples at present made it difficult to conclude on the higher order effects and the possible deviation from the Standard Model. With increasing cumulated luminosity and future efforts to reduce the systematic uncertainties, more precise measurements on the electroweak parameters are foreseen. For example,  $W$ -mass may be fitted from the shape of the charged current  $Q^2$  distribution with more precision. Using  $y$ -distributions of the charged current one may study the helicity structure of  $W^\pm$ , while using  $x$ -distributions one may investigate the interactions due to different parton contributions in the QPM frame.

# Bibliography

- [1] C. Quigg, *Gauge Theories of the Strong, Weak and Electromagnetic Interactions, Frontiers in Physics ed.*
- [2] Particle Data Group, *Phys.Rev.D50(1994)1173.*
- [3] F. Halzen, A. Martin; *Quarks and Leptons, J. Willey and Sons ed. , 1984.*
- [4] S.L. Glashow, *Nucl.Phys.22(1961)579.*
- [5] S. Weinberg, *Phys. Rev. Lett. 19(1967)1264*
- [6] A. Salam, *Elementary Particle Theory, ed. N.Svartholm (Stockholm,1969),p.367.*
- [7] J. Goldstone, *Nuov. Cim. 19(1961)154.*
- [8] E. Witten, *Nucl. Phys. B258(1985)75.*
- [9] J.C. Pati, A. Salam, *Phys. Rev. D10(1974)275*, R.N. Mohapatra, J.C. Pati, *Phys. Rev. D11(1975)*; G. Senjanovic, R.N. Mohapatra, *Phys. Rev. D12(1975)1502.*
- [10] W.Buchmüller et.al., *Proceeding of Phys. at HERA Vol.2(1991)1003, Hamburg.*
- [11] D. Giffiths, *Introduction to Elementary Particles, J. Willey and Sons ed.*
- [12] M.Anselmino et.al., *Phys., Rev. 261(1995)1.*
- [13] M.Anselmino et.al., *Z. Phys., C64(1994)267.*
- [14] W.Fetscher et.al., *Phys.Lett., B173(1986)102.*
- [15] R.E. Taylor, *Rev.Mod.Phys., 63(1991)573.*
- [16] J.Blümlein, M.Klein, *Structure functions and QCD tests, Proceeding of Phys. at HERA, Vol.1(1991)101.*

- [17] G.Ingelman et al., Deep Inelastic Physics and Simulation, Proceeding of HERA workshop, Vol.1(1987)3, Hamburg.
- [18] E. eichten et.al., Rev. Mod. Phys. 56(1984)579 and 58(1986)1047.
- [19] M. Glück et.al., Z.Phys.c13\*1982)119; D.W. Duke, J.F. Owens, Phys. Rev. D30(1984)49; E. Eichten et.al., Rev. Mod. Phys. 56(1984)579,ibid.58 (1986) 1047; A.D. Martin et.al., Rutherford preprint RAL-87-052.
- [20] A. Kwiatkowski et al., HERACLES, an event generator for ep interactions at HERA including radiative processes, V4.4.
- [21] M. Consoli, et.al., CERN 89-08(1989), Vol.1, p.7; W. Hollik, Fortschr. Phys. 38(1990)165
- [22] LEP2 Workshop, CERN 1995.
- [23] LEP Collaborations, A Combination of Preliminary LEP Electroweak Measurement and Constraints on the Standard Model, CERN-PPE/95-172.
- [24] P.Haberl et al., Contact interactions and new heavy bosons at HERA, Proceeding of Phys. at HERA, Vol.2(1991)1133, Hamburg.
- [25] V.Brisson et al.,Measurement of electroweak parameters at HERA, Proceeding of Phys. at HERA, Vol.2(1991)947, Hamburg.
- [26] Evidence for Top Quark Production in  $\bar{p}p$  Collisions at  $\sqrt{s} = 1.8$  TeV, F. Abe et.al., FERMILAB-PUB-94/097-E.
- [27] W.Buchmüller et al.,Electroweak physics, Proceeding of Phys. at HERA, Vol.2(1991)919, Hamburg.
- [28] J.Blümlein et al.,Berlin preprint PHE 88-01(1988).
- [29] K.Charchula,DESY 91-093.
- [30] W.Buchmüller and G.Ingelman eds.,DESY, Hamburg (1992),vol. I,II,III.
- [31] H1 Collab.,I.Abt et al.,The H1 detector at HERA, DESY preprint 93-103(1993).
- [32] B.H. Wiik, HERA Status, Proceeding of Phys. at HERA, Vol.1(1991)1, Hamburg.
- [33] H1 Collab.,C.Berger et al.,Technical proposal for the H1 detector, DESY-report PRC 86-02, Hamburg(1986).

- [34] H1 Collab., B. Andrieu et al., The H1 Liquid argon calorimeter system, Nucl. Instrum. Meth. A336(1993)460-498.
- [35] J. Spiekermann, HV Correction for the H1 LAr Calorimeter; H1-01/95-422.
- [36] H1 Collab., B. Andrieu et al., Beam Test and Calibration of The H1 Liquid Argon Calorimeter with Electrons, DESY 94-055, March 1994.
- [37] E. Borchini et al., H1 calo. group, Electron identification in liquid argon calorimeter, Nucl. Phys. B(Proc. Suppl.)32(1993)97.
- [38] H1 Collab., B. Andrieu et al., Results from pion calibration runs for the H1 liquid argon calorimeter and comparison with simulations ; Nucl. Instr. Meth. A336(1993)499-509.
- [39] M. Korn, J. Spiekermann, Hadron Energy Measurement with the H1 LAr Calorimeter; H1-12/94-417.
- [40] F. Niebergall, Calibration and data correction of the H1 tail catcher at CERN, H1 report 02/91-163, DESY.
- [41] H. Bergstein et al., Beam calibration of the H1 tail catcher at CERN, H1-report 10/91-197.
- [42] H. Bergstein, Ph.D thesis, RWTH Aachen(1993), unpublished.
- [43] E. Fretwurst et al., Nucl. Instrum. Meth. A288(1990)1.
- [44] V. Karimäki, Fast code to fit circular arcs, Helsinki University report HU-SEFT-1991-10, unpublished.
- [45] S. Burke et al., Track finding and fitting in the H1 forward track detector, H1-03/95-434.
- [46] R. Früwirth, Nucl. Instrum. Meth., A262(1987)447.
- [47] H. Krehbiel, The H1 trigger decider: from trigger elements to L1-keep, H1 internal note 239(1992).
- [48] S. Eichenberger et al., Nucl. Instrum. Meth. A323(1992)532. T. Wolff et al., Nucl. Instrum. Meth. A323(1992)537. B. Andrieu et al., Nucl. Instrum. Meth. A336(1993)460. T. Ahmed et al., A pipelined first-level forward muon drift chamber trigger for H1, Proc. Int. Conf. on Computing in High Energy Physics 1992, Annecy, France, 1992, pp. 218-221.

- [49] W.J.Haynes, Experiences at HERA with the H1 data acquisition system, Proc. Int. Conf. on Computing in High Energy Physics 1992, Annecy, France,1992, pp. 151-161.
- [50] F. Sekkow et al., Experience with the first level trigger of H1, H1 Note, H1-11/94-407.
- [51] A. Campbell, IEEE Trans. NS-39(1992)255.
- [52] S. Rieß, Common event vertex from central and forward tracks using a Kalman filter, H1-08/95-453.
- [53] C.Pascaud, A maximum likelihood approach for vertex fitting, private communication.
- [54] Zhiqing Zhang, background filter for F2 study, private communication.
- [55] J.F Laporte, EPOKEPIK version 1.00/00, H1-03/93-280.
- [56] M.Flieser, Ph.D.thesis TU Munich, in lit.
- [57] H1 Collab., S. Aid et.al., Measurement of the  $e^+$  and  $e^-$  induced charged current cross section at HERA, Z. Phys.C67(1995)565.
- [58] H1 Collab.,T.Ahmed et.al.,Z.Phys.C66(1995)529.
- [59] F. Jacquet and A. Blondel, Proceedings of the study of an ep facility for Europe 79/48(1979), p. 391-394, U. Amaldi ed.
- [60] H1 Collab., S. Aid et al., Leptoquarks and compositeness scales from a contact interaction analysis of deep-inelastic  $e^\pm p$  scattering at HERA, Phys. Lett. B 353(1995)578.
- [61] H1 Collab., S. Aid et al., DESY 96-xxx (new F2 paper).
- [62] A.D. Martin, W.J. Stirling and R.G.Roberts, RAL preprint 94-055(1994).
- [63] T. Ahmed et.al., Phys.Lett. B324(1994)241.
- [64] M. Derrick et.al., ZEUS Collaboration, Phys.Rev.Lett. 75(1995)1006.

## Résumé

Le Modèle Standard de la Théorie Electrofaible peut être testé dans les interactions  $e^\pm p$  à HERA. L'énergie de  $\sim 300$  GeV dans le centre de masse permet d'atteindre le domaine cinématique où les interactions via  $Z^0$  ou  $W^\pm$  deviennent prédominantes.

Ce travail présente l'analyse des processus des courants neutres et chargés dans les données  $e^\pm p$  collectées en 1993 et 1994 par l'expérience H1. Après une coupure sur le moment transversal de 25 GeV/c pour le système hadronique, nous avons déterminé le rapport des sections efficaces des courants neutres et chargés, ainsi que la section efficace intégrée des courants chargés. Les événements courants chargés et neutres ont été sélectionnés suivant les mêmes critères techniques, de rejet de bruits de fond, de déclenchement et de détermination du vertex d'interaction (pour ce dernier nous avons proposé une méthode originale). Le calcul de variables cinématiques à partir des variables du système hadronique, a permis de mesurer les distributions des rapports courants neutres et courants chargés en fonction du transfert du moment, ainsi que pour les courants chargés seuls.

Les résultats sont en accord avec le Modèle Standard. La masse du boson  $W$  déterminée dans cette analyse confirme les résultats de mesures dans les autres expériences. L'effet de propagateur du boson  $W$  dans les interactions courants chargés profondément inélastiques a été observé pour la première fois.

### Mots clés:

HERA

H1

Interaction électrofaible

Courant Chargé

Courant Neutre